Aix-Marseille Université

Thèse Doctorale

Modelling peanuts in barred galaxies: Gas flows and constraints on the dark matter content

---

Auteur:
Frantzeska Fragkoudi

Thèse dirigée par:
Dr. Evangélie Athanassoulas

Thèse co-dirigée par:
Dr. Albert Bosma

Astrophysique et Cosmologie
Ecole Doctorale 352
Physique et Sciences de la Matière

30 Octobre 2015

Jury:

Phillip Amram (Président du Jury)
Johan Knapen (Rapporteur)
Heikki Salo (Rapporteur)
Glenn van de Ven (Examinateur)
Evangélie Athanassoulas (Directeur)
Albert Bosma (Co-directeur)

"Σα βγεις στον πηγαιμό για την Ιθάκη, να εύχεσαι νάναι μακρύς ο δρόμος, γεμάτος περιπέτειες, γεμάτος γνώσεις."

Κ. Καβάφης

"It has been said that astronomy is a humbling and character-building experience. There is perhaps no better demonstration of the folly of human conceits than this distant image of our tiny world. To me, it underscores our responsibility to deal more kindly with one another, and to preserve and cherish the pale blue dot, the only home we've ever known."

Carl Sagan

Abstract

In this thesis I explore the dynamical properties of barred galaxies, specifically focussing on those containing Boxy/Peanut (B/P) bulges. I employ *dynamical models*, derived from images of galaxies, to study the amount of baryonic and dark matter present in their central regions, the pattern speed of bars and the effects of substructures such as B/P bulges on gas inflow in galaxies.

Although a large number of barred galaxies contain B/P bulges these have not been included in dynamical models in the past. For the first part of the thesis I explore the effects that the modelling of a B/P bulge has on the estimates of the stellar gravitational potential, forces, orbital structure and bar strength. I show that by neglecting the geometry of a B/P bulge, considerable errors can be introduced in the dynamical modelling.

From extended rotation curves we know that there is a considerable amount of dark matter present in galaxies. However without a robust measurement of the mass-to-light ratio (M/L) of galactic discs, we cannot determine the exact amount of dark matter present. An independent measurement of the M/L can be provided using dynamical probes of the mass distribution, such as the morphology of the dust lanes in barred galaxies. For this part of the thesis, the goal is to constrain the M/L, the bar pattern speed and the height function of the nearby galaxy NGC 1291, by modelling the gas distribution in the galaxy via hydrodynamic simulations. The bar induces shocks in the gas and therefore by matching the shock loci with the observed dust lanes we can constrain the ratio of baryonic to dark matter within the central regions of this galaxy. The results suggest that baryonic matter dominates in the central region of NGC 1291, i.e., the disc is close to "maximal", and that it contains a fast-rotating bar. The questions of disc maximality and whether bars are fast or slow are both controversial and open issues, at the centre of many dynamical studies; by using physically motivated models, I am therefore able to contribute to the ongoing debate on these topics.

In the last part of the thesis I explore one of the main aspects of the secular evolution phase of galaxies, i.e. the bar-induced gas inflow to the central regions. This inflow is responsible for a number of processes which shape the evolution of galaxies, such as the formation of discy bulges, nuclear star formation and the creation of a fuel reservoir for AGN activity. As a large amount of galaxies contain B/P bulges – which I show in this thesis have a considerable effect on the dynamical properties of galaxies – I examine the effect that B/P bulges have on the gas inflow to the central regions by running hydrodynamic gas response simulations. I measure the gas inflow rate and total gas mass within the central kpc, and find that B/P bulges reduce the amount of gas inflow, which could have consequences on the build up of the central regions of barred galaxies.

Résumé

Dans cette thèse, j'explore les propriétés dynamiques des galaxies barrées, en particulier les galaxies contenant des "bulbes cacahuète" (B/P). J'utilise des modèles dynamiques, qui peuvent être dérivés des images de galaxies observées, pour étudier la quantité de matière baryonique et noire dans les régions centrales des galaxies, ainsi que la vitesse de rotation des barres et les effets des structures telles que B/P sur l'écoulement du gaz dans ces galaxies.

Bien qu'un grand nombre de galaxies barrées contiennent des bulbes B/P, ceux-ci n'ont pas été inclus dans des modèles dynamiques dans le passé. Dans la première partie de cette thèse, j'explore les effets de la modélisation d'un B/P aura sur les estimations du potentiel gravitationnel, les forces, la structure orbitale et la force de la barre. Je montre que, en négligeant la géométrie d'un B/P, des erreurs considérables peuvent être introduites dans la modélisation dynamique.

Nous savons, à partir des courbes de rotation étendues, qu'il y a une quantité considérable de matiére noire présente dans les galaxies. Toutefois, sans une mesure solide de la proportion de la valeur du paramètre masse-à-luminosité (M/L) des disques galactiques, on ne peut pas déterminer la quantité exacte de la matière noire présente. Une mesure indépendante du M/L peut être fournie en utilisant des sondes dynamiques de la distribution de la masse, telles que la morphologie des bandes de poussière dans les galaxies barrées. Dans cette partie de la thèse, le but est de contraindre le M/L, la vitesse de rotation de la barre et la fonction de la hauteur de la galaxie proche NGC 1291, par la modélisation de sa distribution de gaz, à partir de simulations hydrodynamiques. La barre induit des chocs dans le gaz et, de ce fait, en faisant correspondre les chocs avec les bandes de poussière observées, nous pouvons contraindre la proportion de matière noire et baryonique dans la région centrale de cette galaxie. Les résultats suggèrent que la matière baryonique domine dans la région centrale de NGC 1291, c'est-à-dire le disque est proche d'être *maximal*. En outre, la rotation de la barre est rapide. J'utilise donc des modèles physiquement motivés, pour contribuer au dèbat en cours sur ces deux questions ouvertes, qui sont au centre de nombreuses études dynamiques.

Dans la dernière partie de la thèse, j'explore l'un des principaux aspects de la phase d'évolution séculaire des galaxies, c'est-à-dire, l'arrivée du gaz dans les régions centrales à cause de la barre. Cet afflux peut être responsable pour un certain nombre de processus qui façonnent l'évolution des galaxies, comme la formation des bulbes *discy*, la formation des étoiles aux regions centrales et la création d'un réservoir de carburant pour l'activité AGN. Un grand nombre de galaxies contiennent des bulbes B/P – qui, comme je démontre dans cette thèse, ont un effet considérable sur les propriétés dynamiques des galaxies –j'examine ainsi l'effet que ceux-ci ont sur le flux de gaz vers les régions centrales, utilisant des simulations hydrodynamiques. Je mesure le flux et la masse totale de gaz dans le kpc central, et je constate que les bulbes B/P réduisent le taux d'accréfion du gaz, ce qui pourrait avoir des conséquences sur l'accumulation de matiére dans les régions centrales des galaxies barrées.

Résumé Étendu

L'objectif de cette thèse était d'utiliser les potentiels dérivés des images de Spitzer, en particulier du relevé S^4G (Sheth et al., 2010), afin de mener à bien un certain nombre d'études dynamiques; ces potentiels sont aussí appelés des modèles dynamiques. Afin d'obtenir ces modèles un certain nombre d'hypothèses doit être fait, l'une d'elles étant la fonction de la hauteur de la galaxie que nous utilisons. J'ai d'abord travaillé à rendre ces modèles dynamiques aussi précis que possible, en explorant les différentes fonctions d' hauteur, en particulier ceux des galaxies barrées qui sont le sujet d'étude principal de la thèse. Par conséquent, dans la première partie de la thèse j'explore les effets des bulbes cacahuète sur les modèles dynamiques. Je décris ensuite les simulations hydrodynamiques utilisés pour effectuer le reste du travail dans la thèse. J'étudie en détail la structure dynamique de la galaxie NGC 1291, et je détermine son rapport masse/luminosité (M/L dans la suite) et la vitesse de rotation de la barre. Enfin, j'explore les effets des bulbes cacahuètes sur l'afflux de gaz vers les régions centrales. Dans les pages qui suivent, je décris brièvement chacune de ces entreprises.

Les effets de bulbes cacahuètes sur les modèles de galaxies

Les modèles dynamiques ont été largement utilisés dans la littérature pour étudier les propriétés des galaxies barrées, à partir de leur structure orbitale et de la cinématique du gaz, de leur M/L et de leur contenu de matière noire. Bien qu'un grand nombre de galaxies barrées contient des bulbes cacahuète (B/P), l'effet de ces bulbes sur les modèles dynamiques n'a pas été étudié dans le passé. Je fais un usage intensif de modèles dynamiques dans les prochains chapitres de cette thèse, afin d'étudier le M/L de NGC 1291, sa teneur en matière noire, la vitesse de rotation de la barre et l'afflux gazeux. Par conséquent, afin d'obtenir des modèles dynamiques aussi précis que possible, j'ai réalisé une étude sur les effets des bulbes cacahuètes sur les modèles dynamiques, à savoir leur effet sur la structure orbitale, les forces et la barre force du modèle. Je trouve qu'un bulbe cacahuète a un effet significatif sur les différentes propriétés du modèle, et devraient donc être incluses dans les modèles afin pour eux d'être aussi précis que possible.

Pour créer un modèle dynamique d'une galaxie nous devons d'abord connaitre sa distribution de densité. La densité de surface projeté peut être obtenu à partir d'images de luminosité de surface d'une galaxie de face disque en supposant un ratio M/L. Il est important que ces images soient prises dans une gamme de longueurs d'onde qui minimise l'effet de l'extinction de la poussière, et ou on trace la vieille population stellaire (par exemple, le Spitzer 3.6 μm bande). Dans ce travail, j'utilise une image d'une galaxie vue de face, qui nécessite pas de rendre compte de l'extinction par la poussière, ni d'attribuer un M/L, vu que notre image bidimensionnelle donne directement la densité de surface. Une fois la densité de surface obtenue, nous devons assigner une fonction d'hauteur, et ensemble, ils nous donnons la distribution de densité en trois dimensions, à partir de laquelle nous pouvons calculer le potentiel de la composante stellaire de la galaxie. Cette méthode de calcul du potentiel comprend une intégration simple

à trois dimensions de la distribution de densité et est appelée la méthode 3DF. Le potentiel est calculé en coordonnées cartésiennes par

$$\Phi(x,y,z) = \\ -G\int_{-\infty}^{\infty}\int_{-\infty}^{\infty}\int_{-\infty}^{\infty}\frac{\rho(x',y',z')}{\sqrt{\sum_{j=1}^{3}(x'_j-x_j)^2+\epsilon^2}}\mathrm{d}x'\mathrm{d}y'\mathrm{d}z', \tag{1}$$

où G est constante gravitationnelle de Newton, ρ est la densité et ϵ est la longueur de lissage qui est nécessaire pour éliminer le bruit au détriment d'un léger biais (Merritt, 1996, Athanassoula et al., 2000).

J'utilise la méthode 3DF sur la distribution de densité dérivée d'une image vue de face d'une galaxie isolée simulée et différentes fonctions de hauteur (qui sont décrits plus bas). Les conditions initiales de la simulation à partir de laquelle l'image a été construite, comprennent un halo de matiere noire de forme spherique, un disque stellaire exponentielle et 75% de gaz (pour plus d'informations sur la simulation, le lecteur est invité à examiner le modele gtr116 dans Athanassoula, Machado, and Rodionov (2013)). L'image est construite à partir de la composante des étoiles et la morphologie rappelle celle de nombreuses galaxies fortement barrées.

Afin d'obtenir la densité en trois dimensions d'un disque de la galaxie à partir d'une image bidimensionnelle nous devons supposer une fonction d'hauteur, ce qui définit la façon dont la densité diminue en fonction de z de l'équatorial $z = 0$. La fonction de la hauteur et le "hauteur d'échelle" (z_0) peuvent affecter les résultats, et nous devons donc utiliser la fonction d'hauteur qui se rapproche le mieux celui de la galaxie que nous essayons de modéliser. La fonction de la hauteur peut être constante ou peut changer avec la position. Dans le cas où elle est constante par rapport a la position je suppose, pour simplifier, que la distribution de densité peut être écrit comme

$$\rho(x,y,z) = \Sigma(x,y)F(z), \tag{2}$$

où ρ est la répartition de densité tridimensionnelle, Σ est la densité de surface à deux dimensions, et F est la fonction de l'hauteur. Dans le cas plus général où la fonction d'hauteur dépend de la position dans la galaxie, comme ce serait par exemple la fonction de la hauteur décrivant une bulbe cacahuète, les changements du hauteur d'échelle sont fonction de la position. Dans ce cas, la distribution de densité serait donnée par,

$$\rho(x,y,z) = \Sigma(x,y)F(x,y,z), \tag{3}$$

où la normalisation de la fonction de la hauteur est

$$\int_{-\infty}^{\infty} F(x,y,z)\mathrm{d}z = 1. \tag{4}$$

Il est à noter que la masse du modèle est toujours le même; la fonction de la hauteur détermine simplement la densité volumique de la galaxie, par ajustement de l'épaisseur du disque.

Jusqu'à présent dans la littérature, des fonctions d'hauter indépendant de la position ou 'fonctions plates' ont été utilisées lors de la modélisation des galaxies barrées. Donc j'utilise également une fonctions d'hauteur plat et une qui represent le bulbe cacahuète dans cette étude pour faire des comparaisons:

$$F(z) = \frac{1}{2z_0}\mathrm{sech}^2\left(\frac{z}{z_0}\right). \tag{5}$$

Pour obtenir la fonction d'hauteur pour le bulbe cacahuète, la distribution des particules le long de différentes coupes sont examiné à partir de la simulation. Je trouve que la somme de deux gaussiennes à deux dimensions peut fournir une approximation raisonnable pour le bulbe cacahuète. La fonction du bulbe cacahuète résultant est une fonction non-séparables de position et est donné par:

$$F(x,y,z) = \frac{1}{2z_0(x,y)}\mathrm{sech}^2\left(\frac{z}{z_0(x,y)}\right). \tag{6}$$

ou z_0(x,y) varie comme la somme de deux gaussiennes à deux dimensions:

$$\begin{aligned} z_0(x,y) =& A\exp\left(-\left(\frac{(x-x_0)^2}{2\sigma^2}+\frac{(y-y_0)^2}{2\sigma^2}\right)\right)+ \\ & A\exp\left(-\left(\frac{(x-x_1)^2}{2\sigma^2}+\frac{(y-y_1)^2}{2\sigma^2}\right)\right)+z_0^{disc}, \end{aligned} \tag{7}$$

Je calcule le potentiel et les forces pour la distribution de densité donnée par l'image utilisé et les différentes fonctions d'hauteur.

1. *Deux fonctions d'hauteur plates: sech et sech*^{2}

   Je compare les modèles obtenus par la mise en œuvre de deux fonctions de hauteur plates, sech et sech ^{2}, avec hauteur d'échelles équivalents, afin de démontrer que les différentes fonctions de hauteur plates n'affectent pas significativement les résultats. Au centre, la différence de potentiel est de seulement 1% et pour les forces, il est 5%, tandis que pour le reste de la grille de la différence entre les deux configurations est bien inférieur à 1% dans tous les cas. Si nous diminuons la valeur de la hauteur d'échelle les deux models produisent des résultats encore plus similaires. Cela arrive parce que le disque tend à

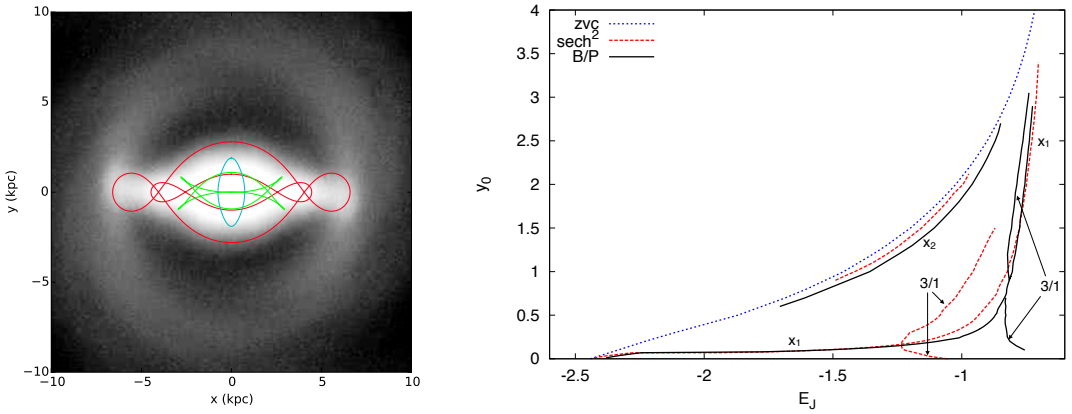

(a) Typical orbits in bar region

(b) Characteristic Diagram

FIGURE 1: *Gauche*: Quelques orbites typiques de la région de la barre pour le modèle avec une fonction d'hauteur $sech^2$, superposée sur l'image de la galaxie simulée gtr116: En rouge des orbites x_1 qui supportent la barre, en cyan des orbites x_2 qui sont perpendiculaire à la barre et en vert les orbites 3/1 (asymétriques par rapport à l'axe y). *A droite*: diagramme caractéristique (l'intersection de chaque orbite avec le y-axis en fonction de l'énergie Jacobi) pour les modèles créés à partir de l'image de la galaxie gtr116 et les deux fonctions de hauteur. La ligne noire solide donne le schéma caractéristique pour le modèle avec le bulbe cacahuète et la ligne en pointillée rouge donne le diagramme caractéristique pour un modèle avec une fonction sech^2. La ligne bleue pointillée montre la courbe de vitesse nulle (ZVC).

devenir infiniment mince, et la forme de la fonction de la hauteur devient moins important. On voit donc que la hauteur d'échelle, et non pas le profil vertical de la fonction de la hauteur, est principalement responsable de la création de différences dans les modèles.

2. *Fonctions d'hauteur plates et cacahuète*

   Je compare une fonction de l'hauteur plate et bulbe cacahuète. Les différences qui résultent de l'utilisation de ces deux configurations sont importants pour le potentiel et les forces. Cela est particulièrement vrai à proximité et autour de la zone de la hauteur maximale de le bulbe cacahuète, et en général dans et autour de la barre. La force peut être différente dans les deux cas jusqu'à 40%, ce qui est pas surprenant puisque autour du maximum du cacahuète, l'hauteur d'échelle est plus de trois fois la valeur de l'hauteur d'échelle du disque. Par conséquent, nous voyons qu'en ne prenant pas en compte la géométrie de la B/P bulbe, nous induisons des erreurs importantes dans le modèle, c'est à dire dans le potentiel et ses dérivés.

J'examine comment certaines des plus importantes familles de orbites périodiques seront influencées par la prise en compte de la géométrie d'un B/P. Pour ce faire, j'étude deux modèles: le modèle avec la fonction de la hauteur d'un bulbe cacahuète, et le modèle avec la fonction sech^2. La vitesse de rotation de la barre des deux modèles est configurée pour être telle que corotation se produise juste à l'extérieur du rayon de bar, de $1.4 > R_{CR}/R_{bar} > 1$, où R_{CR} et

R_{bar} sont respectivement le rayon de corotation et le rayon de la barre (Athanassoula 1992b). Les orbites sont calculées dans un cadre de référence en co-rotation avec la barre.

Dans la figure 2.6(a) je montre quelques orbites typiques de la région de la barre pour les potentiels analysés, superposées sur l'image de la galaxie simulée, gtr116, montrée de face. Les trois plus importantes familles d'orbites dans la région de la barre sont présentées, la famille x_1 (lignes rouges, le long du grand axe de la barre), x_2 (lignes cyan, perpendiculaires à l'axe principal de la barre) et 3/1 (les lignes vertes, asymétriques par rapport à l'axe de y), qui sont stables sur presque toute leur étendue.

Dans la figure 2.6(b) je trace le diagramme caractéristique des orbites périodiques, pour les deux cas avec et sans un bulbe cacahuète. Le diagramme caractéristique donne la valeur pour laquelle l'orbite croise l'axe de y en fonction de son énergie jacobienne (E_J, l'énergie dans le cadre de référence en rotation; Binney and Tremaine (2008)). Nous voyons que le schéma caractéristique des deux modèles diffère sensiblement. L'effet le plus notable en raison de la présence d'un B/P est le changement dans les loci de la bifurcation de la branche supérieure et inférieure de la famille 3/1. Ceci indique que, compte tenu de la géométrie d'un B/P, l'emplacement de la résonance 3:1 est modifiée. Ainsi, les orbites de la famille 3/1 sont diffèrents dans les deux cas.

La famille x_1 subit également des changements, dans la région E_J entre -1.1 et -0.8. Dans cette zone du diagramme, la mesure des orbites le long de l'axe du x atteint la région où l'effet de la B/P est maximal; Par conséquent, pour ces énergies les orbites des deux modèles sont diffèrents. Quand un B/P est présent, la mesure maximale des orbites x_1 est réduite de 12%, tandis que son étendue maximale sur le y-axis est réduite de 46% (mesurée à $x = 0$).

Pour la famille x_2, l'étendue est augmentée d'environ 43%. Comme la mesure de la famille x_2 est liée à la distance entre les deux résonances Lindblad (Inner Lindblad Resonances, ILR; Athanassoula 1992a), la distance entre ces deux résonances augmente aussi. Cette augmentation est due à un affaiblissement de la perturbation non-axisymmetrique: lorsque la géométrie de B/Ps est prise en compte dans le modèle, le hauteur d'échelle de la galaxie augmente et donc – puisque la quantité de masse est le même– la densité volumique dans le plan de la galaxie diminue. Cela conduit à une diminution de les forces tangentielles de telle manière que la perturbation non axisymétrique diminue, ce qui modifie la distance entre les deux ILR.

J'ai également étudiée l'effet des bulbes cacahuète sur la force de bar, comme indiqué par les forçages non-axisymétriques de la barre, Q_T. La forme ainsi que le maximum de Q_T sont affectés de façon significative par la prise en compte de la géométrie d'un bulbe cacahuète. La présence d'un bulbe cacahuète, en particulier sur les points où l'hauteur d'échelle est maximale, réduit la force de la barre. Par conséquent, les bulbes cacahuètes devraient être inclus dans les modèles afin de les rendre aussi précis que possible.

Détermination dynamique du M/L et de la vitesse de rotation de la barre: Le cas de NGC 1291

Depuis la découverte dans les années 70 que les courbes de rotation dérivés des observations HI

- qui vont bien au-delà du disque optique de galaxies - restent à plates (Roberts, 1976, Bosma, 1978, 1981), la nature et la distribution de la matière noire non-baryonique dans les galaxies a été une source de débat dans la communauté scientifique. Un des principaux problèmes avec la détermination de la distribution de la matière non-baryonique dans les régions centrales des galaxies est ce qui est devenu connu sous le nom "disque-halo dégénérescence". Cette dégénérescence se pose en raison du fait que les décompositions de la courbe de rotation dépendent de façon critique du rapport de la masse sur luminosité (M/L ou Υ) qui est affecté à la composante de disque stellaire. van Albada and Sancisi (1986) ont montré que les courbes de rotation peuvent être ajustés avec des valeurs très différentes pour la matière noire et baryonique; avec des modèles sans presque aucun disque jusqu'à des modèles où le disque contribue autant que possible à la courbe de rotation - sans créer un trou dans le halo de matière noire; cela est également connu sous le nom "hypothèse de disque maximale". Sackett (1997) a donné une définition plus concrète du disque maximale en déclarant qu'un disque est maximale si il contribue 85% $\pm$10% de la courbe de rotation à $R = 2.2\ h_r$, où h_r est la longueur d'échelle du disque. Cependant, il n'y a pas de preuve concluante pour prouver ou réfuter l'hypothèse du disque maximal et en fait il y a un certain nombre d'arguments à la fois pour (Athanassoula et al., 1987, Sackett, 1997, Weiner et al., 2001) et contre elle (Kuijken and Gilmore, 1991, Courteau and Rix, 1999), pour la Voie Lactée (Bissantz and Gerhard, 2002, Bissantz et al., 2003, Hamadache et al., 2006, Tisserand et al., 2007) ainsi que pour les galaxies externes (Bottema, 1993, Trott and Webster, 2002, Gnedin et al., 2007, Kranz et al., 2003).

Une façon d'obtenir une estimation du M/L du disque, et de briser la dégénérescence disque-halo, est en utilisant des estimations dynamiques du M/L du disque, comme ce que j'utilise dans cette étude. Pour obtenir une détermination dynamique du M/L, on peut utiliser les non-axisymmetries induites par la barre, ou d'autres structures non-axisymétriques tels que les bras spiraux. Le gaz, en étant collisional, il est sensible à des perturbations induites par les barres et les spirales, et peut donc être utilisé comme traceur de la force non-axisymétriques dans les galaxies. En exécutant des simulations dynamiques du gaz on peut obtenir des modeles qui ressemblent au mieux à la galaxie. L'hypothèse majeure de ces études est que le halo est dominé par la dispersion et donc est plus rond que le component stellaire. Ces types des etudes ont déjà été tentées par le passé pour les galaxies barrées (Lindblad et al., 1996, Weiner et al., 2001, Weiner, 2004, Zánmar Sánchez et al., 2008) et les galaxies spirales (Kranz et al., 2001, 2003). Ce type de modélisation a également été appliquée afin de déterminer la vitesse angulaire de la barre (Pérez et al., 2004, Sánchez-Menguiano et al., 2015).

Dans cette étude, j'examine les bandes de poussière présentes dans la galaxie voisine NGC 1291, et je vise à reproduire leur morphologie en utilisant des simulations dynamiques de gaz. Les bandes de poussière se trouvent dans les régions de la barre de nombreuses galaxies, car elles sont causés par l'augmentation de la densité du gaz en raison de chocs créés par des non-axisymmetries dans le potentiel (Prendergast, 1983, Athanassoula, 1992b). La morphologie des bandes de poussière est très dépendante du M/L du disque, de la vitesse de rotation de la barre, et de la fonction de la hauteur du disque. L'effet de ce dernier paramètre n'a pas été

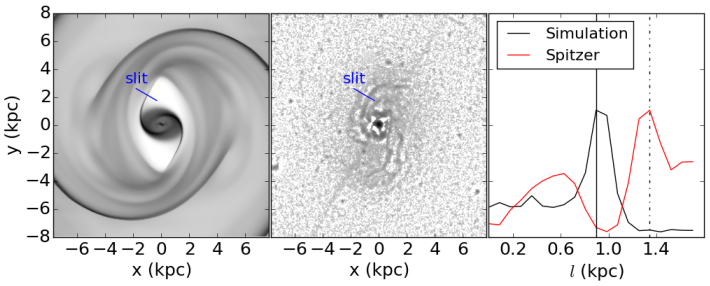

FIGURE 2: La comparaison entre l'emplacement des chocs dans les modèles et les observations. Un pseudo-fente est placée parallèlement au choc dans la simulation (à gauche) et l'image observée de 8μm (au milieu). Dans le panneau de droite, nous montrons la densité au long de la fente dans les deux images en fonction de la distance l.

étudiée dans le passé, mais je montre dans les sections suivantes qu'il joue un rôle crucial sur la forme des chocs créés dans le gaz.

J'ai mis quelques critères qui sont utilisés pour déterminer si un modèle ajuste bien les bandes de poussière observés, afin pour déterminer les meilleurs modèles:

1. L'emplacement des chocs primaires doit être aussi proche que possible des bandes de poussière dans l'image.
2. Le modèle devrait avoir un forte et dominante choc. Il devrait y avoir un choc qui est plus fort que tous les chocs secondaires formées dans le flux de gaz.
3. La forme des chocs doit correspondre aux bandes de poussière dans l'image 8μm et devrait également reproduire des éléments d'image 24μm.

Le méthode que nous utilisons dans cette étude pour quantifier la qualité des modèles, implique une mesure quantitative de la différence entre l'emplacement des chocs dans le modèle et les emplacements des bandes de poussière dans les images observées, noté ΔL. Nous mettons des pseudo-fentes perpendiculaires aux loci de les chocs dans les simulations d'écoulement du gaz et l'image observée, où le débit de gaz est mis en rotation en fonction de la rotation de la galaxie observée. Comme le montre la Figure 2 on trace la densité le long de la fente, où les maxima de la densité indiquent l'emplacement des chocs. L'emplacement des chocs dans la simulation et les observations sont ensuite comparés, et la distance entre ces deux valeurs est de ΔL. Nous plaçons la fente à un emplacement tel que le choc est visible dans les deux images, les image de 8 et 24μm. Cette méthode fournit une mesure quantitative de la qualité de l'ajustement entre le modèle et les observations. Cependant, comme nous ne sommes pas seulement intéressés par l'emplacement des chocs, mais aussi dans la forme des chocs, une inspection visuelle est toujours nécessaire pour une comparaison adéquate entre les modèles et les observations.

Pour trouver les meilleurs modèles d'ajustement aux observations j'ai suivi une procédure par élimination. D'abord, je choisis les meilleurs modèles d'ajustement comme indiqué par

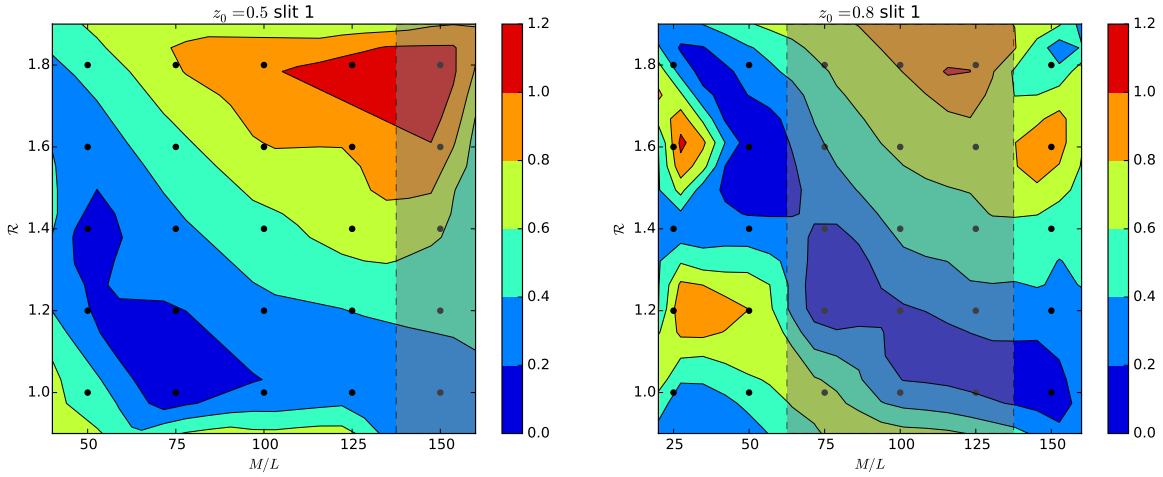

(a) z_0 = 0.5kpc

(b) z_0 = 0.8kpc

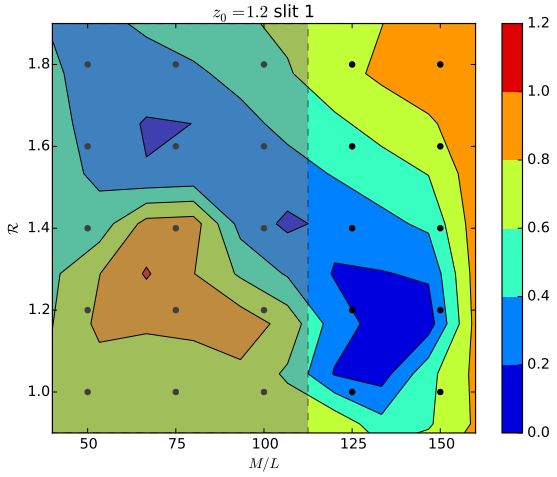

(c) z_0 = 1.2kpc

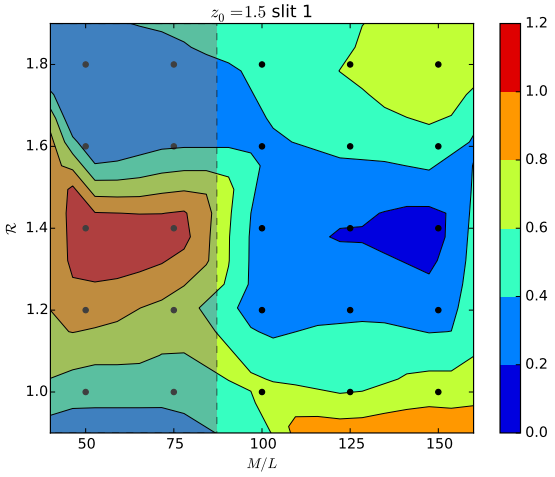

(d) z_0 = 1.5kpc

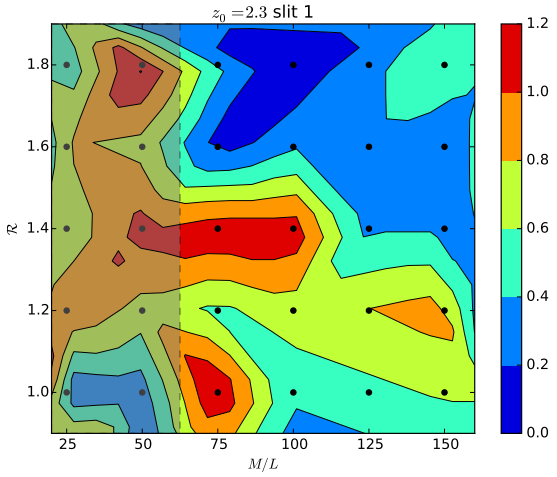

(e) z_0 = 2.3kpc

FIGURE 3: Graphiques de contour pour les séries de modèles avec différentes hauteurs d'échelle, de gauche à droite et de haut en bas, la hauteur d'échelle correspond à 0.5, 0.8, 1.2, 1.5 et 2.3 kpc respectivement. L'axe de x correspondent à M/L (en unités de pourcentage de $\Upsilon_{3.6}$, par exemple, M / L = 75 correspond à $0.75_{3.6}$). L'axe de y -axe donne $\mathcal{R}$, le rapport entre le rayon de Lagrange au rayon de la barre, R_L/R_b. Les points noirs correspondent à des points sur les grilles où nous avons des modèles. L'échelle de couleur donne la distance ΔL entre la position des bandes de poussière dans les images de 8 et 24μm et la densité maximale de gaz le long de la fente. La zone ombrée montre l'espace des paramètres contraints après prise en compte de la dispersion de vitesse verticale de la galaxie.

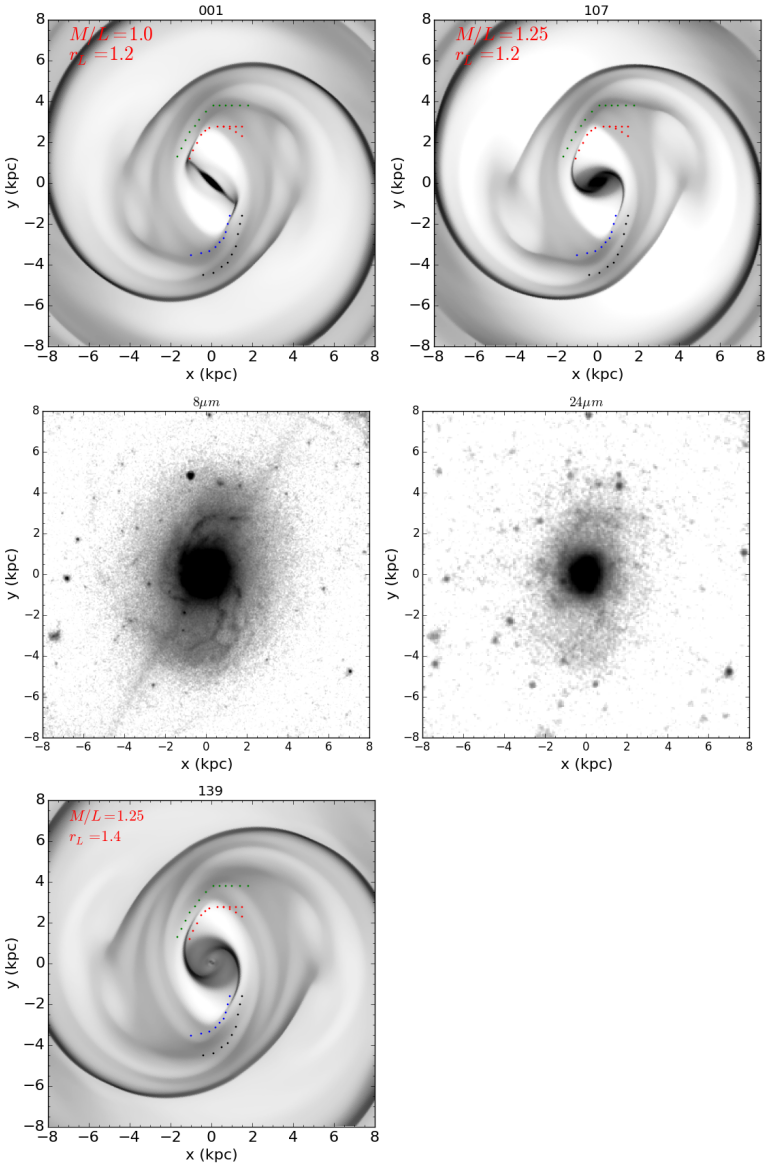

FIGURE 4: La densité de surface de gaz à deux dimensions pour les meilleurs modèles. La rangée du haut montre les modèles 001 et 107 qui ont z_0=0.8 kpc, M/L = 1.0 and 1.25$\Upsilon_{3.6}$ respectivement et r_L=1.2. Les panneaux intermédiaires présentent le 8 et 24μm images de NGC 1291pour comparaison. Dans les panneaux du fond le modèle 139 est montré. Il a z_0=0.8 kpc avec un bulge B/P avec longeur=1.5 kpc, M/L=1.25 et r_L=1.4

les tracés de contours dans les figures 4.13, à partir de l'espace des paramètres permis des modèles. Cela réduit le nombre de meilleurs modèles d'ajustement à 20 modèles. Ensuite, chaque modèle a été examiné visuellement afin de déterminer la qualité de l'ajustement en fonction des critères énoncés.

En general, des modèles avec des disques plus minces conviennent mieux, et un modèle avec hauteur d'échelle 2.3 kpc semble être exclu. Les modèles qui ajustent les mieux ont tous une hauteur d'échelle de 0.8 kpc, tandis que les modèles avec un disque encore plus mince ont tendance à donner un ajustement moins bon. En général, nous attendons l'épaisseur du disque se situe entre 0.8-1.2 kpc. Au dela de 1.2 kpc les modèles sont moins bons.

Les modèles les mieux ajustées sont présentés dans la figure 4.24 avec les images de NGC 1291 à 8 et 24μm pour comparaison; ce sont les modèles 001 et 107 qui correspondent à $z_0 = 0.8$ kpc sans B/P bulbe et ont M/L = 1 et 1.25$\Upsilon_{3,6}$ respectivement et un rayon de Lagrange R_L = 1.2. Le modèle 139 est aussi un ajustement relativement bon pour les bandes de poussière et dispose d'un B/P bulbe qui a une longueur de 1.5 kpc long de la barre, avec un M/L = 1.25 $\Upsilon_{3.6}$ et R_L= 1.4. Dans tous les modèles, les barres rapides sont préférées avec une valeur de $\mathcal{R} \leq 1.4$. Pour les bars plus lents les chocs ont tendance à être généralement trop décalées par rapport à la barre pour correspondre aux emplacements des bandes de poussière.

J'examine les courbes de rotation des meilleurs modèles d'ajustement. Le modèle 001 a un M/L = 1$\Upsilon_{3.6}$, ce qui contribue 74% de la courbe de rotation de la galaxie. Par conséquent, selon la définition par Sackett (1997) le disque de cette galaxie est juste en deçà du maximum. En répétant la même mesure pour les autres modèles les mieux ajustées, les modèles 107 et 139, qui ont tous deux M/L= 1.25 $\Upsilon_{3.6}$, ont un disque qui contribue 80% de la vitesse totale a un rayon $r = 2.2\ h_r$. Par conséquent, selon la définition de Sackett (1997), ces modèles sont des modèles du disque maximum; Ainsi, tous nos modèles les mieux ajustées semblent être compatible avec un disque maximal.

Ces résultats sont compatibles avec la plupart des résultats précédents dans la littérature en utilisant une approche similaire, c'est a dire la modélisation dynamique. Dans le travail par Weiner et al. (2001), ils montrent que la galaxie NGC 4123 ($V_{max} \approx$ 140 km/s), a un disque maximal. Zánmar Sánchez et al. (2008) trouvent que le disque de NGC 1365 est massive, bien que pas tout à fait maximal. Le travail de Kranz et al. (2003) montre que les deux galaxies les plus massives dans leur échantillon (ceux avec $V_{max} \geq 200$ km/s) avaient disques maximaux, tandis que les galaxies moins massives étaient submaximales. Il semble donc qu'il y ait un certaine désacord entre les résultats trouvés dans Weiner et al. (2001) et ceux dans Kranz et al. (2003), car NGC 4123 devrait avoir un disque submaximal selon les conclusions de Kranz et al. (2003). Nous sommes en accord avec leur travaux, c'est à dire le disque de NGC 1291, qui est une galaxie avec $V_{max} \geq 200$ km/s, est maximal. Cela semble montrer que les galaxies massives barrées ont tendance à avoir des disques massives que la plupart des études ci-dessus trouvent également. Savoir ce qui se passe pour des masses inférieures reste une question ouverte.

Nos résultats sont incompatibles avec d'autres méthodes pour déterminer de manière dynamique le M/L, tel que par exemple le sondage DiskMass (Martinsson et al., 2013), qui utilisent la dispersion de vitesse verticale stellaire. Dans leur étude, ils ont constaté que les 30 galaxies utilisées pour l'étude ont des disques submaximaux, même si environ un tiers de leur échantillon est constitué par des galaxies spirales avec $V_{max} \geq 200$ km/s. On ne sait pas pourquoi cette divergence entre les différentes méthodes existe. D'autre part, nous sommes en accord avec les conclusions de Bosma et al. (2010) pour NGC 1291 qui a trouvé, en explorant la dispersion de vitesse verticale ainsi que les propriétés photométriques de la barre, que le disque de la galaxie est maximal.

Nous envisageons d'étendre cette étude à un certain nombre d'autres galaxies de l'échantillon S^{4}G. Il sera intéressant de voir si les galaxies de plus petites vitesses de rotation sont maximales

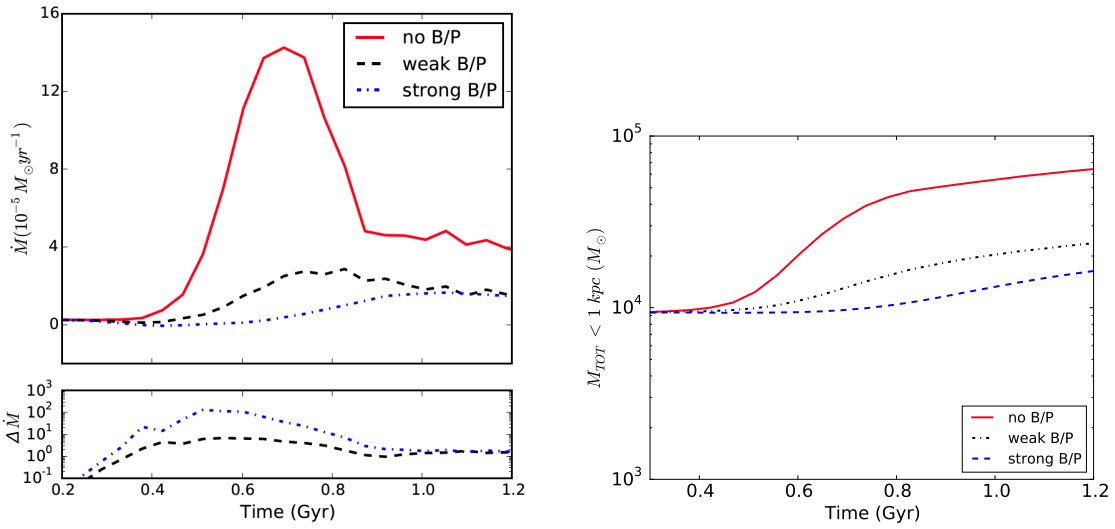

(a) (b)

FIGURE 5: *Gauche*: La fréquence d'afflux de gaz dans un cercle de rayon 1 kpc pour les trois modèles. Dans le panneau du bas, je montre $\Delta M_{\ odot}$, la différence de fréquence d'afflux de gaz entre les modèles *weakBP* et *noBP* (ligne noire pointillée) et la différence entre les modèles *strongBP* et *noBP* (ligne pointillée bleue). *Droit*: La masse totale de gaz dans un cercle de 1 kpc pour les trois modèles

ou submaximales. En outre, dans cette étude, nous avons pas exploré l'effet de différents profils matière sombre halo sur le M/L des meilleurs modèles d'ajustement.

Les effets des sous-structures sur l'afflux de gaz

Les barres sont l'un des plus importants moteurs de la phase séculaire de l'évolution des galaxies, qui domine à des moments tardifs lorsque les interactions entre les galaxies deviennent moins fréquentes. Les barres se trouvent dans environ deux tiers des galaxies à disque dans l'univers local, avec des forces variables (Eskridge et al., 2000, Menéndez-Delmestre et al., 2007, Barazza et al., 2008, Aguerri et al., 2009, Gadotti, 2009, Buta et al., 2010, 2015) et les torsions qu'ils induisent dans les disques des galaxies transfert de moment angulaire vers l'extérieur, ce qui conduit à une redistribution de gaz et d'étoiles (Sellwood and Binney, 2002, Athanassoula, 2003, Roškar et al., 2008, Minchev and Famaey, 2010). Le gaz est un traceur sensible au potentiel gravitationnel, beaucoup plus que la composante stellaire, et même une signature non-axisymétrique faible dans le potentiel peut créer des chocs dans le gaz qui perd ensuite moment angulaire.

Ce transport du gaz au centre de sa galaxie hôte est pensé être responsable pour la formation de pseudo-discy bulbes (Kormendy and Kennicutt, 2004, Athanassoula, 2005, Ellison et al., 2011, Coelho and Gadotti, 2011). Pour les trous noirs supermassifs résidant dans les régions centrales de la plupart des galaxies actives, une source de carburant est nécessaire. On pense que des mécanismes tels que les interactions de marée entre galaxies peuvent induire des torsions dans les galaxies qui vont canaliser le gaz vers les régions centrales (Hopkins et al., 2009). Un autre mode pour fournir du carburant pour l'activité des AGN se fait par des instabilités de disque, tels que par exemple la barre (Shlosman et al., 1990).

Même si l'effet de barres sur le flux de gaz vers les régions centrales a été examiné dans la littérature, une étude sur les effets de B/P bulbes sur l'afflux de gaz n'a pas, jusqu'à présent, été effectué, même si les B/P bulbes sont présents dans un grand nombre de galaxies barrées (Lütticke et al., 2000). En fait, une fois que la barre est formé, un B/P bulbe peut possiblement se former peu après (Athanassoula, 2005, Martinez-Valpuesta et al., 2006).

Le travail que j'ai réapisé sur les effets de B/P bulbes sur les modèles de galaxies, et qui est présenté dans le chapitre 2 de cette thèse, indique que les bulbes pourraient éventuellement diminuer l'effet de barres sur leurs disques, et que cela pourrait conduire à une réduction de gaz dans les regions centrales. J'ai réalisé des simulations hydrodynamiques de gaz en utilisant des modèles avec et sans bulbes B/P, mais qui sont par ailleurs identiques, afin d'examiner les effets des bulbes B/P sur l'afflux de gaz vers les régions centrales.

Je trouve que pour des configurations pour les B/P forts et faibles, la fréquence d'entrée de gaz au kiloparsec centrale est réduite par 1-2 ordres de grandeur. Celá conduit à une réduction significative de la masse totale de gaz présente à l'intérieur de ce rayon comme on peut voir dans la Figure 5.4. Ce résultat persiste pour des vitesses de sons différents, ce qui montre que le résultat est en grande partie insensible à la température du gaz.

Je conclus donc que les bulbes B/P peuvent jouer un rôle important sur la quantité de gaz qui arrive vers les régions centrales des galaxies, en particulier pour les galaxies qui ont un disque maximal ou presque maximal. En présence d'un B/P le taux d'accruétion du gaz est réduit de 1-2 ordres de grandeur, ce qui résulte 3-4 fois moins du gaz dans le kiloparsec central des galaxies barrées.

Acknowledgements

Writing this thesis was challenging to say the least, and finishing it has given me an intense sense of joy and indeed, pride. However, upon reflection, much of this pride is replaced by an immense sense of gratitude, since this thesis is in great part due to the scientific as well as the emotional support I've received throughout these past three years from a number of people.

First and foremost, I thank my supervisor Lia Athanassoula for all she has done for me over the past three years, for her many efforts with me and for all the advice and guidance she gave me in moments in which I was not sure on how to proceed. I thank my co-supervisor Albert Bosma, who together with Lia, guided me these past three years through the non-trivial endeavour of trying to become a good scientist. I especially thank them for their patience, as I imagine that training a young and at times rather stubborn pupil can be no easy task!

I would like to thank Johan Knapen and Heikki Salo for reading through the thesis and for their constructive comments both for the thesis as well as on my work in general at the various DAGAL meetings. I especially thank Johan who, as PI of DAGAL, wrote quite a few letters for my postdoc applications. I thank all my fellow DAGALers for providing a rich scientific atmosphere which stimulated many scientific questions as well as a sense of community, and from which a number of friendships have sprouted. I am thankful to the Laboratoire d'Astrophysique de Marseille for providing a stimulating work environment, and to the Marie Curie FP7 framework which provided the funding for this thesis (PITN-GA-2011-289313), and which gave me the opportunity to be a part of the DAGAL network. I also thank the Centre national d'études spatiales (CNES) for funding during the two months leading up to my defence. I am very grateful to Julien Devriendt, Katarina Kraljic and Pol Mollitor who helped me in my early days as a RAMSES user, and who all very kindly offered their knowledge and help whenever it was needed. I would also like to thank Sergey Rodionov, for the many, many times he helped me when I was stuck with technical or mathematical issues, as well as for all the challenging conversations over the years, and for being a good co-worker and friend.

I am lost for words when trying to express my gratitude towards Francesca Iannuzzi for everything she has done for me these past three years. She has been a scientific mentor, my therapist, my career advisor, a supportive friend and role model/big sister figure all in one. Throughout these three years she's proof-read emails, drafts of papers and postdoc applications, calmed me down, given me advice and sat and listened to my most silliest of problems - both scientific and personal. Without her constant support and unjudgemental ears, these three years would have been a much greater challenge.

A special and heartfelt thanks goes out to Jean-Charles Lambert, a.k.a. the "computer god", for all the times he has helped me with my myriad of technological/programming issues. I

also thank him, from the bottom of my heart, for all the emotional support, advice and help he has provided, especially during this past year.

To the friends I have made over the past three years, my life (and therefore my output as a scientist) has been enriched by your presence. Thank you for the hours of fun and pure joy. To all the people who have at some point passed through 17 Rue Caisserie, I would like to thank (in random order) Elisa (mi chicken), Graeme, Giovanni (my surrogate brother these past three years), Luca, my Adamoushko, Giulia, Dani and Sandra for the beautiful moments of co-habitation and for making that house, and Marseille, feel like home. To all the friends at LAM, thank you for all the moments together, and for making the workplace a joyous one. To la fille Erika (who Marseille brought back), to Elisa (Italian), to the loveliest of Ruthies and to all the wonderful people who have passed through my life in these three years, merci; I will forever carry fond memories in my heart from all the times we spent together. Also, to my friends from Cyprus, England and Spain, who have been constant pillars of strength and support throughout the years, thank you for being there; I am proud and honoured to have you in my life.

To Dimitri. It's been difficult to decide at which point in the acknowledgements your name should go, and what to thank you for, as you have played such an important role, in all parts of my life, these past two and a half years. I guess the simplest place to begin with is thank you for reading a big part of this thesis. Indeed, thank you for reading and filtering almost all my scientific (and not only) ideas, for helping me sort the good from the bad ones. Thank you for all the things you've taught me and for infesting me with your inexhaustible excitement when it comes to galaxies, mountains, and life. Thank you for being a mentor, a shoulder to cry on, a best friend, a partner, and (unfortunately) a punching bag for the various breakdowns this thesis has brought with it - importantly, thank you for your patience and love, and for sticking around.

Last, but most certainly not least; I thank my family, who have been the rock in my life, who have supported me no matter what, and who I know I can always turn to. I leave the last thought for my mother, without whom, I would - quite literally - not be here today. She might not know much about astrophysics, but I would most certainly not have made it this far, if it weren't for her wisdom, love, encouragement and support.

Contents

Abstract ii

Résumé iii

Résumé Étendu iv

Acknowledgements xvi

Contents xviii

1 Introduction 1
- 1.1 Galaxies in a cosmological context . . . 1
  - 1.1.1 ΛCDM . . . 2
  - 1.1.2 The origin of the Hubble Sequence . . . 7
    - 1.1.2.1 Overview of galaxy formation and evolution . . . 10
- 1.2 Barred Galaxies . . . 13
  - 1.2.1 Secular evolution and barred galaxies . . . 14
    - 1.2.1.1 Vertical extent . . . 17
    - 1.2.1.2 Pattern speed . . . 19
  - 1.2.2 Dynamics of barred galaxies . . . 20
    - 1.2.2.1 Equations of motion in a rotating barred potential . . . 20
    - 1.2.2.2 Epicyclic approximation . . . 23
    - 1.2.2.3 Orbits in weak barred potentials . . . 25
    - 1.2.2.4 Resonances . . . 26
    - 1.2.2.5 Orbits in strong barred potentials . . . 26
  - 1.2.3 Dust lanes in barred galaxies . . . 30
  - 1.2.4 Dynamics of boxy/peanut bulges . . . 32
- 1.3 Outline . . . 34

2 The Effects of Boxy/Peanut Bulges on Galaxy Models 36
- 2.1 Introduction . . . 36
- 2.2 Constructing dynamical models . . . 39
  - 2.2.1 Tests on the method . . . 40
  - 2.2.2 The image . . . 43
- 2.3 The height functions used . . . 45
  - 2.3.1 Flat height functions . . . 45
  - 2.3.2 Peanut height function . . . 46

2.3.3 Boxy height function . . . 47
2.4 Should we include B/P bulges in our models? . . . 48
2.4.1 The effects of B/P bulges on forces . . . 48
2.4.2 The effects of B/P bulges on orbital structure . . . 52
2.4.3 The effects of B/P bulges on bar strength . . . 54
2.5 Errors due to Boxy/Peanut Modelling . . . 56
2.5.1 Potential and forces . . . 57
2.5.2 Periodic orbits . . . 60
2.5.3 Bar strength . . . 61
2.6 Summary . . . 66

3 Gas Response Simulations 69
3.1 Introduction . . . 69
3.2 Adapting the code . . . 70
3.3 Which AMR strategy to use? . . . 72
3.4 Effects of resolution . . . 76
3.4.1 On the location of the shock loci . . . 76
3.4.2 On the central concentration . . . 76
3.4.3 On the velocity fields . . . 80
3.5 Summary . . . 83

4 Dynamical Determination of the M/L and Bar Pattern Speed of Galaxies: The case of NGC 1291 84
4.1 Introduction . . . 84
4.2 Observations of NGC 1291 . . . 86
4.3 Constructing the dynamical models . . . 88
4.3.1 Smoothing the 3.6μm image . . . 88
4.3.2 The Mass to Light Ratio . . . 89
4.3.3 The Height Function . . . 89
4.3.4 Stellar component potential . . . 91
4.3.5 Dark matter halo potential . . . 92
4.3.6 Varying the parameters . . . 93
4.4 Comparing the models to the observations . . . 95
4.4.1 Location of shocks along slits . . . 99
4.4.2 Visual inspection . . . 103
4.4.3 Criteria for the best fit model . . . 103
4.5 Results . . . 104
4.5.1 Effect of M/L . . . 105
4.5.2 Effect of Lagrangian radius . . . 105
4.5.3 Effect of height function . . . 106
4.5.4 Models without a dark matter halo . . . 109
4.5.5 Exploring the parameter space . . . 111
4.5.6 Constraining degeneracies in the modelling . . . 118
4.5.7 Best fit models . . . 124
4.6 Discussion . . . 126
4.6.1 Limited effects of the nuclear bar . . . 126
4.6.2 The height function of NGC 1291 . . . 127

4.6.3 Dynamical determination of the 3.6μm M/L . . . 128
4.6.4 The maximal disc of NGC 1291 . . . 128
4.6.5 The fast rotating bar of NGC 1291 . . . 130
4.7 Summary . . . 130

5 The Effects of Substructures on Gas Inflow **132**
5.1 Introduction . . . 132
5.2 Models . . . 134
5.3 The effect of the B/P bulge on gas inflow . . . 135
5.3.1 Gas inflow within 1 and 0.5 kpc . . . 135
5.3.2 Adding a dark matter halo . . . 139
5.3.3 Effect of sound speed . . . 142
5.4 The effect of the nuclear bar on gas inflow . . . 144
5.5 Summary . . . 147

6 Conclusions **149**

Bibliography **154**

List of Figures **177**

List of Tables **182**

1

Introduction

"If you wish to make an apple pie from scratch,
you must first invent the universe."
– Carl Sagan

The purpose of this Chapter is twofold: In Section 1.1 I first set the stage for the cosmological context within which galaxies are found and give some general background on processes of galaxy formation and evolution. In Section 1.2, I then focus on barred galaxies which are the topic of the remainder of this thesis. I give an overview of some results from observations and numerical simulations, and then outline some of the basic dynamics of barred galaxies and Boxy/Peanut bulges which are relevant for the rest of the thesis.

1.1 Galaxies in a cosmological context

The current paradigm of galaxy formation, the ΛCDM model, holds that galaxies were formed in dark matter haloes which were seeded by primordial quantum fluctuations. These primordial fluctuations in the matter density field, grew under the forces of gravity to form virialised dark matter halos. Baryonic mass falls into the dark matter potential wells, and as the gas is able to cool it condenses to form the first stars and galaxies. In this early phase of the Universe these clumps of dark and baryonic matter frequently interacted and coalesced to form larger structures with the passage of time. This simple picture is what has led from the homogeneous early history of the Universe to the massive amounts of complexity seen in galaxies in the observable Universe. In Section 1.1.1 I briefly describe the cosmological background in which galaxies evolve and in Section 1.1.2 I give some background on the processes which have shaped the Hubble sequence of galaxies.

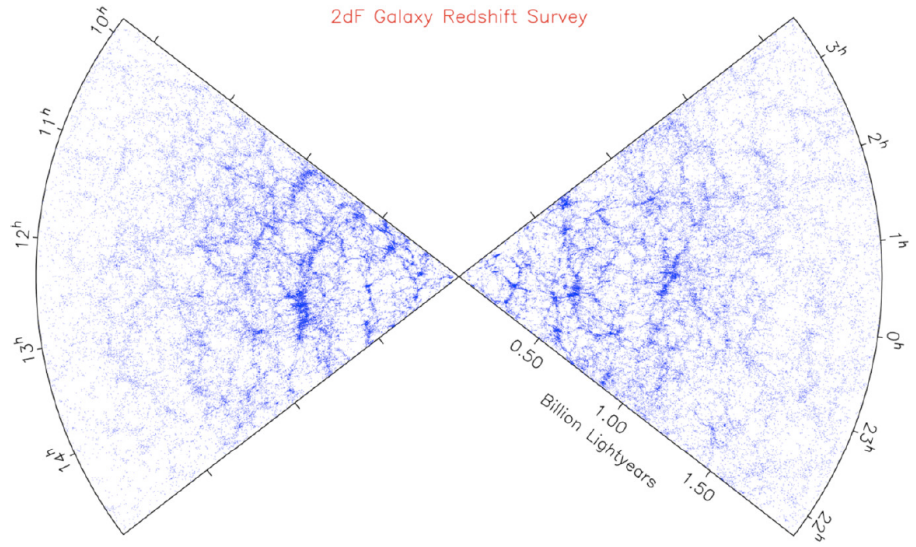

FIGURE 1.1: Map of the galaxy distribution in the nearby universe, obtained from the Two-degree-Field Galaxy Redshift Survey (2dFGRS; (Colless et al., 2001)). The volume covered by the survey is approximately $10^8 h^{-1}\text{Mpc}^3$.

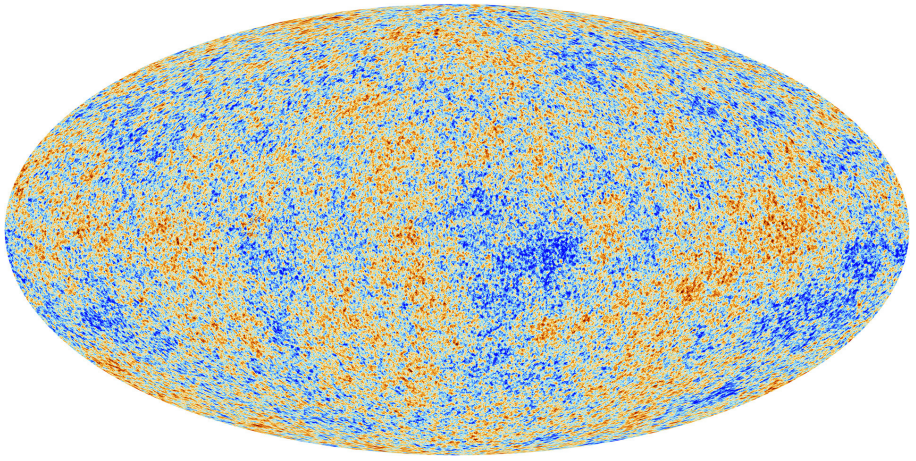

FIGURE 1.2: All-sky CMB measurements from the Planck Collaboration (Planck Collaboration et al., 2015).

1.1.1 ΛCDM

The *Copernican Principle* is a rather philosophical statement, which tells us that our position in the Universe is not special or privileged in any way and that the laws of physics are the same for all observers at all locations. This, together with the observational fact that the Universe is isotropic, as evidenced from large galaxy surveys (see Figure 1.1) and the Cosmic Microwave Background (CMB, see Figure 1.2) leads to the conclusion that the Universe is homogeneous

and therefore also isotropic from any given point. This is known as the *Cosmological Principle*, one of the basic assumptions of all modern cosmological theories.

By assuming the cosmological principle, the Friedman-Lemaître-Robertson-Walker (FLRW) metric can be derived, which is a specific solution to the Einstein Field Equations (EFE) of General Relativity (Einstein, 1915, 1916). For a comoving observer, i.e. an observer moving with the flow of expansion or contraction of the Universe, and in spherical coordinates, the FLRW metric is given by,

$$ds^2 = dt^2 - a^2(t)[\frac{dr^2}{1-kr^2} + r^2(d\theta^2 + \sin^2\theta d\phi^2)] \tag{1.1}$$

where the speed of light c=1. Time is given by the proper time t, and $a(t)$ is the cosmic scale factor. The curvature constant k, takes on the values -1, 0 and 1, for an open, flat and closed Universe respectively.

The EFE which dictate the bending of space-time by matter and energy due to gravitation are given by,

$$R_{\mu\nu} - \frac{1}{2}g_{\mu\nu}R + g_{\mu\nu}\Lambda = 8\pi G T_{\mu\nu} \tag{1.2}$$

where, $R_{\mu\nu}$ is the Ricci Tensor, $g_{\mu\nu}$ is the space-time metric, R is the Ricci scalar, Λ is the cosmological constant, G the gravitational constant and $T_{\mu\nu}$ the stress energy tensor. If we assume that the stress energy tensor is also homogeneous and isotropic, that matter and radiation in the Universe behave as perfect fluids, we can solve the EFE for the FLRW metric, in order to relate the evolution of the scale factor to the matter-energy content of the Universe, via the Friedman equations:

$$\frac{\dot{a}^2}{a^2} + \frac{k}{a^2} = \frac{8\pi G\rho}{3} + \frac{\Lambda}{3} \tag{1.3}$$

$$\frac{\ddot{a}}{a} = -\frac{4\pi G}{3}(\rho + 3p) + \frac{\Lambda}{3} \tag{1.4}$$

which dictate the behaviour of the scale factor a as a function of time.

The observation in the early 20th century by V.M. Slipher, Edwin Hubble and others that galaxies are moving away from us at a speed which is proportional to their distance, led to the surprising discovery that the Universe is expanding, contrary to the scientific beliefs held at the time (Slipher, 1913, Lemaître, 1927, Hubble, 1929, 1936). This discovery led to two major competing cosmological theories, the *Steady State* theory (Bondi and Gold, 1948, Hoyle, 1948)

and the *Big Bang* model (Lemaître, 1931, Alpher et al., 1948, Alpher and Herman, 1948). The Big Bang model states that if one tracks this evolution back in time, there must have been a time in the past history of the Universe in which it was very dense and hot. This "beginning of time" had unpleasant philosophical connotations for some, which led to the formulation of the Steady State theory, which held that although the Universe is expanding, new matter is constantly being created and therefore the Universe is eternal and unchanging. This way, the Universe need not have begun at a determined point in time, as the Big Bang model seemed to suggest.

Cosmic Microwave Background

One of the major pieces of evidence supporting the Big Bang model came from the discovery of the Cosmic Microwave Background in 1965 (Penzias and Wilson, 1965) (Figure 1.2). The CMB is a prediction of the Big Bang model which states that there should be relic radiation emitted from the early history of the Universe (Alpher and Herman, 1948) during the event described as *recombination*. On the other hand, the other competing cosmological theory of the time, the Steady State theory, had no natural way of explaining the presence of the CMB.

Before recombination occurred, due to the high temperatures permeating the Universe, photons constantly interacted with baryonic matter through Thomson scattering, therefore they could not travel very far before being absorbed and re-emitted; thus the Universe was opaque. Due to the expansion of the Universe however, the temperature drops below a certain level at which point Thompson scattering becomes inefficient, which allows electrons and protons to bind and form neutral atoms. When this occurred, the Universe became transparent to photons, since there weren't free floating electrons with which they could scatter. Recombination is thought to have occurred when the Universe was around 300 000 years old, at a redshift of around z=1100. This primordial radiation was therefore free to travel uninterrupted through space, cooling due to the expansion of the Universe and reaching us today at a temperature of 2.7K with a practically perfect black body spectrum, indeed the most perfect black body observed. This radiation should permeate the observable Universe, as indeed is found by observations of the CMB.

The CMB photons we receive give us the surface of last scattering, i.e. they give us a snapshot of the state of the Universe when the radiation was released (Peebles and Yu, 1970). Although the CMB is practically a perfect black body, there are tiny anisotropies in the temperature, of the order of 10^{-5}, which are caused by the fluctuations in the matter density field at the surface of last scattering; therefore this "snapshot" carries information about the initial conditions of the Universe. A particularly successful theory for explaining the origin of these tiny fluctuations in the matter density field is the theory of inflation, which states that the Universe underwent a period of rapid exponential expansion. This expansion was able to "enlarge" the fluctuations in the quantum foam, thus creating classical perturbations in the

matter density field with the required properties, which seed subsequent structure formation (Guth, 1981, Linde, 1982, Albrecht and Steinhardt, 1982).

The CMB propelled cosmology into an era of high precision, since it is now possible to make predictions with an error budget much smaller than ever possible before. It has been used in order to verify a number of predictions of the Big Bang theory, and it is also used to predict the total density of the Universe. This quantity is intimately related to the flatness of the Universe, and indeed the CMB predicts a flat Universe (de Bernardis et al., 2000). This observation however seems to contradict other observational evidence which states that baryonic matter accounts for up to 4% of the critical density. This, along with further observational support discussed in the next sections supports the existence of non-baryonic *dark matter*. Indeed dark matter is thought to permeate the Universe and makes up 23% of the total energetic budget of the Universe.

Cold Dark Matter

Cold dark matter (CDM) is a type of non-baryonic matter which does not interact through the standard forces that normal baryonic matter interacts with, with the exception of gravity. It is believed to be made from particles that are non-relativistic, hence the term 'cold' and is thought to be the primary contributor to the matter content of the Universe.

There is ample observational evidence that supports the existence of this non-baryonic component of the matter budget of the Universe. One of them, the flat rotation curves of galaxies will be discussed in Section 1.1.2. However even from a cosmological point of view there is evidence supporting the existence of dark matter.

The size of the fluctuations seen in the matter density field at present times would not be as observed, had there not been a non-baryonic component of the matter field which seeded the early collapse of material. To put it simply, in the matter dominated epoch of the Universe, before recombination, dark matter fluctuations grow proportional to the growth factor a, while the baryon-radiation fluid keeps oscillating. Once recombination occurs and baryonic matter decouples from radiation, perturbations in the density field are free to grow. Had there been no dark matter, the size of the fluctuations seen in the matter field today would be very small of the order of 1000 times what the fluctuations in the CMB are, i.e. 10^{-2}. However due to the fact that the dark matter component was able to collapse from much earlier times, since it was not coupled to radiation and baryonic matter, the collapse of baryonic matter proceeds much more rapidly after recombination, since the collapse is accelerated by the already present potential wells in the dark matter, leading to the large fluctuations in the matter field observed at present times. Therefore the size of the perturbations observed today compared to the size of the fluctuations in the radiation field at the time of recombination provides strong observational evidence for some form of non-baryonic matter.

However the composition of dark matter is still an open question. Depending on the mass of the particles which make up this non-baryonic matter two extreme regimes can be defined, the *hot* and *cold* dark matter regimes. These two different types of particles create very different scenarios in the evolution of structures. Hot dark matter decouples from the rest of the cosmic fluid when it is still relativistic, while the opposite is true for cold dark matter. The mass of the particle defines the minimum mass scale of collapse of the particles. In the hot dark matter case these minimum fluctuations are seven orders of magnitude larger than the CDM case, which would result in an anti-hierarchical scenario of the formation of structures. Indeed there is observational evidence supporting the hierarchical structure formation, i.e. that smaller objects collapsed first, and then grew through subsequent mergers. For example, there is evidence that clusters of galaxies, which are the largest virtualised structures in the Universe are also the youngest objects that we observe and that therefore the evolution of structures follows a bottom-up hierarchical trend. This favours the CDM hypothesis over the hot dark matter model (Blumenthal et al., 1984).

On the other hand, there exist a number of well established problems with the CDM hypothesis at small scales, which I touch upon in Section 1.1.2.It is worth noting that due to the apparent inability of CDM to reproduce observational results at small scales there has been interest in intermediate mass particles, also referred to as warm dark matter. Due to the very complex and non-linear physics which takes place at these small scales, the question of the validity or not of the CDM hypothesis remains an open and challenging question for modern astrophysics.

Cosmic acceleration

The term Λ (Lambda) in ΛCDM, stands for the cosmological constant, the value of the energy density of the vacuum of space, which is believed to be currently dominating the matter-energy content of the Universe. This cosmological constant was originally proposed by Einstein when he first formulated his theory of General Relativity, in order to maintain a static Universe, as it was believed to be at the time. However, it was later rejected and set equal to zero, when it was discovered by Lemaître (using the observations by Slipher) and Hubble that the Universe was expanding (Einstein and de Sitter, 1932).

Up until the late 90's, it was believed that the Universe is expanding at a decelerated rate, since the pull of gravity of all the matter in the Universe causes it to slow down. In the late 1990's it was shown by two independent teams who were studying Type Ia Supernovae, that the Universe is actually undergoing accelerated expansion (Riess et al., 1998, Perlmutter et al., 1998). To their surprise they found the deceleration parameter to be negative instead of positive (in formal terms this means that the cosmic scale factor has a positive second derivative) i.e. they found that there was some force which seemed to be pushing the very fabric of the Universe to expand in an accelerated fashion; this was dubbed *dark energy*. This

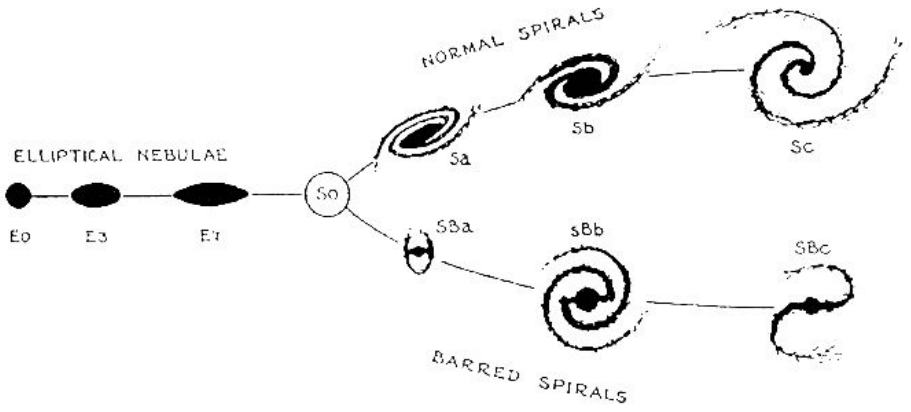

FIGURE 1.3: Original diagram by Hubble in his 1936 book "The realm of nebulae" (Hubble, 1936) showing the separation into early type Elliptical galaxies and late type Spirals.

led the scientific community to re-invoke the cosmological constant, which is the simplest form of dark energy, since it is constant in both space and time.

1.1.2 The origin of the Hubble Sequence

One of the main pursuits of modern astrophysics is to understand the formation and evolution processes which have led to the wide variety of galaxy populations seen today in the Universe. As described in the previous subsection, ΛCDM provides the initial conditions for the seeds of galaxies and for structure growth, but at galactic and cluster scales, complex baryonic processes kick in which lead to a much more interesting and complex picture of galaxy formation. We see a striking variety of galaxies in the Universe, and already from the 1920's Hubble had classified galaxies into three main types, according to his diagram, now known as the *Hubble diagram* or *Tuning-fork diagram* (see Figure 1.3). In the nearby universe 75% of galaxies brighter than M_B=−20 are spiral or disc in morphology, 22% are S0/elliptical and the remaining 2% are peculiar irregular (Conselice, 2006).

In what follows I describe the main types of galaxies seen in the Universe, and then give a *very* brief overview of the basics of galaxy formation and evolution, which are thought to lead to these different types of galaxies. I then focus on observational properties of barred galaxies, which are explored in the rest of this thesis.

Elliptical Galaxies

Elliptical galaxies are given their name due to their characteristic elliptical shape (see Figure 1.4(a)). They are smooth featureless stellar systems which contain little or practically no cold gas or dust, nor do they have a stellar disc. Stars in most elliptical galaxies are old, with ages comparable to the age of the Universe, which subsequently also makes these galaxies redder (Conselice (2006), see Figure 1.6(a)). This is consistent with the fact that there is no cold

(a) Elliptical (b) Spiral (c) Lenticular

FIGURE 1.4: Archetypal examples of an elliptical galaxy (M87), a spiral galaxy (M101) and a lenticular galaxy (NGC 4371).

gas from which new stars could form. Additionally, bright elliptical galaxies are generally classified as slow rotators, i.e. they are dispersion dominated and contain little if any rotation (Krajnović et al., 2011, Emsellem et al., 2011).

The formation of elliptical galaxies is thought to be tightly related to mergers (Toomre and Toomre, 1972, Toomre, 1977), as well as the environment in which these galaxies are found. Indeed they are more numerous in high density regions, where they make up approximately 40% of the galaxy population in the centres of dense galaxy clusters, while in low density regions they make up about 10% (Dressler (1980), see also Figure 1.6(b)).

Spiral Galaxies

Spiral galaxies as the one shown in Figure 1.4(b), contain a stellar disc, along with a disc of gas and dust. The disc contains spiral arms, in which often intense star formation is occurring. In low-density regions of the Universe about 60% of all luminous galaxies are spirals, but the fraction drops to less than 10% in dense regions such as in the centres of dense galaxy clusters (Dressler (1980), see Figure 1.6(b)). Spiral galaxies contain gas which often extends to much larger radii than the stars, thought to be due to the fact that star formation is suppressed when the gas surface density falls below a critical value. By tracing the neutral hydrogen via the 21-cm line, the rotation curves of spiral galaxies can be traced to radii well beyond the outer edge of the stellar distribution.

Using the gas, one can trace the underlying galactic potential; indeed, one of the major lines of evidence supporting the existence of dark matter, is by probing galactic potentials with HI rotation curves. Bosma and others, found from early work in the late 70's that the rotation curves of spiral galaxies remain flat well after the stellar discs have been truncated (Bosma, 1978, 1981). If most of the mass of the galaxy were in stars, we would expect the circular speed curve at these large radii to decline outside the stellar disc. This has only two possible explanations, either the laws of Newtonian physics break down at large galactic scales, or there exists some unseen matter, which does not emit electromagnetic radiation and which

permeates the space around galaxies. This, therefore, further reinforces the need for some form of non-baryonic dark matter.

It is worth pausing to mention another striking feature of spiral galaxies, since this will be used in Chapter 4 of the thesis. This is the tight relation that spiral galaxies obey, between their luminosity and their maximum rotation velocity. This relation was discovered in 1977 by Brent Tully and Richard Fisher (Tully and Fisher, 1977), known as the Tully-Fisher relation. Although one expects a correlation between luminosity and rotational velocity, since luminosity is correlated to mass, and more massive discs should rotate faster, however the small intrinsic scatter of this relation is non-trivial to explain given the paradigm of ΛCDM, since very fine tuning between the amount of stellar mass and the dark matter halo needs to be imposed to justify such small intrinsic scatter (McGaugh et al., 2000, McGaugh, 2012).

Lenticular Galaxies

Lenticular galaxies, as the one seen in Figure 1.4(c), are similar to spirals in that they contain a rapidly rotating disc, a bulge and sometimes a bar, and the disc obeys the exponential surface brightness law, which is characteristic of spirals. On the other hand, like ellipticals, they have little or no cold gas or recent star formation and are smooth and featureless in appearance, without exhibiting spiral structure.

Lenticulars are rare in low density regions but comprise almost half of the galaxies in high-density centres of galaxy clusters. Lenticulars are thought to be in a transition phase between spirals and ellipticals, where in the dense regions of the universe, ram pressure stripping contributes to removing the gas from spirals thus turning them into lenticulars. However, *some* lenticulars are also found in low density regions, where ram-pressure stripping cannot have contributed to the gas stripping (Cappellari et al., 2011). It has therefore been suggested that lenticulars are "faded" spirals, which are unable to undergo further star formation due to some mechanism which stabilises the disc against fragmentation and subsequent star formation (Cappellari et al., 2011, Boselli and Gavazzi, 2006). However, subsequent studies have also shown that the location of lenticulars, i.e. early type fast rotators, in the stellar angular momentum versus ellipticity plane are not compatible with the location of spiral galaxies in the same plane, thus concluding that lenticulars cannot *just* be faded spirals, but some other mechanism must act to change their angular momentum (Falcón-Barroso et al., 2015, Querejeta et al., 2015a). Therefore, although some routes have been proposed for the formation of S0's in dense regions, it is not clear how these galaxies form in the field or in less dense environments.

Irregular Galaxies

Lastly, a minority of galaxies are assigned to the "irregular" bin because they don't fit in any of the other major categories. These galaxies could be spirals or ellipticals which have been violently distorted by a recent encounter with a neighbour, by mergers or which are undergoing an intense burst of star formation.

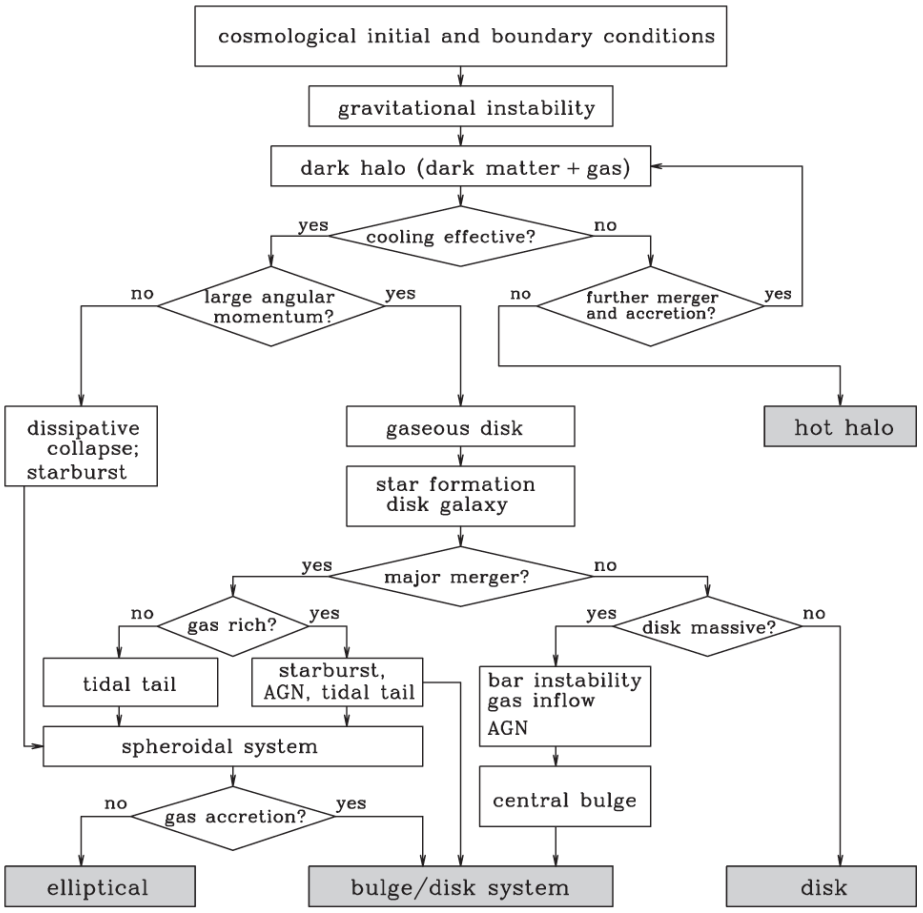

FIGURE 1.5: A schematic flow chart showing the intertwined relations between different processes which play an important role in galaxy formation and evolution. It has to be stressed that this chart is in no way complete however, but provides a zeroth order picture of the drivers of galaxy formation and evolution. Reproduced from (Mo, van den Bosch, and White, 2010).

1.1.2.1 Overview of galaxy formation and evolution

As stated in the previous section, galaxies are thought to form inside dark matter haloes, whose properties were seeded by a Gaussian random field of quantum fluctuations in the early Universe. This therefore provides the "initial conditions" for galaxy formation. Self-gravity subsequently enhances these fluctuations and further collapse ensues, creating a "cosmic web" made up of *filaments*, *walls* and *voids*, i.e. areas of the universe which are over- and under-dense. The cosmic web can be seen in large galaxy surveys (Figure 1.1) and has been simulated extensively in large N-body simulations (for a review see Frenk and White (2012)).

There are a number of processes which play a role in the final properties of the galaxy population today, as summarised partially in Figure 1.5. The initial collapse of baryonic mass in dark matter halos, the subsequent interactions and mergers between galaxies, the re-accretion

of enriched gas and internal secular processes are what is thought to have created the different types of galaxies of the Hubble sequence. Although this diagram was originally proposed for taxonomic purposes, it defines an axis along which there are strong physical trends, such as a near-monotonic dependence in gas content, bulge/total ratio and central density (Efstathiou and Silk, 1983).

In the hierarchical formation scenario, the first stellar systems formed are small and numerous, reflecting the abundances of dark matter halos, and rapid merging of these systems follows. The early merging of stellar systems creates a population of stellar systems supported by velocity dispersion, the progenitors of today's bulges, while continued gas cooling produces discs around them. As halos continue to merge, and in the absence of large gas reservoirs, the discs of stars that had begun to form in them are transformed into ellipsoidal components due to the violently changing gravitational potential (Barnes and Hernquist, 1992). This combined with supernova driven shocks and AGN activity heats most of the remaining gas to very high temperatures, causing these merger remnants to become the "red sequence" galaxies that have little gas and little to no ongoing star formation. On the other hand if gas is able to reaccrete and a disc to reform, star formation continues to be efficient, and these star forming spiral galaxies are what make up the "blue cloud". The terms "red sequence" and "blue cloud" refer to distinct groupings in the colour-magnitude diagram for galaxies (Conselice (2006), Figure 1.6(a)) and reflect, more objectively the distinction between early and late type galaxies already known to Hubble.

There is also a dependence of the morphological type of galaxies on whether they are found in the field or in clusters which has been known since the work of Hubble and Humason (1931) who found that there was a predominance of early type galaxies in clusters. A quantitative measure of this dependence came from the work of Dressler (1980) (see Figure 1.6(b)), where he showed that the abundance of different morphological types depends on the local density; this dependence is due to the processes which galaxies undergo when falling into the centres of galaxies clusters, such as ram-pressure striping, galactic winds, AGN outflows, galaxy-galaxy interactions and the effect of an intra-cluster stellar population.

Ram-pressure stripping states that a galaxy passing through the Intra Cluster Medium (ICM) will feel an external pressure, which depends on the ICM density and the relative velocity of the galaxy and the ICM. There is much observational evidence of galaxies undergoing stripping due to ram-pressure, such as spiral galaxies in the Virgo cluster undergoing stripping as found by HI observations (Kenney et al., 2004, Crowl et al., 2005).

Another mechanism for transferring gas to the ICM is through galactic winds, created by supernova explosions which can drive outflow from a galaxy (Heckman, 2003), and indeed a correlation exists between starburst galaxies and wind, through the finding of hot gas around starburst galaxies (Dahlem et al., 1998). With these winds metals can also be transported to

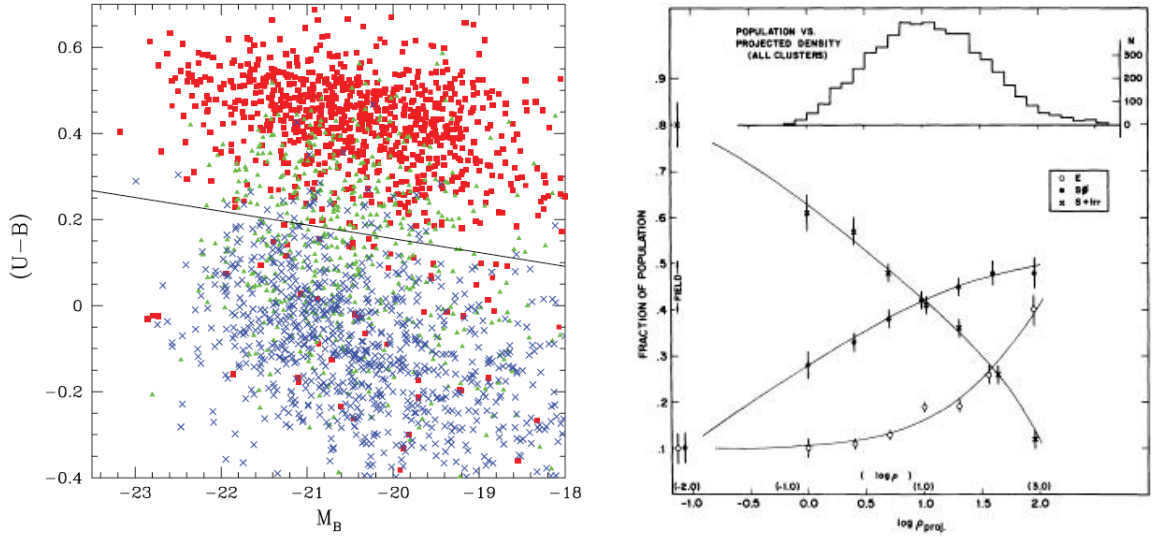

(a) Colour-Magnitude diagram (b) Morphological Segregation

FIGURE 1.6: *Left*:Colour magnitude diagram from Conselice (2006). The solid line divides red-sequence galaxies from blue cloud galaxies. Early types are denoted by solid red squares, while later types are labelled as blue crosses and mid-types are labelled as green triangles. *Right:* The fraction of elliptical, lenticular and spiral and irregular galaxies as a function of the logarithm of the projected density. The upper histogram shows the number distribution of galaxies over bins of projected density. Taken from Dressler (1980)

the ICM, where the amount of metal transportation depends on various galaxy parameters such as the total mass of the galaxy and on the environmental conditions; in the centre of massive clusters the pressure of the ICM can suppress the winds (Kapferer et al., 2006).

The aforementioned processes can strip galaxies of their gas, and enrich the IGM, which can then be re-accreted onto the galaxy via gas cooling, a process which is of vital importance in galaxy formation and evolution (Dekel et al., 2009, Dubois et al., 2012, Joung et al., 2012, Fraternali et al., 2013). The amount of cooling depends on the temperature and density of the gas, as well as on its chemical composition.

In massive halos the virial temperature can exceed 10^7K, gas is fully collisionally ionised and cools mainly through bremsstrahlung emission from free electrons. For lower gas temperatures in the range of $10^4\text{K} \leq T_{vir} \leq 10^6$ K, a number of excitation and de-excitation mechanisms can play a role. Electrons can recombine with ions emitting a photon, or atoms can be excited by a collision with another particle thereafter decaying radiatively to the ground state. In halos with $T_{vir} \leq 10^4$K, gas is predicted to be almost completely neutral. This strongly suppresses the aforementioned cooling processes, unless heavy elements or molecules are present, in which case cooling is still possible through the collisional excitation/de-excitation of fine and hyperfine structure lines (for heavy elements) or rotation/vibrational lines (for molecules). For these processes the cooling involves the interaction between two particles and is therefore generally

more efficient in higher density regions. If cooling times are short, gas accretes directly onto the protogalaxy, without settling into a state of hydrostatic equilibrium (Mo et al., 2010).

This overall picture of galaxy formation and evolution, is thought to be broadly correct because it accounts for the distribution of galaxies through the Universe and some of their properites Springel et al. (2006). Yet there are a number of important predictions of the model that seem to be inconsistent with known galaxy properties. Perhaps one of the most striking ones, is that many disc-like galaxies lack the types of bulges produced by mergers, among which our own Milky-Way (Kormendy et al., 2010, Shen et al., 2010, Ness et al., 2014, Di Matteo et al., 2015), whereas the merging hierarchy of ΛCDM predicts substantial, dense bulges in most large galaxies. Other problems are the central density of dark matter in the halos of galaxies, which seems to be less than the models predict (de Blok et al., 2001, de Blok, 2010), as well as the number and properties of dwarf satellite galaxies surrounding each major galaxy, which seems inconsistent with what we observe (Boylan-Kolchin et al., 2012).

At lower redshift, z ≈ 1, dark energy causes the original slowing universal expansion to reaccelerate. This increases the isolation of galaxies, reducing the later merger rate and allowing galaxies to settle in a more dynamically quiescent period (Sellwood, 2014). Galaxies are still forming and evolving today, however there has been a shift from the violent and rapid formation processes which dominated the early Universe, to a more quiescent phase at recent times. This slow evolution is what has become known as *secular evolution*, by which is meant the gradual restructuring of a galaxy over time scales much longer than a crossing time of galaxies. This evolution is mostly driven by the outward redistribution of angular momentum in a galaxy, which enables it to reach a state of lower energy (Athanassoula, 2003, Sellwood, 2014).

We are specifically interested in internal secular evolution, since much of the rest of this thesis deals with this phase of galactic evolution. Therefore, in the next subsection I focus on describing some observational properties of barred galaxies, since bars are thought to be one of the main drivers of secular evolution.

1.2 Barred Galaxies

In this section I give an overview of barred galaxies and their properties. I first describe some results from observations and numerical studies on the properties of barred galaxies and the effects they have on the secular evolution process (Section 1.2.1). In Section 1.2.2 I give a *brief* overview of the dynamics of barred galaxies and orbital structure, and introduce some of the concepts which are used in Chapter 2 of the thesis. I then focus on dust lanes found in barred

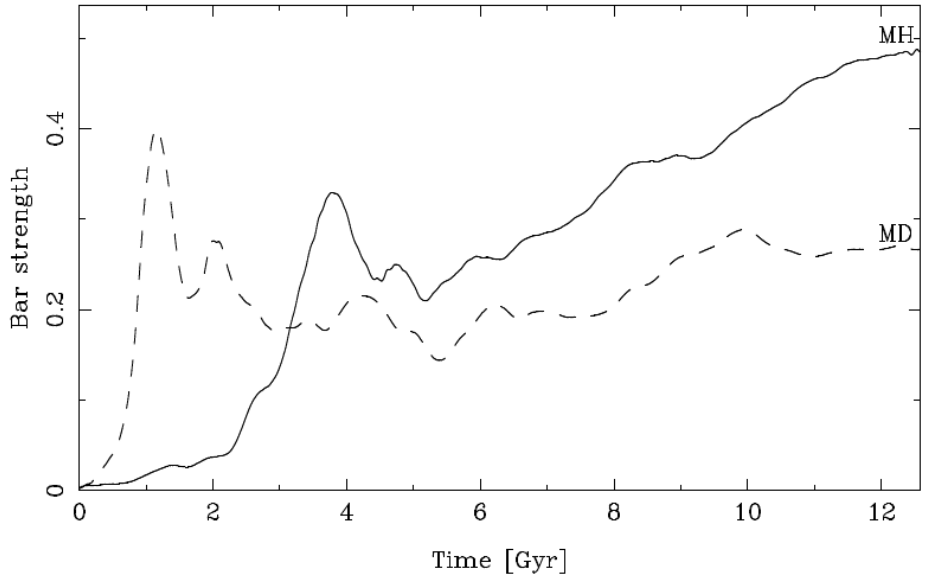

FIGURE 1.7: The evolution of bar strength as a function of time. A model with a massive halo (MH) and a model with a dominant disc (MD). We see that the bar in both cases goes through a buckling phase, and then resumes secular growth, with the MH model eventually obtaining a stronger bar. From Athanassoula (2013)

galaxies (Section 1.2.3) since these will play an important role in Chapter 4 of the thesis and in Section 1.2.4 I briefly discuss the dynamics of B/P bulges.

1.2.1 Secular evolution and barred galaxies

A large fraction of disc galaxies contain a central elongated structure called a bar, which can vary in size and shape, from being a weak oval distortion, to dominating the visual image. Although it is difficult to determine an *exact* fraction of discs that are barred galaxies – since this depends on how one defines the bar – a number of independent studies find bars in about two thirds of disc galaxies in the local universe, with variable strengths (Nilson, 1973, de Vaucouleurs et al., 1976, Eskridge et al., 2000, Knapen et al., 2000, Menéndez-Delmestre et al., 2007, Barazza et al., 2008, Aguerri et al., 2009, Gadotti, 2009), with bars being found in galaxies from a redshift of $z \approx 1$ (Knapen, 2007, Sheth et al., 2008). Bars tend to make up around 10% of the total mass of the galaxy although there is a spread in values, from about 30% for early type galaxies to a smaller fraction for late type galaxies (Sellwood and Wilkinson, 1993, Gadotti, 2011, Herrera-Endoqui et al., 2015, Díaz-García et al., 2015). Bars can have different sizes depending on the galaxy in which they are found, but a general trend is that in early type galaxies they tend to be larger relative to the size of the disc (Elmegreen and Elmegreen, 1985).

The existence of bars has been a topic of much interest to the community, since it reveals information about the dynamics, and specifically about the stability of galactic discs. Indeed

it was found from the early 70's, that even if Toomre's criterion for local stability is satisfied – and therefore the disc is stable against axisymmetric disturbances – bars can still be formed in the disc (Hohl, 1971). In fact the inability to suppress bar formation in simulations of disc galaxies was a considerable problem in the 70's and 80's; since not all disc galaxies in the universe contain bars, a method was necessary in order to suppress bar formation, such that a bar would not *always* form in a stellar disc. This was achieved by adding a dark matter halo, since the halo stabilised the disc against bar formation (Ostriker and Peebles, 1973, Efstathiou et al., 1982), which was used as an additional argument for the necessary existence of dark matter haloes. In fact, dark matter halos were so effective at suppressing bar formation, that the opposite problem appeared, that is, how to induce bar formation in *some* disc galaxies. However, it was later shown (Athanassoula and Misiriotis, 2002, Athanassoula, 2003) that dark matter haloes simply delay bar formation, and that once a bar is formed, massive dark matter halos increase the strength of the bar, as is shown in Figure 1.7. This is due to the angular momentum exchange between bars and the halo and outer disc at the resonances (Athanassoula (2003), see Figure 1.8). Earlier works which had found that dark matter haloes suppress bar formation, came to this result because they employed static dark matter halos – due to computational limitations of the time – and these halos were *de facto* unable to exchange angular momentum with the disc.

Bar formation is now understood to be a complex process which depends on a number of factors and which is related to the emission and absorption of angular momentum from different components in the galaxy such as the disc, the halo and the bulge. Even though halos suppress bar formation at the initial stages, later bar evolution is enhanced by the presence of the halo. Bars can lose angular momentum by trapping particles which were on quasi-circular orbit outside the bar into elongated orbits in its outer part. This way angular momentum is lost from the disc inner parts, while the bar will become longer, i.e. stronger (Athanassoula, 2003). Additionally, stars outside the bar will be pushed into larger circular orbits. To quote Lynden-Bell & Kalnajs: "Let us note here that if this sense of angular momentum flow" i.e. *outwards* "is achieved then the outer parts of a galaxy will move into larger orbits while the inner parts will contract". This transfer of angular momentum can move the system, i.e. the galaxy, towards a lower energy configuration, which is why bars and non-axisymmetric disturbances are frequent in nature (Lynden-Bell and Kalnajs, 1972). However there is a limit beyond which the disc is not able to emit sufficient angular momentum, either because it is not sufficiently massive or if it is too dynamical hot and under these circumstances it is possible that a bar could not grow within an astronomically relevant time (Athanassoula and Misiriotis, 2002, Athanassoula, 2003).

Additionally the central mass concentration (CMC) – be that in the form of a compact nuclear star cluster or super-massive black hole –also plays a significant role on the evolution of bars,

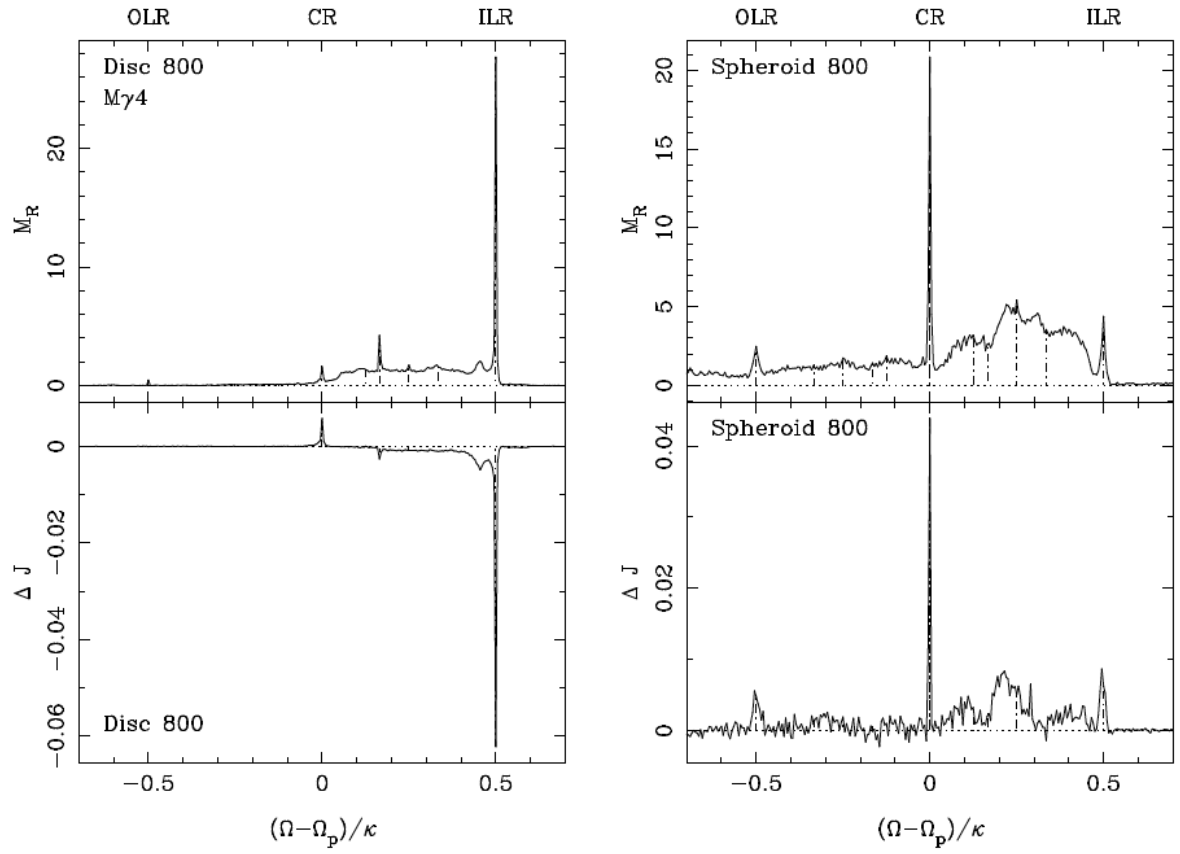

FIGURE 1.8: Exchange of angular momentum at the resonances between the disc and the spheroid. The upper panels give for time t=800 the mass per unit frequency ratio as a function of that ratio. The lower panels give the angular momentum gained or lost by the particles between times 800 and 500, plotted as function of their frequency ratio calculated at time 800. The left panels correspond to the disc component and the right ones to the spheroid. Taken from Athanassoula (2003)

and indeed a very large CMC can weaken, or destroy bars (Hasan et al., 1993, Norman et al., 1996, Shen and Sellwood, 2004, Athanassoula et al., 2005).

Due to the angular momentum exchange that they induce, bars are now thought to be the main drivers of the secular phase of galaxy evolution. The torque they induce into the disc causes outward angular momentum transfer, which in turn will cause a redistribution of matter in the disc. They are thus thought to be responsible for driving gas to the centre of their host galaxy (Athanassoula, 1992b, Regan and Teuben, 2004), where they can form discy pseudo-bulges (Kormendy and Kennicutt, 2004, Athanassoula, 2005) and induce star formation in the central region Knapen et al. (1995, 2002), Ellison et al. (2011), Coelho and Gadotti (2011). Additionally, gas inflow to the centres of galaxies is thought to provide a fuel reservoir for AGN activity (Knapen et al. 2000, Shlosman et al. 1990, Coelho and Gadotti 2011, Emsellem et al. 2014. For a review see Combes 2001). Furthermore, bars redistribute stars in the galactic disc via radial migration processes, thus changing the metallicity gradients in discs (Sellwood and Binney, 2002, Roškar et al., 2008, Minchev and Famaey, 2010, Kubryk et al., 2013, 2015a,b).

FIGURE 1.9: Galaxy ESO 597-G036 which has a characteristic peanut shaped bulge.

Barred galaxies often contain both inner and outer rings and/or lenses (Buta, 1986) due to the redistribution of matter which galaxies undergo in the presence of a bar (although note that unbarred galaxies are also found to contain nuclear and outer rings (Knapen et al., 2004, Comerón et al., 2014)). Since rings are visible in the near infrared (Comerón et al., 2014), as well as in the gas, they cannot be exclusively hydrodynamical phenomena that influence only the distribution of young stars.

1.2.1.1 Vertical extent

The vertical structure of bars is non-trivial to assess since it is difficult to identify bars when the galaxy is seen edge on. However, many edge-on disc galaxies can be seen to contain boxy-, peanut- or X-shaped isophotes, which are usually grouped together into the category of Boxy/Peanut (hereafter B/P) bulges due to their shape which resembles that of a peanut (see Figure 1.9). As a result of a number of theoretical studies (see Athanassoula 2008a, 2015 for general reviews of this subject), including orbital structure and stability analysis (Binney, 1981, Pfenniger, 1984, 1985, Berentzen et al., 1998, Patsis et al., 2002, Skokos et al., 2002a,b, Martinez-Valpuesta et al., 2006, Harsoula and Kalapotharakos, 2009, Contopoulos and Harsoula, 2013), and numerical simulations (Combes and Sanders, 1981, Combes et al., 1990, Raha et al., 1991, Mihos et al., 1995, Athanassoula and Misiriotis, 2002, Athanassoula, 2003, 2005, Bureau and Athanassoula, 2005, Martinez-Valpuesta et al., 2006), these structures are now known to be due to vertical instabilities in the bar, which cause it to 'puff up', giving rise to boxy or peanut-like shapes. These studies also show that once a bar forms, a B/P bulge will form soon after, often going through a 'buckling' phase where the bar becomes asymmetric in the vertical plane. During the buckling instability, the bar strength is seen to decrease, after which the bar obtains its characteristic symmetric peanut shape (see Figure 1.10 for a sequence showing the formation of the B/P bulge in a simulation as seen edge-on, by Martinez-Valpuesta et al. (2006)). The bar then continues to grow secularly after the B/P bulge has formed (Martinez-Valpuesta et al., 2006).

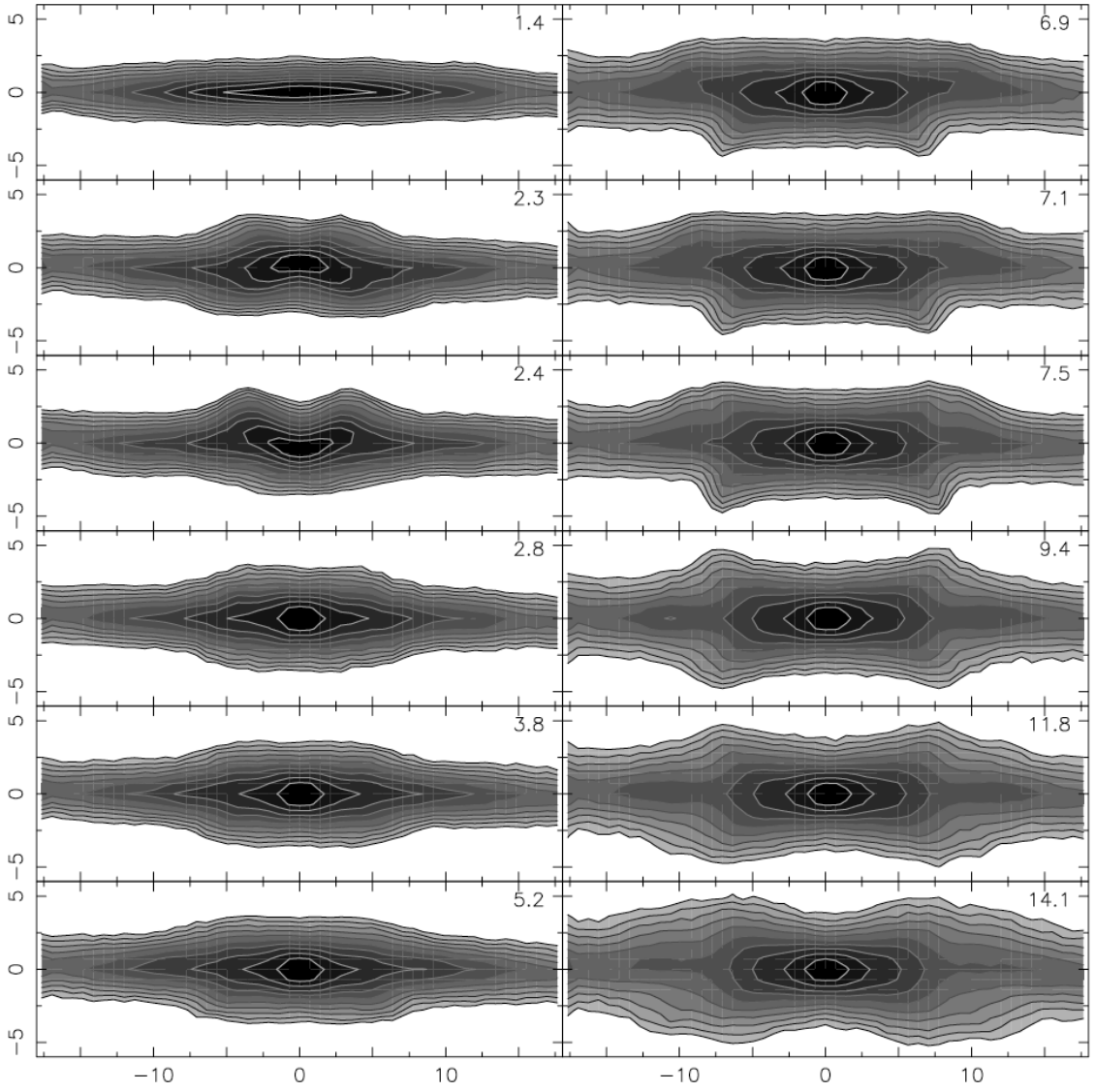

FIGURE 1.10: Evolution of the vertical structure in an N-body simulation as seen from an edge-on view. The bar can be seen to go through two buckling phases at 2.4 and 7 Gyr. From Martinez-Valpuesta et al. (2006).

Observational studies have further confirmed the link between B/P bulges and bars (see Kormendy and Kennicutt 2004 and Kormendy 2015 for reviews on the subject), by showing that the fraction of edge-on disc galaxies with B/P bulges is comparable to the fraction of disc galaxies containing bars (Lütticke, Dettmar, and Pohlen, 2000). Kinematic studies of edge-on barred galaxies and B/P bulges also confirm the connection between the two structures (Athanassoula and Bureau, 1999, Bureau and Athanassoula, 1999, Chung and Bureau, 2004, Bureau and Athanassoula, 2005, and references therein). Therefore, barred galaxies at present and past epochs will contain B/P bulges, and in fact, one is also believed to be present in our own Galaxy (Weiland et al. 1994, Howard et al. 2009, Shen et al. 2010, McWilliam and Zoccali 2010, Ness et al. 2012, 2013a,b, Vásquez et al. 2013, Wegg and Gerhard 2013, Gardner et al.

2014, Nataf et al. 2013, 2014, 2015).

It is also worth noting that effort has been made to observe features of B/P bulges in face-on or almost face-on barred galaxies, which would allow to identify B/P bulges in un-inclined systems. For example, Athanassoula et al. (2014) found that, by viewing a large number of N-body+SPH simulations, and covering a wide range of viewing angles, B/P bulges manifest themselves in face-on projections as the so called 'barlens' (Laurikainen et al., 2011, Laurikainen and Salo, 2015), which renders their detection fairly easy. Another method for detecting B/P bulges in face-on galaxies has been proposed by Debattista et al. (2005), who uses signatures of B/P bulges in the stellar kinematics of face-on or almost face-on galaxies. This was tested by Méndez-Abreu et al. (2008) on a number of barred galaxies who confirmed the existence of a B/P bulge in NGC 98. Furthermore, it is possible to detect signatures of B/P bulges by examining the morphological features of inclined galaxies, as shown by Athanassoula and Beaton (2006) for the Andromeda galaxy, and extended to a larger sample of galaxies by Erwin and Debattista (2013).

1.2.1.2 Pattern speed

One of the most important dynamical properties of a barred galaxy is the bar pattern speed Ω_p. The bar pattern speed sets the corotation radius of the bar, which in strong bars is equivalent to the Lagrangian radius, i.e. the distance between the centre of the galaxy and the L_1 point (this is discussed further in Section 1.2.2). Due to a number of reasons, one of them being the straight shape of the bar, it is believed that bars have a well-defined pattern speed. This is parametrised by the ratio $\mathcal{R}=r_{CR}/r_B$ where r_{CR} is the corotation radius and r_B the bar semi-major axis.

Dynamical arguments show that self consistent bars must have $\mathcal{R}\geq1$, that is, bars cannot extend beyond corotation (Contopoulos, 1980, Athanassoula, 1980). On the other hand, what controls the upper limit of the Lagrangian radius is the angular momentum transfer in the galaxy; due to the fact that angular momentum is a conserved quantity, whatever angular momentum is emitted by the bar, must be absorbed by the outer disc and halo (Athanassoula, 2003). Therefore the slow down of the bar will depend on the amount of resonant material available which is able to absorb angular momentum from the inner parts of the discs. The slow down of bars embedded in live dark matter halos has also been interpreted as being due to the dynamical friction caused by dark matter halos (Debattista and Sellwood, 2000). Bars are therefore often separated into two categories: as *fast* rotating bars if $1\leq\mathcal{R}\leq1.4$ and *slow* rotating bars if $\mathcal{R}\geq1.4$ (Debattista and Sellwood, 2000).

The only direct method for measuring the bar pattern speed is via the Tremaine-Weinberg method, which, due to the fact that it relies on the continuity equation, is best suited for

stellar populations which approach that. Hence it has been used for early type galaxies such as SB0s (Tremaine and Weinberg, 1984, Corsini, 2011). Indirect methods for measuring the bar pattern speed involve the distribution and kinematics of gas in late type galaxies (Lindblad et al., 1996, Weiner et al., 2001, Pérez et al., 2004, Rautiainen et al., 2008). These methods seem to suggest that bars, especially those found in early type galaxies, in general rotate fast, i.e. that corotation occurs near the end of the bar, and that $\mathcal{R}$ is of the order of 1.2 (Elmegreen, 1996, Corsini, 2011), while there is some evidence that bars in late type galaxies are slow (Rautiainen et al., 2008). This is compatible with theoretical predictions by Athanassoula (1992b), which suggest that in order to reproduce the shapes of dust lanes seen in barred galaxies, bars should extend to about 80% of their corotation radius.

1.2.2 Dynamics of barred galaxies

During the 60's most theoretical work on galaxy dynamics was done analytically. In order to do this the potentials of galaxies were assumed to be steady-state or quasi steady-state which we know of course is a crude approximation to real galaxies. However, physical insight can be gained on the celestial mechanics governing barred galaxies with these methods, and so I present some of the most relevant results which serve as background for the rest of this thesis; I give an overview of the dynamics of barred galaxies, focusing on some of the concepts which are of use for Chapter 2 of the thesis, such as the main families of periodic orbits and the characteristic diagram. Most of the topics covered in this section follow results from Chapter 3 of Binney and Tremaine (2008), along with a number of other seminal papers which are referenced in the text; for more details on these topics the reader is referred to Binney and Tremaine (2008) and references therein.

1.2.2.1 Equations of motion in a rotating barred potential

Except in the immediate neighbourhood of a star, the gravitational attraction of nearby stars is generally negligible compared with that from the large-scale distribution of matter in a galaxy. We can therefore treat the potentials of galaxies as smooth, and stars as test particles within this smooth potential. Barred galaxies are generally modelled with an axisymmetric component which models the disc, and a non-axisymmetric m=2 type potential, which rotates with a constant pattern speed, thus mimicking the behaviour of the bar.

The equations of motion in a rotating frame of reference, where the frame rotates with $\boldsymbol{\Omega_p}=\Omega_p\hat{\mathbf{e}}_z$, where Ω_p is the pattern speed of the bar, are given by,

$$\ddot{\boldsymbol{r}} = -\boldsymbol{\nabla}\Phi - 2(\boldsymbol{\Omega_p} \times \dot{\boldsymbol{r}}) - \boldsymbol{\Omega_p} \times (\boldsymbol{\Omega_p} \times \boldsymbol{r}) \tag{1.5}$$

where the terms $-2(\Omega_p \times \dot{r})$ and $-\Omega_p \times (\Omega_p \times r)$ represent the Coriolis and centrifugal forces respectively.

We can define E_J, Jacobi's integral as,

$$E_J = \frac{1}{2}\dot{\boldsymbol{r}}^2 + \Phi - \frac{1}{2}|\boldsymbol{\Omega_p} \times \boldsymbol{r}|^2, \tag{1.6}$$

which can be thought of as the energy in the rotating frame of reference. In the non-rotating frame the energy is given by $E{=}\frac{1}{2}\acute{\mathrm{r}}^2 + \Phi$; this however is not conserved in the rotating frame, nor is the angular momentum L. However the combination of the energy and the angular momentum, E-$\Omega_p L = E_J$, i.e. the Jacobi integral, is conserved. We define an effective potential, which we can think of as the potential in the rotating frame of reference, which combines the centrifugal potential energy with the potential energy of the dynamical system,

$$\Phi_{eff} = \Phi - \frac{1}{2}\Omega_p^2 R^2. \tag{1.7}$$

Then the equations of motion can be re-written as,

$$\ddot{\boldsymbol{r}} = -\boldsymbol{\nabla}\Phi_{eff} - 2(\boldsymbol{\Omega_p} \times \dot{\boldsymbol{r}}) \tag{1.8}$$

and the Jacobi integral as

$$E_J = \frac{1}{2}|\dot{\boldsymbol{r}}|^2 + \Phi_{eff}. \tag{1.9}$$

The surface $\Phi_{eff} = E_J$ is called the *zero-velocity surface* or *zero-velocity curve*, since on this surface the velocity of a star is instantaneously zero. All regions $\Phi_{eff} > E_J$ are forbidden to the star, since in these regions the kinetic energy of the star would have to be negative. In Figure 1.11 I show contours of Φ_{eff} for a bar like potential.

All m=2 bar-like potentials, have five stationary points in Φ_{eff}, which are typically denoted from L_1 to L_5 and which are referred to as *Lagrange points*. At these points the derivatives of the effective potential are equal to zero,

$$\frac{\partial \Phi_{eff}}{\partial x} = 0, \tag{1.10}$$

$$\frac{\partial \Phi_{eff}}{\partial y} = 0 \tag{1.11}$$

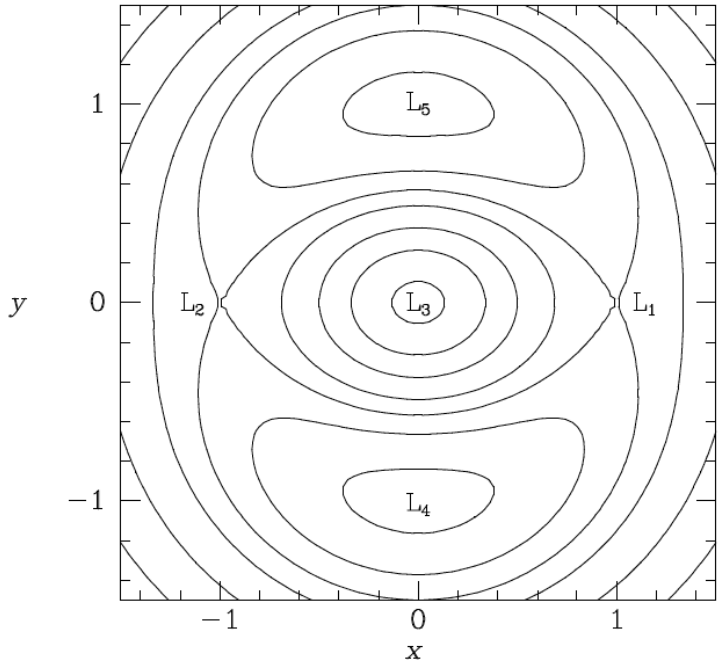

FIGURE 1.11: Contours of constant effective potential for a barred-like model of a galaxy. We see the five Lagrangian points marked from L_1 to L_5. The Lagrangian point L_3 is the minimum of the effective potential and the points L_1 and L_2 are saddle points. The distance between L_3 and L_1 (or L_2) is called the Lagrangian radius. L_1, L_2, L_3 and L_4 mark points at which a star would appear to be stationary in the rotating frame of reference. From Binney and Tremaine (2008)

i.e. the force in the rotating frame of reference is equal to zero. This occurs at the points where the gravitational and Coriolis forces are exactly balanced out. L_3 is located at the centre of the effective potential, as can be seen in Figure 1.11, and is a minimum of the effective potential.

If there is a star on a circular orbit around the centre of the galaxy, at the rest of the Lagrange points, L_1, L_2, L_4 and L_5, it will appear to be stationary in the rotating frame. Since L_1 and L_4 are not necessarily at the same distance from the centre we don't refer to a corotation radius, but rather a corotation annulus or region of corotation. While L_4 and L_5 are maxima of the potential, L_1 and L_2 are saddle points and are therefore always unstable (i.e. they cannot trap stable periodic orbits around them). The distance between the centre and the point L_1 is referred to in the rest of this thesis as the Lagrangian radius r_L, and is used extensively in Chapter 4.

We are interested in finding periodic orbits in galactic models, in order to know what trajectories stars would follow in these potentials. For consistency I give some nomenclature:

- A **periodic orbit** is an orbit which closes up upon itself periodically after a given amount of time T.
- A **stable orbit** is that which, when another orbit has initial conditions in its vicinity, will tend to stay (for infinite time) around the original orbit. Stable periodic orbits trap

around them regular non-closed orbits. This means that an orbit that starts near (in phase-space, i.e. in velocity and in position) to a stable periodic orbit, will tend to stay in its vicinity for infinite time.

Stable periodic orbits can be thought of as the building blocks of galaxies, because they can trap stars and gas around them in stable non-closed orbits (such as those shown in Figure 1.14), thus giving rise to the complex morphological features we observe in galaxies. This can also be due to preferred orbital paths around the unstable L_1 and L_2 Lagrange points, which are used in the manifold theory (Romero-Gómez et al., 2006, Athanassoula et al., 2009).

1.2.2.2 Epicyclic approximation

The epicyclic approximation describes the motions of stars on nearly circular orbits, which is appropriate for studying the motions of stars in disc galaxies, since the rotation velocity is much larger than the velocity dispersion for a large variety of stellar populations e.g. in the solar neighbourhood.. Additionally, the approximation offers insight in understanding the approximation of orbits in a weakly barred potential. I therefore show the main steps in deriving the orbits in the epicycle approximation focusing in the motion in the meridional plane.

The acceleration of a star in cylindrical coordinates is given by

$$\ddot{R} - R\dot{\phi}^2 = -\frac{\partial \Phi}{\partial R}. \tag{1.12}$$

Given that $\Omega(R) = L_z^2/R^4 = \dot{\phi}^2$ together with the equation for the effective potential (Equation 1.7) we define the effective potential as,

$$\Phi_{eff} = \Phi(R, z) + \frac{L_z^2}{2R^2}. \tag{1.13}$$

Therefore we can write the acceleration of a star in cylindrical coordinates as,

$$\ddot{R} = -\frac{\partial \Phi_{eff}}{\partial R}. \tag{1.14}$$

The minimum of Φ_{eff} is the energy of a circular orbit with angular speed $\dot{\phi}$ which occurs at a radius R_g. For a star which is on a nearly circular orbit we can define a parameter x such that

$$x = R - R_g \tag{1.15}$$

i.e. where R gives the radius of the orbit which is perturbed by a small amount x from the radius R_g of the circular orbit of that energy. The effective potential Φ_{eff} can be expanded in a Taylor series about the point x to give,

$$\Phi_{eff} = \frac{1}{2}\Big(\frac{\partial^2\Phi_{eff}}{\partial R^2}\Big)_{(R_g,0)}x^2 + \frac{1}{2}\Big(\frac{\partial^2\Phi_{eff}}{\partial z^2}\Big)_{(R_g,0)} + O(xz^2) + constant. \tag{1.16}$$

Note that the term that is proportional to xz vanishes because Φ_{eff} is symmetric about $z = 0$. We can now define a new quantity:

$$\kappa^2 = \Big(\frac{\partial^2\Phi_{eff}}{\partial R^2}\Big)_{(R_g,0)} \tag{1.17}$$

and then by inserting Φ_{eff} from the epicyclic approximation (Equation 1.7) into the equation of motion in the meridional plane (Equation 1.14) we obtain,

$$\ddot{x} = -\kappa^2 x \tag{1.18}$$

where x evolves like the displacement of a harmonic oscillator with frequency κ, called the epicyclic frequency. This equation has a general solution given by,

$$x(t) = X\cos(\kappa t + \psi). \tag{1.19}$$

As mentioned above, the tangential velocity is $\dot{\phi} = \frac{L_z}{R^2}$ and if we plug in $R = x + R_g$ we get,

$$\dot{\phi} = \frac{L_z}{R^2}\Big(1 + \frac{x}{R_g}\Big)^{-2}. \tag{1.20}$$

Since $\Omega_g = L_z/R_g^2$ is the angular speed of the circular orbit with angular momentum L_z we get,

$$\dot{\phi} = \Omega_g\Big(1 + \frac{x}{R_g}\Big)^{-2}. \tag{1.21}$$

By substituting x (from Equation 1.19) into Equation 1.21 and integrating, we obtain

$$\phi = \Omega_g t + \phi_0 - \frac{2\Omega_g X}{\kappa R_g}\sin(\kappa t + \psi) \tag{1.22}$$

If we define y as a slight perturbation from the circular orbit, where the guiding centre is given by $\phi = \Omega_g t + \phi_0$ then y can be written as,

$$y(t) = -\frac{2\Omega_g}{\kappa} X \cos(\kappa t + \psi) \tag{1.23}$$

$$y(t) = -Y \cos(\kappa t + \psi) \tag{1.24}$$

where X and ψ are arbitrary constants. Equations 1.19 and 1.24 are the complete solution for the orbit in the epicycle approximation where this cartesian axis has its origin at the guiding centre $R = R_g$ and $\phi = \Omega_g t + \phi_0$. In the (x, y) plane the star moves on an ellipse called the epicycle around the guiding centre.

1.2.2.3 Orbits in weak barred potentials

For weak bars one can find analytic solutions to the equations of motion, in order to determine the behaviour of orbits in the models, especially near the resonances. The bar is weak if it can be considered as a perturbation on an axisymmetric background. In such systems most stellar orbits can be described as a superposition of the circular motion of a guiding centre and small oscillations around this guiding centre. Hence the treatment of orbits in a weak non-axisymmetric potential is similar to the epicycle theory of nearly circular orbits in an axisymmetric potential. Assuming an m=2 potential, we find the equation of displacement of the radius of the orbit from the axisymmetric case to be given by the equation of motion of a harmonic oscillator, of natural frequency κ_0, that is driven at frequency $m(\Omega_0 - \Omega_p)$. This has a general solution given by,

$$R_1(\phi_0) = C_1 \cos\Big(\frac{\kappa_0 \phi_0}{\Omega_0 - \Omega_p} + \psi\Big) + C_2 \cos(m\phi_0) \tag{1.25}$$

where

$$C_2 = -\frac{1}{\Delta}\Big[\frac{d\Phi_b}{dR} + \frac{2\Omega\Phi_b}{R(\Omega - \Omega_p)}\Big]_{R_0} \tag{1.26}$$

and

$$\Delta = \kappa_0^2 - m^2(\Omega_0 - \Omega_p)^2 \tag{1.27}$$

If C_1=0 then $R_1(\phi_0)$ becomes periodic in ϕ_0 and therefore the orbit is a closed loop orbit. The orbits with $C_1 \neq 0$ are non closed loop orbits. We are interested in the periodic closed loop orbits so we assume C_1=0.

1.2.2.4 Resonances

Even weak perturbations can add up if they happen to be in resonance with the system they drive. By examining where equation 1.25 becomes singular, we examine what occurs at the resonances. This equation becomes singular at a number of values of R_0:

At the **Corotation resonance**, when

$$\Omega_0 = \Omega_p \tag{1.28}$$

At the **Lindblad resonances**, when

$$m(\Omega_0 - \Omega_p) = \pm\kappa_0 \tag{1.29}$$

where the star encounters successive crests of the potential at a frequency that coincides with the frequency of its natural radial oscillations. The plus sign corresponds to the case in which the star overtakes the potential and is called the *inner Lindblad resonances* while the minus sign corresponds to the case where the bar potential overtakes the star and is known as the *outer Lindblad resonance*.

A galaxy can have 0, 1 or 2 inner Lindblad resonances, depending on the shape of the rotation curve and on the bar pattern speed. From Equation 1.25 it also follows that the orbit is aligned with the bar whenever $C_2 > 0$ and is aligned perpendicular to the bar when $C_2 < 0$. So when passing through a resonance the sign of C_2 and the orientation of the closed loop orbit changes.

1.2.2.5 Orbits in strong barred potentials

The aforementioned is valid in the case of a weak bar perturbation, i.e. when the non-axisymmetric component can be considered as a perturbation on an axisymmetric background. However for strong bars, numerical integration of the orbits is necessary. The equations of motion in equation 1.5 can be numerically integrated to obtain orbits in a strongly barred potential. An important concept in dynamics of galaxies is that of the characteristic diagram which is a way of summarising the properties of families of periodic orbits of a model. The characteristic diagram gives the value at which the orbit cuts the minor axis, i.e. in our case the y-axis, as a function of the Jacobi constant, i.e. the energy in the rotating frame of reference as shown in Figure 1.12. The dotted line in the diagram gives the zero velocity curve which was referred to above, i.e. above this curve is the *forbidden region* where orbits are not allowed to populate the diagram. Each point of the solid curves in this diagram is a closed

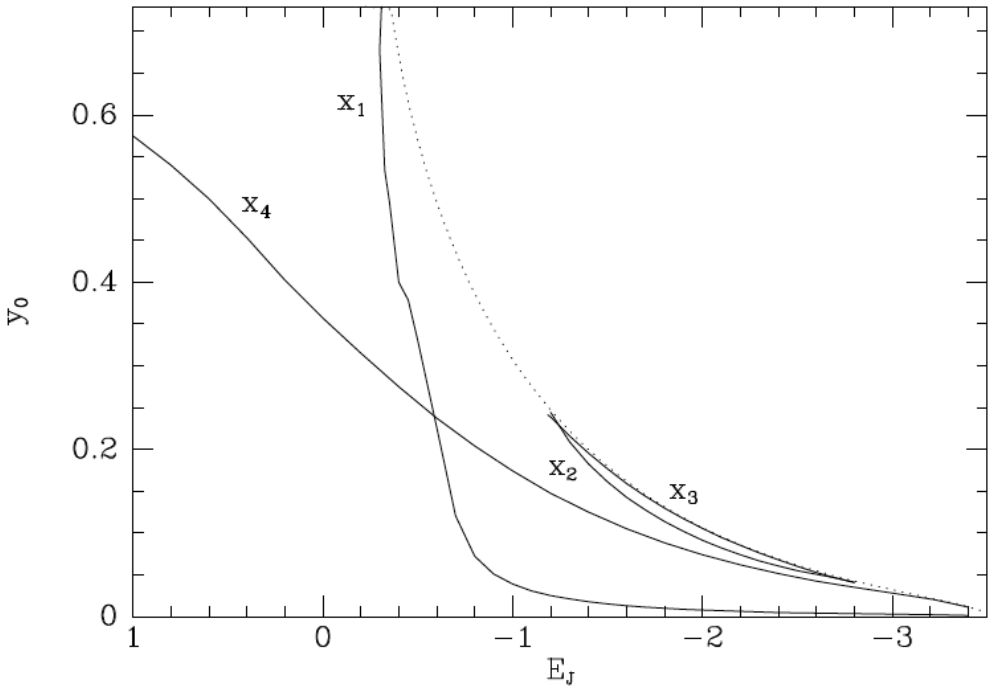

FIGURE 1.12: Characteristic diagram in which the value y_0 at which a closed periodic orbit cuts the minor axis of the bar is plotted against the Jacobi constant E_J. The dotted line is the zero-velocity-curve (E_J=Φ_{eff}) above which is the forbidden region in which orbits are not allowed to populate the diagram. The curves corresponding to the families x_1, x_2, x_3 and x_4 are shown. From Binney and Tremaine (2008).

periodic orbit, and each solid line is a sequence of closed periodic orbits which all belong to the same family.

We find that in the bar region there is one important stable family of periodic orbits, the so called x_1 family (see Figure 1.13(a)), where the naming convention comes from Contopoulos and Papayannopoulos (1980). These are prograde orbits, i.e. they rotate in the same direction as the bar and they are elongated along the bar, therefore they are thought to constitute the bar.

Another important family of periodic orbits found in barred galaxy potentials is the x_2 family, which has orbits perpendicular to the bar (see Figure 1.13(b)). The x_2 family tends to appear together with its unstable counterpart, the x_3 family.

Another important family of periodic orbits found in barred galaxy potentials is the x_4 family, which are circular retrograde orbits, extending from the central regions to the outer parts of galaxies (see Figure 1.13(c))

Each sequence of closed orbits generates a continuous curve in this diagram known as the characteristic curve of that sequence as can be seen in Figure 1.12. These stable closed orbits are associated with substantial families of non-closed orbits. A star on a non closed orbit may execute stable oscillations about one of the fundamental closed orbits. The amplitude of the

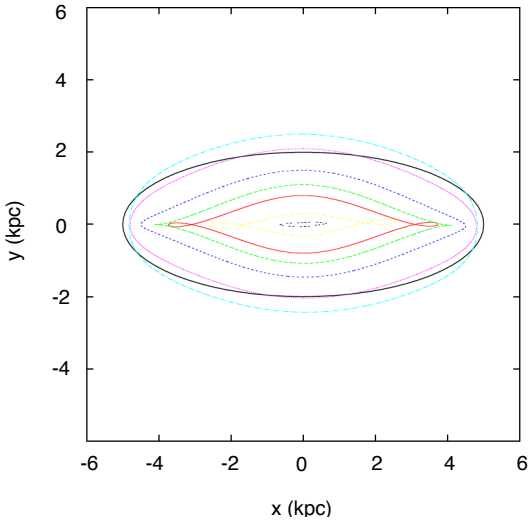

(a) x_1

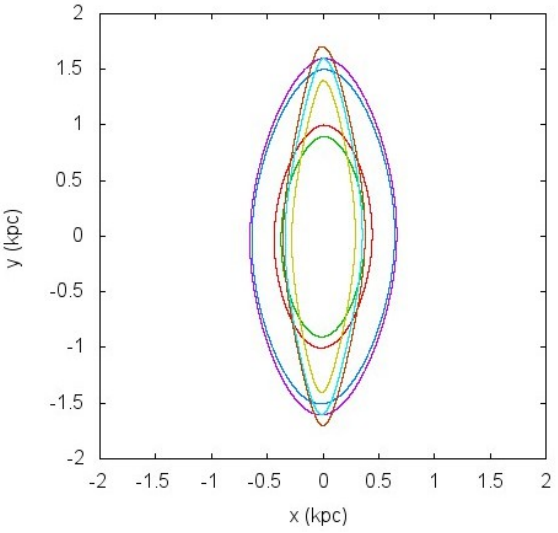

(b) x_2 and x_3

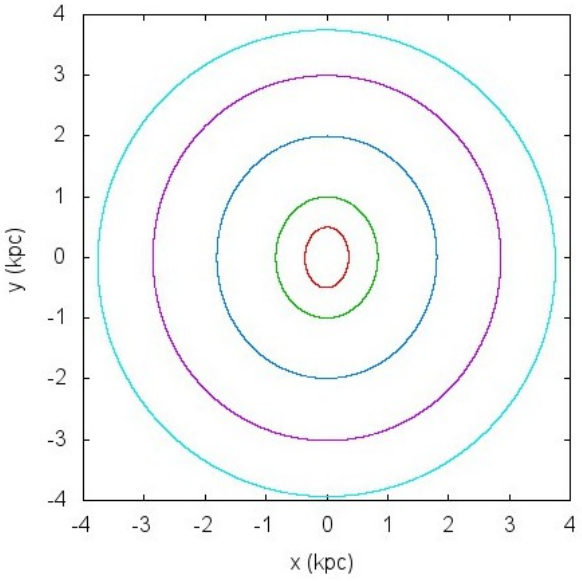

(c) x_4

FIGURE 1.13: Some examples of orbits found in models of barred galaxies (the model consists of a disc and a Ferrers' bar (Ferrers, 1877)). In Figure 1.13(a) I plot some x_1 orbits. The solid black curve shows the outline of the bar. We see that some of the x_1 orbits have loops, characteristic of strong bars. In Figure 1.13(b) I plot some x_2 and their unstable counterpart, some x_3 orbits (the x_3 orbits are more elongated than the x_2 orbits.) In Figure 1.13(c) I plot some retrograde x_4 orbits which rotate opposite to the sense of rotation of the bar. They are more elongated in the inner parts and become rounder as we move further away from the centre. Note that each panel has a different scale.

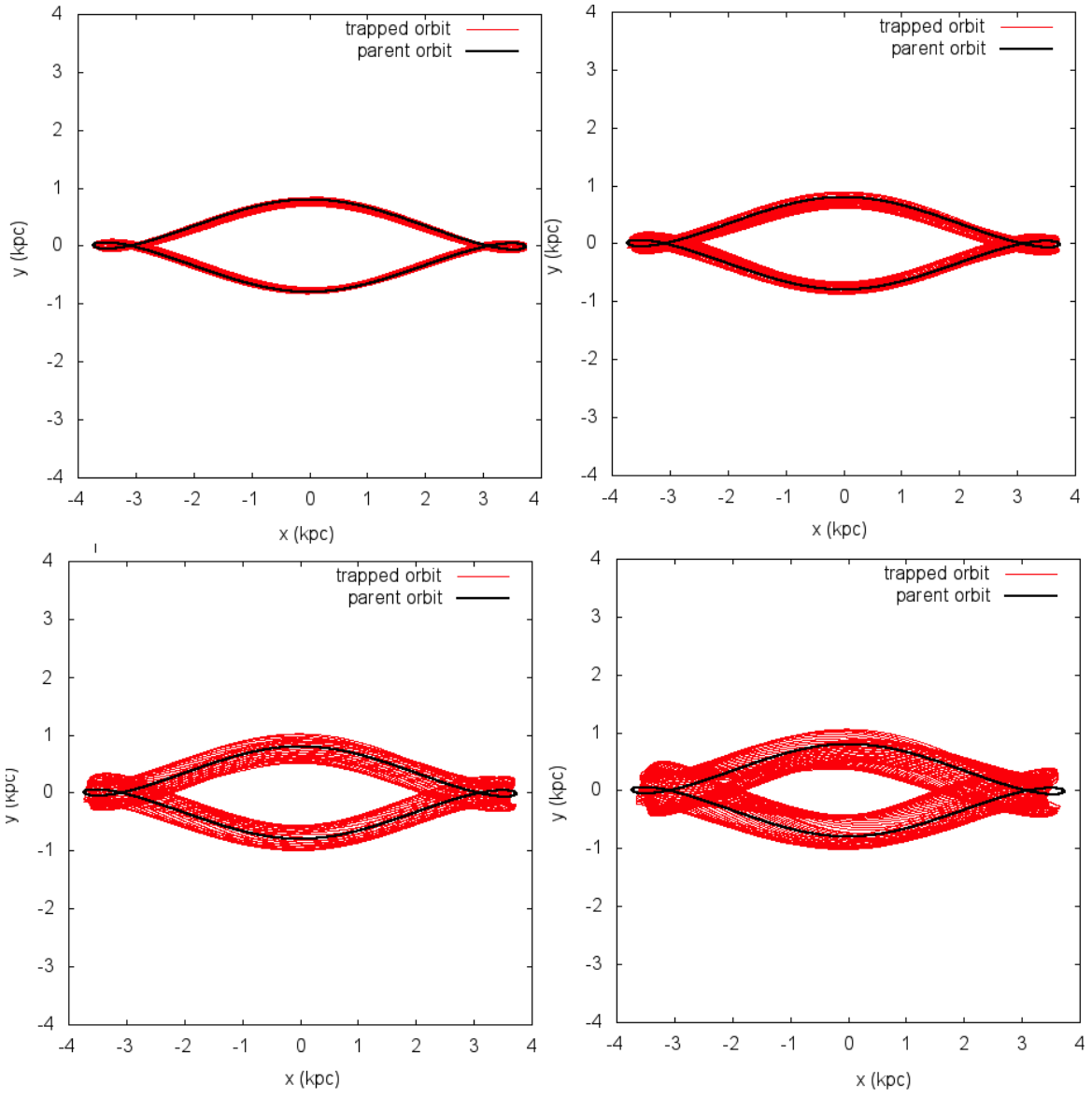

FIGURE 1.14: Examples of trapped orbits (red line) around a parent closed periodic orbit (black line). From top left to bottom right, the orbit is less and less trapped, i.e. the orbit has initial conditions in phase space further away from the parent periodic orbit.

oscillation will depend on how far in phase-space the initial conditions of the orbit are from the parent closed periodic orbit. Figure 1.14 shows a sequence of trapped non-closed periodic orbits with initial conditions starting further away from the parent periodic orbit from top left to bottom right. We see that in each step the oscillation around the parent periodic orbit grows.

In Chapter 2 I will return to these orbits (specifically the x_1 and x_2 orbits) and the characteristic diagram in order to examine the effects of B/P bulges on galaxy models.

The periodic orbits in each galaxy model will depend on the specific properties of those models. However from investigation into the properties of a number of two-dimensional barred galaxy

models Contopoulos and Grosbol (1989) found a number of generic properties for barred galaxies. I list the most important of these for the rest of this thesis are listed below:

- The main bar supporting family of periodic orbits is the x_1 family, elongated along the bar. Most x_1 orbits have elliptical shapes often with loops at both ends.
- If there are two 2/1 resonances in the bar, the orbits between these two resonances are oriented perpendicular to the bar, i.e. they are the stable x_2 family of periodic orbits. In stronger bars the family x_2 becomes insignificant or disappears.
- In slowly rotating bars with two ILRs the energy along the x_1 family increases outwards and this family is (horizontally) stable up to the corotation region. However in fast rotating bars the energy along the x_1 family increases to a maximum then decreases to a minimum, and later on increases again. between the maximum and minimum of the energy the orbits are unstable, therefore the role of the x_1 family in trapping non periodic orbits is important only in the inner parts of the galaxy
- Orbits near the Lagrangian points L_4 and L_5 are either slightly elliptical or like elongated bananas parallel to the bar. Such orbits produce density plateaus near L_4 and L_5 that appear as secondary maxima of density

1.2.3 Dust lanes in barred galaxies

One of the most notable features in barred galaxies are the dust lanes as those seen in the four barred galaxies of Figure 1.15, which extend from the nucleus into the spiral arms, on each side of the bar. Assuming spirals are trailing, dust lanes occur on the leading side of the bar. Predergast (1962, unpublished) was the first to associate these dust lanes with shocks in the gas flow and since then several independent lines of evidence support this, most notably from hydrodynamical simulations of barred galaxies (Athanassoula, 1992b, Weiner et al., 2001, Lin et al., 2013).

Observationally, the most straightforward way to test whether dust lanes are associated with shocks in the gas, is by measuring velocities across the dust lanes and to look for jumps in the velocity. These kinds of studies were carried out by Joersaeter (1985), Lindblad and Jorsater (1987), Pence and Blackman (1984a,b) and Mundell and Shone (1999) who found clear evidence of such jumps at the positions of the dust lanes in the velocity field of a number of galaxies.

Furthermore, barred galaxies have been observed in the radio continuum, where it has been found that there is an enhancement in the radio continuum emission at the locations of the dust lanes (Ondrechen and van der Hulst, 1983, Ondrechen, 1985). This is due to the fact that

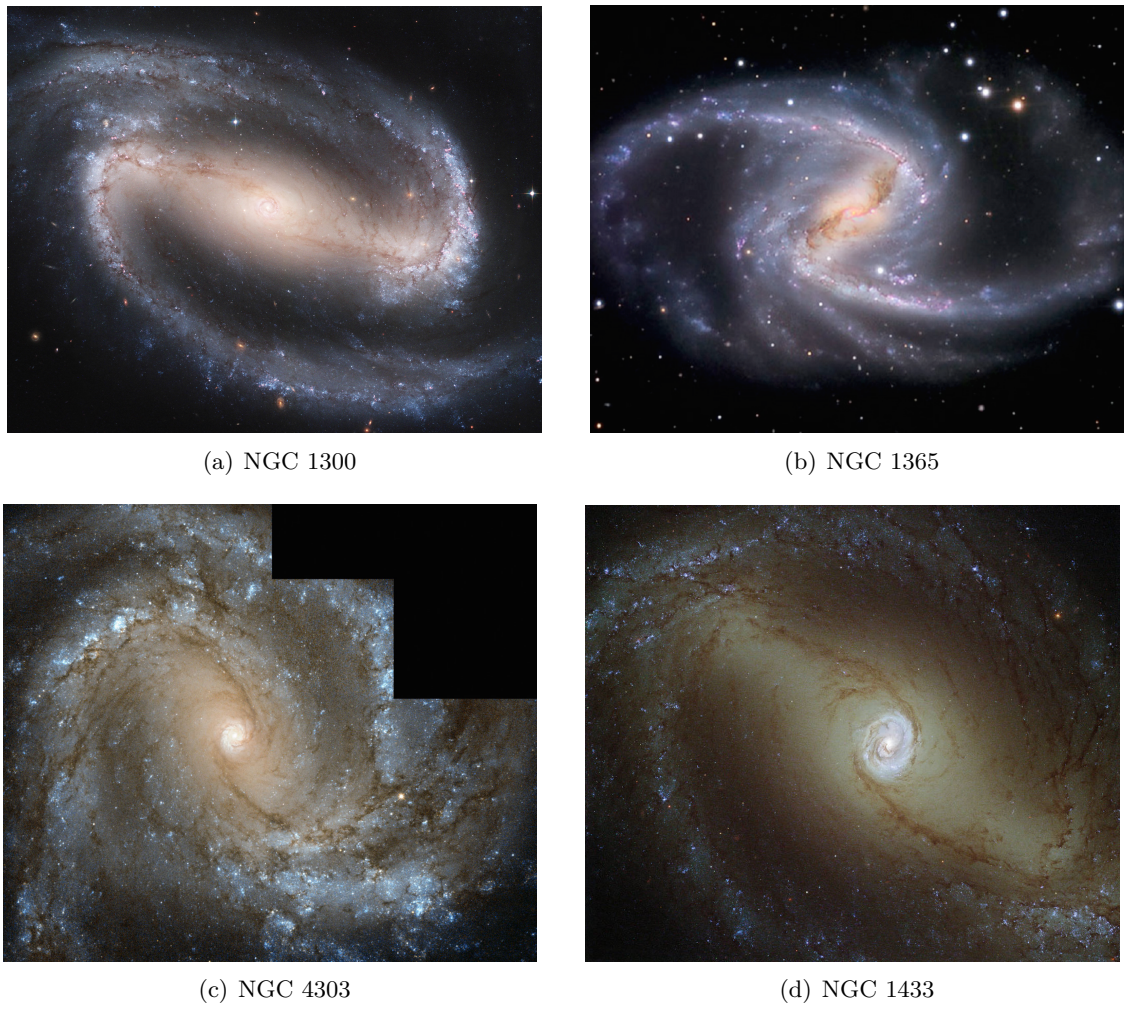

(a) NGC 1300 (b) NGC 1365

(c) NGC 4303 (d) NGC 1433

FIGURE 1.15: Dust lanes in four classical examples of barred spiral galaxies. NGC 1300 is considered a classic example of a galaxy with straight dust lanes while NGC 4303 and 1433 are considered to have more curved dust lanes.

shocks are loci of compressed gas, dust, and magnetic fields with high energy particles, and they are subsequently also regions with enhanced radio emission. Additionally, observations of galaxies in the near infrared Spitzer bands shows enhanced dust emission in the regions of dust lanes.

Dust lanes have different shapes, and Athanassoula (1992b) separated them in two classes, (i) *straight* and (ii) *curved*. Straight dust lanes are parallel to each other, and are either parallel to the bar, or form a slight angle to it, while curved ones have their concave sides towards the major axis. In both cases the dust lanes can often be seen to curve around the central region of the galaxy which sometimes results in the appearance of a ring-like structure. Examples of straight dust lanes are NGC 1300 (see Figure 1.15(a)), while examples of curve dust lanes are found for example in NGC 4303 and 1433 (see Figures 1.15(c) and 1.15(d)). These properties of the dust lanes are now known to be tightly correlated to properties of the bar, such as the strength of the bar and the pattern speed (Athanassoula, 1992b, Sánchez-Menguiano et al.,

2015). I will go into more details on how the various properties of the galaxy effect the shape of the dust lanes in Chapter 4, but it is already known that strong bars tend to produce straighter dust lanes, while weaker bars will produce curved dust lanes. The shape of dust lanes is related to the strength and pattern speed of bars, due to the relation of the dust lanes to the periodic orbits found in bars. Gas can follow simple periodic orbits so long as these do not intersect and this may happen if the bar or oval is not very massive and not very eccentric. If the main families of periodic orbits intersect then shocks are formed (Athanassoula, 1992b, Sormani et al., 2015).

As Athanassoula (1992b) showed, in the outermost parts of the bar the flow lines have the form and orientation of the periodic orbits of the x_1 family and in the innermost parts resemble the orbits of the x_2 family. In between there is a gradual shift from the one to the other which gives the shock loci their characteristic shape. For models with no x_2 or x_3 family the flow lines have the orientation of the x_1 family at all radii. If the gas flow in such models forms shocks, they will be very near the bar major axis. When the gas flow develops offset shock loci then the x_2 family must exist, and indeed it max also have a significant extent. The existence of the shocks is intimately linked to the value of the curvature of the x_1 orbits at their apocentres. More cuspy x_1 orbits, or orbits with loops at their ends will lead to stronger shocks.

The shocks are accompanied by very strong shear, which could explain the smoothness of the observed dust lanes and the absence of signs of star formation in them, in spite of the high gas density (Athanassoula, 1992b, Emsellem et al., 2014).

1.2.4 Dynamics of boxy/peanut bulges

Studying the orbital structure of bars in three dimensions is a non trivial issue, and a lot of work has been put into this from both the analytical and numerical side (for example Combes et al. (1990), Pfenniger and Friedli (1991), Skokos et al. (2002a), Martinez-Valpuesta et al. (2006) etc.)

Pfenniger and Friedli (1991) found in their models which are based on N-body simulations of isolated disc galaxies, that the x_1 family, which as already mentioned the one responsible for maintaining the bar, has vertical instability strips which lead to bifurcations, creating a number of vertical families. Among these the simplest, and considered one of the most important for the structure of the B/P bulge, is the x_1v_1 family, also called the *banana* orbits (see Figure 1.16).

Patsis, Skokos and Athanassoula, in a series of papers, investigated the 3D orbital structure of analytic barred galactic models, where the bar is modelled using a Ferrers bar (Skokos et al.,

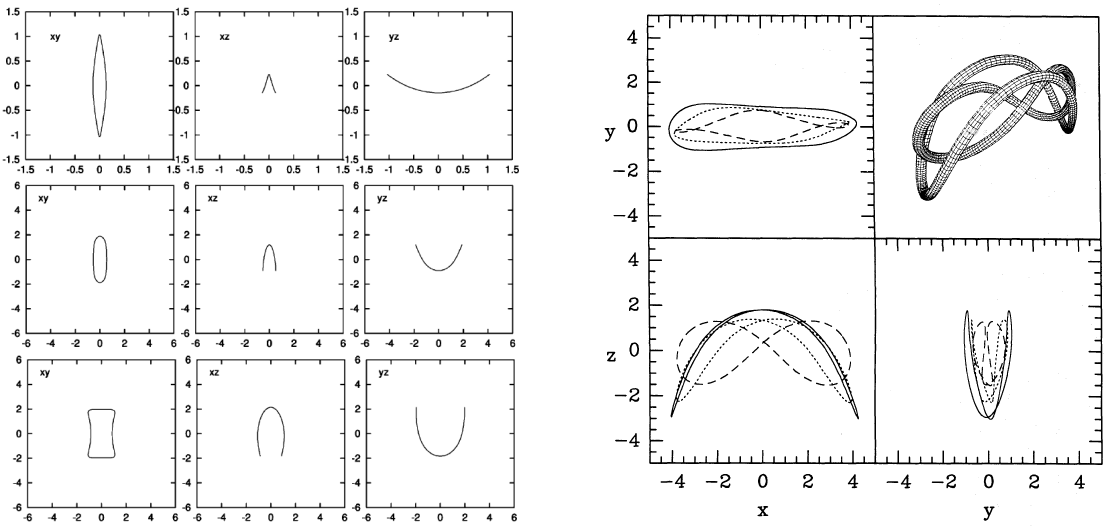

(a) (b)

FIGURE 1.16: *Left:* Three orbits belonging to the x_1v_1 family of three-dimensional periodic orbits, the so-called banana orbits, found in three dimensional bars. From Skokos et al. (2002a). *Right:* Banana orbits and anti-banana orbits (BAN and ABAN in the notation of Pfenniger and Friedli (1991)) which occur from vertical bifurcations in the x_1 family. In projection on the xy-plane are both shaped as x_1 orbits. The figure shows the progressive transformation from an ABAN orbit (dashed line) to a BAN orbit (solid line). The top right frame shows a "tube-view" of a BAN orbit (the downward bent banana shaped orbit) and an ABAN orbit (with the infinity shape).

2002a, Patsis et al., 2002). Some of the results they found were that families that make up the edge-on view of barred galaxies have orbital families that are of 'stair-type'. That is to say that orbital families bifurcated at higher energies have lower mean heights. They found that B/P bulges are supported mainly by the x_1v_1 family which bifurcates from the two-dimensional x_1 family. These orbits were especially found to support the B/P shape for strong and slow bars, as long as this family is stable. They also found that the x_1v_4 supported the B/P shape although these families tend to make the length of the peanuts comparable to the length of the bar, which is not usually the case, since subsequent work from, for example, Athanassoula et al. (2014) showed that B/P bulges tend to end before the end of the bar.

Recent work by Portail et al. (2015) showed that in their models, which are based on an N-body simulation of an isolated galaxy, a significant amount of the X-shaped structure is due to *brezel*-like orbits, i.e. orbits associated with higher frequency resonances. A possible origin of these type of brezel orbits could be the 5:3 vertical resonance of the $x_1$mul$_2$ planar orbit (in the notation of Skokos et al. (2002a)), which is like the usual x_1 orbit but which closes up upon itself after two rotations instead of one. They thus concluded that it is not the banana x_1v_1 orbits which are the most important for creating the B/P bulge, especially the inner parts, but that the brezel orbits also play a significant role.

Vertical resonances in the bar can induce vertical heating into the galaxy, since B/P bulges are due to vertical resonances in the bar region (Pfenniger and Friedli, 1991). Some authors such as Raha et al. (1991) suggested that the B/P is caused due to the symmetry breaking 'fire-hose' instability or 'buckling', which causes the galaxy to become asymmetric during the buckling phase (see Figure 1.10). However it is clear that the B/P is due to vertical resonances in the bar, as analytic work by Pfenniger and Friedli (1991), Patsis et al. (2002), Martinez-Valpuesta et al. (2006) has shown. Even if the bar is not allowed to buckle and form an asymmetry, the model still forms a B/P bulge through orbital heating, albeit this occurs on longer time-scales compared to those in which the buckling is allowed to occur (Martinez-Valpuesta et al., 2006).

Recent work by Athanassoula et al. (2014), Laurikainen et al. (2014) has also shown that there is a relation between the face-on density distribution in the bar and the edge-on view. This relates to the topic of bar-lenses a structure which has been noted to exist in the central regions of barred galaxies. These structures are usually thicker than the bar. Athanassoula et al. (2014) showed that it is possible to relate these structures with the edge-on view. Orbits that make up the inner part of B/P bulges are responsible for the face-on luminosity projection.

1.3 Outline

In the above, I discuss the cosmological context and the major processes which contribute to the formation and evolution of galaxies. I then focus on barred galaxies which are the topic of this thesis, describing some results from observations and numerical simulations, while also outlining some analytic results from the literature.

The structure of the rest of this thesis is as follows:

- In Chapter 2, I study the effect of adding the B/P bulge geometry to dynamical models of galaxies on the forces, orbital structure and bar strength of these models. Additionally, I discuss the amount of error introduced in the models if the geometry introduced does not exactly correspond to the "real" geometry of the B/P bulge.
- In Chapter 3, I discuss the hydrodynamic gas response simulations which are used in the rest of this thesis. I describe modifications which were done on the RAMSES code in order to adapt it to the purposes of this study, and discuss the adaptive mesh refinement strategy I chose to employ. I then show a number of tests which were carried out in order to determine the dependence of the locations of the shocks and velocity field of the gas on the resolution of the simulation. Furthermore, I explore the morphology of the central regions of the simulations also as a function of grid resolution.

- In Chapter 4, I explore the dynamical structure of the nearby galaxy NGC 1291, using gas dynamical response simulations. I modify three parameters in the models, namely the M/L, the bar pattern speed and the height function. The parameter space of the models is explored in order to find the best fit models, i.e. those in which the density enhancements seen in the simulations match the observed dust lanes. This allows for constraints to be placed on the M/L, the bar pattern speed, as well as the thickness and height function of the galaxy.

- In Chapter 5, I present a study on the effects of substructures in barred galaxies, namely the B/P bulge and inner bar, on gas inflow to the central regions. I employ hydrodynamic simulations, as those presented in Chapter 3 and compare models with and without B/P bulges, and with and without the inner bar. I show that, as expected from the results of Chapter 2, the B/P bulge reduces the gas inflow to the central regions of galaxies.

- In Chapter 6 I give some concluding remarks and future prospects of the work presented in this thesis.

2

The Effects of Boxy/Peanut Bulges on Galaxy Models

The results presented in this chapter have been published in:
F. Fragkoudi, E. Athanassoula, A. Bosma, F. Iannuzzi (2015) MNRAS, ***450****, 229-245.*

Dynamical models have been used extensively in the literature to study the properties of barred galaxies, from their orbital structure and gaseous kinematics, to their mass-to-light ratio and dark matter content. Though a large number of barred galaxies contain Boxy/Peanut bulges, the effect of these bulges on dynamical models has not been studied in the past. I make extensive use of dynamical models in the next chapters of this thesis, in order to study the M/L of NGC 1291, its dark matter content, pattern speed and gaseous inflow. Therefore, in order to ensure the dynamical models are as accurate as possible, I carried out a study on the effects of Boxy/Peanut bulges on dynamical models, i.e. their effect on the orbital structure, forces and bar strength of the model. I found that Boxy/Peanut bulges have a significant effect on the various properties of the model, and should therefore be included in the models in order for them to be as accurate as possible.

2.1 Introduction

Many edge-on disc galaxies can be seen to contain boxy-, peanut- or X-shaped isophotes, which are usually grouped together into the category of B/P bulges. As a result of a number of theoretical studies (see Athanassoula 2008a, 2015 for general reviews of this subject), including orbital structure and stability analysis (Binney, 1981, Pfenniger, 1984, 1985, Patsis et al., 2002, Skokos et al., 2002a,b, Martinez-Valpuesta et al., 2006, Harsoula and Kalapotharakos, 2009, Contopoulos and Harsoula, 2013), and numerical simulations (Combes and Sanders, 1981, Combes et al., 1990, Raha et al., 1991, Mihos et al., 1995, Athanassoula and Misiriotis, 2002,

Athanassoula, 2003, 2005, Bureau and Athanassoula, 2005, Martinez-Valpuesta et al., 2006), these structures are now known to be due to vertical instabilities in the bar, which cause it to 'puff up', giving rise to boxy or peanut-like shapes. These studies also show that once a bar forms, a B/P bulge will form soon after.

Observational studies have further confirmed the link between B/P bulges and bars (see Kormendy and Kennicutt 2004 and Kormendy 2015 for reviews on the subject), by showing that the fraction of edge-on disc galaxies with B/P bulges is comparable to the fraction of disc galaxies containing bars (Lütticke, Dettmar, and Pohlen, 2000). Kinematic studies of edge-on barred galaxies and B/P bulges also confirm the connection between the two structures (Athanassoula and Bureau, 1999, Bureau and Athanassoula, 1999, Chung and Bureau, 2004, Bureau and Athanassoula, 2005, and references therein). Therefore, barred galaxies at present and past epochs will contain B/P bulges, and in fact, one is also believed to be present in our own Galaxy (Weiland et al. 1994, Howard et al. 2009, Shen et al. 2010, McWilliam and Zoccali 2010, Ness et al. 2012, 2013a,b; Vásquez et al. 2013, Wegg and Gerhard 2013, Gardner et al. 2014, Nataf et al. 2013, 2014, 2015).

Bars are found in about two thirds of disc galaxies in the local universe, with variable strengths (Eskridge et al., 2000, Menéndez-Delmestre et al., 2007, Barazza et al., 2008, Aguerri et al., 2009, Gadotti, 2009), and are known to be the main drivers of the secular phase of galaxy evolution. The torque they induce into the disc causes outward angular momentum transfer, which in turn will cause a redistribution of matter in the disc. They are thus responsible for driving gas to the centre of their host galaxy (Athanassoula, 1992b), forming discy pseudo-bulges (Kormendy and Kennicutt, 2004, Athanassoula, 2005), redistributing stars in the galactic disc (Sellwood and Binney, 2002, Roškar et al., 2008, Minchev and Famaey, 2010), and possibly creating a fuel reservoir for AGN activity (Shlosman et al. 1990, Coelho and Gadotti 2011, Emsellem et al. 2014, but see also Lee et al. 2012. For a review see Combes 2001). However, even though the effect of bars on all these processes has been thoroughly examined, a study of the effects of B/P bulges on all these processes has not, until present, been carried out.

As a first step towards understanding the effect B/P bulge geometry may have on the aforementioned processes, for the first part of my thesis I focused on their influence on dynamical models of their host galaxies. These models are obtained directly from images of the galaxies' surface brightness, by first assuming a vertical density distribution, or height function, and subsequently deriving the potential of the galaxy. They have been used extensively in the literature, with one of their most important implementations being in simulations that study the response of gas in a fixed potential. These response simulations are used to study the dark matter content of galaxies and to test the maximum disc hypothesis (Kranz et al., 2001, Weiner et al., 2001, Slyz et al., 2003, Kranz et al., 2003, Pérez et al., 2004), the bar pattern speed (Lindblad, Lindblad, and Athanassoula, 1996, Kalapotharakos, Patsis, and Grosbøl, 2010b) as

well as the kinematical and morphological properties of gas in galaxies (Lin et al., 2011, 2013). Dynamical models have also been used in studies determining the bar strength (Buta and Block, 2001, Laurikainen and Salo, 2002) and the orbital structure of galaxies (Quillen et al., 1994, Patsis et al., 1997, Kalapotharakos et al., 2010a, Patsis et al., 2010). Furthermore, they have been used to study gravitational torques in barred and spiral galaxies in order to establish the amount of gas inflow and by extension determine the importance of secular evolution (Zaritsky and Lo, 1986, Haan et al., 2009, Foyle et al., 2010). In all of these aforementioned studies, the geometry of the B/P bulge is not taken into account when constructing the height function, and instead a position independent, 'flat' height function is assumed. This is partly due to the lack of an analytical model for a B/P bulge, as well as to the inherent difficulty of detecting these bulges in face-on or intermediate inclination galaxies, which are the galaxies generally used in these studies.

Various methods however have been proposed over the past few years, which allow either for the detection of B/P bulges, or at least for an educated guess at their existence. By viewing a large number of N-body+SPH simulations, and covering a wide range of viewing angles, Athanassoula et al. (2014) have shown that B/P bulges manifest themselves in face-on projections as the so called 'barlens' (Laurikainen et al., 2011), which renders their detection fairly easy. Strong observational arguments for this have been presented in Laurikainen et al. (2014). Another method proposed by Debattista et al. (2005), uses signatures in the stellar kinematics of face-on or almost face-on galaxies and was implemented by Méndez-Abreu et al. (2008) who confirmed the existence of a B/P bulge in NGC 98. Furthermore, it is possible to detect signatures of B/P bulges by examining the morphological features of inclined galaxies (Athanassoula and Beaton, 2006, Erwin and Debattista, 2013).

A study of the effects of B/P bulges on models of their host galaxies, and by extension of the necessity of including the geometry of B/P bulges in the height function of these models, was therefore called for. To this aim, I first introduce in Section 2.2 a straightforward and reliable method for calculating the potential, forces and derivatives of forces of a general density distribution ρ(r,ϕ,z). This method was chosen among a variety of other methods, due to its robustness and high precision. I present tests which demonstrate that the method can give highly accurate results, while also allowing the flexibility to choose an arbitrary height function, without being restricted to one which is constant with position.

I then use this code on an artificial "observational" image of an N-body+SPH simulated galaxy, which is presented in Section 4.3.1, thus obtaining a realistic potential for a barred galaxy, directly from the mock light distribution. In order to create this model, I assign a thickness and a height function to the galaxy. These height functions are introduced in Section 2.3 and include two 'flat' height functions, a function which describes peanut bulges (from which I construct our fiducial B/P model), and another which describes boxy bulges.

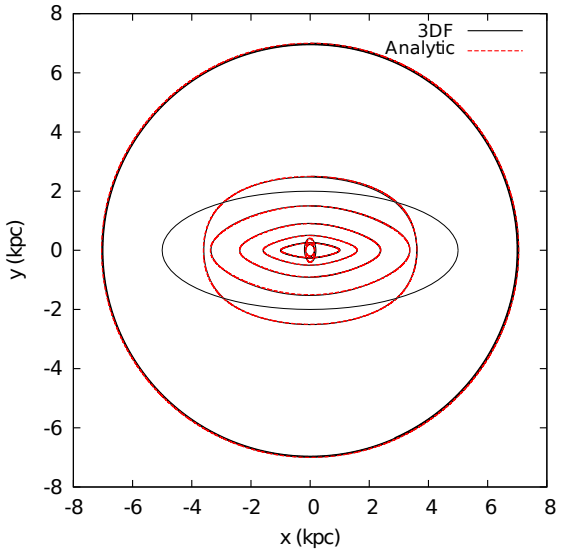

FIGURE 2.1: Comparison of orbits in the analytic and 3DF potentials of our model galaxy. The thin black line gives the outline of the bar. The orbits calculated in the 3DF potential are given in solid thick black lines, and the orbits calculated in the analytic potential are given in dashed red lines. I plot some x_1 orbits (along the bar), some x_2 orbits (perpendicular to the bar), and an almost circular orbit outside the bar region. We see that the orbits in the two potentials almost completely overlap, so that the red and black lines are practically indistinguishable.

The main results of this study are presented in Section 2.4, where I examine the effect B/P bulges have on the potential and forces (2.4.1), on the periodic orbits (2.4.2) and on the bar strength (2.4.3). I find that B/P bulges indeed have a significant effect on the results and therefore conclude that they should be included when modelling their host galaxy.

In Section 2.5 I explore the errors which will be induced in the results by using a B/P model which is not exactly the 'correct' one. This is necessary since it is not trivial to observationally obtain the exact parameters of B/P bulges, and this can introduce errors in the model. I show that for a range of uncertainties, the errors induced in the results are less than those induced by not modelling the B/P at all. I also introduce a new method for calculating the bar strength, Q_T^{int}, which takes into account the variation of the non-axisymmetric forcings along the whole extent of the bar.

In Section 2.6 I give a summary and list the main conclusions of this study.

2.2 Constructing dynamical models

To create a dynamical model of a galaxy we first need its density distribution. The two-dimensional surface density can be obtained from surface brightness images of a face-on disc galaxy by assuming a M/L ratio. It is important that these images are taken in a wavelength range which minimises the effect of dust extinction and traces the old stellar population (for

example, the Spitzer 3.6 μm band). In this work I use an image of a face-on simulated galaxy, and thus do not need to account for dust extinction, nor assign a M/L ratio, as our two-dimensional image gives the surface density directly. Once the surface density is obtained, we also need to assign a height function, and together these give us the three-dimensional density distribution, from which we can calculate the potential of the galaxy due to the stellar component. This method for calculating the potential involves a straightforward three-dimensional integration over the density distribution and is referred to as the 3DF method. The potential is calculated in Cartesian coordinates by

$$\Phi(x,y,z) = \\ -G\int_{-\infty}^{\infty}\int_{-\infty}^{\infty}\int_{-\infty}^{\infty}\frac{\rho(x',y',z')}{\sqrt{\sum_{j=1}^{3}(x'_j-x_j)^2+\epsilon^2}}\mathrm{d}x'\mathrm{d}y'\mathrm{d}z', \tag{2.1}$$

where G is Newton's gravitational constant, ρ is the density and ϵ is the softening length which is necessary to eliminate the noise at the expense of a small bias (Merritt, 1996, Athanassoula et al., 2000). We can differentiate the expression in Eq. 4.8 analytically with respect to x, y and z, to obtain expressions for the the force and its derivatives. This method thus relies heavily on an adequate integration algorithm, specifically one which can deal with singularities. To tackle this I use CQUAD, a doubly adaptive integration algorithm (Galassi et al., 2003), which requires more function evaluations than other integration routines, but is more successful in dealing with difficult integrands. It computes the integral within the desired relative error limits (or precision), which the user can set. Since our work involves mainly the z=0 plane, I focus in what follows on the non-zero quantities in the plane: the potential Φ and the two non-zero components of the force F_x and F_y. As mentioned, the above, as well as what follows, concerns the potential and forces of the stellar component of the galaxy.

2.2.1 Tests on the method

In order to test the accuracy of our method, I create a model of a barred galaxy containing a disc, a bar and a classical bulge, using density distributions which have analytic solutions for the potential and forces. I then calculate the potential and forces for this model using the 3DF method, and compare the results against the analytic solutions. The general results of these tests are very positive, which demonstrates the ability of our code to deal with difficulties such as cuspy and/or non-axisymmetic density configurations. Additionally, I compare the orbits obtained in our potential with the orbits obtained in the analytic potential, to further confirm that the method for calculating the potential has high precision and accuracy, and that orbits run smoothly in our potential.

Analytic Model

To model the disc I use a Miyamoto-Nagai density (Miyamoto and Nagai, 1975) which is defined by the potential-density pair,

$$\Phi_{MN}(R,z) = -\frac{GM_D}{\sqrt{R^2+(a+\sqrt{z^2+b^2})^2}}, \tag{2.2}$$

$$\rho_{MN}(R,z) = \left(\frac{b^2M_D}{4\pi}\right)\frac{aR^2+(a+3\sqrt{z^2+b^2})(a+\sqrt{z^2+b^2})^2}{[R^2+(a+\sqrt{z^2+b^2})^2]^{5/2}(z^2+b^2)^{3/2}}, \tag{2.3}$$

where R and z are the cylindrical coordinates, G is Newton's gravitational constant, M the total mass of the system and a and b are its characteristic lengths. I set the parameters a and b to 9 and 1.8 respectively, in order to obtain a realistic exponential disc with a scalelength of about 3 kpc with its mass set to 0.56 times the total mass of the system (Gadotti, 2011).

The bulge is modelled using a Dehnen sphere (Dehnen, 1993), where γ=0.5 in order to obtain a cuspy density distribution. The potential density pair is given by,

$$\rho(r) = \frac{5}{8\pi}\frac{r_B M_B}{\sqrt{r}(r_B+r)^{7/2}}, \tag{2.4}$$

and

$$\Phi(r) = \frac{-2GM_B}{3r_B}(1-(\frac{r}{r+r_B})^{3/2}), \tag{2.5}$$

where r_B is a characteristic radius of the system. The mass of the bulge is set to 0.34 the total mass of the model which is a typical value for the bulge mass (Gadotti, 2011).

The bar is modelled using a Ferrers ellipsoid (Ferrers 1877), whose density is given by,

$$\rho = \begin{cases} \rho_0(1-m^2)^n & m \le 1 \\ 0 & m \ge 1 \end{cases}, \tag{2.6}$$

where m^2 is

$$m^2 = \frac{x^2}{\alpha^2}+\frac{y^2}{\beta^2}+\frac{z^2}{\gamma^2}. \tag{2.7}$$

The central density of the bar is given by ρ_0, while n sets the decrease in bar density as a function of position and α, β and γ give the sizes of the three semi-principal axes. The mass

of the bar is 0.1 times the total mass, which is again a typical value for real galaxies (Gadotti, 2011). The bar's semi-major axis is set to a=5 kpc, with an axial ratio of a/b=2.5, and I use the inhomogeneous n=1 case.

When integrating orbits in these potentials, I do so in the rotating frame of reference of the bar, where the bar potential rotates with a pattern speed which is set such that corotation occurs just outside the end of the bar within the range $1.4 > R_{CR}/R_{bar} > 1$, where R_{CR} and R_{bar} are the corotation and bar radius respectively (e.g. Athanassoula 1992b). The equations of motion in a rotating frame of reference are taken from Chapter 3 of Binney and Tremaine (2008), where the fictitious forces due to rotation are taken into account.

Relative errors

To calculate the relative errors of the potential and the derivatives of the force, I use the relation

$$\text{Error} = 0.5\frac{|R_1 - R_2|}{|R_1| + |R_2|}, \tag{2.8}$$

where R_1 and R_2 are respectively the analytic and 3DF solutions.

The relative errors for the force are given by

$$\text{Error} = \frac{|F_{i1} - F_{i2}|}{\sqrt{F_{i1}^2 + F_{j1}^2}}, \tag{2.9}$$

where i and j can be either the x or the y component of the force, and the subscripts 1 and 2 stand for the analytic and 3DF solutions respectively. The error of each component of the force is therefore normalised by the *total* force at each point. This is done because our main interest in the forces is for the calculation of orbits and because on the symmetry axes of the x- and y- components of the force (in the static frame of reference), the analytic estimates of F_x and F_y will be equal to zero.

I stress that the precision with which the code calculates the results is an input parameter to the code. The accuracy can be as high as the user wants it to be, at the expense, of course, of computation time. A three dimensional integration is required and, due to the propagation of error at each integration, the relative precision we ask of the CQUAD algorithm for each integration has to be larger than that which we wish to achieve. Practically this means that if we ask for a relative precision of 10^{-3}, we will obtain a relative precision of approximately 10^{-1}. This is sufficient for our purposes as the error is less than 1% for all variables. The softening is set to 10 pc for this study. For this precision and softening, the maximum error of the potential is 0.3%, of F_x 0.6% and of F_y 0.7%.

Orbits Even though from the results of the relative errors we see that the 3DF method gives highly accurate results, I would like to confirm that the noise in the force field does not prevent

(a) IC 4290 (b) gtr116

FIGURE 2.2: Visual comparisson between IC 4290 and gtr116. The two galaxies have striking morphological similarities and are classified as having the same bar strength (for more details see Section 2.4.3).

orbits from running smoothly, as they would in an analytic potential. To do this, I calculate a number of periodic orbits in the analytic potential and in the potential derived using the 3DF method for the galaxy in the frame co-rotating with the bar, in the model described above. The grid used for the orbits and in what follows is 200×200, and the orbits are calculated using a Kick-Drift-Kick leapfrog algorithm (Hockney and Eastwood, 1988, Quinn et al., 1997, Springel, 2005).

In Fig. 2.1, we plot a few of these orbits. In this figure and all throughout this study the bar major axis is along the x-axis. In the figure I show some x_1 orbits, which are elongated along the bar, some x_2 orbits which are perpendicular to the bar, as well as some nearly circular orbits outside the bar region. We see that the orbits calculated in the 3DF potential are a very good approximation of those calculated in the analytic potential, as the two practically coincide. Thus the error which is introduced in the potential from our 3DF method and the adopted value of precision is sufficient for our purposes.

2.2.2 The image

I use the 3DF method on the density distribution derived from a face-on image of a simulated isolated galaxy and different height functions (which are described in Section 2.3). The initial conditions of the simulation from which the image was constructed, include a live spherical dark matter halo, an exponential stellar disc and 75% gas (for more information on the simulation the reader is referred to run gtr116 in Athanassoula, Machado, and Rodionov (2013)). The snapshot is taken well into the secular evolution phase of the galaxy, specifically at 8 Gyr after the start of the simulation, by which point a strong bar and B/P bulge have formed. The image is constructed from the 'stars' component of the snapshot and has a morphology reminiscent of that of many strongly barred galaxies, such as IC 4290 (see Fig. 2.2).

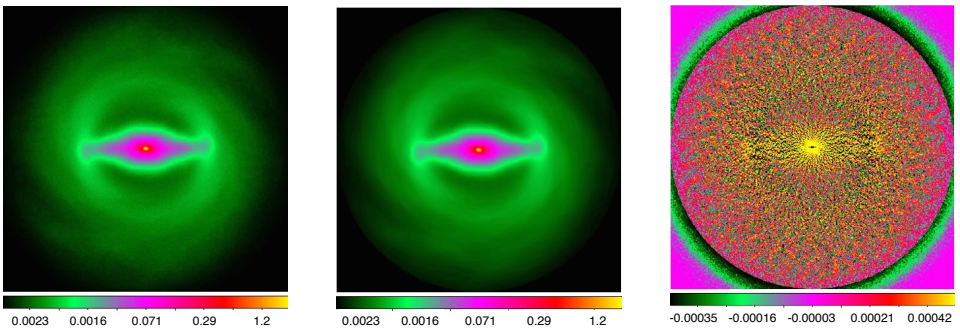

(a) Original Image (b) Model (c) Residual

FIGURE 2.3: *Left*: Original image showing the surface density of the stellar component of the gtr116 simulation. *Middle*: Model from the Fourier recomposition, using up to n_F=26 even Fourier components. *Right*: Residual image after subtracting the model from the original image.

In order to decrease the noise of the image a snapshot with a large number of particles is required, and so I use a snapshot with 40 times the particles of the original snapshot, which was created following the procedure described in Athanassoula (2005). To further reduce the noise in the image I apply some smoothing, by Fourier decomposing and recomposing it.

The Fourier components are calculated as follows:

$$a_n(r) = \frac{1}{\pi}\int_{-\pi}^{\pi} \Sigma(r,\theta)\cos(n\theta)\,\mathrm{d}\theta, \tag{2.10}$$

$$b_n(r) = \frac{1}{\pi}\int_{-\pi}^{\pi} \Sigma(r,\theta)\sin(n\theta)\,\mathrm{d}\theta, \tag{2.11}$$

where a_n and b_n are the even and odd Fourier components, θ is the azimuthal angle, r the radius and Σ gives the surface density. The high frequency noise is then reduced by recomposing the image as

$$\Sigma(r,\theta) = \frac{a_0}{2} + \sum_{m=2}^{m=n_F} \left(a_m(r)\cos(m\theta) + b_m(r)\sin(m\theta)\right), \tag{2.12}$$

using only a limited number of even Fourier components (in our case n_F=26). I show in Figs. 4.2(a) and 4.2(b) the surface density of the original image and of the Fourier recomposed image, respectively, both in arbitrary units, and in Fig. 4.2(d) the residual image of the two. As the images of surface density are in arbitrary units, the density, as well as the potential and its derivatives will also be in arbitrary units in what follows.

2.3 The height functions used

In order to obtain the three-dimensional density of a galaxy disc from a two-dimensional image we need to assume a height function, which defines how the density drops off as a function of z from the equatorial plane z=0. The height function and the scaleheight (z_0) will of course affect the results, and we therefore need to use the height function which best approximates that of the galaxy we are trying to model.

The height function can be either constant or can change with position. In the case where it is constant with respect to position I assume, for simplicity, that the density distribution can be written as

$$\rho(x, y, z) = \Sigma(x, y)F(z), \tag{2.13}$$

where ρ is the three-dimensional density distribution, Σ is the two-dimensional surface density, and F is the height function. In the more general case where the height function depends on position in the galaxy, as would be for example the height function describing a B/P bulge, the scaleheight changes as a function of position. In this case, the density distribution would be given by,

$$\rho(x, y, z) = \Sigma(x, y)F(x, y, z), \tag{2.14}$$

where the normalisation of the height function is

$$\int_{-\infty}^{\infty} F(x, y, z)\mathrm{d}z = 1. \tag{2.15}$$

It is worth noting that the mass of the model is always the same; the height function simply determines the volume density of the galaxy, by setting the thickness of the disc.

2.3.1 Flat height functions

Up to now in the literature, position-independent or 'flat' height functions have been used when modelling barred disc galaxies. I therefore also use two flat height functions in this study, to check the discrepancy which will be created in the model by a) using a flat height function and a B/P height function, and b) using two different flat height functions. I adopt two commonly used functions, the isothermal-sheet model (van der Kruit and Searle, 1981):

$$F(z) = \frac{1}{2z_0}\mathrm{sech}^2\left(\frac{z}{z_0}\right), \tag{2.16}$$

and the sech-law model (van der Kruit, 1988):

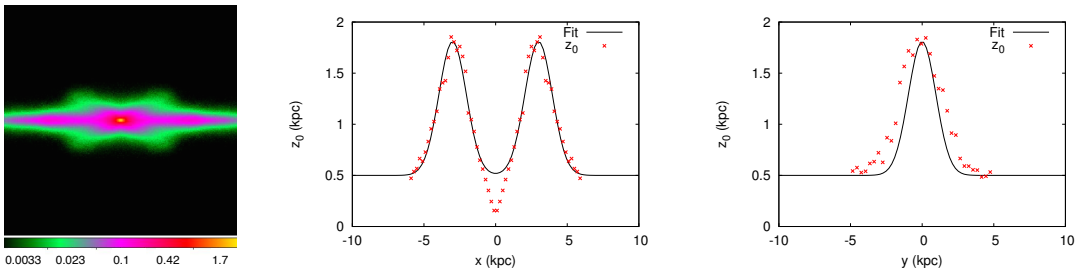

(a) gtr116: Side-on (b) Edge-on: Side-on (c) Edge-on: End-on

FIGURE 2.4: *Left*: side-on image of the surface stellar density of the simulated galaxy gtr116. *Middle*: The scaleheight of the simulation (red crosses) is plotted along the x-axis (for y=0, i.e. the side-on projection). The solid black line shows the fit of $z_0(x, 0)$ to the data, which gives the scaleheight of the fiducial peanut height function. *Right*: Plot of the scaleheight of the simulation (red crosses) along x=3 which is where the maximum of the peanut occurs (end-on projection). The solid black line shows the values of $z_0(x, y)$ along x=3.

$$F(z) = \frac{1}{\pi z_0} \text{sech}\left(\frac{z}{z_0}\right), \tag{2.17}$$

where $1/(2z_0)$ and $1/(\pi z_0)$ are the respective normalisation factors.

2.3.2 Peanut height function

To obtain a height function for the peanut, the particle distribution along different cuts in x and y is examined from the simulation introduced in the previous section. I found that the sum of two two-dimensional gaussians for the scaleheight can provide a reasonable approximation to the B/P shape. As can be seen in Fig. 2.4 and as commented below, this choice may fail at certain points, but provides an overall fair representation of the structure.

The resulting B/P height function is a non-separable function of position and is given by:

$$F(x, y, z) = \frac{1}{2z_0(x, y)} \text{sech}^2\left(\frac{z}{z_0(x, y)}\right). \tag{2.18}$$

The scaleheight z_0(x,y) varies like the sum of two two-dimensional gaussians:

$$\begin{aligned} z_0(x, y) =& A \exp\left(-\left(\frac{(x - x_0)^2}{2\sigma^2} + \frac{(y - y_0)^2}{2\sigma^2}\right)\right) + \\ & A \exp\left(-\left(\frac{(x - x_1)^2}{2\sigma^2} + \frac{(y - y_1)^2}{2\sigma^2}\right)\right) + z_0^{disc}, \end{aligned} \tag{2.19}$$

where A is the maximum scaleheight of the peanut above the disc scaleheight, z_0^{disc}. The variance of the gaussians is given by σ^2, (x_0, y_0) is the position of the maximum of the first

gaussian and (x_1, y_1) the position of the maximum of the second gaussian. I fit these two two-dimensional gaussians to values of the scaleheight obtained from the simulation along $y = 0$ and $x = 3$ (which is where the maximum of the scaleheight occurs). In the remainder of this chapter, I refer to this as our fiducial peanut (or B/P) model.

To obtain the scaleheights, cuts are taken along the x- and y- axes and the vertical particle distribution is fitted with a sech^2 function. The variation of z_0 is therefore determined from bin to bin along the cut. The results can be seen in Fig. 2.4. In the side-on view (panel (b)) we see that the scaleheight along $y = 0$ behaves approximately like the combination of two gaussians, except in the central region where the scaleheight drops below that of the outer disc. For a cut along $x = 3$, where the peanut is maximum (end-on view, panel (c)), the behaviour of z_0 is still well approximated by a gaussian, although our fit slightly under predicts the value of the scaleheight.

Along some cuts at x values intermediate between the centre and the peanut maximum, the gaussian approximation fails to represent the behaviour of the scaleheight with y. In fact the behaviour of the scaleheight in the presence of a B/P bulge is quite complex, and cannot be grasped entirely by a simple analytic function. However, as it turns out, the fitted function shown in Fig. 2.4 underestimates the value of z_0 at these points. This directly translates into an underestimation of the effect of the peanut in those regions. In summary, our fiducial model for the peanut height function shown in Fig. 2.4 will result into a conservative estimate of the effect of the real peanut present in the image I adopt as the starting point. Given the scope of this study, which is to demonstrate the generic effect of a peanut bulge on a galaxy model, this approximation is more than satisfactory.

2.3.3 Boxy height function

The B/P bulge might at times have rather boxy isophotes. This could be due to projection effects, whereby the peanut is projected at such an angle that the isophotes appear boxy (Athanassoula and Misiriotis, 2002). However, boxy isophotes might be present even when the bar is seen side-on, i.e. they might be the real shape of the B/P bulge (see Patsis et al. (2002) for a discussion based on orbits). This tends to be the case for galaxies with weak bars, where instead of a strong x-shape or peanut forming, boxy isophotes are seen (Athanassoula, 2006).

To model a boxy bulge I use a height function which drops off as sech^2 with height from the z=0 plane,

$$F(x, y, z) = \frac{1}{2z_0(x, y)} \mathrm{sech}^2 \left(\frac{z}{z_0(x, y)} \right), \tag{2.20}$$

where the scaleheight is a top-hat function,

$$z_0(x,y) = \begin{cases} z_0^{bulge} & |x| \leq x_{max} \,\&\, |y| \leq y_{max} \\ z_0^{disc} & \text{otherwise.} \end{cases}, \tag{2.21}$$

and where z_0^{disc} gives the scaleheight of the disc and z_0^{bulge} gives the scaleheight, or strength, of the boxy bulge. This is quite a simplified model of the boxy bulge, with only two free parameters, its strength and length (which is set by L=$2x_{max}$). The thickness of the box, i.e. y_{max}, is set by the width of the bar.

I create the fiducial boxy height function such that it best approximates the fiducial peanut height function, in order to examine whether the former can be used as an approximation for the latter, as there is one less parameter to model. The fiducial boxy height function therefore has a height equal to the height of the fiducial peanut model and its length is such that the boxy bulge finishes approximately where the peanut scaleheight is in between its maximum and minimum (see top right panel of Fig. 2.5).

2.4 Should we include B/P bulges in our models?

To investigate whether one should account for the geometry of the B/P bulge in dynamical models, in the next three subsections I examine the effects of the B/P bulge on the forces (2.4.1), orbital structure (2.4.2) and bar strength (2.4.3) of the model.

2.4.1 The effects of B/P bulges on forces

I calculate the potential and the forces for the density distribution given by the image described in Section 4.3.1, and the different height functions described in Section 2.3. The results of this subsection are shown in Fig. 2.5. In the top row I plot the scaleheight along the bar major axis for the two setups being compared in the plots. Two-dimensional plots of the relative difference are shown, for the potential in the second row, of the x component of the force in the third row, and of the y component of the force in the fourth row. The green line represents an ellipse fitted to the outer isophote of the bar. Each column gives one of the following comparisons (from left to right):

1. *Two flat height functions: sech and sech^2*

   I compare the models obtained by implementing two flat height functions, sech and sech^2, with equivalent scaleheights, in order to demonstrate that different flat height functions

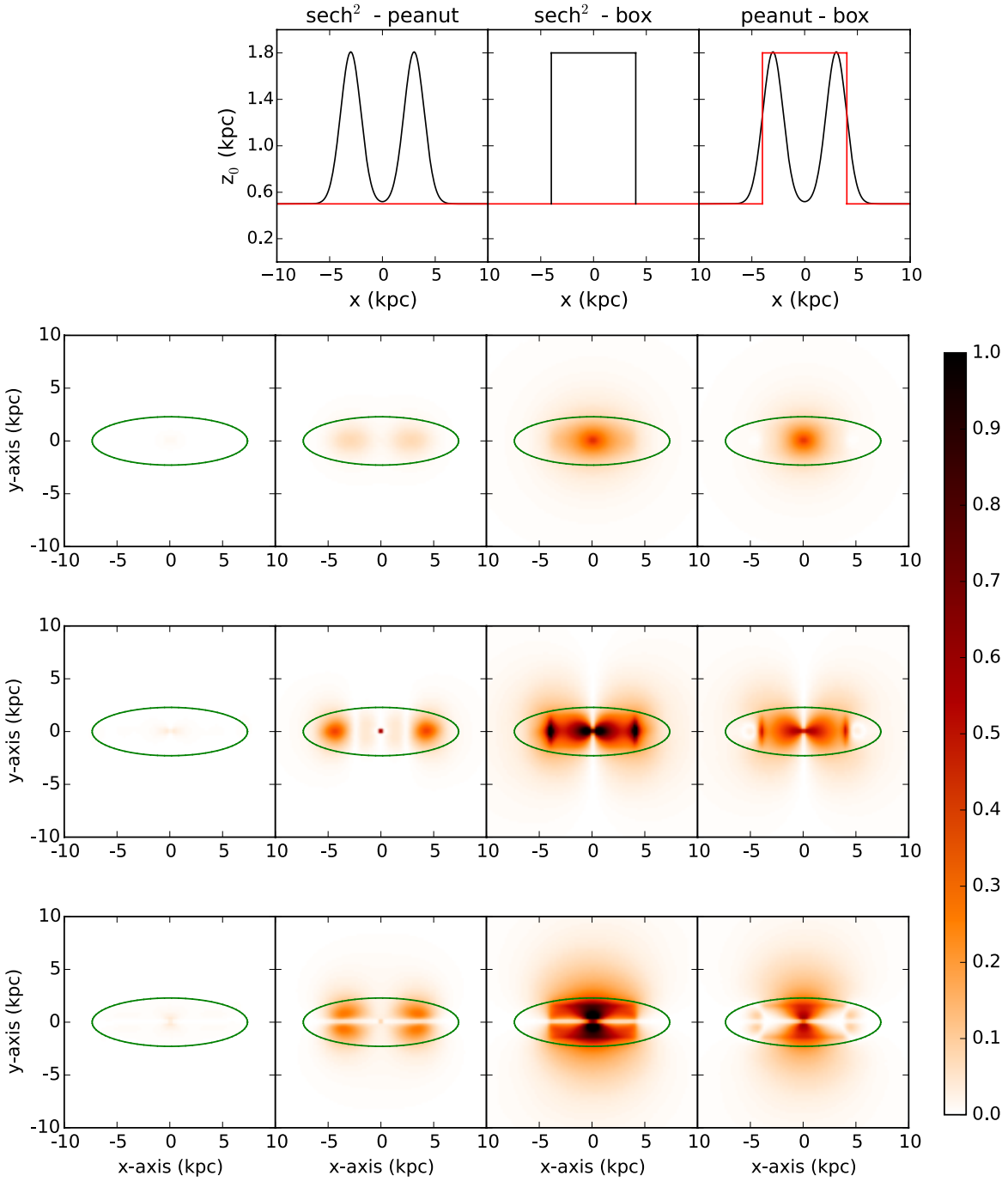

FIGURE 2.5: **Errors from not taking into account the proper B/P geometry:** The top row gives the scaleheight (in red and black lines) along the bar major axis for the setups we are comparing in the plots. The second, third and fourth rows give the relative difference between the two setups being compared for the potential, F_x and F_y, respectively (see the colourbar for values of the relative difference). The dark green line represents the ellipse fitted to the outer isophote of the bar. *First Column*: Difference between the sech and sech^2 setup. *Second Column*: Difference between the fiducial peanut height function and a sech^2 height function. *Third Column*: Difference between a boxy height function and a sech^2 height function. *Fourth Column*: Difference between a boxy height function and our fiducial peanut height function. We see that not including a peanut or a boxy bulge where there is one will induce large errors in the potential and forces and also that a boxy height function is not a good approximation for a peanut height function. For details see the text (Section 2.4.1).

do not significantly affect the results. In the very centre, the difference for the potential is only around 1% and for the forces it is 5%, while for the rest of the grid the difference between the two setups is well below 1% in all cases. If we decrease the value of the scaleheight the two height functions produce even more similar results. This happens because as the disc tends to become infinitesimally thin, the shape of the height function becomes less important. Equivalently, if we increase the value of the scaleheight, and hence the thickness of the disc, then the difference in the results obtained with the two height functions increases.

We see therefore that the scaleheight, and not the vertical profile of the height function, is primarily responsible for creating differences in the models.

2. *Flat and peanut height functions*

I compare a flat height function and the height function of our fiducial peanut bulge, i.e. a peanut with parameters fitted to our simulated galaxy. The differences that arise from using these two setups are significant for the potential and forces, as can be seen in the second column of Fig. 2.5. This is especially true near and around the region of the maximum height of the peanut, and in general in and around the bar. The force can be different in the two cases by up to 40%, which is not surprising since around the maximum of the peanut the scaleheight is more than three times the value of the scaleheight of the disc. This can be seen in the top row of the figure, which demonstrates how the scaleheight varies along x for the two height functions. The larger scaleheight reduces the forces in the plane of the disc, due to a reduction of the density in the plane.

Therefore, we see that by not taking into account the geometry of the B/P bulge, we induce significant errors in the model, i.e. in the potential and its derivatives.

3. *Flat and boxy height functions*

In the third column of Fig. 2.5 I compare a flat height function and the height function of the fiducial boxy bulge. We see that a boxy height function will also induce large differences compared to the flat height function, and in fact in the central regions our fiducial boxy height function has an even larger effect than the peanut. Boxy bulges are usually associated to weaker bars in simulations and are therefore typically less strong than peanut bulges (although at early times boxy bulges can be as strong as peanut bulges - see Figs. 2 and 3 in Athanassoula and Misiriotis (2002)). In observations, boxy bulges can appear as strong as peanut bulges (see for example Chung and Bureau (2004)) although it is hard to distinguish whether these are truly boxy bulges, or simply peanut bulges seen at an angle. It is therefore reasonable to assume that a substantial

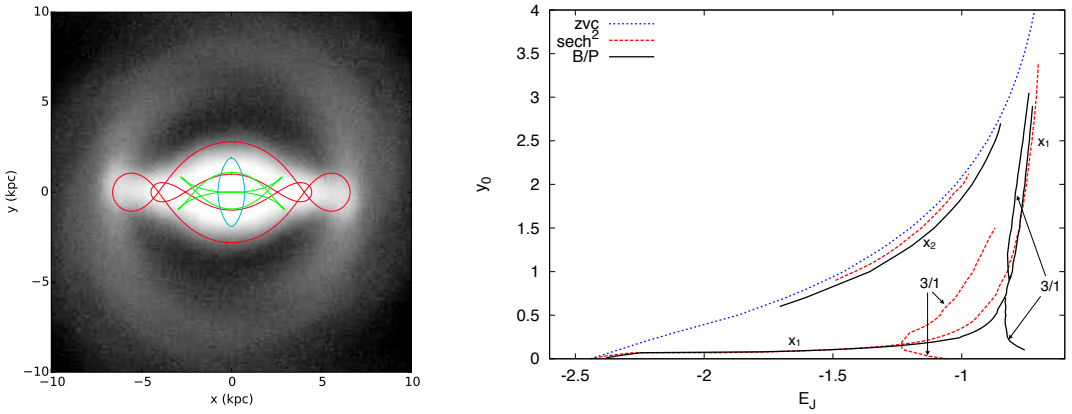

(a) Typical orbits in bar region

(b) Characteristic Diagram

FIGURE 2.6: *Left*: Some typical orbits in the bar region for the model with a sech^2 height function, over-plotted on the image of the simulated galaxy gtr116: In red the x_1 bar supporting orbits, in cyan an x_2 orbit perpendicular to the bar and in green the 3/1 orbits (asymmetric with respect to the y-axis). *Right*: Characteristic diagram (intersection of each orbit with the y-axis as a function of the Jacobi energy) for the models created from the image of the simulated galaxy gtr116 and the two height functions. The solid black line gives the characteristic diagram for the model with the fiducial peanut bulge and the dashed red line the characteristic diagram for a model with a flat sech^2 height function. The dotted blue line shows the zero velocity curve (ZVC) for the sech^2 model (the ZVC of the two models are very similar).

amount of boxy bulges will be somewhat less strong than our fiducial boxy height function. However, for the sake of simplicity and to be able to compare our fiducial boxy height function with our fiducial peanut height function, we give the former the same strength as the latter. Therefore our fiducial boxy height function can be thought of as an upper limit for the effect of a boxy bulge on the model of its galaxy.

4. *Peanut and boxy height functions*

I compare our fiducial peanut height function to our fiducial boxy height function in order to see to what extent the boxy height function approximates the peanut height function as it has one less free parameter than the peanut height function. These results can be seen in the fourth column of Fig. 2.5. For the potential and forces the match between the boxy height function and the peanut height function is quite poor, especially in the central region where the scaleheights of the two height functions are very different. Therefore the boxy height function is not a good approximation to a peanut bulge.

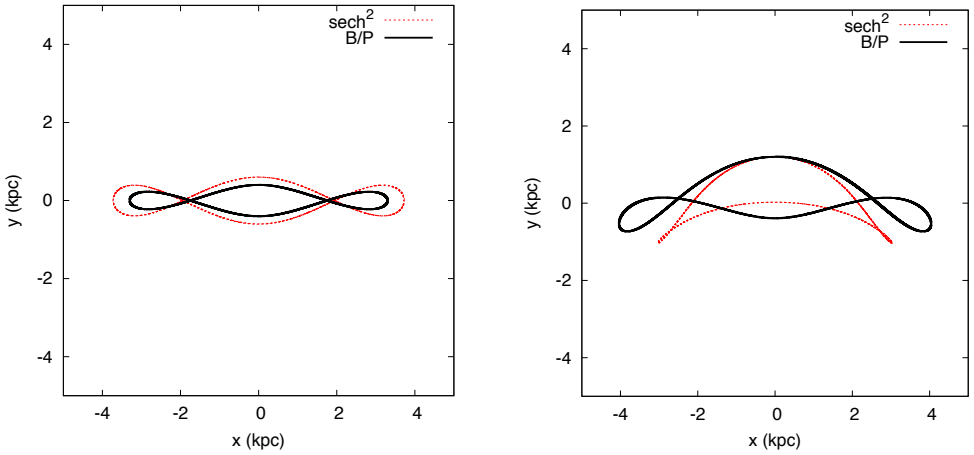

(a) Comparing x_1 orbits (b) Comparing 3/1 orbits

FIGURE 2.7: *Left*: Two x_1 orbits with the same Jacobian energy (E_J=-0.9) calculated in the two potentials: with (solid black line) and without (dashed red line) a B/P bulge. We see that in the B/P model the x_1 orbit's length and height are reduced (its extent along the x-axis is reduced by ∼12% and along the y-axis by ∼46% -measured respectively at y=0 and x=0). *Right*: Two 3/1 periodic orbits for y_0=1.2 in the two potentials (colours as before). Again the orbits differ significantly.

2.4.2 The effects of B/P bulges on orbital structure

In this section I examine how some of the most important families of periodic orbits will be influenced by taking into account the geometry of a B/P. To do this I study two models: the model with the fiducial peanut bulge height function, and the model with the sech^2 height function *without* a B/P bulge. The pattern speed of both models is set to be such that corotation occurs just outside the bar radius, within the range $1.4 > R_{CR}/R_{bar} > 1$, where R_{CR} and R_{bar} are the corotation and bar radius respectively (e.g. Athanassoula 1992b). The orbits are calculated in a frame of reference co-rotating with the pattern speed of the bar.

In Fig. 2.6(a) I show a few typical orbits in the bar region for the potentials being examined, overplotted on the image of the simulated galaxy, gtr116, shown face-on. The three most important families of orbits in the bar region are shown, i.e. the x_1 (red lines, extended along the bar major axis), x_2 (cyan lines, perpendicular to the bar major axis) and 3/1 (green lines, asymmetric with respect to the y-axis) families, which are stable along most of their extent.

In Fig. 2.6(b) I plot the characteristic diagram of periodic orbits, for the two cases with and without a peanut. The characteristic diagram gives the value at which the orbit intersects the y-axis (y_0) as a function of its Jacobian energy (E_J, i.e. energy in the rotating frame of reference; Binney and Tremaine (2008)). The Jacobian energy is in arbitrary units, since, as already mentioned, the mass is also in arbitrary units. We see that the characteristic diagram of the two models differs significantly. The most noticeable effect due to the presence of a B/P is the change in the bifurcation loci of the upper and lower branch of the 3/1 family. This

indicates that taking into account the geometry of a B/P in the model changes the location of the 3:1 resonance, and therefore the 3/1 family of periodic orbits appears at higher energies. Thus orbits of the 3/1 family will differ in the two cases, as can be seen in Fig. 2.7(b), where I plot two 3/1 orbits in the two models for the same cut along the y-axis. The extent of the 3/1 family of orbits is also significantly increased for the case with a B/P bulge, surpassing the extent of the x_1 family of periodic orbits, which is in fact shorter compared to the x_1 family in the model without a B/P bulge.

The x_1 family also suffers changes, in the E_J region between -1.1 and -0.8. In this area of the diagram, the maximum extent of the orbits along the x-axis reaches the region where the effect of the B/P is maximum; therefore, for these energies the orbits of the two models differ. In Fig. 2.7(a) I show an x_1 orbit of the same energy (E_J=-0.9) plotted in the two models. When a B/P is present, the maximum extent of the orbit along the x-axis is reduced by 12%, while its maximum extent along the y-axis is reduced by 46% (measured at x=0).

For the x_2 family, the highest (lowest) value of y_0 increases (decreases) for the model with a B/P bulge (see Fig. 2.6(b)), i.e. the entire extent of the x_2 family is increased by about 43% . As the extent of the x_2 family is related to the distance between the two Inner Lindblad Resonances (ILRs; Athanassoula 1992a), the distance between these two resonances will therefore also increase. This increase is due to a weakening of the non-axisymmetric perturbation: when the geometry of B/Ps is taken into account in the model, the scaleheight of the galaxy is increased, where the B/P is maximum, and therefore – since the amount of mass is the same– the volume density in the plane of the galaxy is decreased. This leads to a decrease in the radial and tangential forces in such a way that the non-axisymmetric perturbation is diminished, thus changing the distance between the two ILRs. This is in accordance with results from both Contopoulos and Grosbol (1989) and Athanassoula (1992a), the latter of which showed that there are a number of model parameters which can affect this distance. In particular, in Figures 6 & 7 of Athanassoula (1992a), we see that the distance between the ILRs can increase due to a decrease in the bar mass or the pattern speed, or due to an increase in the central mass concentration of the galaxy or the axial ratio of the bar.

The differences between the orbital families of the two models will have effects on their stellar, as well as their gaseous dynamics. The extent of the x_2 orbits plays a crucial role on the shape of the shock loci in the gas (Athanassoula, 1992a,b), and therefore the shape of the gas shocks in the two models should differ significantly; conversely, the shape and strength of the shocks influence the amount of gas inflow towards the centre of the galaxy, and it is therefore likely that there will be a measurable difference in the amount of gas inflow in models with and without a B/P bulge. This is further supported by the results in Section 2.4.3, where I show that B/P bulges reduce the strength of the bar; I plan to address in upcoming work the extent to which the gas flows will be affected.

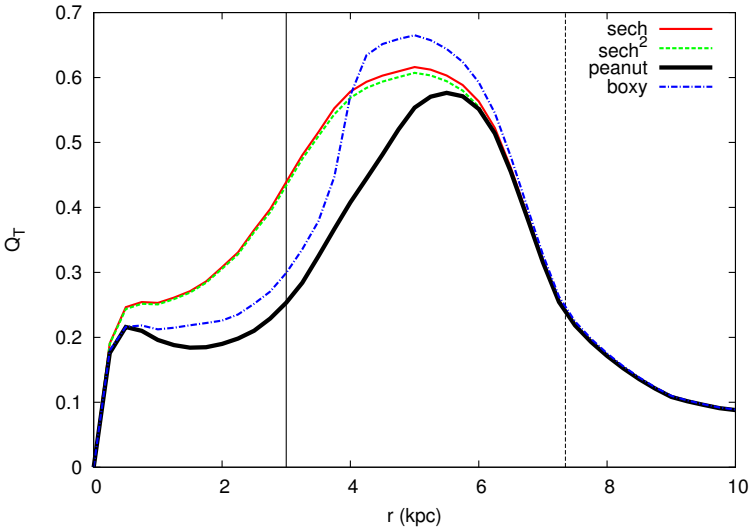

FIGURE 2.8: Strength of non-axisymmetric forcings (Q_T) as a function of radius, for models with different height functions: sech (solid red line), sech^2 (dashed green line), the fiducial peanut setup (thick black solid line) and the fiducial boxy setup (dash-dotted blue line). The vertical solid black line indicates the radius at which the scaleheight of the fiducial peanut is maximum and the vertical dashed black line indicates the end of the bar.

2.4.3 The effects of B/P bulges on bar strength

I study the effect of the B/P bulge on one of the measures of bar strength, which involves calculating the non-axisymmetric forcings on the disc due to the bar, i.e. the bar-induced torque (Combes and Sanders, 1981, Buta and Block, 2001). The magnitude of this non-axisymmetric perturbation is given by

$$Q_T(r) = \frac{F_{\rm T}^{max}(r)}{\langle F_{\rm R}(r) \rangle}, \tag{2.22}$$

where F_T is the tangential force $F_T(r)=(1/r)\ (\partial\Phi/\partial\phi)$, and $\langle F_R(r)\rangle$ is the average over azimuth of the radial force $F_R(r)=\partial\Phi/\partial r$. The forces are calculated directly from the image, as described in Section 2.2. In order to obtain a single measure of the bar strength for a galaxy, the quantity Q_b, which is the maximum of Q_T in the bar region, is commonly defined as the bar strength. In what follows I investigate the effect that a B/P height function will have on both Q_b and Q_T.

The results of this study are discussed in paragraphs (*i*), (*ii*) and (*iii*), where I examine models with the flat, the fiducial peanut and the fiducial boxy height function respectively. In Table 2.1 I show the maximum and average relative errors of Q_T, denoted MAX(Error Q_T) and $\langle$Error $Q_T\rangle$ respectively, as well as the relative error of Q_b, when comparing two models with different height functions. The average relative error of Q_T over radius is calculated according to:

TABLE 2.1: Errors in bar strength

Comparison	$\langle$Error $Q_T\rangle$	MAX(Error Q_T)	Q_b
sech - sech^2	1%	1.6%	1.5%
peanut - no peanut	27%	74%	4%
peanut - boxy	14%	42%	16%

The average and maximum of the relative errors of Q_T, as well as the relative error of Q_b, for three different comparisons of the setups.

$$\langle \text{Error } Q_T \rangle = \frac{1}{n} \times \sum_{i=1}^{n} (\text{abs}(\frac{Q_{T_1}(r_i) - Q_{T_2}(r_i)}{Q_{T_1}(r_i)}) \times 100). \tag{2.23}$$

Plots of these results can also be seen in Fig. 2.8, where it is worth noting that for the flat and peanut height functions, the strength of the bar is $Q_b \approx 0.55$-0.6. According to Buta and Block (2001), this represents a strong bar case (between bar class 5 and 6), which corresponds to approximately 20% of their sample of SB galaxies. I have already shown in Fig. 2.2 the striking morphological similarity between IC 4290 and our galaxy, and I note here that IC 4290 is also classified by Buta and Block (2001) as a class 6 barred galaxy, with Q_b=0.56. Therefore the results presented in this section, as well as in previous and subsequent sections, correspond straightforwardly and quantitatively to strongly barred galaxies. However, even weakly barred galaxies will have B/P bulges, albeit weaker ones, and therefore the results will also apply to these galaxies although to a lesser extent. I intend to carry out a full statistical study of the effects of different strength B/P bulges on the models of their host galaxy, together with a full comparison to observations, elsewhere.

1. *A model with a sech and sech^2 height function*

   In previous work by Laurikainen and Salo (2002) the effect of position-independent height functions and height functions which only vary as a function of radius was examined, and these were found not to change Q_b in a significant way. For realistic height functions such as the exponential, sech, or sech^2 models, they found that Q_b was affected by less than 5%, which is consistent with our own results. This is confirmed in Fig. 2.8 and Table 2.1, where we see that for an equivalent scaleheight, the height functions of sech and sech^2 will produce very similar bar strengths, which will tend to become even more similar the thinner the disc.

2. *A model with the fiducial peanut height function*

   I plot Q_T for our fiducial B/P height function. In the region around the scaleheight maxima (at r=3), Q_T is significantly flatter than the model without a peanut, due to

the reduction of the strength of the tangential and radial forces. The value of Q_b will not be significantly different from the case with the flat height function, due to the fact that the maxima of the peanut and the maximum of Q_T are at a relatively large distance from each other. The torque induced by the bar in the two cases however is significantly different, as can be seen both in the plot and in the second row of Table 2.1. By using the Q_b method of measuring bar strength, the bars will be judged as having the same strength (class 6), and hence the same effect on the disc, even though the forces in the plane of the galaxy are significantly reduced in the presence of a peanut. Therefore, in Section 2.5.3 I introduce another measure of bar strength, which can capture the reduction in bar strength when a B/P bulge is present.

3. *A model with the fiducial boxy height function*

   I also plot Q_T for our fiducial boxy height function. We see again that where the boxy bulge is maximum, Q_T is flattened due to the decrease in the strength of the bar forces in the plane. We also see that where the top-hat boxy function ends, Q_T exceeds the values of the sech and sech^2 curves. This is due to the effect of the boxy bulge on the tangential and radial forces, with the former increasing just outside the boxy bulge while the latter is decreased in the whole disc due to the overall decrease in mass-density in the plane of the galaxy. The combination of these two effects results in the torque becoming large in the region just outside the boxy bulge. As a consequence, Q_b is overestimated by 16% compared to the fiducial peanut case (third row of Table 2.1). I investigate the boxy height function as an alternative to using the peanut height function - since there is one parameter less to model - and conclude that even if one is merely interested in Q_T, a simple boxy height function is not a good approximation to a peanut function.

2.5 Errors due to Boxy/Peanut Modelling

In this section I investigate how much error will be induced if a B/P bulge is included in the model, but with the main peanut parameters differing from that of our fiducial model. This type of error is induced due to observational uncertainties, as it is not trivial to observationally obtain the correct parameters for the B/P bulge we want to model. This is due to the physics of the problem, not the numerical part of the calculation (which can be made arbitrarily small) and is therefore practically an unavoidable source of uncertainty. Nevertheless, as I will discuss below, there do exist empirical and theoretical arguments which can constrain the parameter space of a B/P bulge.

The height function I have chosen for our fiducial B/P bulge, the sum of two two-dimensional gaussians, has three degrees of freedom. Thus inaccuracies in the modelling of the B/P bulge

can also be introduced in three ways: by estimating wrongly the height of the gaussians (which corresponds to a change in peanut strength), or the distance between the maxima of the gaussians (which corresponds to a change in the peanut length), or the widths of the gaussians (which corresponds to a change in peanut 'width', i.e. how peaked or thin the peanut is at its maximum).

2.5.1 Potential and forces

In this subsection I investigate how much error is introduced in the potential and forces by incorrectly modelling the B/P bulge.

Peanut strength uncertainties

The maximum value of the scaleheight of the peanut, also called the peanut strength, is a value which is not trivial to find observationally. Numerical studies have shown that the strength of the peanut correlates with the bar strength (Athanassoula 2006). However this relation has a considerable scatter, and can merely give an approximate estimate. Debattista et al. (2005) showed that for face-on, or nearly face-on N-body simulated galaxies, an indicator of the presence and strength of a B/P bulge is the fourth order Gauss-Hermite moment of the line-of-sight velocity dispersion, h_4. However this relation has not been quantified in such a way which would allow a direct measurement of peanut strength from h_4. Studies of orbital structure (Patsis et al., 2002, Skokos et al., 2002a) have also suggested specific families of periodic orbits which are responsible for giving the B/P bulge its height, but no direct measurement of the strength of the B/P bulge is available from orbital structure either.

In order to measure the error due to peanut strength uncertainties, I use a grid of models with varying peanut strength and compare them to our fiducial peanut setup. These results can be seen in Table 2.2 below. In this and in all subsequent tables, the term 'Average Error', indicates the average error within the outer isophote of the bar and 'Maximum Error' corresponds to the maximum error found in the grid, excluding the central-most point. We see that an over- or under-estimation of the error by the same amount will produce similar errors in the model. In all the cases studied, the error induced by an incorrect peanut strength is always less than that induced by not modelling a B/P bulge at all.

Peanut width uncertainties

In Table 2.3 I show the errors for a grid of models with different peanut width errors. For all cases considered, the error induced due to a miscalculation of the peanut width is less than that induced by not modelling a peanut at all, apart from the maximum error induced in the potential when the peanut width is 50% larger than in the fiducial scenario. This is due to a sharp increase in scaleheight in the central region for large peanut widths (see solid red line in Fig. 2.10(c)), which is where the potential is most affected. This error however is confined only

TABLE 2.2: Percentage Error due to Peanut Strength Uncertainty

Peanut Strength	Average Error			Maximum Error		
	Φ	F_x	F_y	Φ	F_x	F_y
+50%	1.3%	2%	3%	3%	10%	6%
+25%	0.7%	1%	2%	1.5%	5%	3%
-25%	0.7%	1%	2%	1.5%	6%	4%
-50%	1.4%	3%	4%	3%	14%	10%
no peanut	3%	8%	10%	7%	37%	28%

Average and maximum errors of the potential and forces for setups with different peanut strength error, within the area enclosed by the outer isophote of the bar. The last row gives the error induced by not including a B/P bulge in the model at all.

TABLE 2.3: Percentage Error due to Peanut Width Uncertainty

Peanut Width	Average Error			Maximum Error		
	Φ	F_x	F_y	Φ	F_x	F_y
+50%	3%	5%	6%	15%	26%	27%
+25%	1%	2%	3%	4%	10%	12%
-25%	1%	2%	3%	3%	11%	6%
-50%	2%	5%	6%	5%	11%	15%
no peanut	3%	8%	10%	7%	37%	28%

Average and maximum errors of the potential and forces for setups with different peanut width errors within the area enclosed by the outer isophote of the bar. The last row gives the error that would be present if we do not model a B/P bulge at all.

to the potential and to the central most grid points, and should not have significant effects on orbital calculations in most of the galaxy.

Peanut length uncertainties

Of the three parameters - length, strength and width - length has the least uncertainty, due to a method proposed by Athanassoula et al. (2014). The method determines the length of B/Ps for face-on and moderately inclined galaxies, which uses the shape of the projected isophotes in the bar region. They demonstrated that the barlens and the peanut are the same component and therefore that the size of the former can be used to estimate the length of the latter. For galaxies with larger inclinations the length can be estimated from other morphological features in the isophotes created by the B/P bulge (Athanassoula and Beaton, 2006, Erwin and Debattista, 2013), while orbital structure studies confirm the aforementioned results and also give clues as to the length of the peanut (Patsis et al., 2002, 2003). Due to all this, the uncertainties of the length estimates are rather small, certainly smaller than the corresponding ones for strength and width, which is why I use a smaller range of uncertainties for the peanut length.

TABLE 2.4: Percentage Error due to Peanut Length Uncertainty

Peanut Length	Average Error			Maximum Error		
	Φ	F_x	F_y	Φ	F_x	F_y
+30%	1%	6%	5%	4%	24%	13%
+16%	0.9%	3%	3%	3%	12%	7%
-16%	1%	4%	4%	5%	11%	10%
-30%	3%	8%	9%	13%	25%	28%
no peanut	3%	8%	10%	7%	37%	28%

Average and maximum errors of the potential and forces for setups with different peanut length errors within the area enclosed by the outer isophote of the bar. The last row gives the error induced by not modelling a B/P bulge at all.

I carry out comparisons for a grid of models with different peanut length errors and give the results in Table 2.4. As expected, the more the length of the peanut is changed from the fiducial value, the larger the errors will be, although there is an asymmetry in the error induced with respect to over- and under-estimating the length; by underestimating the peanut length by a certain amount, we induce more error than by overestimating it by the same amount. By decreasing the length of the peanut we induce more error in the central regions of the galaxy, which is where the potential is most affected, due to the two gaussians overlapping in the centre and thus increasing the scaleheight (see dotted magenta line, Fig. 2.10(e)). This can be seen in Table 2.4, for the case of -30% peanut length where, for the potential, the maximum and average errors are larger than that of the +30% peanut length case.

For all the cases considered, the average error induced is smaller or equal to that of not modelling the B/P bulge. Given that the length is a fairly well constrained quantity, large errors are not expected to be present due to the peanut length in the modelling of the B/P bulge.

Combinations of uncertainties

It is likely that a combination of different kinds of error will contribute to the total error budget of a model of the B/P. It is not in the scope of this paper to explore the full parameter space of the possible error combinations, instead I choose a few cases in order to get a feel of the amount of error that can be induced. By 'combination of error' I refer to a combination of all the different sources of error. By '+50%' ('-50%') I refer to a setup with peanut strength and width which are 50% larger (smaller) than the fiducial value, and a peanut length which is 30% larger (smaller) than the fiducial. I do not find it necessary to further increase the error in peanut length, since it is the best constrained quantity out of the three parameters. The '+25%' ('-25%') setup corresponds to one with peanut strength, width and length which is 25% larger (smaller) than the fiducial value. In Table 2.5 we see that all the combinations of uncertainties will introduce less error in the model than not including a B/P bulge at all.

TABLE 2.5: Percentage Error due to Combination of Uncertainties

Combination	Average Error			Maximum Error		
	Φ	F_x	F_y	Φ	F_x	F_y
+50%	2%	3%	5%	6%	23%	22%
+25%	1%	4%	4%	6%	19%	18%
-25%	1%	6%	6%	5%	29%	22%
-50%	2%	7%	8%	6%	35%	26%
no peanut	3%	8%	10%	7%	37%	28%

Average and maximum errors of the the potential and forces for setups with different combinations of errors within the area enclosed by the outer isophote of the bar. The last row gives the error induced by not modelling a B/P bulge at all.

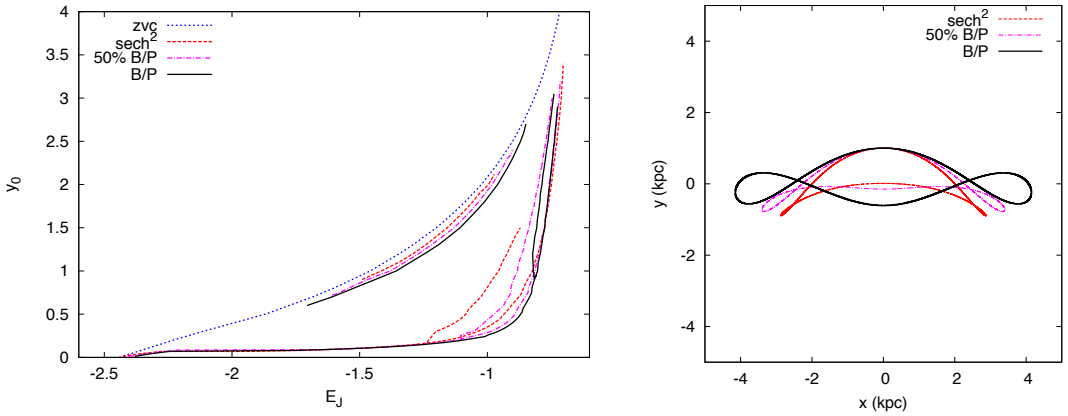

(a) (b)

FIGURE 2.9: *(a)* Characteristic diagram for models with different B/P setups. See Fig. 2.7 and the text in Section 2.4.2 for more details on the interpretation of the characteristic diagram. The dotted blue line gives the zero velocity curve; the characteristic diagram for the model with 0%, 50% and 100% the fiducial peanut strength is given by the dashed red line, the magenta dashed-dotted line and the solid black line respectively. *(b)* The same 3/1 orbit, which cuts the y-axis at y=1, in three models: without a B/P bulge (dashed red line), with 50% peanut strength (magenta dashed-dotted line) and with 100% peanut strength (black solid line).

2.5.2 Periodic orbits

As shown in Section 2.4.2, the presence of a B/P bulge will affect the extent and shape of the different families of periodic orbits which make up the bar. In this section I qualitatively explore the errors introduced in the calculation of periodic orbits due to incorrect modelling of a B/P bulge. To do this I examine the characteristic diagram of the most relevant families of periodic orbits for three models with different peanut strengths (100%, 50% and 0% of the fiducial strength), shown in Fig. 2.9(a).

For the model with 50% the fiducial strength the extent of the x_2 orbits is reduced by ∼19%, while if we do not add a B/P at all, the extent of the x_2 family is reduced by ∼43% (more

than double the error for the 50% peanut strength case).

The bifurcation locus of the 3/1 family for the model with 50% the peanut strength occurs about halfway between the locus of the models with and without a B/P bulge. Additionally, the extent of the 3/1 family in the characteristic diagram for this model is almost the same as for the model with the fiducial peanut, while the extent of the 3/1 family without a B/P is significantly shortened. In Fig. 2.9(b) we can see how the 3/1 orbits are affected by the incorrect modelling of the B/P bulge: for the same cut along the y-axis the 3/1 orbits are more elongated in the case with the fiducial peanut model, while they become less elongated and more concave with respect to the bar as the peanut strength is reduced. However, as expected, the orbits in the model with 50% the peanut bulge better match the orbit of the fiducial B/P setup than the model without the B/P bulge.

As already noted in Section 2.4.2, the x_1 family of orbits is also affected by the presence of the B/P bulge, when the maximum extent of the orbits reach the region where the effect of the B/P is maximum, i.e. around $(x,\ y)$=($\pm$3 kpc, 0 kpc). On the characteristic diagram this occurs in the region around $(E_J,\ y_0)$=(0.9, 0.5 kpc). However even by underestimating the strength of the B/P by 50%, the x_1 family is quite similar to the x_1 family of the fiducial B/P case.

We see that in general, the characteristic diagram of the model with 50% the fiducial strength has features which are more towards the fiducial peanut model and therefore even with such a large error in peanut strength, the characteristic diagram of this model reproduces relatively well the characteristic diagram of the fiducial B/P model and certainly better than the model without a B/P bulge. Similar results are found when considering errors in peanut width and length, and I therefore conclude that it is preferable to include a B/P in the model; the orbital structure of the model is significantly affected when a B/P bulge is present, and by adding a B/P, even with large errors in its parameters, the periodic orbits reproduce the correct structure more closely than when not including a B/P at all.

2.5.3 Bar strength

In this section I examine how both the relative errors of Q_T and those of its maximum value Q_b will be affected by uncertainties in the different parameters of the peanut model. I also introduce a new measure of bar strength, Q_T^{int}, which takes into consideration the integrated bar-induced torque, along the entire range of the bar. I do so because even though Q_b remains relatively unchanged when adding a B/P bulge to the model, Q_T over its whole range is significantly affected (see for example Fig. 2.10(f) and Table 2.1), and we wish to have a measure of this change with a single number. The bar strength as defined by Q_T^{int} is given by

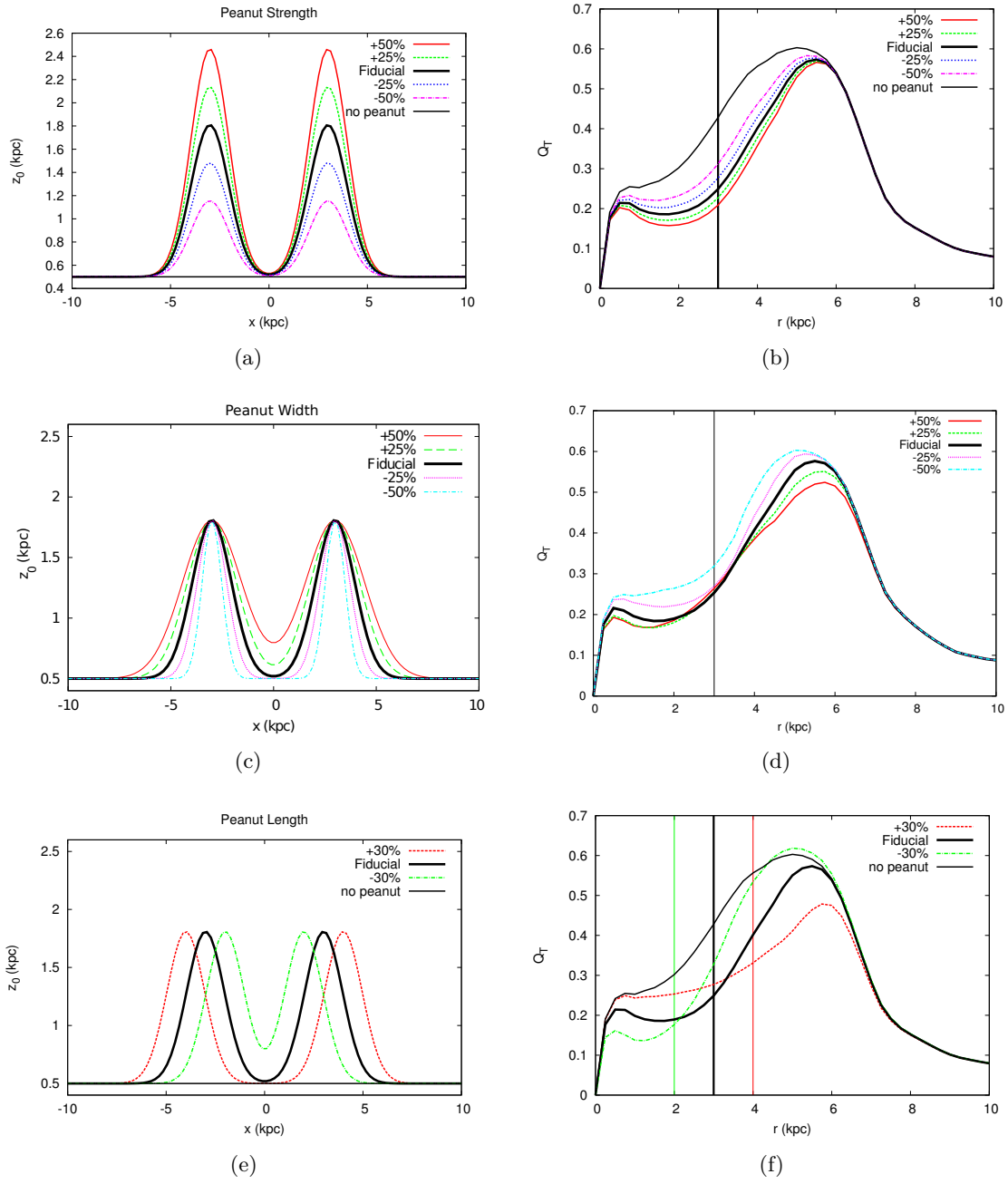

FIGURE 2.10: *Top Row: Left:* Values of z_0 for the fiducial peanut strength (solid thick black line), for 50% larger (solid thin red line), 25% larger (dashed green line), 25% less (dotted magenta line), 50% less (dot-dashed cyan line) and 0% peanut strength, i.e. an isothermal sheet (thin solid black line). *Right:* Bar-induced torque Q_T as a function of radius for models with the aforementioned height functions (respective colours). *Middle Row: Left:* The values of z_0 for the fiducial peanut width (solid thick black line), 50% larger (solid thin red line), 25% larger (dashed green line), 25% less (dotted magenta line) and 50% less peanut width (dot-dashed cyan line). *Right*: Bar-induced torque Q_T, for aforementioned models (respective colours). *Bottom Row: Left:* The values of z_0 for models with the fiducial peanut length (thick solid black line), 30% longer peanut (dashed red line), 30% shorter peanut (dashed-dotted green line) and a model without a peanut (i.e. 0% peanut strength-thin solid black line. *Right:* Bar-induced torque Q_T for the aforementioned models (respective colours). In all plots, the vertical lines correspond to the positions of the peanut maxima for each respective height function.

$$Q_T^{int} = \frac{1}{r_{disc}} \int_0^{\mathrm{r_{bar}}} Q_T \, \mathrm{d}r, \tag{2.24}$$

where r_{disc} is the disc scalelength.

To get a good estimate of the difference of Q_T between two models over the entire radial range, it is best to carry out a point by point comparison, and then consider the radially averaged relative Q_T error. The relative error of Q_T^{int} is a better proxy for this error than Q_b, although there are cases where the relative error of Q_T^{int} is small, while the average relative error of Q_T is much more significant (such as the first row of Table 2.8) or vice-versa (first row of Table 2.9) . Therefore it is possible to have two cases with identical Q_T^{int}, but locally different Q_T.

Peanut strength uncertainties

We see in Figs. 2.10(a) and 2.10(b) that Q_T increases by reducing the strength of the peanut, and it reaches its maximum value when the peanut strength is zero, which corresponds to the height function of a flat isothermal sheet.

The values of the average and maximum relative errors of Q_T ($\langle$Error $Q_T\rangle$ and MAX(Error Q_T) respectively), as well as the relative error of Q_b and Q_T^{int} can be seen in Table 2.6 (and in all subsequent tables in the following subsections). We see that when we compare an isothermal sheet to the fiducial peanut model the error in Q_b is of the order of 4%. This is not representative of the large change that the average relative error of Q_T undergoes (27%). This is due to the fact that the maximum of Q_T does not change much, even though Q_T itself is affected by a significant amount over its entire range (see Fig. 2.10(b)). On the other hand, the change in Q_T^{int}, which takes into account the whole bar region, is more representative of the change in the average relative error of Q_T (20%).

In all the cases and for all the measurements of bar strength, the error introduced in the model due to uncertainty in peanut strength is not as large as the error introduced when not including a B/P bulge in the model.

Peanut width uncertainties

I compare setups with varying peanut widths to our fiducial model. Comparisons for Q_T can be seen in Figs. 2.10(c) and 2.10(d) and as previously mentioned, the mismatch between the different models is found when the scaleheights of the models are different. The extent of the region of Q_T which is flattened is reduced when the width of the B/P is reduced, as expected. Conversely, when the width of the B/P bulge is increased, the area of Q_T which is flattened is increased.

Values for the errors in the bar region are given in Table 2.7. We see that errors in peanut width do not induce very large errors in the average relative error of Q_T, compared to the

TABLE 2.6: Percentage Error of Bar Strength due to Peanut Strength Uncertainty

Peanut Strength	$\langle$Error $Q_T\rangle$	MAX(Error Q_T)	Q_b	Q_T^{int}
+50%	8%	17%	1.4%	6%
+25%	4%	9%	0.7%	3%
-25%	5%	11%	0.5%	4%
-50%	11%	26%	1.6%	7%
no peanut	27%	74%	4%	20%

The error induced in the bar strength due to different amount of error in the peanut strength. We see the effect of these uncertainties on the average and maximum relative error in Q_T ($\langle$Error $Q_T\rangle$ and MAX(Error Q_T) respectively), as well as on the relative errors of Q_b and Q_T^{int}.

TABLE 2.7: Percentage Error of Bar Strength due to Peanut Width Uncertainty

Peanut Width	$\langle$Error $Q_T\rangle$	MAX(Error Q_T)	Q_b	Q_T^{int}
+50%	6%	12%	9%	6%
+25%	4%	11%	5%	4%
-25%	7%	20%	3%	6%
-50%	16%	39%	5%	13%
no peanut	27%	74%	4%	20%

As in Table 2.6 but for errors in peanut width.

errors induced when not including a B/P bulge. The errors induced in Q_T^{int} are not very large either, although Q_b, in the case of +50% peanut width, has a relative error larger than that of not including a B/P bulge. This again shows the importance of carrying out a point by point comparison, and a comparison of Q_T^{int}, in order to determine the errors induced in bar strength due to uncertainties.

Peanut length uncertainties

The results of this study are shown in Figs. 2.10(e) and 2.10(f) and in Table 2.8. Something worth noting in the Fig. 2.10(f) is that the flattening of Q_T occurs at the positions where the maxima of the peanut are found (which are indicated by the corresponding vertical lines).

In Table 2.8 we see the errors induced in the different measurements of bar strength due to uncertainties in peanut length. For the case where the peanut length is 30% larger than the fiducial value, Q_b has a relative error of 17% compared to the error of 4% in Q_b when we do not add a peanut. This seems to suggest that it can be counter-productive to include a B/P in the model when there exist uncertainties in peanut length. However, if we examine the average relative error in Q_T, we see that the error induced in Q_T is in fact larger when we do not model a B/P than when we miscalculate its length by +30%. This points once again to

TABLE 2.8: Percentage Error of Bar Strength due to Peanut Length Uncertainty

Peanut Length	$\langle$Error $Q_T\rangle$	MAX(Error Q_T)	Q_b	Q_T^{int}
+30%	16%	35%	17%	5%
+16%	9%	19%	7%	3%
+8%	5%	10%	3%	1%
-8%	4%	10%	2%	1%
-16%	9%	19%	4%	3%
-30%	16%	39%	8%	8%
no peanut	27%	74%	4%	20%

As in Table 2.6 but for errors in peanut length.

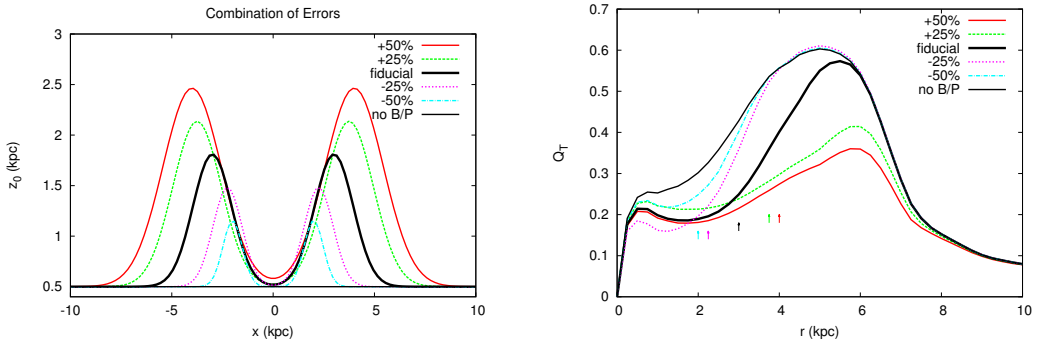

FIGURE 2.11: *Left:* Values of z_0 for different combinations of uncertainties. *Right:* Strength of non-axisymmetric forcings Q_T as a function of radius, for the different combinations of uncertainties. In order to not over-clutter the plot, the positions of the peanut maxima are given by the vertical arrows, from left to right, for the -50%, -25%, fiducial, +25% and +50% cases.

the need for examining the average errors of Q_T and not just Q_b, as the errors induced in Q_b are not representative of the error induced in Q_T.

We also see in Fig. 2.10(f), that even though Q_T of the two cases (of fiducial peanut and +30% peanut length) differs significantly point by point, the area under the curve for the two cases is quite similar. This is reflected in the value of the relative error of Q_T^{int}, which only suffers a change of around 5% while the average error of Q_T suffers a change of 16%. We see therefore that Q_T^{int} is not always a good approximation for the average relative error of Q_T.

The important thing to note is that all the cases considered induce less error in the average error of Q_T than not modelling the B/P at all.

Combinations of uncertainties

As has already been discussed, the most likely scenario is that of a combination of different sources of error affecting our model. The combinations of errors shown in Table 2.9 are as in Section 2.5.1. We see that the average and maximum relative error in Q_T for all the

TABLE 2.9: Percentage Error of Bar Strength due to a Combination of Uncertainties

All Errors	$\langle$Error $Q_T\rangle$	MAX(Error Q_T)	Q_b	Q_T^{int}
+50%	19%	42%	47%	25%
+25%	16%	35%	28%	14%
-25%	16%	50%	7%	11%
-50%	20%	63%	7%	17%
no peanut	27%	74%	4%	20%

As in Table 2.6 but for different combinations of uncertainties.

combinations is less than that of not modelling the B/P at all. The scaleheights and bar strength for these models can be seen in Figs. 2.11(a) and 2.11(b) respectively.

2.6 Summary

In this chapter I present the effects of a Boxy/Peanut height function on the potential, forces, periodic orbits and bar strength of a barred galaxy. I show that such height functions significantly affect the results, which consequently hints to the effects that a Boxy/Peanut bulge will have on its host galaxy.

I present a method for calculating the potential and forces due to the stellar component of a disc galaxy, based on a three-dimensional integration of the stellar density distribution, which can be obtained from images of not too inclined galaxies combined with a given height function. The method gives robust results for different test cases, as well as allowing for any general height function to be used, thus allowing for complex density distributions to be modelled. It is used in Chapter 4 in order to accurately model the potential of NGC 1291, which we study in detail in order to determine its dynamical structure by constraining the disc M/L and the dark matter content.

I used the code on an image extracted from a N-body+SPH simulation of an isolated galaxy, together with two flat, position-independent height functions, and two position-dependent height functions. Of the two position-dependent height functions, one models a peanut bulge and one models a boxy bulge. To create an accurate and physically motivated fiducial height function for the peanut, I shaped and fitted the peanut height function to the Boxy/Peanut bulge of the simulated galaxy.

I found, in accordance with previous results in the literature (Laurikainen and Salo, 2002), that for the two flat height functions the potential and forces do not vary much, provided the setups have equivalent scaleheights. This also holds true for the bar strength Q_T, which does not change much for different flat height functions.

However, I found that for boxy or peanut height functions the potential and forces vary significantly with respect to the case in which a flat height function is used (see Figure 2.5). For the potential, the difference can be up to 7% for an extended region within the bar. For F_x the difference can be as large as 37%, while for F_y this difference can be as large as 28%. I therefore concluded that if a Boxy/Peanut bulge is present, one should include it when creating a dynamical model of the galaxy.

To further confirm this result, I examined the effect of the Boxy/Peanut bulge on the morphology of the most important families of periodic orbits found in barred galaxies. By taking into account the B/P geometry (i.e. by using our fiducial peanut height function) for a given energy, the elongation of the x_1 orbits – the bar-supporting orbits elongated parallel to the bar – is decreased; this effect is most noticeable for orbits in the region where the Boxy/Peanut is maximum (around ± 3 kpc, see Figure 2.7(a)) as expected. By adding a Boxy/Peanut to the model the extent of the x_2 family – the family of orbits perpendicular to the bar – is increased by $\sim$43% (see Figure 2.6(b)), as is the distance between the two Inner Lindblad Resonances (ILRs). Additionally, the position of the 3:1 resonance is changed; the 3/1 family – elongated along the bar and asymmetric with respect to the y-axis – appears at larger energies and is much more extended in the characteristic diagram (see Figure 2.6(b)). All the aforementioned effects will have an impact on the stellar as well as the gaseous kinematics of the galaxy. The shape and strength of the shocks in the gas will be affected, which in turn affects the amount of gas inflow to the central parts of the galaxy. This could have an impact on the formation of discy bulges and possibly on the fuel reservoir for AGN activity. To confirm this, in Chapter 5, I investigate the extent of the effects of B/P bulges on gas flows in galaxies.

I also studied the effect of the Boxy/Peanut bulge on the bar strength, as given by the non-axisymmetric forcings due to the bar, Q_T. The shape as well as the maximum of Q_T are significantly affected by taking into account the geometry of a Boxy/Peanut bulge. I found it useful to define a new quantity for measuring bar strength, Q_T^{int}, which allows us to extract information about the strength of the bar by using its whole extent. The presence of a Boxy/Peanut bulge, especially at the points where its scaleheight is maximum, reduces the bar strength (see Figure 2.8) which confirms that the presence of a Boxy/Peanut bulge reduces the bar induced torques.

Even though taking into account the geometry of Boxy/Peanut bulges will affect the model, it is not trivial to obtain their parameters observationally. I therefore examined how much error would be introduced in the results by introducing uncertainties in the Boxy/Peanut parameters. Each source of error individually (peanut strength, peanut length and peanut width), as well as combinations of the different sources of error, induce errors in the results which in general are considerably less than those induced by not modelling the peanut at

all. So, for realistic values of uncertainties in the peanut parameters, the error in including a peanut will be less than the error induced by not including a peanut in the model.

The simulated galaxy I chose for this particular study contains a strong bar, corresponding to bar classes 5 and 6 from the Buta and Block (2001) classification. Therefore the results of this study can be straightforwardly and quantitatively applied to real galaxies with similar bar and peanut strength, which account for approximately 20% of SB galaxies in the local universe. These results are also qualitatively relevant to all barred galaxies in the secular evolution phase, although for reduced bar and peanut strength the effect of the Boxy/Peanut bulge on the model is also reduced. In this work I presented an in depth study of the effects of a Boxy/Peanut bulge on its galaxy model, focusing on a particular test case; in the future, a quantitative statistical study of the effects of these bulges on their host galaxies will be carried out.

3

Gas Response Simulations

In this chapter I present the hydrodynamic simulations which are extensively used in the remainder of the thesis, specifically in Chapters 4 & 5. The simulations are also referred to as gas response simulations, since they are fixed potential simulations, in which the gas is let to gradually respond to the potential. I present a number of technical details and tests regarding the simulations, and how they are affected by different parameters.

3.1 Introduction

Interstellar gas in galaxies is generally assumed to be a perfect fluid, which allows the use of the Euler equation for describing the flow – a particular case of the Navier-Stokes equation with zero viscosity and zero thermal conductivity. A number of studies have been carried out in the past few decades, in an attempt to model the fluid flow of the interstellar medium with a number of numerical techniques, for example using grid methods (van Albada, 1985), the beam scheme method (Sanders and Prendergast, 1974), the sticky particles technique (Combes and Gerin, 1985) and Smoothed Particle Hydrodynamics (SPH) (Lucy, 1977, Gingold and Monaghan, 1977), where each method is best suited for a specific type of problem.

In the next two chapters I use hydrodynamic simulations in order to model the behaviour of gas in galactic models; in Chapter 4, I model the shocks that are created in the gas due to non-axisymmetric structures, in order to determine the disc M/L and bar pattern speed, while in Chapter 5, I model the gas inflow to the central kiloparsec of galaxies which contain B/P bulges. For this work, a method which is particularly suited to capturing the shocks created in the gas is necessary, which is why I therefore use a grid-based hydrodynamic code.

To solve the Euler equations I use the hydrodynamic Adaptive Mesh Refinement (AMR) code RAMSES (Teyssier, 2002), a publicly available grid code which solves the Euler equations by

means of a second-order Godunov solver. The simulations are run in two dimensions, as the main plane of interest is the z=0 plane of the galaxy, since to zeroth order we can assume that gas is confined to a thin plane in galactic discs. This simplifying assumption allows to save on computing resources, such that a large number of models can be run; furthermore, we assume that the gas is isothermal. The simulations used in this thesis were run on local machines of the Galaxy Dynamics group at Laboratoire d'Astrophysique de Marseille (LAM), on the cluster at LAM, and on the MESO centre machines of the Aix-Marseille University.

In Section 3.2 I describe the modifications (also referred to as "patches") that I made to the code in order to adapt it for our purposes. I describe the initial conditions of the model and the routine for changing the potential at different timesteps as well as the patch which supplies the forces to the grid.

In Section 3.3 I describe tests carried out in order to determine the effects of the AMR strategy on the gas flow, paying special attention to its effects on the shocks produced in the gas, since these are extensively used in Chapter 4. In Section 3.4 I explore the effects of grid resolution on the shock loci and on the central region of the model. For the aforementioned tests I make use of the analytic barred galaxy models used in Athanassoula (1992a,b); the models contain two axisymmetric components corresponding to a disc and a bulge, as well as a non-axisymmetric component, which models the bar described by a Ferrers' ellipsoid (Ferrers 1877). The four main parameters of the models are the central concentration, the bar axial ratio (b/a), the Lagrangian radius and the bar quadruple moment. The Lagrangian radius is equivalent to the bar pattern speed, with a higher pattern speed corresponding to a smaller Lagrangian radius, and the bar quadrupole moment is equivalent to the relative mass of the bar. For these tests, I make use of a suite of models which in general only differ from one to another in their quadrupole moment (i.e. they have different mass bars). For more details on the models the reader is referred to Athanassoula (1992a). In Section 3.5 I give a brief summary of the conclusions from the tests.

3.2 Adapting the code

I patched a number of modules in the code including the initial conditions (*condinit.f*90), the force supplying (*gravana.f*90) and the time updating (*update_time.f*90) subroutines.

For the initial conditions of the simulations I setup a two dimensional axisymmetric gaseous disc, with a homogeneous density distribution, in hydrostatic equilibrium, which fulfils the following relation:

$$\frac{1}{\rho}\frac{\partial p}{\partial R} + \frac{\partial \Phi}{\partial R} = \frac{V_{rot}^2}{R} \tag{3.1}$$

where ρ, p, V_{rot} and Φ are the density of the gas, the gas pressure, the azimuthal rotation velocity and the gravitational potential of the system. As I work in two dimensions space, the disc need only be in hydrostatic equilibrium in the plane of the galaxy. The above equation states that the inward gravitational pull in the radial direction is counterbalanced by the centrifugal force and the pressure gradient of the gas, which is a function of the temperature.

The disc is tapered using an exponential tapering function. Special attention has to be paid, especially for gases with high temperatures, to not taper the disc too abruptly, otherwise the sudden decrease in density will lead to a very large pressure gradient which can give imaginary solutions for the rotational velocity. The gas is modelled as an isothermal gas with adiabatic index 5/3 which corresponds to HI gas (neutral atomic hydrogen), and in most of the runs, I assign a value of 10km/s to the sound speed of the gas, which corresponds to temperatures characteristic for neutral hydrogen gas of the interstellar medium in galaxies (Kamphuis, 1993).

The time updating module is modified such that over a user selected period of time the non-axisymmetric potential replaces the axisymmetric potential, with which the simulations are initialised, by implementing,

$$\Phi = \Phi_{axi} \times (f_i - 1) + \Phi_{non-axi} \times f_i \tag{3.2}$$

where Φ is the total potential, Φ_{axi} is the axisymmetric potential, $\Phi_{non-axi}$ is the non-axisymmetric potential and f_i goes from 0 to 1 in the desired time period. In order to avoid transients, f_i is introduced gradually according to Equation 3.3,

$$f_i = \begin{cases} 0 & t \leq t_{in} \\ \frac{1}{2} + \frac{3}{16}\xi^5 - \frac{5}{8}\xi^3 + \frac{15}{16}\xi & t_{in} < t < t_f \\ 1 & t \geq t_f \end{cases} \tag{3.3}$$

where,

$$\xi = 2\frac{(t - t_{in})}{t_f - 1} \tag{3.4}$$

where t_{in} is the time at which the non-axisymmetric potential is introduced and t_f the time by which it has been fully grown. Therefore the mass and the first and second derivatives are continuous functions of time. It is important that the non-axisymmetric potential be introduced gradually in order to avoid unphysical transients in the gas. The time over which the non-axisymmetric potential is grown, was found empirically as ∼3 bar rotations, which is

enough in order to converge to a stable model, while minimising the computing time; this was in accordance with previous studies (Athanassoula, 1992b, Patsis and Athanassoula, 2000).

I patched the force supplying module in order to assign forces to the grid for the axisymmetric potential, non-axisymmetric potential and dark matter halo as a function of time, as described in Equation 3.2. The original force grid has a resolution of 0.1 kpc even though the simulation grid reaches much higher resolutions (of the order of 30 parsec). A linear interpolation is carried out in order to find the forces at all points in the simulation grid. I carried out tests with finer force grids in order to determine the effect of increased resolution on the shocks in the gas and found that increasing the resolution of the force grid does not have a significant effect on the shocks, and that therefore a resolution of 0.1 kpc is sufficient. The only region in which this grid has an effect is in the very central regions of the galaxy, within the centermost ∼300pc, which we are not interested in for this study. The non-axisymmetric potential is rotated according to the pattern speed, which is supplied from the RAMSES parameter file. The units of the code are set to $M_{\odot}$, Gyr, kpc for the mass, time and length respectively.

3.3 Which AMR strategy to use?

In past studies which make use of gas response simulations, a Cartesian grid has usually been used. I therefore tested whether by using the Adaptive Mesh Refinement available to the RAMSES code, it is still possible to adequately capture the shocks formed in the bar region. RAMSES has various strategies implemented for refining the mesh, the most relevant for our study being:

1. The quasi-lagrangian strategy: Each level is refined if the baryonic mass in a cell exceeds $n \times mass_{sph}$, where n is set for each level and $mass_{sph}$ is used as a typical mass scale.

2. The discontinuity based strategy: Each level is refined according to relative density variations. Above a certain amount of relative density variation the cell is refined according to $\rho_{refine} \geq \frac{\nabla \rho}{\rho}$.

I tested the aforementioned AMR strategies using analytical models of barred galaxies, containing a disc, a bulge and a bar, namely models 001 and 052 from Athanassoula (1992a). Model 052 has a higher quadrupole moment than model 001, i.e. a stronger bar; all other parameters of the models are the same.

To examine the properties of the shocks, I placed pseudo-slits perpendicular to the shocks, and measured the density and velocity jumps along the slits (as can be seen in Figure 3.1). As we are mainly interested in capturing the shocks, and specifically the shock loci, I first

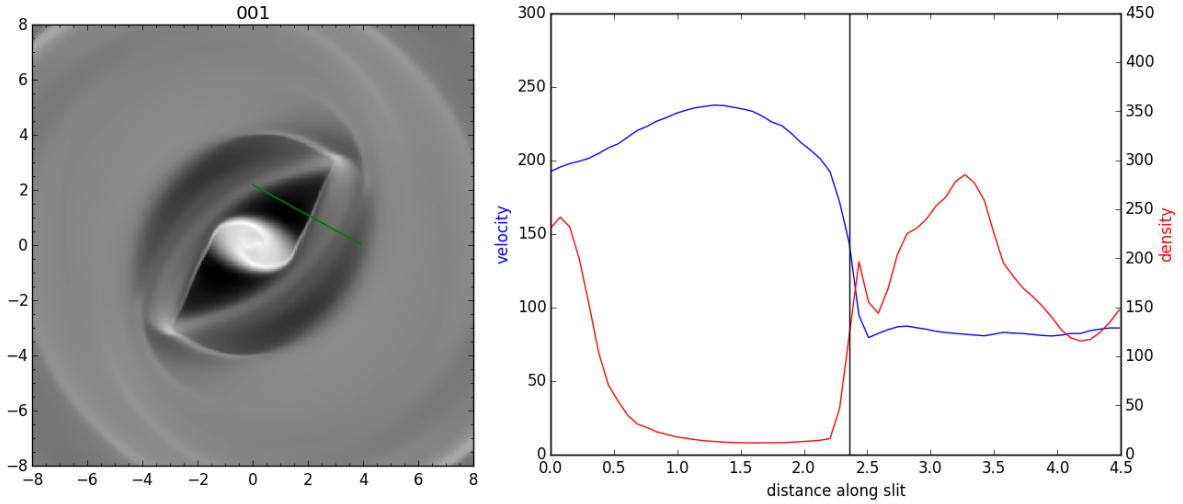

(a) Grid 2^{10}

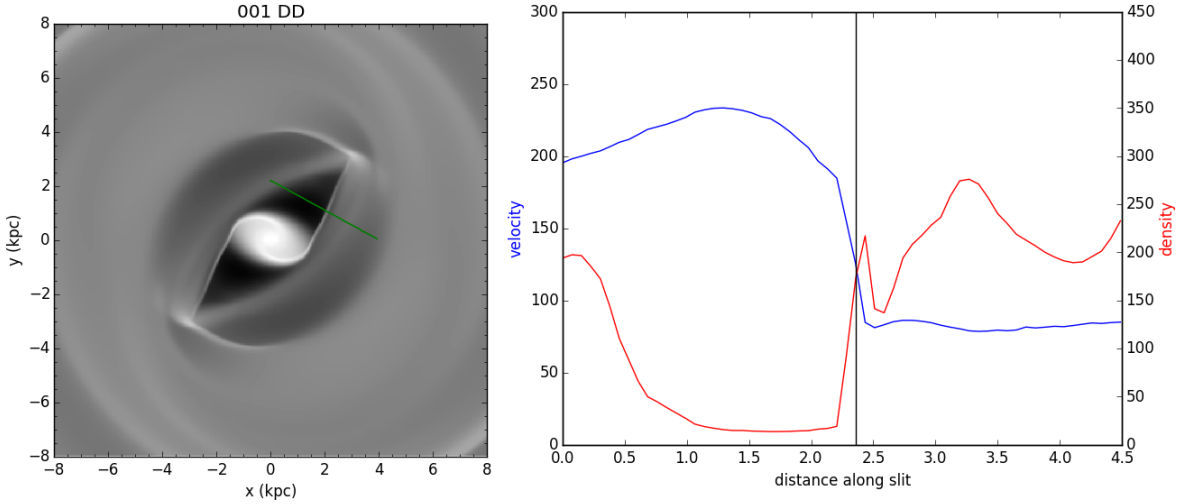

(b) AMR 2^{10} Density Discontinuity Scheme

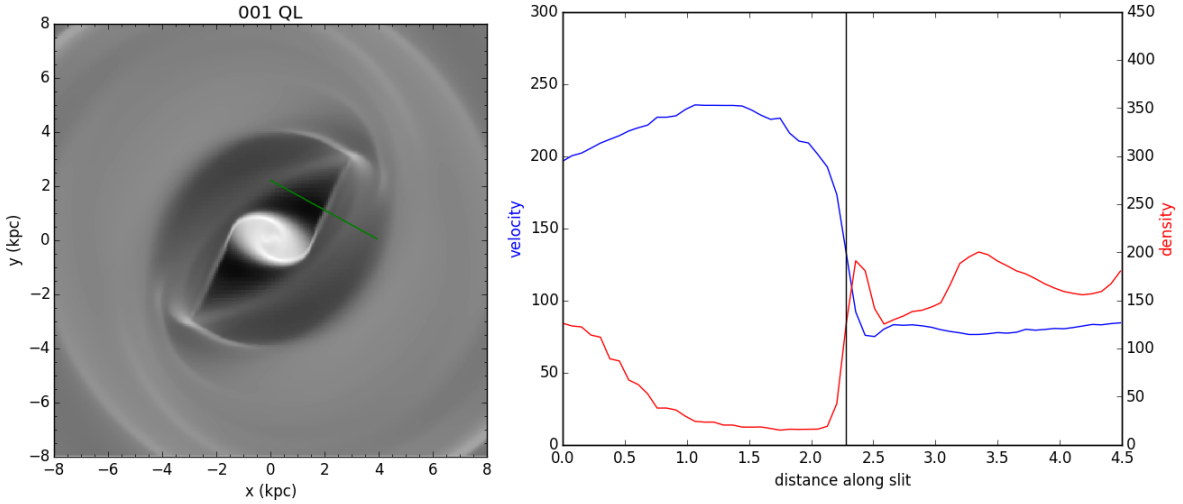

(c) AMR 2^{10} Quasi-Lagrangian Scheme

FIGURE 3.1: Shocks in the gas for a Cartesian grid and different AMR strategies for model 001. From top to bottom, a Cartesian grid with 2^{10} grid points, an AMR grid refined with the density-discontinuity scheme and an AMR grid refined with the quasi-lagrangian scheme. Both the AMR grids have the same number of maximum levels as the Cartesian grid. In the left panels we show the gas surface density with the location of the slit indicated. In the right panels we show the density (in arbitrary units) and velocity (in km/s) along the slit.

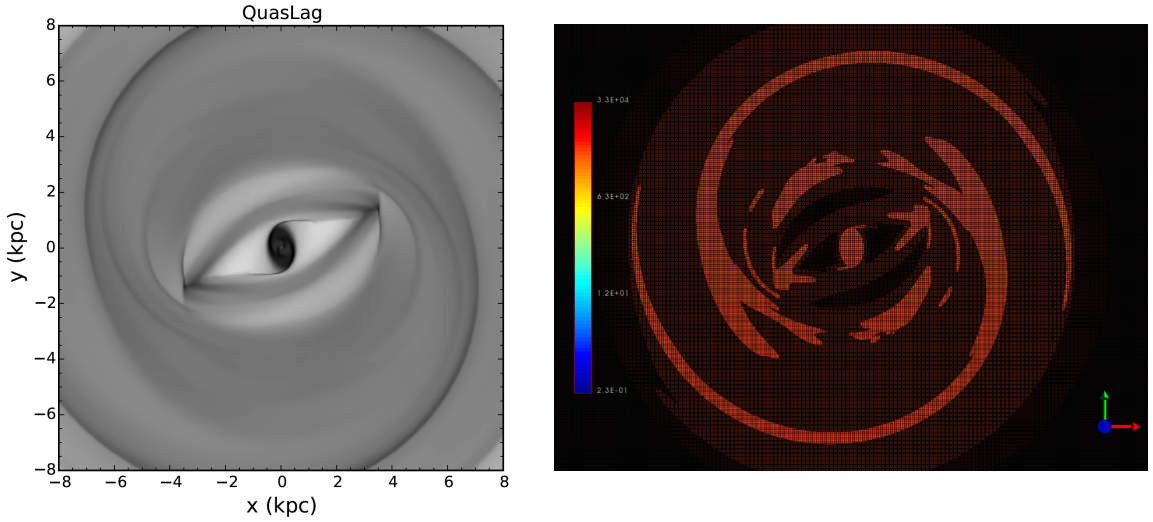

(a) Quasi Lagrangian refinement

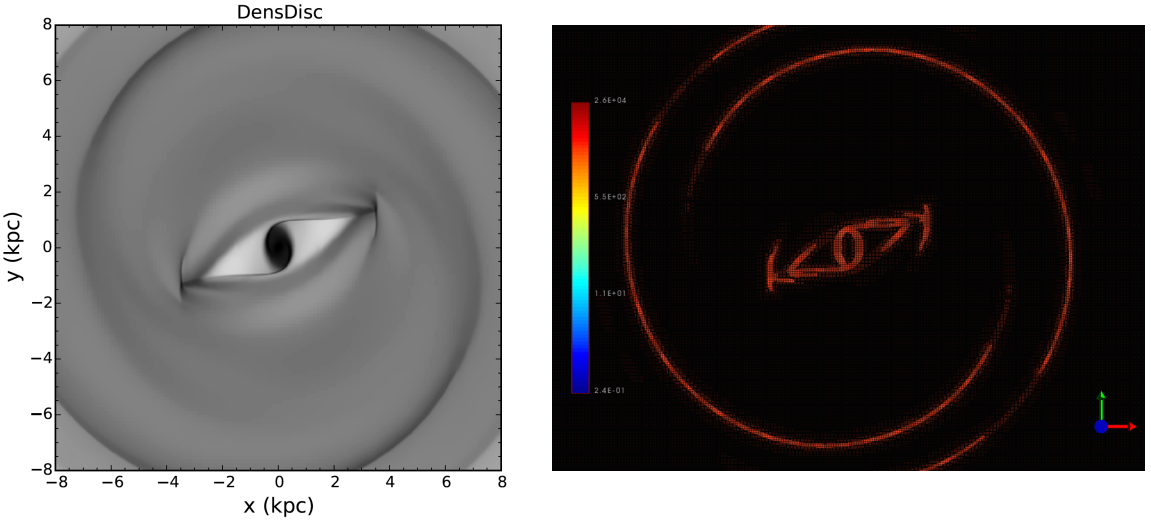

(b) Density Discontinuity refinement

FIGURE 3.2: The effect that the AMR strategy has on the gas shocks. In the top panels we show the results for the quasi-lagrangian scheme, and in the bottom panels the results for the density-discontinuity scheme. The left panels show the 2D gas surface density, while the right panels show the locations of the grid refinement. It is clear that if one is interested in properly capturing the shocks, the density-discontinuity strategy is more appropriate.

examined various methods for obtaining the location of the shock. One of the methods used was ascribing the location of maximum density and minimum velocity as the shock loci. As these two locations do not necessarily coincide, I also used a second method which involves taking the maximum of the gradient of the density and velocity. By using these two latter values we can get an unambiguous value for the location of the shock, since in general these two values coincide.

I carried out a comparison of the different AMR strategies versus the Cartesian grid, using models 001 and 052. I ran three types of simulations: a Cartesian grid of $(2^{10})^2$ grid points, and two AMR grids with maximum refinement equivalent to the Cartesian grid. For the AMR grids I used two different AMR strategies, i.e. the quasi-lagrangian and the density discontinuity scheme. The results of this can be seen in Figures 3.1(a), 3.1(b) and 3.1(c) for the cartesian grid, the AMR grid with the density discontinuity strategy and the AMR grid with the quasi-lagrangian strategy respectively. We see that the location of the shock is the same in the Cartesian grid and the AMR density discontinuity strategy, while it is slightly displaced for the quasi-lagrangian AMR strategy. Additionally the shape of the shock is different for the simulation with the quasi-lagrangian strategy.

The discrepancy becomes stronger for stronger bars and when we go to higher resolutions. The reason for this becomes clear when we examine the regions of the grid which have been refined. I show in Figure 3.2, in the top panels the quasi-lagrangian scheme and on the bottom panels the density discontinuity scheme for model 052. We can see already from the left panels that the shock in the quasi-lagrangian scheme is not captured as well, i.e. the shock is not as "sharp", as in the density discontinuity scheme. The right panels show the grid[1], and where it has been refined, for the two strategies. The density discontinuity scheme applies the refinement along the shocks which is what we are interested in, while the quasi-lagrangian scheme applies the refinement where the highest mass regions are found, i.e. mostly in the central region of the model. Also, the difference in wallclock time between these two runs is about a factor of 10 (the density discontinuity run is $\times 10$ faster than the quasi-lagrangian scheme.) To obtain the same refinement in the shock regions as in the density-discontinuity strategy, by using the quasi-lagrangian scheme, would required a lot more computational resources. This is because the code would first have to refine all the regions with the highest density, such as the central parts of the model, in order to reach the shock regime which has lower density than the central regions. Therefore the density discontinuity scheme is more adapted for the purposes of this work and is used throughout the remainder of this thesis. This is important to note in general when carrying out studies in which capturing the shocks is of vital importance. I also carried out more tests at higher resolutions and for different models, and the results from all these tests confirm the aforementioned findings.

[1]For this we use the software glnemo2 http://projets.lam.fr/projects/glnemo2.

3.4 Effects of resolution

I carried out tests on a number of the analytic models from Athanassoula (1992a) , to determine the effects of resolution on the shocks induced in the gas flows in barred spiral galaxies. This was additionally motivated by the findings in recent work by Sormani et al. (2015), who showed that gas flows are highly dependent on resolution. It is worth noting that this discrepancy in the gas flow due to resolution has not been reported in previous studies (Weiner et al., 2001, Kranz et al., 2001, Pérez et al., 2004).

3.4.1 On the location of the shock loci

A number of analytic models from Athanassoula (1992a) were run with increasing bar strength, and increasing resolution, as is shown in Figure 3.3 and 3.4. I measured the location of the shock, by placing a slit perpendicular to it, and taking the maximum gradient of the velocity (Figure 3.4). I found that the shock loci coincide for the different resolutions to within 5%. In order to examine whether the slight change in the location of the shock is due to temporal oscillations in the gas flow, I also took averages for this value for 11 different times, from 1Gyr to 1.5Gyr. This error of 5% in the shock loci however persists even when averaged over different times.

3.4.2 On the central concentration

By visual examination of the gas surface density in Figure 3.3 we can already see that the central disc (also referred to as the "x_2" disc) is reduced for higher resolutions. This is in agreement with recent results presented by Sormani et al. (2015), who argue that the decrease in the size of the "x_2" disc is due to the gas being able to better resolve the x_1 and x_2 orbits. I measured the extent of the x_2 disc along the bar minor axis for the different resolutions, and found that the disc size converges for higher resolutions and lower resolutions with a transition region between the two extremes (see Figure 3.5), which is also in agreement with what was found by Sormani et al. (2015). Model 052 has a smaller x_2 disc than model 001, since, as is expected from orbital structure theory, the strongest bar has the smallest x_2 extent (see panel a in Figures 6 & 7 of Athanassoula (1992a)).

Another interesting feature to note is the fact that the nuclear, or x_2, disc that is formed does not necessarily trace the largest x_2 orbits (which are overplotted in Figure 3.6), which is in accordance with what is also found in Li et al. (2015). This indicates that the extent of the x_2 orbits, and consequently the location of the Inner Lindblad Resonance, cannot be used to trace the size of the inner disc or ring (which is also hinted at in Kim et al. (2012)). Li et al.

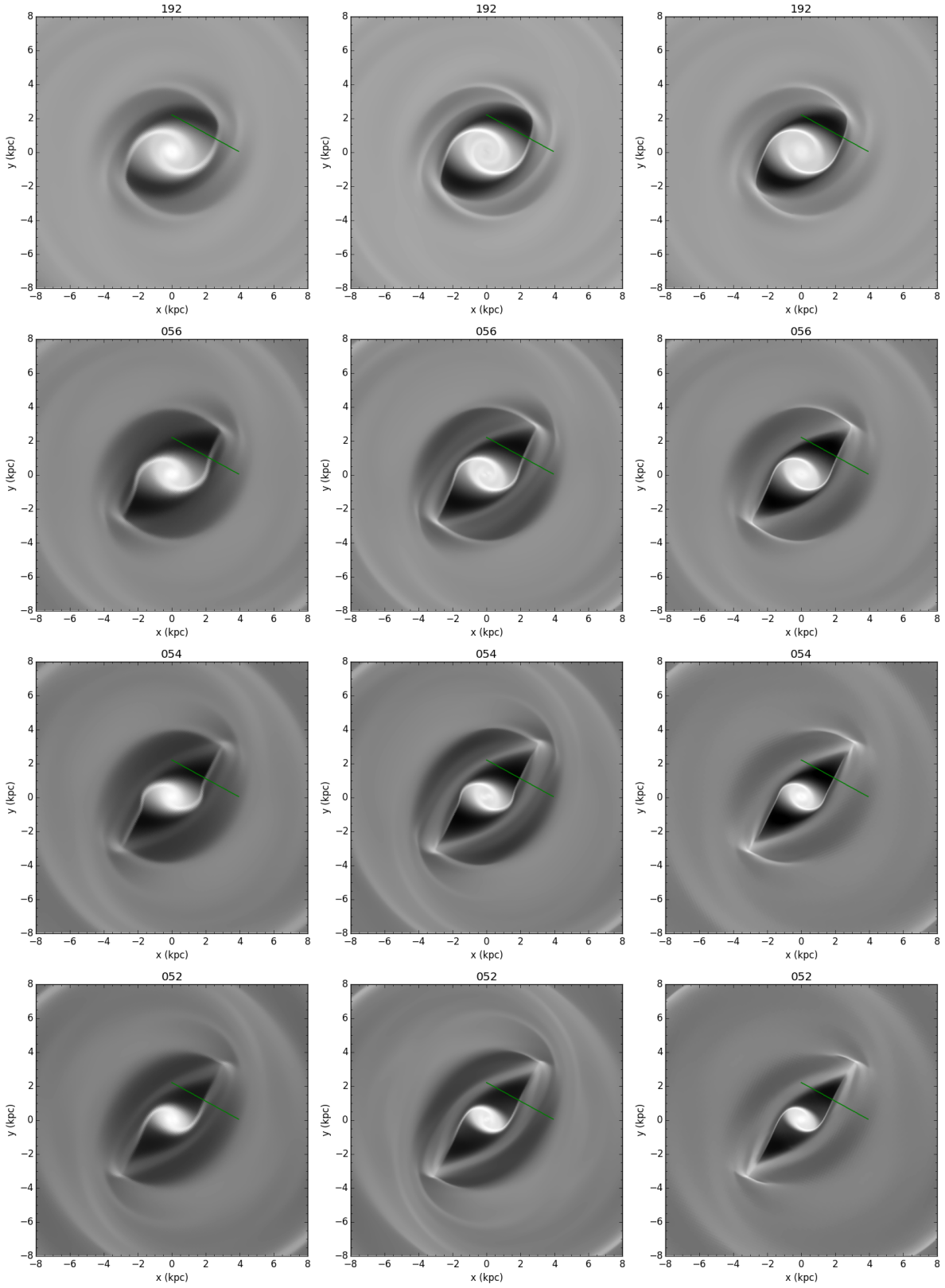

FIGURE 3.3: Surface density of the gas for a grid of analytic models. From top to bottom: models 192, 056, 054, 052 with increasing bar strength. From left to right the resolution of the grid is increased as 2^9, 2^{10} and 2^{11} where the last grid has an AMR grid.

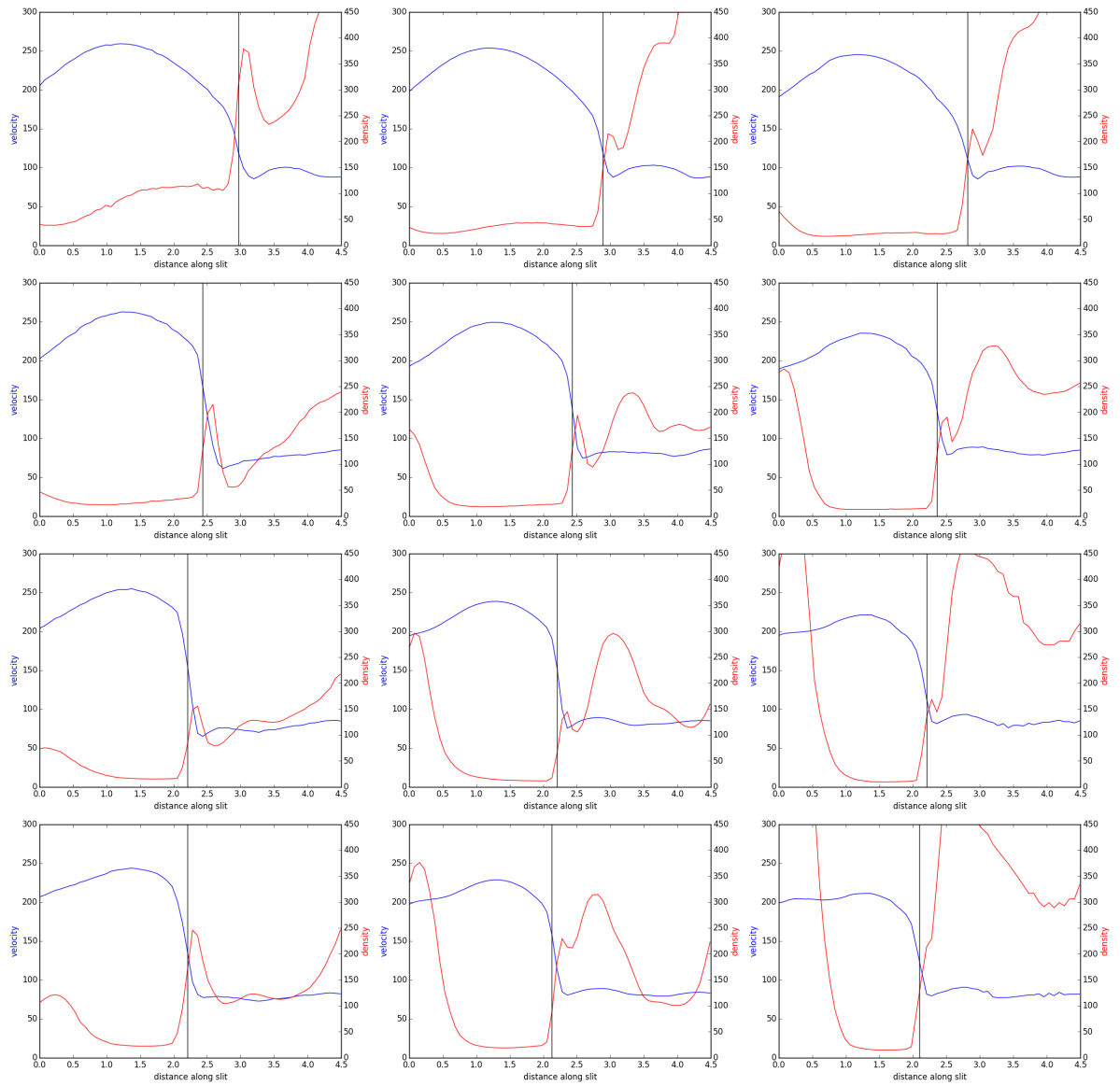

FIGURE 3.4: Density and velocity along the slit for a grid of analytic simulations with different resolutions. From top to bottom: models 192, 056, 054, 052 with increasing bar strength. From left to right the resolution of the grid is increased as 2^9, 2^{10} and 2^{11} where the last grid has an AMR grid with a density discontinuity refinement strategy.

(2015) suggest that the ring forms at the radius where the residual angular momentum of infalling gas balances out the centrifugal force, which they argue can be computed from the rotation curve. The question of where the nuclear disc or ring forms with respect to the x_2 orbits present in the models, that is to say, *where* the transition from x_1 to x_2 orbits occurs, is still an open and very interesting question.

In Figure 3.6, I show snapshots for model 052 for six different resolutions, ranging from 40pc to 1.25pc, overplotted with the periodic orbits of the model in the bar region. We can see that for the highest resolution, the gas starts developing instabilities, which was also found by Sormani et al. (2015) and Kim et al. (2012). There is no consensus as to why the flow

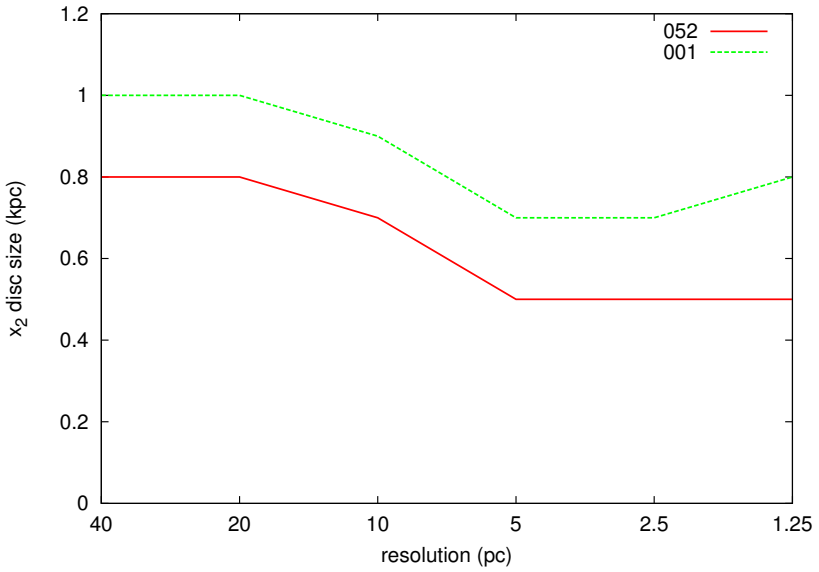

FIGURE 3.5: Size of the x_2 disc (along the bar minor axis), as a function of grid resolution for two models, 001 and 052 from (Athanassoula, 1992a). Model 052 has a stronger bar than model 001. The size of the x_2 disc seems to converge for higher and lower resolutions with a transition region between the two extremes. For model 001 the size of the disc seems to increase for higher resolutions but this could be also due to instabilities in the gas (see text). It is expected from orbital structure theory that the strongest bar has the smallest x_2 extent (see panel *a* in Figures 6 & 7 of Athanassoula (1992a)).

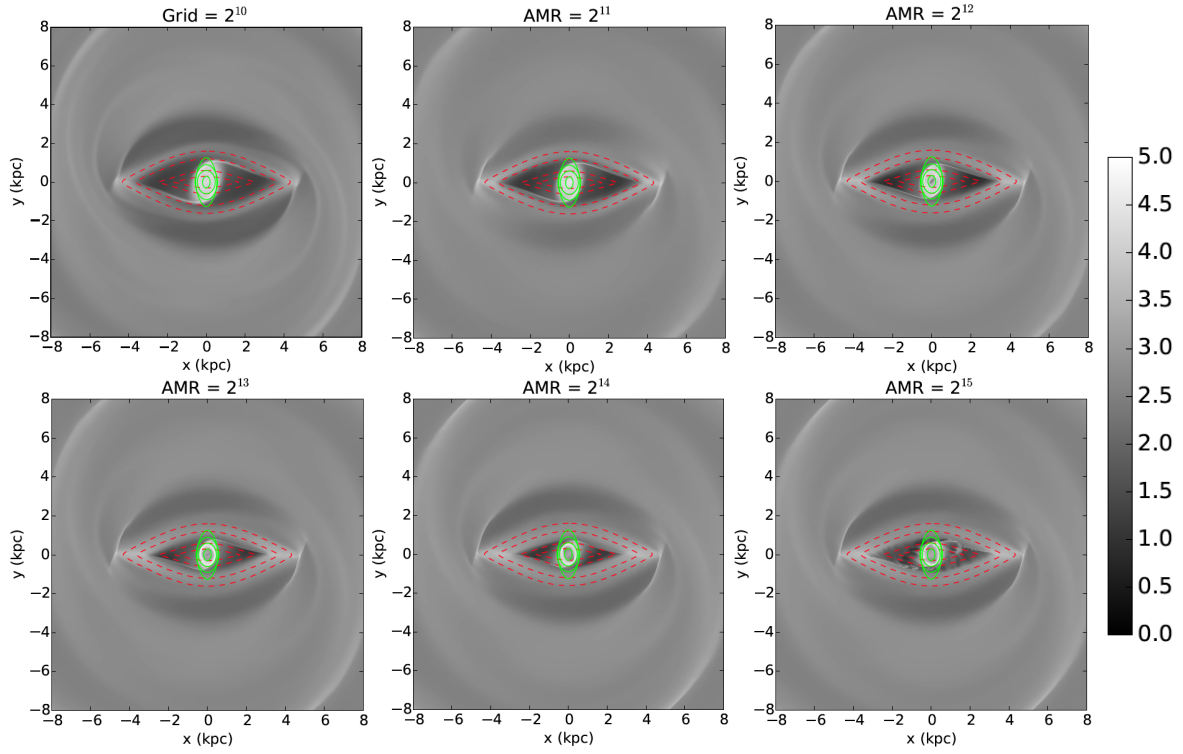

FIGURE 3.6: The gas surface density is plotted for a range of grid resolutions, from 2^{10} to 2^{15}, which corresponds to resolutions of 40pc to 1.25pc respectively. We see that for the highest resolution the gas develops instabilities. A number of x_1 and x_2 orbits of the model are overplotted. It has been proposed that for higher resolutions the gas can resolve the orbits closer to the centre, which is why the size of the x_2 disc is reduced (Sormani et al., 2015).

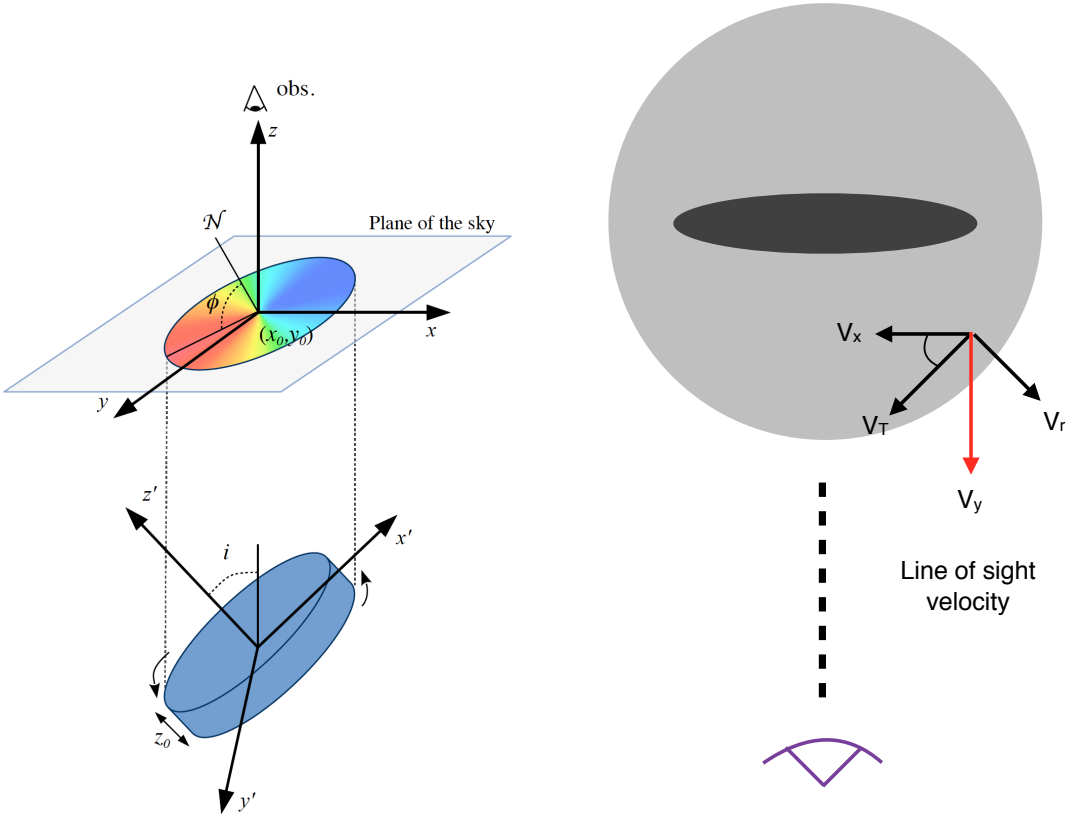

(a) (b)

FIGURE 3.7: *Left panel*: Schematic depiction of the parameters taken into account when deriving the rotation curve of a galaxy. The angle i gives the inclination of the galaxy and ϕ the position angle which identifies the position of the major axis as taken counterclockwise from North direction (reproduced from Di Teodoro and Fraternali (2015).) *Right panel*: Velocity component (V_y) we are interested in for our assumed edge-on galaxy models.

becomes unstable at high resolutions, but it is a feature which appears to be common to all hydrodynamic codes, and could be connected with the onset of turbulence due to high shear (Kim et al., 2012).

To summarise the results from this section, I found that for the purposes of this study, the shock loci are the most robust morphological comparison, since it is not dependent on the resolution of the simulations (within an uncertainty of 5%). For high enough resolutions the central gaseous disc seems to also converge and therefore for high enough resolutions this can be used as another constraint when comparing our models with the observations.

3.4.3 On the velocity fields

I also explored the effects of resolution on the velocity fields created from the models. Although, for the study of NGC 1291 in Chapter 4, I do not use the velocity fields in order to fit the

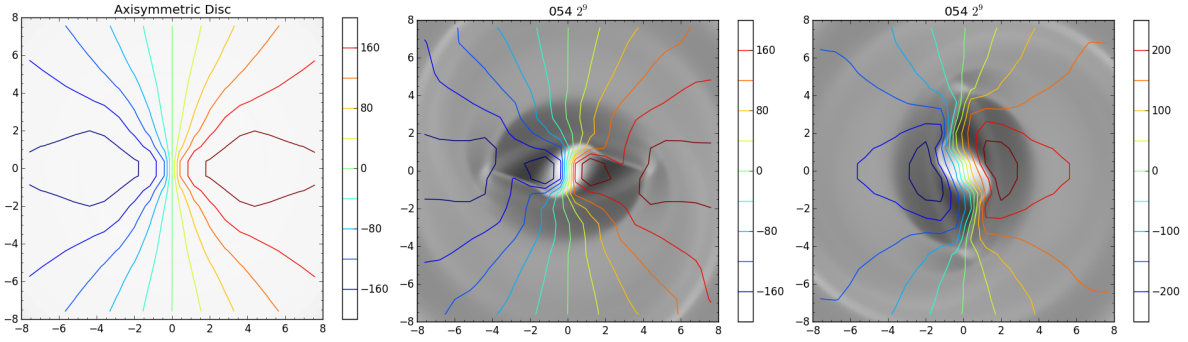

FIGURE 3.8: *Left:* Velocity field for an axisymmetric of a galaxy. *Middle:* Velocity field of model of galaxy with a bar where the galaxy is viewed along the bar minor axis. *Right:* Velocity field for a model of a galaxy with a bar, where the galaxy is viewed along the bar major axis.

models to the observation, as we do not have information about the gas in the bar region, velocity fields will be used for other galaxies in the near future, and so I briefly mention these tests here.

The velocity fields are calculated by assuming that the galaxy is edge on and we have "infinite" resolution, such that we can know the line of sight (*los*) velocity for each point in the galaxy. Velocity along line of sight in our case is then V_y (see Figure 3.7) due to the light arriving in parallel due to distance from the galaxy. Of course for observed galaxies we are interested in inclined galaxies, but this can be adapted to whichever inclination we want. In order to recover the circular velocity from the *los* velocity, a large number of observational studies assume that the velocity in the plane of the sky is given by:

$$V(x, y) = V_{sys} + V_C(R)\sin(i)\cos(\phi.) \tag{3.5}$$

where V_{sys} is the systemic velocity of the galaxy, V_C is the circular rotation of the galaxy, i is the inclination of the galaxy with respect to the observer and ϕ is the position angle of the major axis on the receding half of the galaxy, taken anti-clockwise from the North direction on the sky(Bosma (1978), Di Teodoro and Fraternali (2015), see also Figure 3.7(a)). In nearly all galaxies there exist deviations from this simple model of a disc in circular motion, due to the presence of features such as bars and warps. However, the deviations are generally an order of magnitude smaller than the rotational velocities themselves. Therefore an estimate of the rotation curve can still be derived from the distorted velocity fields using this simple model (Bosma, 1978), although more complex methods can be used in order to try and model the non-circular motions in the gas (see reviews by Sofue and Rubin (2001), Teuben (2002)).

In Figure 3.8 I plot the velocity field as obtained from the the galaxy edge-on, projected onto the galaxy as it is seen face-on, in order to visualise the velocity field, for an axisymmetric

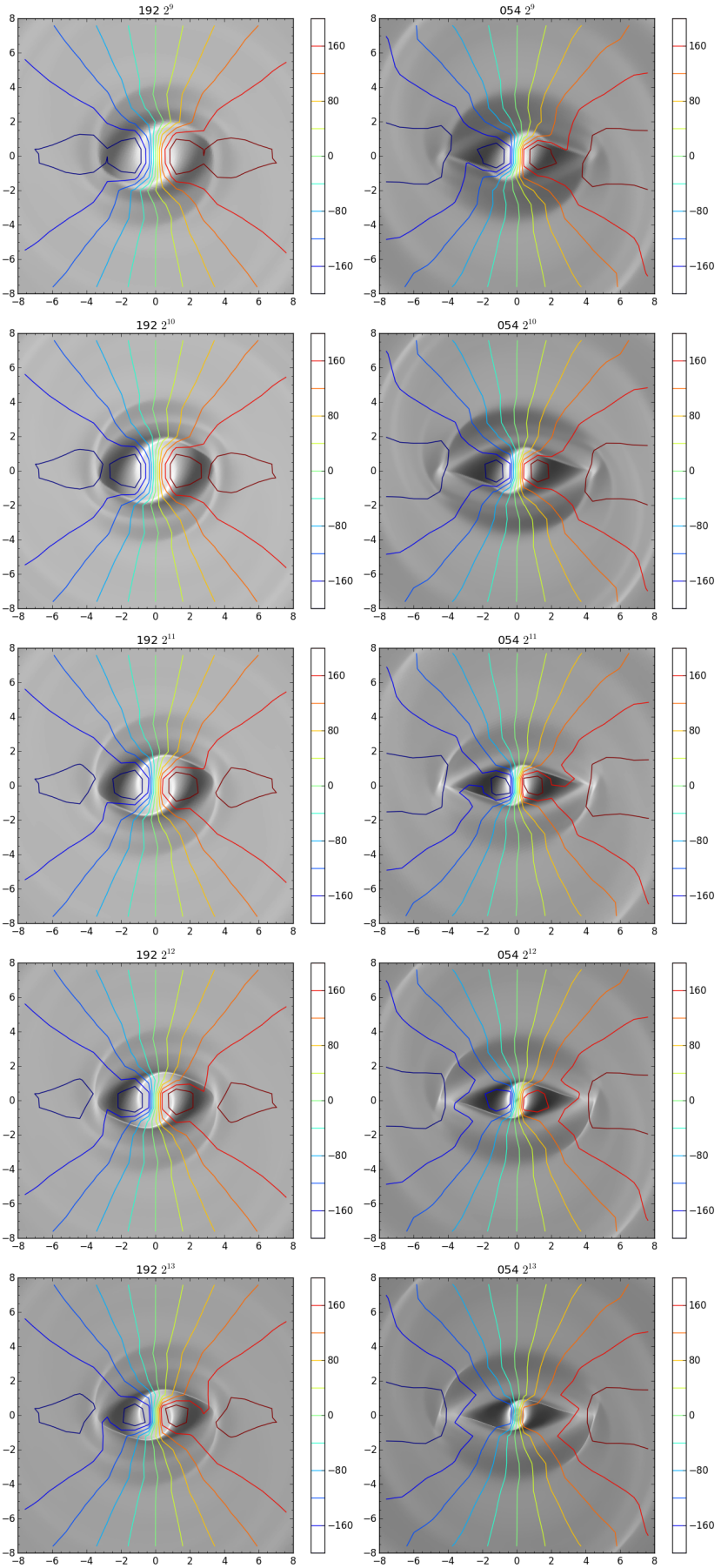

FIGURE 3.9: Velocity field for models 192 (left) and 054 (right) for five different grid resolutions, starting from lowest resolution at the top and increasing as we move down. The five different resolutions are from 2^9 to 2^{13} where from 2^{11} to 2^{13} we are using an AMR grid.

disc, a disc with a horizontal bar, and a disc with a bar oriented north-south. We see how the velocity field shows signs of non-circular motion when a bar is present, and how the signature changes depending on the orientation of the bar (Athanassoula, 1984).

In Figure 3.9 I show how the velocity fields for two models vary with resolution. In the plots the isovelocity contours have 40 km/s difference between each other and range from -200 to 200 km/s. We can already see by eye that there are slight variations in the velocity fields due to resolution effects, although they do not appear to have a drastic effect. However attention must be paid when using these models for comparing with velocity fields of observed galaxies, a fact that has not been commented on in previous studies (Weiner et al., 2001, Kranz et al., 2001, 2003, Lin et al., 2013). This will be further investigated in detail in the future.

3.5 Summary

In this chapter I present the simulations used in the next two chapters of the thesis, the modifications made to the RAMSES code and the tests that were carried out in order to determine the effects of the different AMR strategies and resolution on the shock loci.

While a quasi-Lagrangian AMR strategy does not adequately capture the shocks in the gas, a density discontinuity based strategy is able to capture the shocks as well as a Cartesian grid of the same maximum resolution by using less computational resources. Attention needs to therefore be paid in studies which aim at capturing the shocks produced in the gaseous flow, where an AMR grid is used, since, depending on the refinement strategy used, the shocks are not always well captured.

Additionally, I found, in accordance with the results of Sormani et al. (2015), that the resolution of the simulation has a significant effect on the morphology of the gas flow, specifically in the central region; the size of the central x_2 disc can be reduced by a significant amount (up to 38%) for increasing resolutions. The locations of the shocks on the other hand are robust to within 5% for different resolutions. Furthermore, I find that the size of the central gaseous disc seems to converge for higher resolutions. In Chapter 4, where the aim is to compare morphological features of the models to the observations, I therefore make use of the shock loci as the main diagnostic, since these are robust to changes in resolution. I avoid using the central x_2 disc, since the simulations used in Chapter 4 do not have the maximum resolution required in order for the x_2 disc to converge.

I also examined the effect of resolution on the velocity fields and found that that there is indeed a noticeable effect, which merits further investigation, especially since velocity fields have been used in a number of studies in the past (eg. Weiner et al. (2001), Kranz et al. (2001)) as a diagnostic for comparing the models with the observations.

4

Dynamical Determination of the M/L and Bar Pattern Speed of Galaxies: The case of NGC 1291

In order to break degeneracies in the mass distribution in barred spiral galaxies, we studied the gas flow in the nearby galaxy NGC 1291, in order to constrain the amount of dark matter in the inner parts using the morphology of the observed dust lanes. As a basis for the potential, we used a mid-infrared image at 3.6 μm, which is dominated by the older stellar populations. A large number of gas dynamical response simulations are run with different mass-to-light ratios, bar pattern speed and disc scaleheights. We find that there are a set of allowed values for these quantities, and further constrain these by making using of observations of the vertical stellar velocity dispersion. The results indicate that the disc of NGC 1291 is maximal, i.e. that in the central regions, baryonic matter dominates over dark matter and that bars that rotate fast are preferred.

4.1 Introduction

Since the discovery in the 70's that rotation curves derived from HI observations – which extend well beyond the optical disc of galaxies – remain flat (Roberts, 1976, Bosma, 1978, 1981), the nature and distribution of non-baryonic dark matter in galaxies has been a source of debate. One of the main issues with determining the non-baryonic distribution of matter in the central regions of galaxies is what has become known as the "disc-halo degeneracy" which arises due to the fact that rotation curve decompositions depend critically on the mass-to-light ratio (M/L or Υ) assigned to the stellar disc component. van Albada et al. (1985) showed that

the rotation curve of a galaxy can be fit equally well with a variety of dark matter halo and stellar disc components, from models with barely any disc contribution, to models where the disc contributes as much as possible to the rotation curve – without creating a hole in the dark matter halo; this is also known as the "maximum disc hypothesis". Sackett (1997) gave a more concrete definition of the maximum disc by stating that a disc is maximum if it contributes 85%±10% of the rotation curve at r=2.2h_r, where h_r is the scalelength of the disc. However, there is no conclusive evidence to either prove or disprove the maximum disc hypothesis and in fact there are a number of arguments both for (Athanassoula et al., 1987, Sackett, 1997, Weiner et al., 2001) and against it (Kuijken and Gilmore, 1991, Courteau and Rix, 1999), for the Milky-Way (Bissantz and Gerhard, 2002, Bissantz et al., 2003, Hamadache et al., 2006, Tisserand et al., 2007, Bovy and Rix, 2013) as well as for external galaxies (Bottema, 1993, Trott and Webster, 2002, Kranz et al., 2003, Gnedin et al., 2007).

One way to obtain an estimate of the disc M/L ratio, and therefore break the disc-halo degeneracy, is from stellar population synthesis (SPS) models. These however require a number of assumptions which depend on the detailed star formation history (SFH), the modelling of late phases of stellar evolution, and the initial mass function (IMF), quantities which in general contain a large amount of uncertainty, and which propagate through to the determination of the physical parameters of galaxies (Bell and de Jong, 2001, Conroy et al., 2009). Recent work, such as from the S^{4}G survey (Meidt et al., 2014, Röck et al., 2015) point to a M/L = 0.6 $M_\odot/L_\odot$, with smaller error bars than in previous studies, however other independent methods are needed to strengthen these findings.

Another way to break the degeneracy between the disc and the dark matter halo is by using dynamical estimates of the M/L ratio of the disc, which is what I employ here. To obtain a dynamical determination of the M/L one can use the amplitude of non-axisymmetries induced by a bar, if present, or other non-axisymmetric structures such as spiral arms, to constrain the M/L of the stellar disc. Gas, being collisional, is sensitive to the torques induced by bars and spirals, and can therefore be used as a tracer of the strength of the non-axisymmetric forcings in galaxies, by running hydrodynamic gas response (or sticky-particles) simulations in the relevant potentials. The major assumption of these studies is that the halo is dispersion dominated and therefore rounder than the non-axisymmetric stellar component.This has already been attempted in studies in the past for barred galaxies (Lindblad et al., 1996, Salo et al., 1999, Weiner et al., 2001, Weiner, 2004, Zánmar Sánchez et al., 2008) and spiral galaxies (Kranz et al., 2001, 2003). This type of modelling has also been applied in order to determine the pattern speed of barred galaxies (Salo et al., 1999, Pérez et al., 2004, Sánchez-Menguiano et al., 2015).

In this study I examine the dust lanes present in the nearby galaxy NGC 1291, and aim to reproduce their morphology using hydrodynamic gas response simulations. Dust lanes are

TABLE 4.1: Some basic properties of NGC 1291

Property	Value
Classification	SB0/a
Inclination (deg)	12
Distance	9.7 Mpc
1”	47 pc
1 pixel	35.25 pc
h_r	5.8 kpc
primary, r_B	5.1 kpc
nuclear, r_B	≈1 kpc

found in the bar regions of many galaxies, since they are caused from gas density enhancements due to shocks created by non-axisymmetries in the potential (Prendergast, 1983, Athanassoula, 1992b). The morphology of dust lanes is highly dependent on the M/L of the disc, on the bar pattern speed and on the height function of the disc. The effect of this last parameter has not been extensively studied in the past, however, following up on our previous work (Fragkoudi et al., 2015), I show in the following sections that it plays a crucial role on the strength and shape of the shocks created in the gas.

This Chapter is organised as follows: in Section 4.2 I describe the available observations of NGC 1291 and in Section 4.3 I describe how we go from these observations to dynamical models of the galaxy. In Section 4.4 I describe how the comparison between the models and the observations is carried out and the criteria I apply to the models in order to determine the goodness of the fit. In Section 4.5 I present results obtained from the gas response simulations where I emphasise general trends which appear due to the changes in M/L (Section 4.5.1), Lagrangian radius (which is equivalent to the pattern speed, Section 4.5.2) and height function (Section 4.5.3), as well as exploring models which do not contain a dark matter halo (Section 4.5.4). In Section 4.5.5 I explore the parameter space of all the models and in Section 4.5.6 I place some additional constraints in order to reduce the allowed parameter space. In Section 4.5.7 I show the models which were obtained as best fits to the observations. It’s important to note that there is no model which perfectly reproduces the morphology of the dust lanes, however conclusions can be drawn from the general trends seen in the simulations. In Section 4.6 I discuss some of the results and then give a brief summary of this study in Section 4.7.

4.2 Observations of NGC 1291

NGC 1291 is an early type barred galaxy (SB0/a) (de Vaucouleurs et al., 1991b) which in addition to the primary bar, contains a smaller nuclear bar, as well as an outer ring. In Table 4.1 we list some of the basic properties of the galaxy, which are described in this section. There is active star formation in the outer ring, as evidenced by GALEX images (Thilker

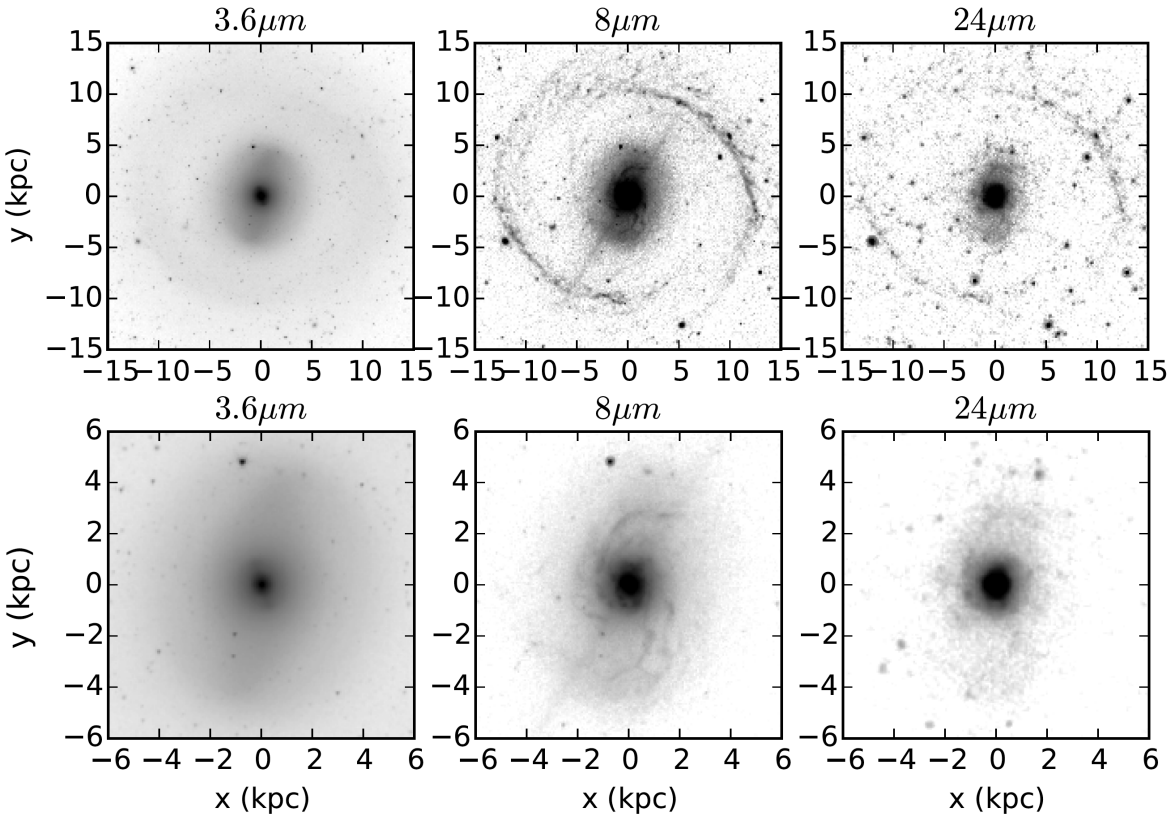

FIGURE 4.1: The 3.6, 8 and 24μm images for NGC1291. In the top panels the whole galaxy is shown, including the outer ring, while in the bottom panels I zoom in on a region encompassing the bar. In the 3.6μm image in the bottom panel the nuclear bar can be seen in the central 1 kpc of the galaxy.

et al., 2007). The inclination of the galaxy, is at most 12 degrees so it is practically face-on (Bosma et al., 2010). It is at a distance of 9.7 Mpc, as found using the Extragalactic Distance Database (Tully et al., 2009), which leads to 1" = 47 pc, and the galaxy doesn't seem to be undergoing any interactions. The galaxy contains hot gas in the centralmost region, mostly in the region of the bulge, as evidenced by X-ray studies (Bregman et al., 1995, Hogg et al., 2001). It is possible that the hot X-ray gas has heated the dust such that the formation of observable CO is prohibited.

The main body of work in this study is done using the 3.6μm, 8μm and 24μm images (see Fig. 4.1). The 3.6μm image is taken from the Spitzer Survey of Stellar Structure in Galaxies (S^4G, Sheth et al. (2010)) and is used to obtain the gravitational potential of the galaxy. From photometric decompositions of the galaxy (Bosma et al., 2010) using the BUDDA code (Gadotti, 2008), it was found that the scalelength of the disc is h_r=5.8 kpc, and the bar length r_B=5.1 kpc.

To extract information about the dust lanes in the galaxy, we use the 8 and 24μm image taken from the SINGS survey (Kennicutt et al., 2003) which trace the emission due to Polyaromatic

Hydrocarbons (PAHs) and hot dust respectively. PAH emission is correlated to the emission from cold dust $\leq$20K (Bendo et al., 2010) and is likely to occur in shocked regions of the ISM (Tielens, 2008). The dust lanes are used as a proxy for the underlying molecular gas distribution, as it has been noted in various studies that the 8μm and 24μm bands correlate well with the presence of molecular gas (Regan et al., 2006, Bendo et al., 2007, Schinnerer et al., 2013) and that enhanced PAH emission will be produced in the regions where the interstellar radiation field has increased (Bendo et al., 2008).

4.3 Constructing the dynamical models

To obtain a dynamical model of NGC 1291, we need to account for the mass distributions of the different components which make up the potential, both baryonic and non-baryonic.

To obtain the density distribution of the stellar component from the two-dimensional 3.6μm image, there are a number of steps to be carried out. First the bright foreground stars are masked out and then the image is smoothed (Section 4.3.1). One then needs to account for the amount of mass which corresponds to the surface brightness of the image (i.e. the M/L, Section 4.3.2). Finally, we assign a shape and thickness to the galaxy in the third dimension, i.e. we assume a behaviour for the density distribution of the stellar component in the vertical direction (Section 4.3.3).

In general one also needs to account for the gaseous component in the galaxy in order to have a complete picture of the potential of the galaxy. However, for NGC 1291 the mass of HI gas is negligible in the bar region, and we therefore make the simplifying assumption that it will not affect the forces in that region. There is evidence of cold gas due to the presence of dust, however a conversion from dust to molecular gas is also not straightforward and can lead to large uncertainties in the gas mass (Leroy et al., 2008, Martinsson et al., 2013). Additionally, the mass of the hot gas found in the galaxy is thought to be even less than the HI gas mass (Bregman et al., 1995); we therefore do not include the gaseous potential, assuming that the gas mass is minimal, and we use the gas therefore only as a tracer of the underlying potential.

Additionally to the baryonic component of the potential, we need to assume the density distribution of the dark matter halo, which we describe in Section 4.3.5.

4.3.1 Smoothing the 3.6μm image

I remove the bright foreground stars in the image, by replacing those pixels in which a foreground star is found, with pixels from the symmetrically opposite part of the galaxy; this

can be done due to the bisymmetric nature of NGC 1291. I then smooth the image to further reduce the noise, by Fourier decomposing and recomposing it with the first five even Fourier components, which removes the high frequency noise from the image, while keeping its important features.

4.3.2 The Mass to Light Ratio

To obtain the mass distribution of a spiral galaxy from a two-dimensional image of the surface brightness, we need to assume a M/L (Υ) for the stellar component. For this study I use a fiducial colour corrected $\Upsilon_{3.6\mu m}$.

The M/L for the 3.6μm band is assumed to be $\Upsilon_{3.6\mu m}$=0.6$M_{\odot}/L_{\odot}$, as given by a number of studies both from SPS modelling and from other considerations (Meidt et al., 2014, Röck et al., 2015). The M/L can vary slightly for colour even in the infrared due to dust and late stellar evolution (although less so than for optical wavelengths) and a correction for the dust in a galaxy should be applied. This procedure was done for the sample of over 2000 S^{4}G galaxies by Querejeta et al. (2015b) by using the Independent Component Analysis method which separates the images into the old stellar component and dust. However no such separation was available for NGC 1291 which is too blue ([3.5]-[4.5]$\leq$0) to be passed through the pipeline procedure, and no reliable separation of the image in two maps could be obtained. However we know there is a considerable amount of dust in the central regions from the dust lanes present in the 8 and 24μm images. We therefore assume a fiducial Υ=0.6 which however is colour corrected by combining information from the 3.6 and 4.5μm images, using a formula by Eskew et al. (2012) with a new calibration by Querejeta et al. (2015b) based on a large number of S^{4}G galaxies. The equation for transforming from luminosity to mass is given by,

$$\frac{M_{\star}/M_{\odot}}{L_{3.6}/L_{\odot}} = S_{3.6}^{0.85} \times S_{4.5}^{-0.85} \times 0.316, \tag{4.1}$$

which transforms the images from solar luminosity $L_{\odot}$ to solar masses $M_{\odot}$. This transformation is carried out on a pixel by pixel basis, in order to correct for colour variations due to the dust in the galaxy (for more information the reader is referred to Eskew et al. (2012) and Querejeta et al. (2015b)).

4.3.3 The Height Function

Once the two dimensional surface density distribution is obtained (by dividing the mass in each pixel by the physical area of the pixel), we need to consider the behaviour of the galaxy in the third dimension, i.e. the thickness of the disc. I therefore assume a height function,

which defines how the density drops off as a function of z from the equatorial plane z=0. Combining this with the two-dimensional surface density gives us the three-dimensional density distribution of the model.

The height function and the scaleheight (z_0) smooth out the potential, and we therefore need to use the height function which best approximates that of the galaxy we are trying to model. For example, for galaxies containing a B/P bulge, it was shown in Chapter 2, that the geometry of the B/P height function should be taken into account in order to avoid inducing large errors in the dynamical models.

The density distribution of a galaxy is given by,

$$\rho(x, y, z) = \Sigma(x, y)F(x, y, z), \tag{4.2}$$

where $\Sigma(x, y)$ is the surface density, and F(x, y, z) is the height function of the model. The normalisation of the height function is

$$\int_{-\infty}^{\infty} F(x, y, z)\mathrm{d}z = 1. \tag{4.3}$$

It is worth noting that the mass of the model is always the same; by changing the height function we change the volume density of the galaxy.

The isothermal-sheet model (van der Kruit and Searle, 1981) which we adopt for the "flat disc" cases is given by:

$$F(z) = \frac{1}{2z_0}\mathrm{sech}^2\left(\frac{z}{z_0}\right), \tag{4.4}$$

where $1/(2z_0)$ is the normalisation factor and z_0 is the scaleheight.

The B/P height function is a non-separable function of position and is given by:

$$F(x, y, z) = \frac{1}{2z_0(x, y)}\mathrm{sech}^2\left(\frac{z}{z_0(x, y)}\right), \tag{4.5}$$

where the scaleheight z_0(x,y) varies like the sum of two two-dimensional gaussians:

$$\begin{aligned} z_0(x, y) =& A_{sim}\exp\left(-\left(\frac{(x-x_0)^2}{2\sigma^2}+\frac{(y-y_0)^2}{2\sigma^2}\right)\right)+ \\ & A_{sim}\exp\left(-\left(\frac{(x-x_1)^2}{2\sigma^2}+\frac{(y-y_1)^2}{2\sigma^2}\right)\right)+z_0^{disc}, \end{aligned} \tag{4.6}$$

and A_{sim} is the maximum scaleheight of the peanut above the disc scaleheight, z_0^{disc} and σ^2 is the variance of the gaussians. Parameters (x_0, y_0) give the position of the maximum of the first gaussian and (x_1, y_1) the position of the maximum of the second gaussian.

To obtain an initial set of values for the parameters of the B/P height function, we fitted the parameters such that they reproduce the scaleheight of an isolated galaxy N-body simulation, taken from Athanassoula et al. (2014). In what follows in this chapter, we adopt a fiducial value for the maximum scaleheight of the peanut A_{fid}, which is half that obtained by the fit to the simulated galaxy A_{sim} i.e.,

$$A_{fid} = \frac{A_{sim}}{2} = 0.65\,\mathrm{kpc} \tag{4.7}$$

This is done because the height of the B/P, also known as the strength of the B/P, is known to be correlated with the bar strength (Athanassoula, 2008b) – although there is a large amount of scatter in this relation. The simulated galaxy used to fit the B/P height function (see Chapter 2), develops a very strong bar, stronger than that of NGC 1291. I therefore reduce the strength of the B/P for the model of NGC 1291 to half that used in Chapter 2, since such a strong B/P is not likely to be present in more weakly barred galaxies. Additionally I modify the length of the peanut, i.e. parameters x_0, x_1, y_0 and y_1 such that the maxima of the B/P bulge occur at the end of the barlens of NGC 1291, (i.e. at ± 2 kpc) as was shown to be the case in Athanassoula et al. (2014).

4.3.4 Stellar component potential

The method for calculating the potential (3DF – which has been described in Chapter 2.2), involves a straightforward three-dimensional integration over the density distribution. I calculate the potential in Cartesian coordinates by

$$\begin{aligned}&\Phi(x,y,z) = \\ &-G\int_{-\infty}^{\infty}\int_{-\infty}^{\infty}\int_{-\infty}^{\infty}\frac{\rho(x',y',z')}{\sqrt{\sum_{j=1}^{3}(x'_j - x_j)^2 + \epsilon^2}}\mathrm{d}x'\mathrm{d}y'\mathrm{d}z',\end{aligned} \tag{4.8}$$

where G is Newton's gravitational constant, ρ is the density and ϵ is the softening length which is necessary to eliminate the noise at the expense of a small bias (Merritt, 1996, Athanassoula et al., 2000). The indices of j, from 1 to 3, indicate the x, y and z components respectively.

I differentiate the expression in Eq. 4.8 analytically with respect to x, y and z, to obtain expressions for the the force and its derivatives. The rotation curve of the disc can then be obtained by transforming from Cartesian to cylindrical coordinates and applying the relation,

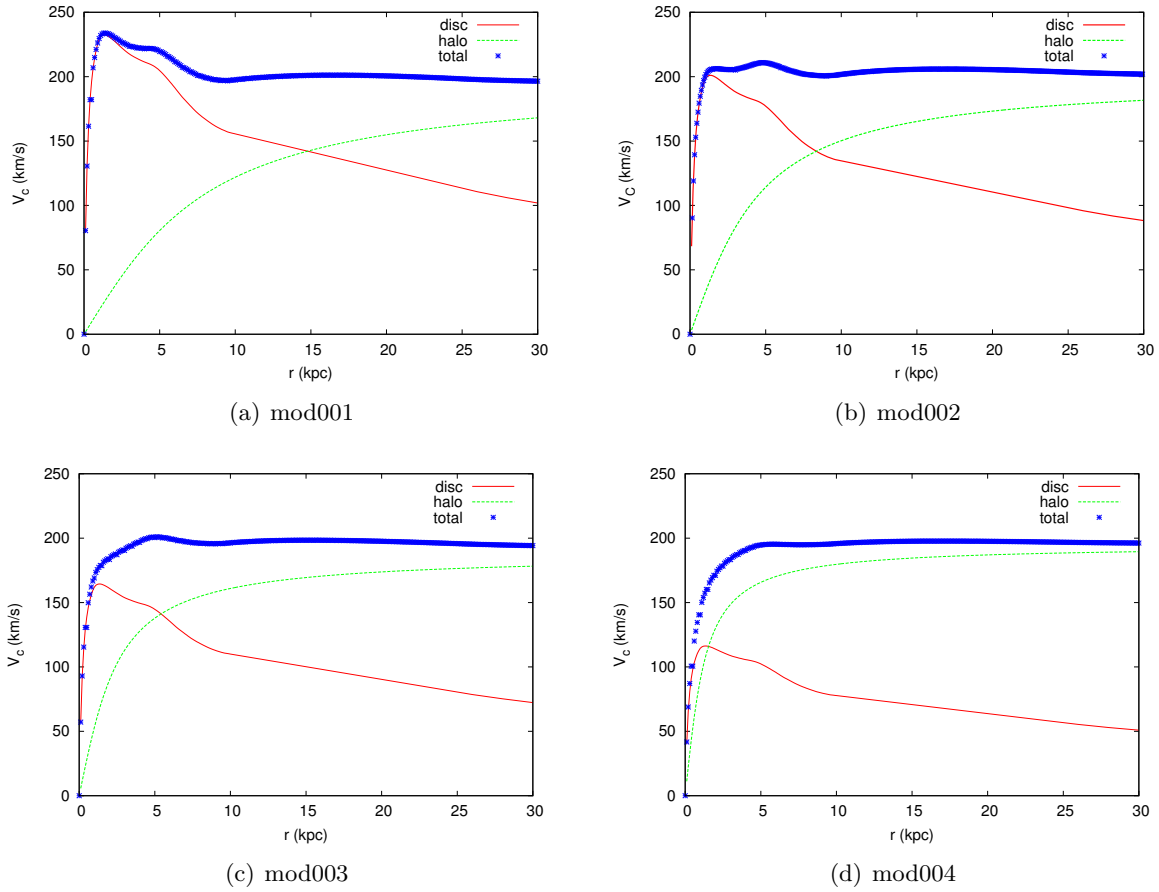

(a) mod001 (b) mod002

(c) mod003 (d) mod004

FIGURE 4.2: Rotation curves for models 001 to 004. The M/L is decreasing from $1\times\Upsilon_{3.6}$ to $0.25\times\Upsilon_{3.6}$ in steps of 0.25.

$$V_c^2 = r\frac{\partial\Phi}{\partial r} \tag{4.9}$$

where V_c is the circular speed, and r is the radius.

4.3.5 Dark matter halo potential

The dark matter halo of the models is obtained by assuming a spherical pseudo-isothermal halo. The parameters of the halo are obtained by adjusting the rotation curve of the galaxy, such that it reproduces the rotation velocity in the outer parts (V_{flat}), as predicted by the Tully-Fisher (TF) relation for NGC 1291. V_{flat} can be obtained either by the luminosity based TF relation for the 3.6μm band (Ponomareva et al. in prep.) or by using the Baryonic Tully Fisher relation (BTFR) (McGaugh et al., 2000, McGaugh, 2012). Both relations give the same result for V_{flat} to within a few km/s. To obtain V_{flat} I calculate the total baryonic mass, by obtaining the stellar mass using the fiducial M/L described in Section 4.3.2, and assuming that the gas mass is negligible compared to the stellar mass (for NGC 1291 the gas mass of HI

is of the order of 2% of the stellar mass, while the hot gas mass is even less (Bregman et al., 1995)). I therefore obtain a circular velocity in the outer flat part of the rotation curve of V_{flat} = 200 km/s.

I use this value to construct the rotation curves for the galaxy, since due to the galaxy being practically face-on, it is not possible to construct a rotation curve from HI data, since the errors will be very large. Examples of the rotation curves used for models 1-4 can be seen in Figure 4.2, where the M/L ranges from 1 to 0.25 times the fiducial $\Upsilon_{3.6}$.

The density of the pseudo-isothermal halo is given by,

$$\rho(r) = \rho_c \Big[1 + \Big(\frac{r}{r_c}\Big)^2\Big]^{-1} \tag{4.10}$$

where r_c, the core radius, and ρ_c, the central density, are adjusted such that V_{flat}=200 km/s. The circular velocity at a given radius r, is given by,

$$V(r) = V_\infty \Big[1 - \frac{r_c}{r}\arctan\Big(\frac{r}{r_c}\Big)\Big]^{1/2} \tag{4.11}$$

where V_∞ is the circular velocity at infinity.

4.3.6 Varying the parameters

The goal of this work is to explore the parameter space for the three free parameters of the models, i.e. the disc M/L, the Lagrangian radius and the height function of the disc by running gas response simulations, as those described in Chapter 3. I then aim to obtain the best fit between the gas density enhancements in the simulations to the morphology of the dust lanes of NGC 1291. In this subsection I describe how each of the free parameters is varied in order to explore the parameter space.

In total I ran approximately 250 models, which are listed in Table 4.2 to 4.7. In addition to running models for different combinations of the three main free parameters, I also ran models without a dark matter halo (discussed in Section 4.5.4) and a model without a nuclear bar in order to determine the effects of the nuclear bar on the morphology of the gas shocks (discussed in Section 4.6.1).

The Mass-to-Light ratio

The fiducial value of the stellar M/L (Υ) is calculated as explained in Section 4.3.2. I then change this value, by assuming different fractions of the fiducial $\Upsilon_{3.6}$ according to,

$$\Upsilon = f_d \Upsilon_{3.6}, \tag{4.12}$$

where f_d takes on values between 0.25 and 1.75 in steps of 0.25. I then re-calculate the disc rotation curve of the galaxy each time and add a dark matter halo with parameters such that the rotation curve in the outer parts of the galaxy matches the value predicted by the TF relation, as shown in Figure 4.2.

There are constraints on the upper limits of the value of the M/L from the accepted range of values for V_{max}, obtained from the TF relation. If M/L is too high then V_{max} will be higher than the values allowed by the scatter in the TF relation. I use the relation by Ponomareva et al. (in prep.) in order to calculate the allowed range of values in V_{max}. For NGC 1291 the maximum value of the velocity is 222 km/s, with a scatter in log scale of 0.11 which gives an uncertainty of 18-19 km/s for the value of V_{flat}. Therefore models which give a $V_{max} \geq$ 240 km/s are deemed as unphysical, which helps constrain the allowed parameter space, as will be further discussed in more detail in Section 4.5.6.

The Lagrangian radius

The Lagrangian radius is the distance from the centre of the galaxy to the L_1 (or L_2) which are the locations at which the forces in the rotating frame of reference are exactly zero. It gives the radius at which, in the rotating frame of reference, the stars in the disc rotate at the same speed as the bar, and is an equivalent to the corotation radius for a weak bar case. Therefore by varying the Lagrangian radius while keeping all the other parameters of a model constant, we effectively vary the pattern speed of the bar.

I vary this value between 1.8 and 1. times the bar semi-major axis r_B, i.e. r_L=$\mathcal{R}$ r_B, where 1≤$\mathcal{R}$≤1.8. There are theoretical arguments which show that self consistent bars cannot have a corotation radius smaller than the bar length (Contopoulos, 1980, Athanassoula, 1980), i.e. $\mathcal{R}$ cannot be smaller than 1. On the other hand, what controls the upper limit of the Lagrangian radius, is the angular momentum transfer in the galaxy; due to the fact that angular momentum is a conserved quantity, whatever angular momentum is emitted by the bar, must be absorbed by the outer disc and halo (Athanassoula, 2003). Therefore the slow-down of the bar will depend on the amount of resonant material available which is able to absorb angular momentum from the inner parts of the discs; we see therefore that the speed at which the bar rotates can gives us valuable information on the dynamical state of the galaxy.

Previous studies of the shape of dust lanes in gas response simulations have set limits to $\mathcal{R}$, placing the corotation radius r_L=1.2±0.2r_B (Athanassoula, 1992b), however there is still no consensus in the literature regarding the value of $\mathcal{R}$ (Corsini, 2011). Bars in general are separated into fast and slow rotating according to the criteria $\mathcal{R} \leq 1.4$ and $\mathcal{R} > 1.4$ respectively (Debattista and Sellwood, 2000); we therefore vary $\mathcal{R}$ in this study between 1≤$\mathcal{R}$≤1.8 in order to explore whether bars rotate fast or slow.

The height function

I vary the height function of the disc by assuming different height functions and scaleheights, from an isothermal thin disc to a thick disc, with scaleheights of $z_0 = 0.5$ and 2.3 kpc respectively, while also creating models with scaleheights in between these two values.

Kregel et al. (2002) find that 90% of the spiral galaxies in their sample have scaleheight $<$ 0.6 kpc which is why I adopt 0.5 kpc as an approximate lower limit for the scaleheight of the disc. Additionally, from inspecting the rotation curve of the disc of NGC 1291, for models with $z_0 \leq 0.5$, the maximum velocity V_{max}, becomes too large, and overshoots the value predicted by the TF; thus models with thinner discs than 0.5 kpc are unrealistic for NGC 1291.

de Grijs (1998) determined the ratio of the scalelength to the scaleheight, h_r/z_0, for a sample of edge-on galaxies of different morphological types, using K-band data for some galaxies, and i-band data for others. According to their findings, for galaxies of type SB0/a (such as NGC 1291), the value of h_r/z_0=2-2.5; the scalelength of NGC 1291 is obtained from photometric decompositions (Bosma et al., 2010) using the BUDDA code (Gadotti, 2008) and is found to be h_r=5.8 kpc, which therefore leads to a value of z_0=2.3 kpc, according to the findings from de Grijs (1998). I use this as an upper limit on the scaleheight of the disc, since this value seems large if one considers other observational studies of the thickness of discs (e.g. Kregel et al. (2002)). From Figure 6b in Kregel et al. (2002), we find that for NGC 1291 a value of z_0 in the range of 1.2-1.4 kpc (note that in Kregel et al. (2002) they use h_z, the exponential scaleheight which is equal to $z_0/2$.).

I also explore the effect of adding a B/P bulge on the gas flows, since it is possible that NGC 1291 contains a B/P due to the presence of what appears to be a barlens (Laurikainen et al., 2014, Athanassoula et al., 2014). I explore the effects of two types of B/P bulges, one with a length which extends to ±2kpc along the bar, and one which extends to ±1.5 kpc along the bar. The maximum height of the B/P depends on the scaleheight of the disc (as can be seen in Equation 4.6), and is given by $A+z_0$ kpc, where A=0.65 kpc is the height of the B/P above the disc and z_0 is the scaleheight of the disc (for more details see Section 4.3.3).

4.4 Comparing the models to the observations

Below I describe the two methods used for comparing the models to the observations, as well as the criteria which are defined in order to determine the model which best reproduces the locations of the dust lanes in NGC 1291.

Model	z_0	M/L	$\mathcal{R}$	Ω_b	ρ_c $(\times 10^8)$	r_c	Δl
1	0.8	100	1.2	46.8	2E+07	6	0.18
2	0.8	75	1.2	42.5	6E+07	3.5	0.09
3	0.8	50	1.2	41.8	1.8E+08	1.9	0.8
4	0.8	25	1.2	39.9	7E+08	1	0.9
5	0.8	100	1.6	32.5	2E+07	6	0.63
6	0.8	100	1.4	38.65	2E+07	6	0.45
7	0.8	100	1	55.1	2E+07	6	0.27
8	0.8	100	0.8	66.6	2E+07	6	1.25
9	0.8	75	1.6	31.9	6E+07	3.5	0.4
10	0.8	75	1.4	37.3	6E+07	3.5	0.18
11	0.8	75	1	51.75	6E+07	3.5	0.63
12	0.8	75	0.8	61.85	6E+07	3.5	0.36
13	0.8	50	1.6	30.6	1.8E+08	1.9	0.089
14	0.8	50	1.4	35.45	1.8E+08	1.9	0.27
15	0.8	50	1.0	48.7	1.8E+08	1.9	0.54
16	0.8	50	0.8	58.1	1.8E+08	1.9	0.18
17	0.8	25	1.6	29.85	7E+08	1	0.99
18	0.8	25	1.4	34.15	7E+08	1	0.34
19	0.8	25	1.0	46.75	7E+08	1	0.36
20	0.8	25	0.8	56.17	7E+08	1	0.6
21	0.5	150	1.2	56.75	9.1E+06	9	0.44
22	0.5	125	1.2	52	9.1E+06	9	0.4
23	0.5	100	1.2	46.95	1E+07	8.5	0.36
24	0.5	75	1.2	44.65	4.6E+07	4	0.18
27	1.5	150	1.2	52	1.3E+07	7	0.27
28	1.5	125	1.2	48.45	1.85E+07	6	0.37
29	1.5	100	1.2	44.7	2.7E+07	5	0.26
30	1.5	75	1.2	42	5.7E+07	3.5	0.72
31	1.5	50	1.2	43.65	6.7E+08	1	0.9
32	0.8BP	150	1.2	54.4	1.1E+07	8	0.09
33	0.8BP	125	1.2	50.45	1.5E+07	7	0.006
34	0.8BP	100	1.2	46.1	2E+07	6	0.006
35	0.8BP	75	1.2	42.3	3.6E+07	4.5	0.006
36	0.8BP	50	1.2	41.9	1.8E+08	2	0.16
38	0.5BP	150	1.2	56.2	1.1E+07	8	0.36
39	0.5BP	125	1.2	52	1.5E+07	7	0.27
40	0.5BP	100	1.2	47.5	2E+07	6	0.09
41	0.5BP	75	1.2	44.15	4.6E+07	4	0.09
43	0.5BP	25	1.2	40.87	7.4E+08	1	0.26
44	0.8BP	100	1.8	27.7	2E+07	6	0.9

TABLE 4.2: Table of models used in this study. From left to right the columns denote: the model name, the scaleheight z_0 in kpc, the M/L in fractions of $\Upsilon_{3.6}$, $\mathcal{R}$ which is r_L/r_B, the bar pattern speed in km/s/kpc, the core density of the dark matter halo (in $10^8 M_\odot$), the core radius of the halo in kpc and Δl the distance between the primary shock and the dust lane in the images. In the second column, whenever the scaleheight of the model is followed by BP, a B/P height function has been added to the model; the maximum height of the peanut is given by z_0+0.65 kpc where z_0 is the disc scaleheight; the length of the B/P is ±2 kpc along the bar major axis. If the scaleheight is followed by BPx1.5, the model has a B/P height function, with the same maximum as in the BP case, but with a length which extends to ±1.5 kpc along the bar major axis.

Model	z_0	M/L	$\mathcal{R}$	Ω_b	ρ_c $(\times 10^8)$	r_c	Δl
45	0.8BP	100	1.6	32.35	2E+07	6	0.6
46	0.8BP	100	1.4	38.45	2E+07	6	0.36
47	0.8BP	100	1.0	53.4	2E+07	6	0.08
48	0.8BP	100	0.8	63.6	2E+07	6	0.34
49	0.5BP	50	1.3	39.15	1.8E+08	2	0.09
50	0.5BP	50	1.4	36.2	1.8E+08	2	0.43
51	0.8BP	50	1.3	38.75	1.8E+08	2	0.1
52	0.8BP	50	1.4	35.85	1.8E+08	2	0.34
53	0.5BP	50	1.5	33.5	1.8E+08	2	
54	2.3	150	1.2	48.5	9E+06	9	0.9
55	2.3	125	1.2	45.3	1.5E+07	7	0.81
57	2.3	75	1.2	40	5.7E+07	3.5	0.54
58	2.3	50	1.2	40.9	3.1E+08	1.5	0.72
59	2.3	100	1.8	26.55	2E+07	6	0
60	2.3	100	1.6	30.4	2E+07	6	0.36
61	2.3	100	1.4	35.4	2E+07	6	1.17
63	2.3	100	0.8	58.1	2E+07	6	0.18
65	0.8BP x1.5	125	1.2	50.5	1.5E+07	7	0.8
66	0.8BP x1.5	100	1.2	46.15	2E+07	6	0.9
68	0.8BP x1.5	50	1.2	41.9	1.8E+08	2	0.14
69	0.8BP x1.5	25	1.2	40.1	7.2E+08	1	0.2
70	0.8BP x1.5	100	1.5	35.125	2E+07	6	
71	0.8BP x1.5	100	1.4	38.45	2E+07	6	0.18
72	0.8BP x1.5	100	1.3	42.1	2E+07	6	
73	0.8BP x1.5	100	1.1	50.1	2E+07	6	
74	0.8BP x1.5	100	1.0	53.65	2E+07	6	0.54
75	2.3	75	1.8	26.45	5.7E+07	3.5	0.45
76	2.3	75	1.6	29.95	5.7E+07	3.5	0.09
77	2.3	75	1.4	34.5	5.7E+07	3.5	1.17
78	2.3	75	1.0	46.3	5.7E+07	3.5	1.25
79	2.3	75	0.8	54.75	5.7E+07	3.5	0.72
80	2.3	50	1.8	27.3	3.1E+08	1.5	1.25
81	2.3	50	1.6	30.95	3.1E+08	1.5	0.72
82	2.3	50	1.4	35.35	3.1E+08	1.5	1.08
83	2.3	50	1.0	47.6	3.1E+08	1.5	0.27
84	2.3	50	0.8	56.6	3.1E+08	1.5	0.09
85	2.3	125	1.8	28.35	1.5E+07	7	0.36
86	2.3	125	1.6	32.6	1.5E+07	7	0.36
87	2.3	125	1.4	38.3	1.5E+07	7	0.36
88	2.3	125	1.0	53.15	1.5E+07	7	0.54
89	2.3	125	0.8	63.85	1.5E+07	7	0.27
90	2.3	150	1.8	29.66	9E+06	9	0.54
91	2.3	150	1.6	34.4	9E+06	9	0.27
92	2.3	150	1.4	40.7	9E+06	9	0.36
93	2.3	150	1.0	57.12	9E+06	9	0.63
94	2.3	150	0.8	68.95	9E+06	9	0.36

TABLE 4.3: Models (continued)

Model	z_0	M/L	$\mathcal{R}$	Ω_b	ρ_c $(\times 10^8)$	r_c	Δl
104	0.8	100	1.8	27.8	2E+07	6	0.81
105	0.8	100	2.0	24.65	2E+07	6	
106	0.8	25	1.8	26.35	7E+08	1	0.36
107	0.8	125	1.2	51.15	1.5E+07	7	0.3
108	0.8	150	1.2	55.25	1.1E+07	8	0.36
109	0.8	125	1.4	42.15	1.5E+07	7	0.54
110	0.8	125	1.6	34.92	1.5E+07	7	0.7
111	0.8	125	1.8	29.75	1.5E+07	7	1
112	0.8	125	1.0	60.53	1.5E+07	7	0.18
113	0.8	125	0.8	73.55	1.5E+07	7	1.17
114	0.8	150	1.4	45.25	1.1E+07	8	0.5
115	0.8	150	1.6	37.28	1.1E+07	8	0.9
116	0.8	150	1.8	31.56	1.1E+07	8	0.36
117	0.8	150	1.0	65.55	1.1E+07	8	0.09
118	0.8	150	0.8	79.95	1.1E+07	8	0.7
119	0.8	50	1.8	26.8	1.8E+08	1.9	0.3
120	0.8	75	1.8	27.7	6E+07	3.5	0.6
121	2.3	25	1.8	27.6	2.9E+09	0.5	0.36
122	2.3	25	1.6	31.15	2.9E+09	0.5	0.8
123	2.3	25	1.4	35.7	2.9E+09	0.5	0.63
124	2.3	25	1.2	41.5	2.9E+09	0.5	0.99
125	2.3	25	1.0	49.05	2.9E+09	0.5	0.2
126	2.3	25	0.8	59.8	2.9E+09	0.5	1.25
127	08BP	125	1.8	29.65	1.5E+07	7	0.99
128	08BP	125	1.6	34.75	1.5E+07	7	0.7
129	08BP	125	1.4	41.8	1.5E+07	7	0.4
130	08BP	125	1.0	58.6	1.5E+07	7	0.09
131	08BP	125	0.8	69.85	1.5E+07	7	1.34
132	08BP	75	1.8	26.4	3.6E+07	4.5	0.6
133	08BP	75	1.6	30.35	3.6E+07	4.5	0.4
134	08BP	75	1.4	35.7	3.6E+07	4.5	0.09
135	08BP	75	1.0	48.7	3.6E+07	4.5	0.63
136	08BP	75	0.8	57.3	3.6E+07	4.5	0.36
137	08BPx1.5	125	1.8	29.65	1.5E+07	7	0.81
138	08BPx1.5	125	1.6	34.75	1.5E+07	7	0.54
139	08BPx1.5	125	1.4	41.8	1.5E+07	7	0.27
140	08BPx1.5	125	1.0	58.9	1.5E+07	7	0.54
141	08BPx1.5	125	0.8	69.65	1.5E+07	7	0.45
142	08BPx1.5	100	1.8	27.7	2E+07	6	0.72
143	08BPx1.5	100	1.6	32.2	2E+07	6	0.45
144	08BPx1.5	100	0.8	63.2	2E+07	6	0.36
145	08BPx1.5	75	1.8	26.4	3.6E+07	4.5	0.45
146	08BPx1.5	75	1.6	30.35	3.6E+07	4.5	0.27
147	08BPx1.5	75	1.4	35.7	3.6E+07	4.5	1.08
148	08BPx1.5	75	1.0	48.85	3.6E+07	4.5	0.45
149	08BPx1.5	75	0.8	57.1	3.6E+07	4.5	0.27

TABLE 4.4: Models (continued)

Model	z_0	M/L	$\mathcal{R}$	Ω_b	ρ_c $(\times 10^8)$	r_c	Δl
401	0.5	150	1.8	31.6	9.1E+06	9	1.25
402	0.5	150	1.6	37.55	9.1E+06	9	1
403	0.5	150	1.4	46	9.1E+06	9	0.63
404	0.5	150	1.0	67.35	9.1E+06	9	0.3
405	0.5	150	0.8	82.15	9.1E+06	9	0.19
412	0.5	125	1.8	29.15	9.1E+06	9	1.24
413	0.5	125	1.6	34.6	9.1E+06	9	0.8
414	0.5	125	1.4	42.3	9.1E+06	9	0.72
415	0.5	125	1.0	61.7	9.1E+06	9	0.27
416	0.5	125	0.8	75.2	9.1E+06	9	1.08
417	0.5	100	1.8	26.7	1E+07	8.5	0.99
418	0.5	100	1.6	31.5	1E+07	8.5	0.81
419	0.5	100	1.4	38.3	1E+07	8.5	0.54
420	0.5	100	1.0	55.55	1E+07	8.5	0.18
421	0.5	100	0.8	67.55	1E+07	8.5	1.08
422	0.5	75	1.8	27.25	4.6E+07	4	0.81
423	0.5	75	1.6	31.4	4.6E+07	4	0.54
424	0.5	75	1.4	37.25	4.6E+07	4	0.36
425	0.5	75	1.0	52.15	4.6E+07	4	0
426	0.5	75	0.8	62.45	4.6E+07	4	1.3
427	0.5	50	1.8	26.9	1.7E+08	2	0.45
428	0.5	50	1.6	30.7	1.7E+08	2	0.27
429	0.5	50	1.4	35.9	1.7E+08	2	0.08
430	0.5	50	1.0	49.5	1.7E+08	2	0.54
431	0.5	50	0.8	58.9	1.7E+08	2	0.81
432	05BP	150	1.8	31.6	1.1E+07	8	1.16
433	05BP	150	1.6	37.55	1.1E+07	8	0.98
434	05BP	150	1.4	46	1.1E+07	8	0.63
435	05BP	150	1.0	67.35	1.1E+07	8	0.9
436	05BP	150	0.8	82.15	1.1E+07	8	1.17

TABLE 4.5: Models (continued)

4.4.1 Location of shocks along slits

The first method I use throughout this study involves a quantitative measure of the difference between the location of the shocks in the model and the locations of the dust lanes in the observational images, denoted Δl.

I place pseudo-slits perpendicular to the shock loci in both the gas flow simulations and the observed image, where the modelled gas flow is rotated to match the orientation of the observed image. As shown in Figure 4.3 we trace the density jumps along the slit, where the maxima in the density indicate the location of the shocks. The location of the shocks in the simulation and observations are then compared, and the distance between these two values is Δl. I place

Model	z_0	M/L	$\mathcal{R}$	Ω_b	ρ_c $(\times 10^8)$	r_c	Δl
501	1.5	75	1.8	27	5.7E+07	3.5	0.27
502	1.5	75	1.6	30.75	5.7E+07	3.5	0.36
503	1.5	75	1.4	35.85	5.7E+07	3.5	1.17
504	1.5	75	1.0	48.8	5.7E+07	3.5	0.45
505	1.5	75	0.8	58.1	5.7E+07	3.5	0.18
506	1.5	50	1.8	28.25	6.7E+08	1	0.36
507	1.5	50	1.6	32.18	6.7E+08	1	0.18
508	1.5	50	1.4	37.25	6.7E+08	1	1.34
509	1.5	50	1.0	51.3	6.7E+08	1	0.45
510	1.5	50	0.8	62	6.7E+08	1	0.19
511	1.5BP	75	1.8	26.9	5.7E+07	3.5	0.18
512	1.5BP	75	1.6	30.62	5.7E+07	3.5	0.4
513	1.5BP	75	1.4	35.52	5.7E+07	3.5	1.1
514	1.5BP	75	1.2	41.5	5.7E+07	3.5	0.7
515	1.5BP	75	1.0	47.8	5.7E+07	3.5	0.5
516	1.5BP	75	0.8	56.2	5.7E+07	3.5	0.08
517	1.5BP	50	1.8	28.2	6.7E+08	1	0.36
518	1.5BP	50	1.6	32.1	6.7E+08	1	1.17
519	1.5BP	50	1.4	37.1	6.7E+08	1	1.17
520	1.5BP	50	1.2	43.35	6.7E+08	1	0.9
521	1.5BP	50	1.0	50.65	6.7E+08	1	0.45
522	1.5BP	50	0.8	60.7	6.7E+08	1	0.99
523	1.5	100	1.8	27.75	2.7E+07	5	0.45
524	1.5	100	1.6	32	2.7E+07	5	0.36
525	1.5	100	1.4	37.67	2.7E+07	5	0.27
526	1.5	100	1.0	52.45	2.7E+07	5	0.63
527	1.5	100	0.8	63	2.7E+07	5	0.36
528	1.5	125	1.8	29.4	1.85E+07	6	0.63
529	1.5	125	1.6	34.125	1.85E+07	6	0.45
530	1.5	125	1.4	40.5	1.85E+07	6	0.18
531	1.5	125	1.0	57.1	1.85E+07	6	0.54
532	1.5	125	0.8	69	1.85E+07	6	1.3
533	1.5	150	1.8	31	1.3E+07	7	0.8
534	1.5	150	1.6	36.25	1.3E+07	7	0.54
535	1.5	150	1.4	43.3	1.3E+07	7	0.09
536	1.5	150	1.0	61.55	1.3E+07	7	0.7
537	1.5	150	0.8	74.7	1.3E+07	7	1.3

TABLE 4.6: Models (continued)

Model	z_0	M/L	$\mathcal{R}$	Ω_b	ρ_c $(\times 10^8)$	r_c	Δl
601	0.8	125	1.8	26.8	-	-	1.16
602	0.8	125	1.6	32.25	-	-	0.99
603	0.8	125	1.4	39.75	-	-	0.54
604	0.8	125	1.2	49.05	-	-	0.27
605	0.8	125	1.0	58.65	-	-	0.09
606	0.8	125	0.8	71.95	-	-	0.6
607	0.8	100	1.8	24	-	-	1.2
608	0.8	100	1.6	28.85	-	-	0.8
609	0.8	100	1.4	35.55	-	-	0.54
610	0.8	100	1.2	43.85	-	-	0.27
611	0.8	100	1.0	52.45	-	-	0.18
612	0.8	100	0.8	64.35	-	-	0.99
613	0.8	75	1.8	20.8	-	-	0.99
614	0.8	75	1.6	25	-	-	0.72
615	0.8	75	1.4	30.8	-	-	0.4
616	0.8	75	1.2	38	-	-	0.18
617	0.8	75	1.0	45.4	-	-	0.36
618	0.8	75	0.8	55.7	-	-	0.99
620	0.5	100	1.8	24.2	-	-	1.34
621	0.5	100	1.6	29.25	-	-	0.99
622	0.5	100	1.4	36.4	-	-	0.54
623	0.5	100	1.2	45.3	-	-	0.36
624	0.5	100	1.0	54.1	-	-	0.27
625	1.5	100	1.8	23.35	-	-	0.81
626	1.5	100	1.6	27.75	-	-	0.54
627	1.5	100	1.4	33.7	-	-	0.09
628	1.5	100	1.2	41.05	-	-	0.36
629	1.5	100	1.0	49	-	-	0.45
630	2.3	100	1.8	22.55	-	-	0.45
631	2.3	100	1.6	26.6	-	-	0.09
632	2.3	100	1.4	31.9	-	-	0.36
633	2.3	100	1.2	38.4	-	-	0.9
634	2.3	100	1.0	45.55	-	-	0.54

TABLE 4.7: Models (continued)

the slit at a location such that the shock is captured in both the 8 and 24μm images. This method provides a quantitative measure of the goodness of fit between the model and the observations. However, as we are not only interested in the location of the shocks, but also in the shape of the shocks, a visual inspection is still necessary for an adequate comparison between the models and the observations.

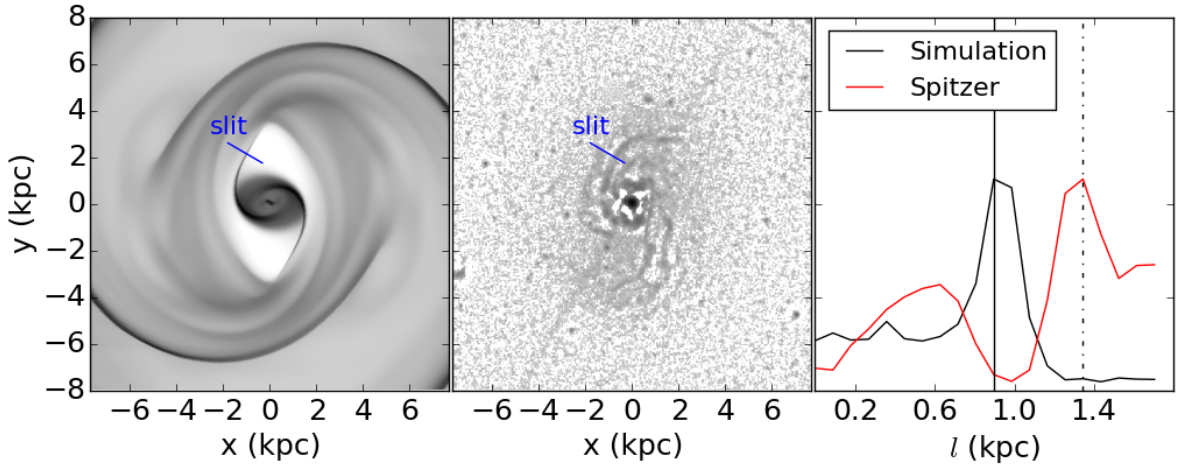

FIGURE 4.3: Comparison between the location of the shocks in the models and the observations. A pseudo-slit is placed along the shock in the simulation (left) and the observed unsharp masked 8μm image (middle). In the rightmost panel we show the density along the slit in the two images as a function of distance l along the slit. The solid vertical line shows the location of the shock in the simulation and the dash-dotted vertical line shows the location of the shock in the observed images.

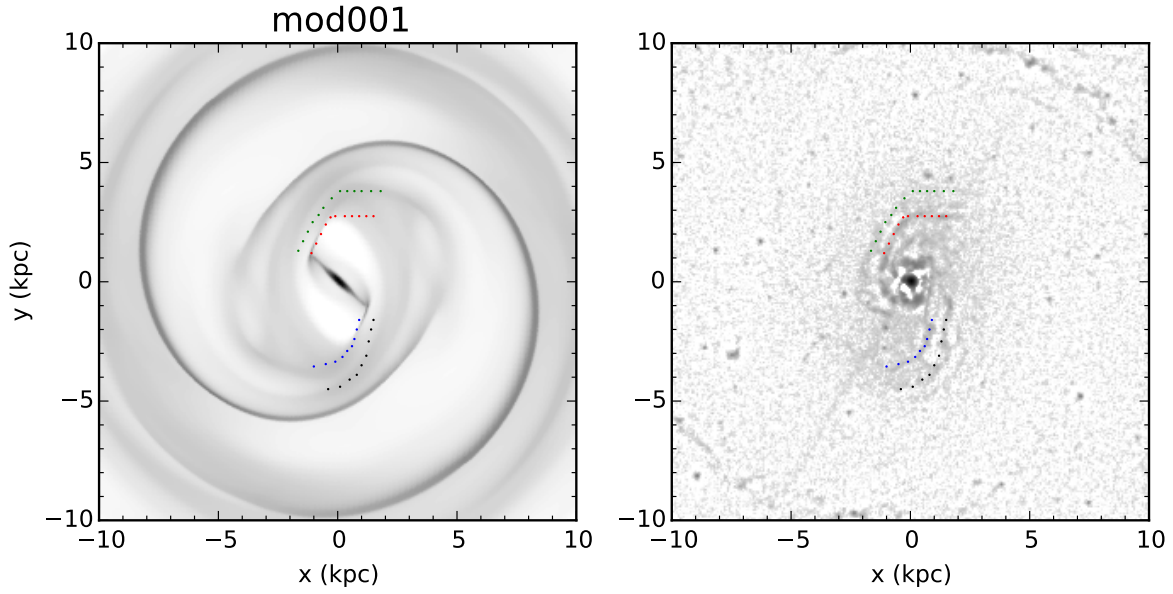

FIGURE 4.4: Example of how we carry out visual comparison between the models and the observed image. The shocks which can be seen in the 8μm image are over plotted with coloured dots on both images (colours correspond to the same shock in both images).

4.4.2 Visual inspection

For a visual inspection of the models, I create two-dimensional plots of the gas density for the models, and add markings which indicate the location of the shocks from the 8 and 24μm image as can be seen in Figure 4.4. The aim is to fit the primary dust lane, which is denoted by the red and blue dots for the upper and lower part of the galaxy respectively. The green and black dots denote secondary shock enhancements and are used as a secondary measurement of the goodness of fit. An additional important point to note, is that although the dust lanes in the galaxy are not symmetric, the model is symmetric by construction, since we only use even Fourier modes when constructing the potential; therefore it is not necessary that both sides fit the observations. This method is used as a second measure of the goodness of fit, after the best fits from a suite of models are determined using the first method described above. Once the best fit models are determined by the minima of Δl, then a visual inspection is applied to the image, and I apply the criteria of Section 4.4.3 in order to determine the quality of the fit.

4.4.3 Criteria for the best fit model

I set some criteria which are used to determine whether a given model fits the observed dust lanes, and which are used in Sections 4.5.5, 4.5.6 and 4.5.7 in order to determine the best fit models:

1. The location of the primary shocks should be as close as possible to the dust lanes in the image.
2. The model should have a *dominant* strong shock, i.e. there should be one shock which is stronger than any secondary shocks formed in the gas flow.
3. The shape of the shocks should match the dust lanes in the 8μm image and should also reproduce features in the 24μm image.

Criterium 1 is checked using method 1 for determining the locations of the shocks. For criteria 2, method 1 can also be used in order to examine the density contrast along the pseudo-slit, while this can be confirmed with a visual inspection; for criterium 3 I carry out a visual inspection.

In Sections 4.5.5 and 4.5.6 I use method 1 to create contour plots of Δl for the various models. Then, from the regions in this contour plots which have the smallest value for Δl, I visually compare the models in order to examine whether they fulfil criteria 2 & 3.

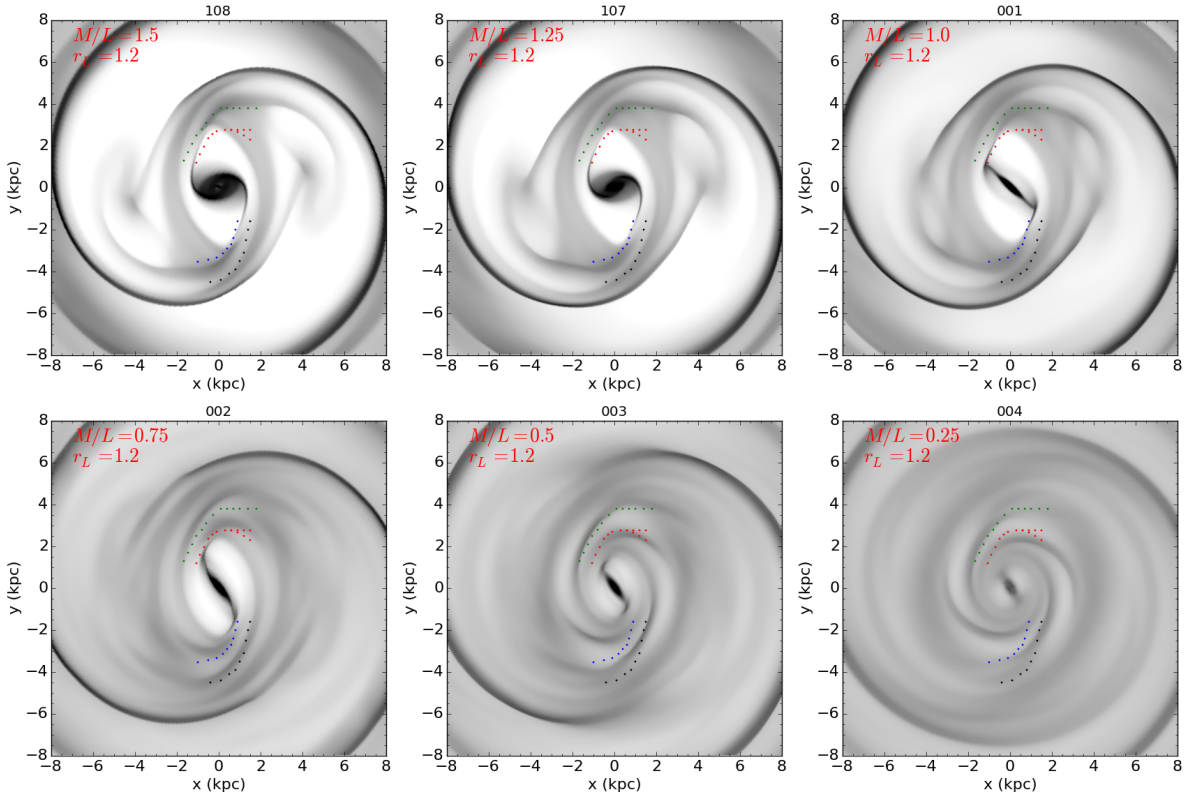

FIGURE 4.5: The gas response to models with different M/L: The M/L decreases from top left to bottom right from 1.5 to $0.25\Upsilon_{3.6}$ (the value is given in the top left corner of the plots). The rest of the parameters are the same for each model, namely the height function is an isothermal disc with scaleheight z_0=0.8 and Lagrangian radius r_L=1.2r_B (the value of r_L is given in the top left corner of the plot in units of r_B.)

4.5 Results

In this section I present results from the approximately 250 gas dynamical simulations which were run for this study. In the next three subsections I present some general trends that can be observed in the gas flows when changing the M/L (Section 4.5.1), the Lagrangian radius (Section 4.5.2) and the height function (Section 4.5.3). In Section 4.5.4 I present results on a suite of models without a dark matter halo. I then present some global results on a number of suites of models, where each suite is for a given height function with varying values of the M/L and Lagrangian radius (Section 4.5.5). Due to the strong degeneracies between the different parameters in the models, in Section 4.5.6 I introduce some additional constraints in the modelling, in order to reduce the allowed parameter space. Finally, in Section 4.5.7 I present some of the best fit models to the morphologies of the dust lanes.

4.5.1 Effect of M/L

Decreasing the M/L of the stellar disc of the model has a significant impact on the strength and shape of the shocks formed in the gas. By reducing the M/L, and accordingly increasing the contribution of the dark matter halo in order to match the outer parts of the rotation curve with that predicted by the TF relation, we effectively reduce the non-axisymmetric perturbation in the model, and increase the axisymmetric component. The strength of the non-axisymmetric component determines the strength of the shocks, since by reducing the bar potential we effectively grow the x_2 family of periodic orbits and the gas tends to stay on more circular orbits. The effect of reducing the M/L on the gas flow can be seen in Figure 4.5, where I decreases the M/L from 1.5 to 0.25 $\times\Upsilon_{3.6}$ in steps of 0.25.

By decreasing the M/L the shocks become progressively weaker, and the shape of the shocks becomes rounder. Additionally the amount of gas present in the bar region increases since the bar is not strong enough to deplete the gas there. We can use this change in the morphology of the shocks in order to place a lower limit on the M/L, below which the shocks become too round to accurately reproduce the observations. An upper limit on the M/L is also set by the shape of the shocks, as well as by the shape of the rotation curve and by the V_{max}, predicted by the TF relation.

4.5.2 Effect of Lagrangian radius

By changing the pattern speed of the bar, the location of the corotation (or more accurately, the Lagrangian) radius in the disc changes. There are lower limits placed on the allowed values of corotation from theory, since it is thought that self consistent bars cannot extend beyond corotation (Contopoulos, 1980, Athanassoula, 1980). However, in principle, the corotation radius can be much larger than the bar. In Figure 4.6, I show the effect of changing the Lagrangian radius while leaving all other parameters in the models the same. By increasing the Lagrangian radius, i.e. reducing the pattern speed of the bar, the distance of the shocks from the centre of the bar increases in accordance with previous results in the literature (Athanassoula, 1992b, Sánchez-Menguiano et al., 2015), while the shocks formed at the leading edge of the bar are also stronger.

I place a pseudoslit perpendicular to the shocks in order to observe the density along the slit, as described in Section 4.4.1. We show plots of the density along the slit in the second and fourth rows of Figure 4.6, for the model and the 8μm image; the plots correspond to the model on their left. We see that the shocks in the gas are farther away from the dust lanes for models with slower bars (larger Lagrangian radius), while the shocks in the gas approach the location of the dust lanes as the pattern speed is increased. For very high pattern speeds

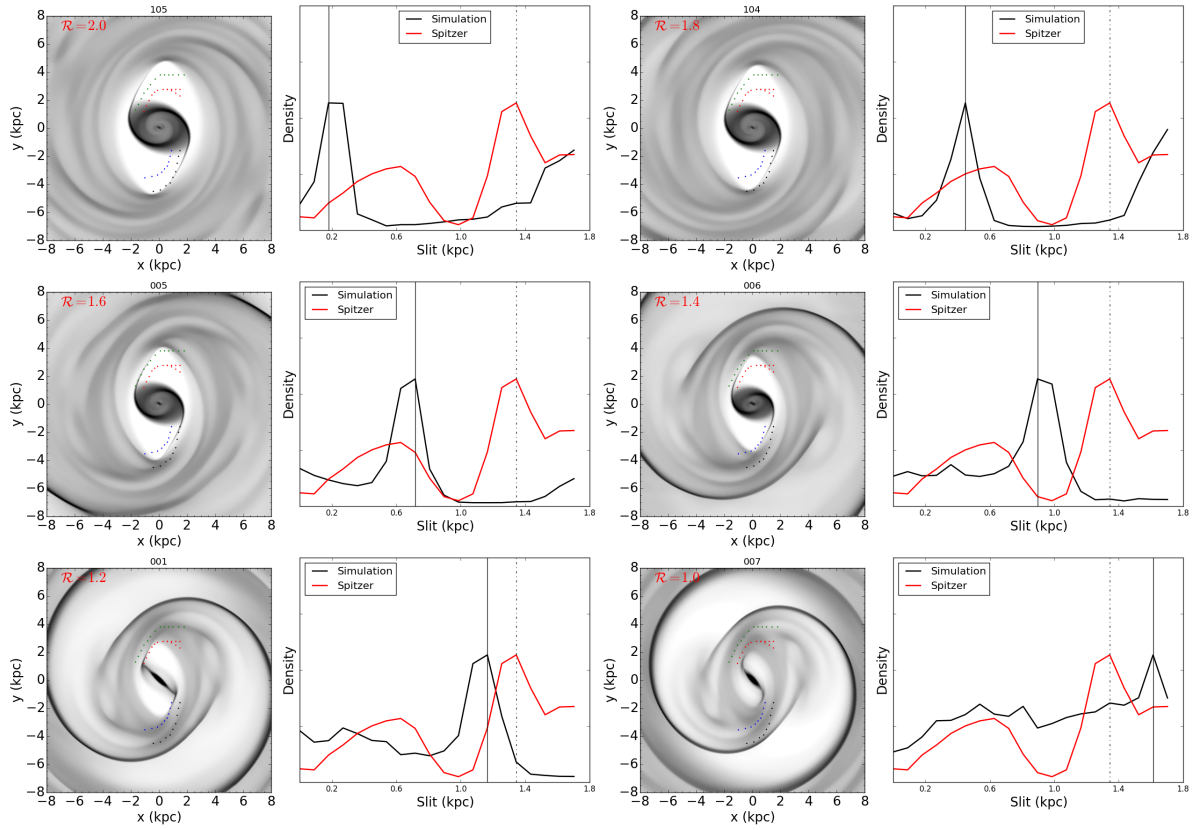

FIGURE 4.6: The gas response to models with different Lagrangian radii: We plot models with decreasing Lagrangian radius (increasing pattern speed) where the value $\mathcal{R}=r_L/r_B$, i.e. the ratio of the Lagrangian to bar radius, is noted in the upper left corner of the surface density plots. We place a slit perpendicular to the shocks in order to observe the density along the slit. In the second and fourth columns we plot the density along the slit for both the model and the 8μm image; I show the locations of the shocks for the model (solid vertical line) and the location of the dust lanes in the 8μm image (dot-dashed vertical line).

the shocks move towards the inside of where the dust lanes occur (see model 007 in 4.6) and the strength of the shock also decreases. That is, the difference between the shock - no shock regions reduces for higher pattern speeds.

We already start to see an issue between changing the Lagrangian radius and the M/L, in that there are similarities in the ways changing the M/L and the pattern speed affect the gas flow. In both cases, i.e. by decreasing the M/L and the Lagrangian radius, the shocks are weakened and become rounder, which leads to degeneracies between the different models. To our knowledge, this degeneracy between these two parameters has not been noted previously in the literature.

4.5.3 Effect of height function

By increasing the scaleheight of the disc, we reduce the density in the plane of the galaxy, which effectively reduces the strength of the forces in the plane. This results in weaker shocks

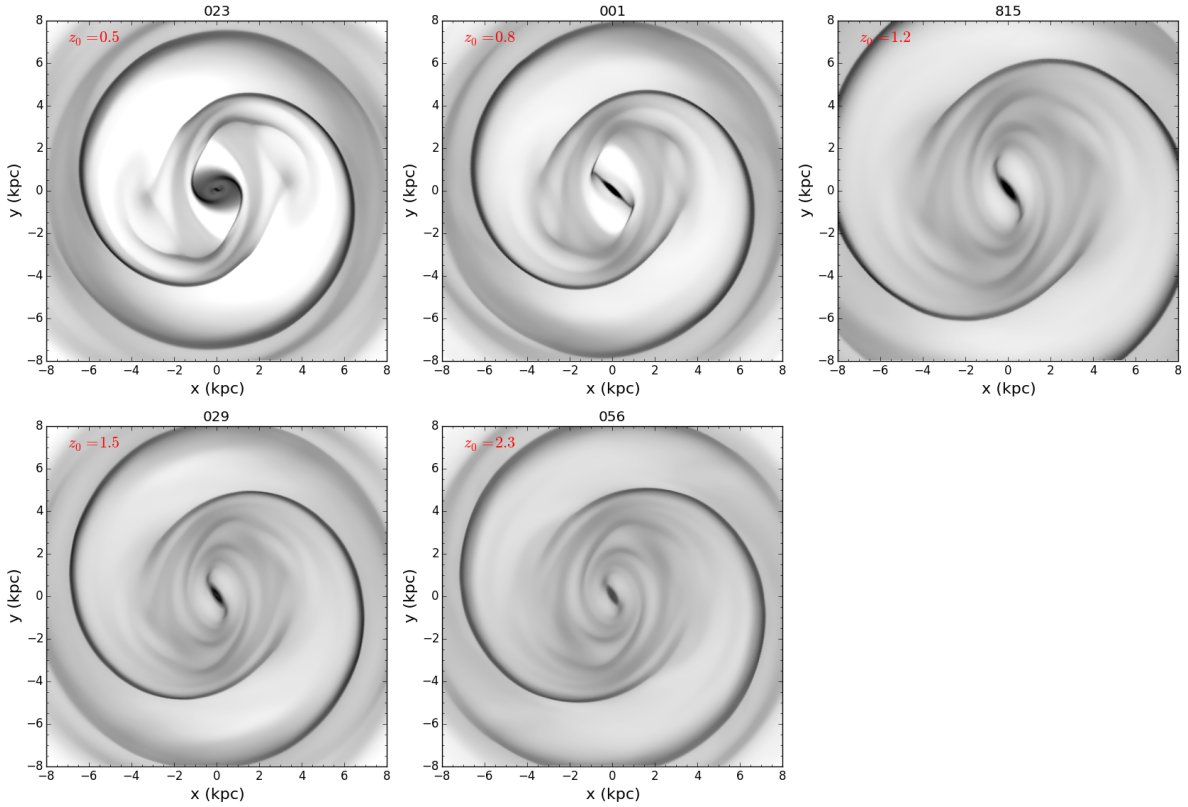

FIGURE 4.7: The gas response to models with different scaleheights (given in kpc in the upper left corner of the image). From left to right and top to bottom we have models 023, 001, 815, 029 and 056 which have scaleheights of z_0=0.5, 0.8, 1.2, 1.5 and 2.3kpc respectively. The other parameters of the models are the same, namely M/L = $\Upsilon_{3.6}$ and $\mathcal{R}$ =1.2 and the plots have the same grayscale.

in the gas, since the ratio of the non-axisymmetric-to-total forcings is also smaller. This can be seen in Figure 4.7 where I plot the gas response simulations in five models with increasing scaleheight (where the scaleheight of the model is noted in the upper left corner of the plot). These models all have flat height functions. We can clearly see how the strength of the shocks reduces for thicker discs; the shocks become rounder, less extended, and there is more gas present in the gas region, since the bar cannot deplete the gas. Furthermore, there is less of a central concentration in the models with thicker discs, since due to the weakening of the bar, less gas is funnelled to the central regions.

When a B/P height function is added to the model, the effect of reducing the non-axisymmetric forces is localised around the area where the B/P is maximum; this occurs because the forces in the central region of the galaxy are reduced, due to the thickening of the disc at the locations where the B/P is maximum. We model two different B/P geometries, where the maxima occur at r=2 and 1.5 kpc respectively along the bar (which correspond to the end of the barlens). In Figure 4.8 I show the effect of adding these two B/P bulge models on the rotation curve of the disc, where we see that the B/P bulges reduce the height of the rotation curve in the region where the B/P is maximum. For the model with a B/P length of 2 kpc (dashed green line)

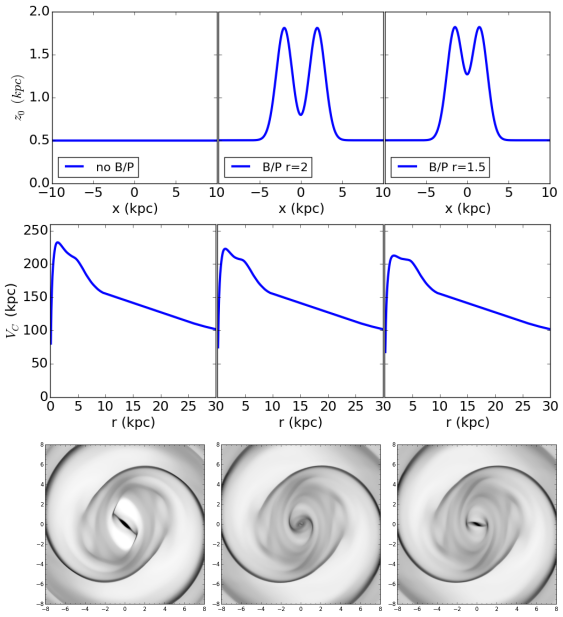

FIGURE 4.8: Effect of changing the length of B/P bulge on the disc rotation curves and gas response of the models: We show results for model 001 which does not contain a B/P bulge, model 034 which contains a B/P bulge with length 2 kpc and model 066 which contains a B/P bulge with length 1.5 kpc (left, middle and right columns respectively). *Top row:* The variation of the scaleheight of the model along the x-axis. *Second row:* The disc rotation curve of the three models. *Bottom row:* Effect of changing the length of B/P bulge on the gas response of the models.

the rotation curve is reduced compared to the model without a B/P bulge (solid red line), while for the model with a B/P length of 1.5 kpc (dotted blue line) the height of the rotation curve is decreased even further since the thickening of the disc occurs at 1.5 kpc, exactly at the location where the peak of the rotation curve occurs.

The effect of the B/P bulge on the shape of the shocks is also evident in the gas response to these models, as can be seen in the bottom row of Figure 4.8. We see that the shocks are less strong in the models with B/P bulges, and the area within the bar region is not as depleted of gas as in the model without the B/P. The shocks also become rounder and have discontinuities.

From Figures 4.5 and 4.7 we can again see how increasing the scaleheight of the disc has a similar effect on the gas flow as decreasing the M/L; the shocks become weaker and rounder. We see thus a threefold degeneracy to this problem between the height function, the M/L, and the Lagrangian radius of the models, although the degeneracy between the M/L and scaleheight is stronger. These degeneracies can be broken by applying additional criteria in order to restrict the allowed parameter space in Section 4.5.6.

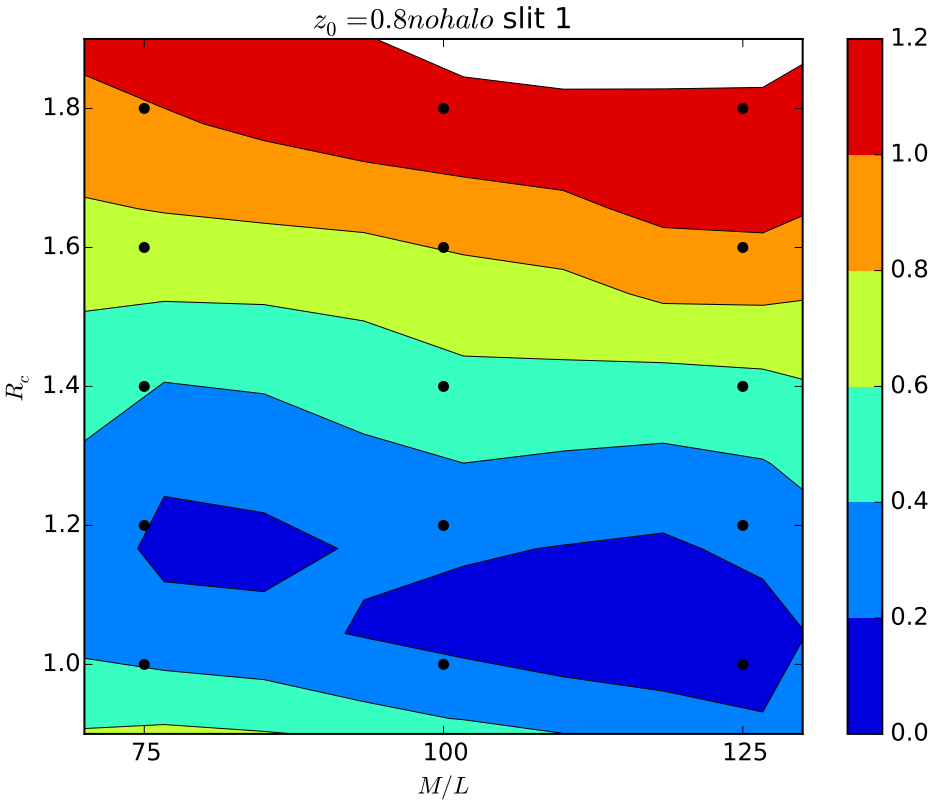

FIGURE 4.9: Contour plots of Δl for models with scaleheight 0.8 kpc with different M/L and Lagrangian radii for models without a dark matter halo. In this and in all subsequent contour plots the black dots correspond to points on the grids where we have models. The colour scale is for the distance Δl between the position of the dust lanes in the 8 and 24μm images and the maximum gas density along the slit.

4.5.4 Models without a dark matter halo

I ran a suite of models without a dark matter halo in order to see whether it is possible to reproduce the morphology of the dust lanes in the observations without the need for a dark matter halo. If this were the case, it would be a strong indication for the fact that the disc is maximal, since just by using the stellar potential the dust lanes are reproduced.

In Figure 4.9 I show a contour plot for a suite of models without a dark matter halo, which have a constant scaleheight of z_0=0.8 kpc, where the M/L and the Lagrangian radius are varied. By changing the M/L of these models, while keeping the Lagrangian radius the same (even if that means different pattern speeds), the pattern in the gas flow remains more or less the same; this is hinted at by the near horizontal contours in Figure 4.9 and can be seen in Figure 4.10 where I plot the surface density of the gas for these models. This is due to the fact that the shape of the rotation curve stays the same even though the absolute value changes. Therefore, the gas "feels" the same proportion of non-axisymmetric to axisymmetric forces in the cases with models with different M/L and the same Lagrangian radius.

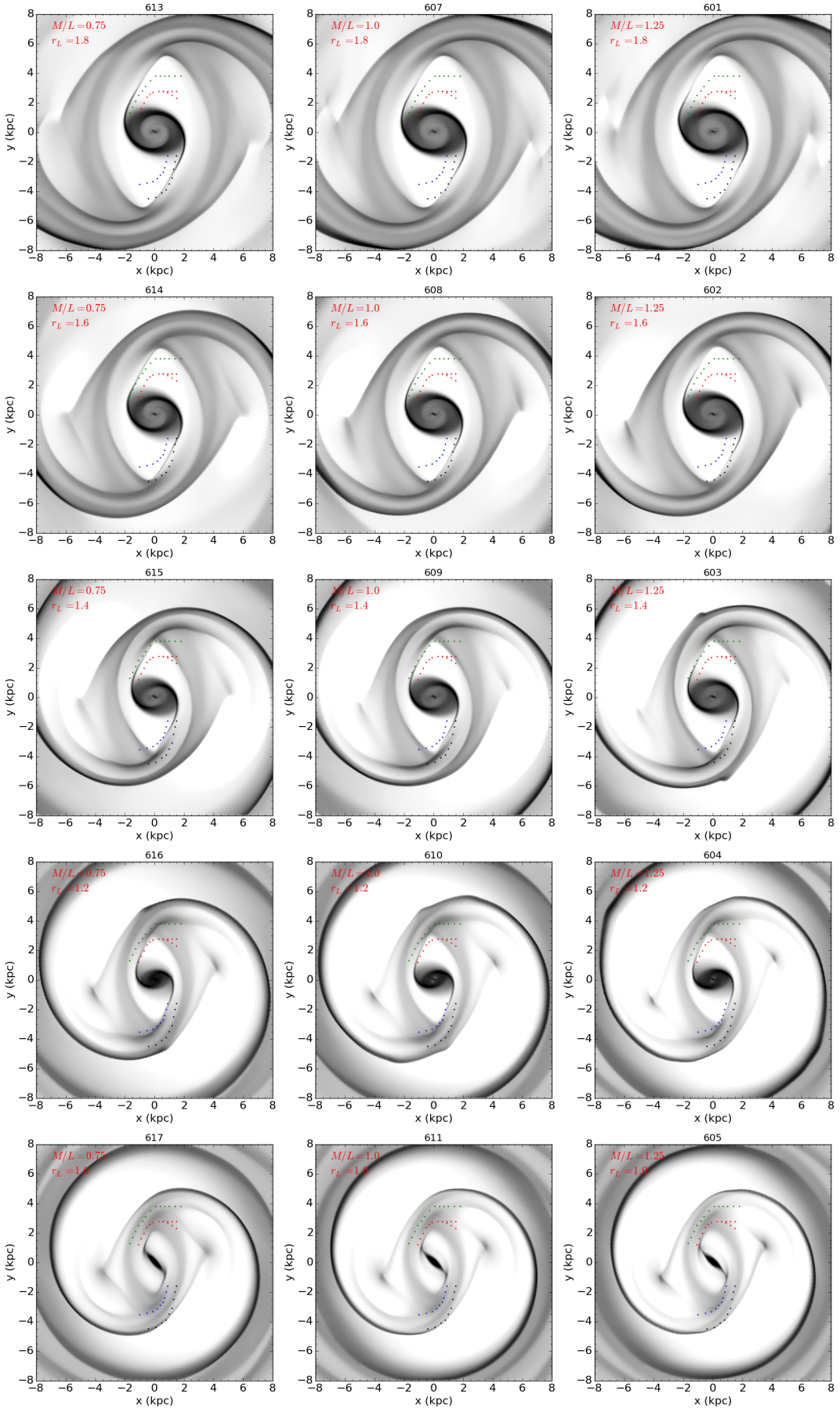

FIGURE 4.10: Models without a dark matter halo. All models have a scaleheight z_0=0.8 kpc with different M/L and Lagrangian radii indicated in the top left corner of each plot. From left to right M/L = 0.75, 1., 1.25 times the fiducial $\Upsilon_{3.6}$. From top to bottom r_L = 1.8, 1.6, 1.4, 1.2, 1.0 r_B

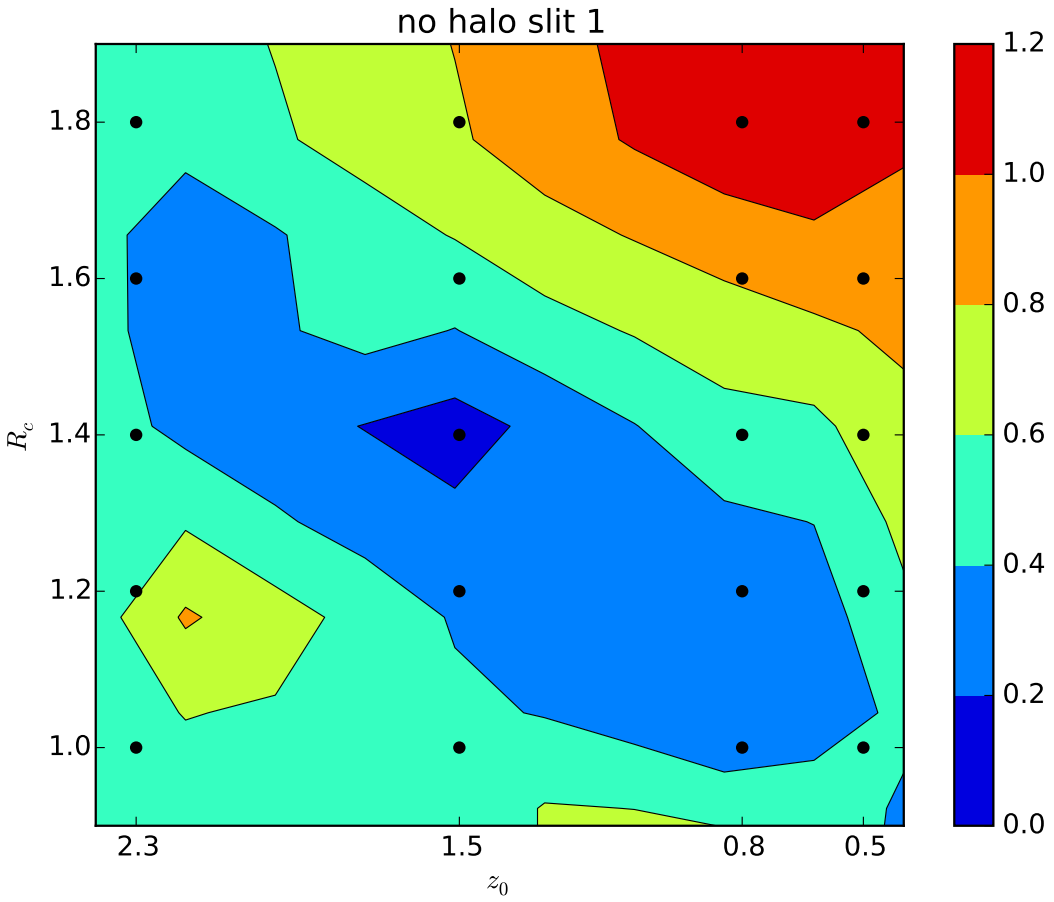

FIGURE 4.11: Contour plot of grid of models without a dark matter halo where the Lagrangian radius (in units of R_B) is plotted versus the scaleheight (in units of kpc) of the model for a constant M/L=$\Upsilon_{3.6}$.

Therefore by running models without a dark matter halo one of the parameters does not need to be explored, i.e. that of the M/L since for each scaleheight the models will vary little with varying M/L, and the main difference in the gas flows will occur due to the Lagrangian radius. In Figure 4.11 I show contour plots for a grid of models with different scaleheight and Lagrangian radius for models without a dark matter halo. We see that for thick discs slower bars are preferred, while for thinner discs faster bars are preferred. By visually examining the gas pattern of the models in Figure 4.12, we see that, if the disc is close to maximal and the halo does not have a significant contribution to the gas flows in the disc, the best fit models according to the criteria set in the previous section are for models with relatively thinner discs and faster bars.

4.5.5 Exploring the parameter space

Out of the different suite of models that were run I construct a number of grids for which I create contour plots showing the value of the distance between the dust lane in the 8μm and

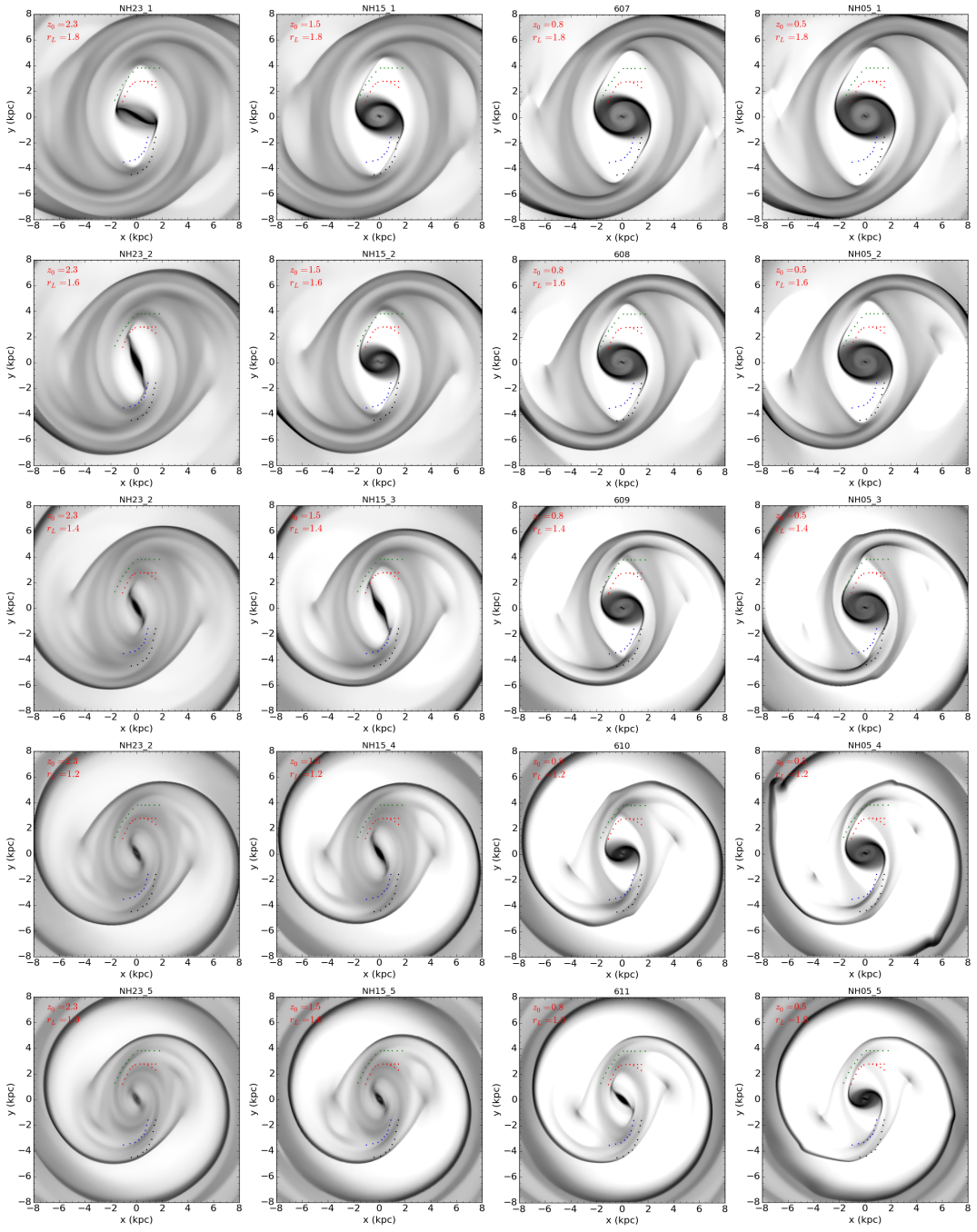

FIGURE 4.12: Gas surface density for a grid of models without a dark matter halo, with varying Lagrangian radius and scaleheight. The scaleheight from left to right is 2.3, 1.5, 0.8 and 0.5 kpc. The Lagrangian radius from top to bottom is 1.8, 1.6, 1.4, 1.2 and 1.0 r_B

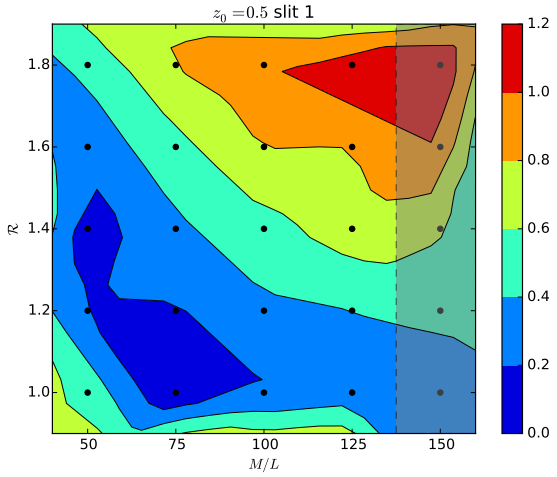

(a) z_0 = 0.5kpc

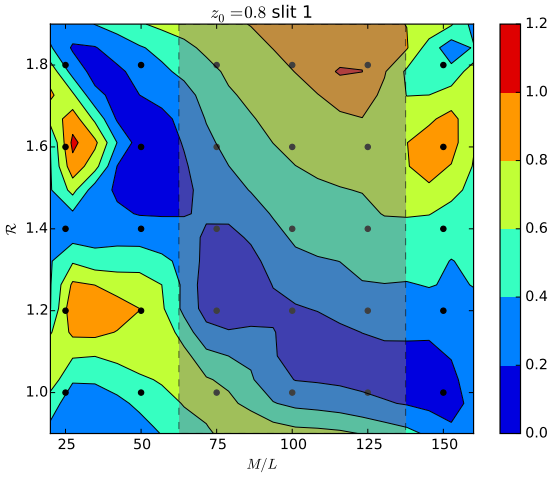

(b) z_0 = 0.8kpc

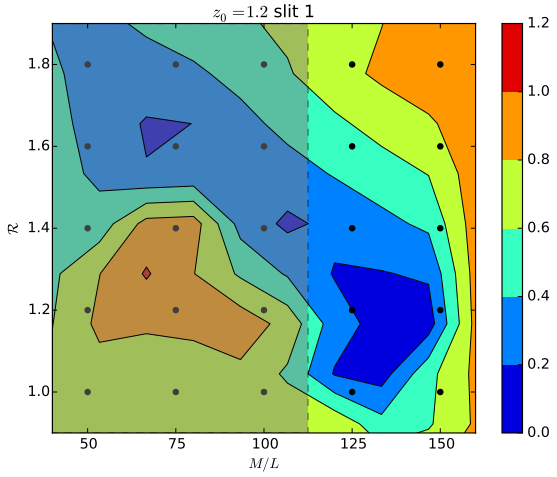

(c) z_0 = 1.2kpc

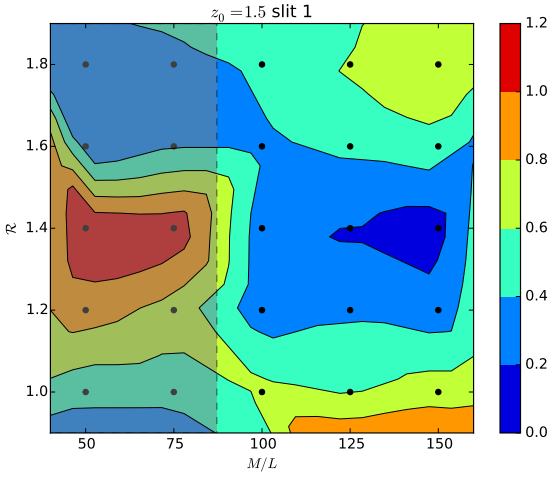

(d) z_0 = 1.5kpc

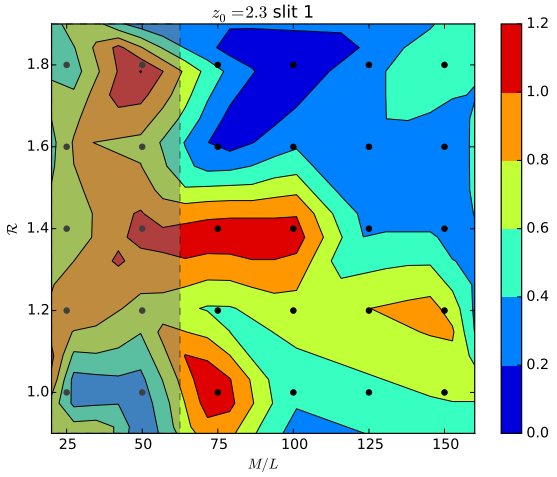

(e) z_0 = 2.3kpc

FIGURE 4.13: Contour plots for suites of models with different scaleheights, from left to right and top to bottom, the scaleheight corresponds to 0.5, 0.8, 1.2, 1.5 and 2.3kpc respectively. The x-axis of the plots correspond to M/L (in units of percentage of $\Upsilon_{3.6}$, e.g. M/L = 75 corresponds to $0.75\Upsilon_{3.6}$). The y-axis gives $\mathcal{R}$, i.e. the ratio of the Lagrangian radius to bar semi-major axis, r_L/r_B. The black dots correspond to points on the grids where we have models. The colour scale gives the distance Δl between the position of the dust lanes in the 8 and 24μm images and the maximum gas density along the slit. The shaded area of the plots shows the constrained parameter space after taking into account the vertical velocity dispersion of the galaxy (see text in Section 4.5.6).

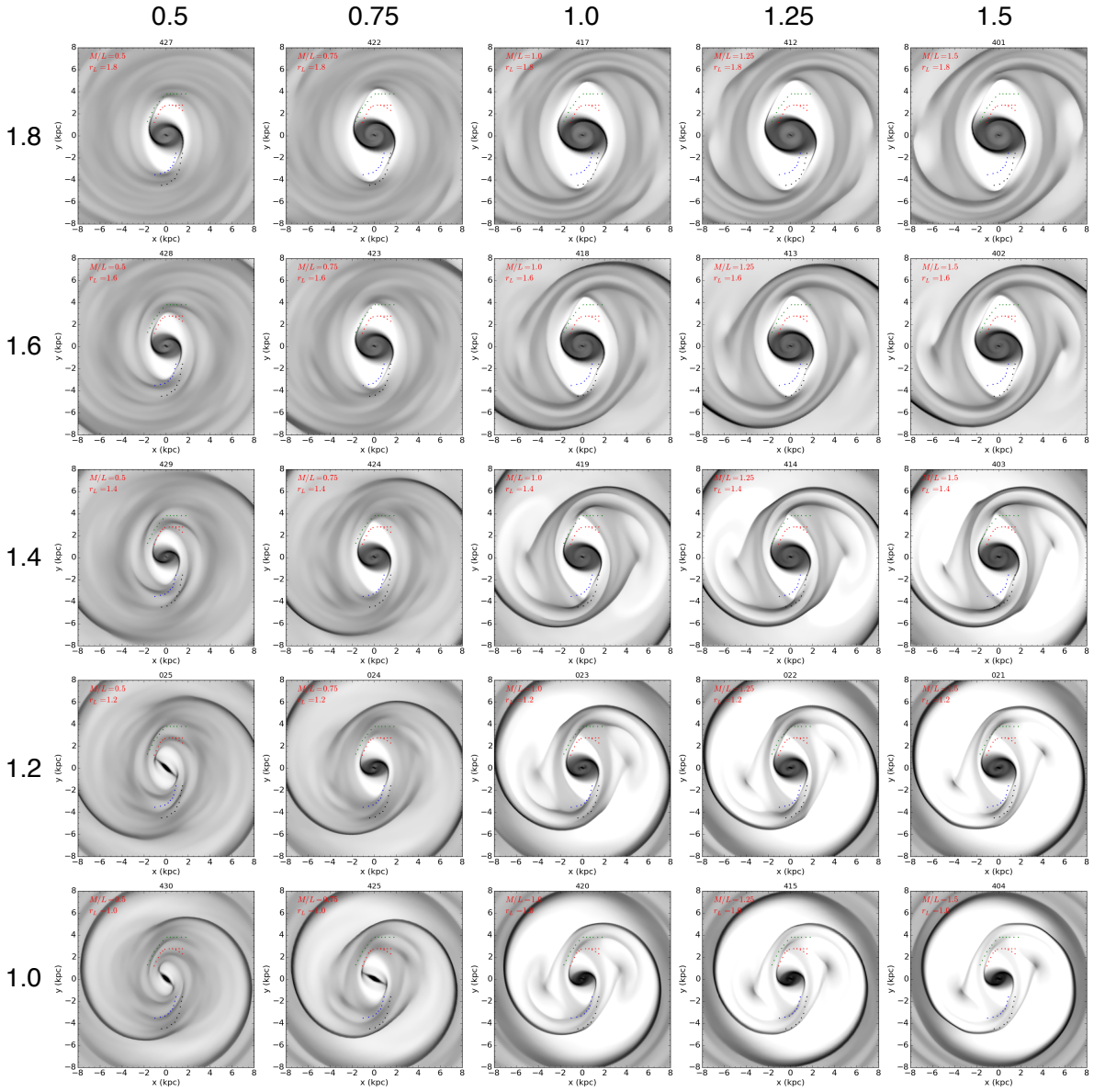

FIGURE 4.14: Grid of models for a flat sech^2 height function with z_0=0.5 kpc. The M/L decreases from top to bottom in steps of $0.25\Upsilon_{3.6}$ and the pattern speed decreases from right to left in steps of $0.2r_B$. The M/L is denoted at the top of each column and $\mathcal{R}$ is denoted at the left of each row.

24μm images and the maximum of the density in the hydrodynamic simulations (denoted Δl). For a given scaleheight and height function, I make a grid in the parameter space with models with different M/L and different Lagrangian radii (i.e. pattern speeds) as is shown in Figure 4.13.

For models with a scaleheight of 0.5 kpc the forces in the plane of the galaxy are strong since the disc is very thin, and the non-axisymmetric component dominates over the axisymmetric component especially for high M/L. For models with high M/L, fast bars with $\mathcal{R}$ less than 1.4 are preferred, as can be seen from the contour plot in Figure 4.13(a), while models with

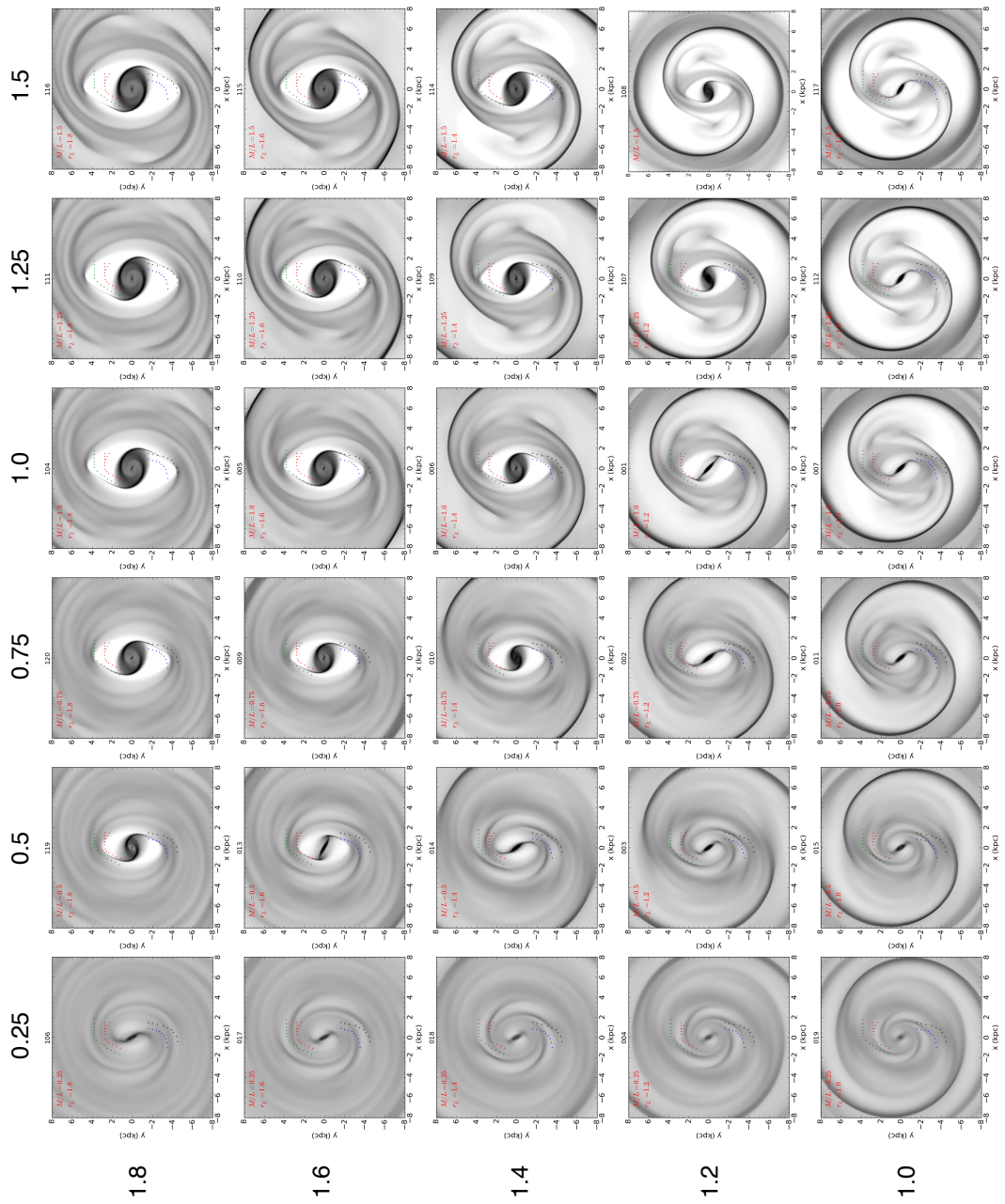

FIGURE 4.15: Grid of models for a flat sech^2 height function with z_0=0.8 kpc. The M/L decreases from top to bottom in steps of $0.25\Upsilon_{3.6}$ and the pattern speed decreases from right to left in steps of $0.2r_B$. The M/L is denoted at the top of each column and R is denoted at the left of each row.

slow bars and high M/L are rejected since the shocks in the simulations do not coincide with the shocks seen in the observed images. Therefore, there is a trend in Δl, going from top left to bottom right, in which Δl is minimum, showing that these models are preferred. For models with small M/L i.e. M/L=$0.25\Upsilon_{3.6}$ a value of $\mathcal{R}$=1.4 also gives an acceptable fit to the observations, while slower bars also give acceptable fits. Plots of the surface density of the gas for models with a scaleheight of 0.5 kpc can be seen in Figure 4.14, where the trend shown in the contour plot of Figure 4.13(a) becomes evident.

We see in Figure 4.13(b) and 4.13(c) that for models with a scaleheight of 0.8 and 1.2 kpc, there is an even stronger trend than in the 0.5 kpc suite of models, going from the top left

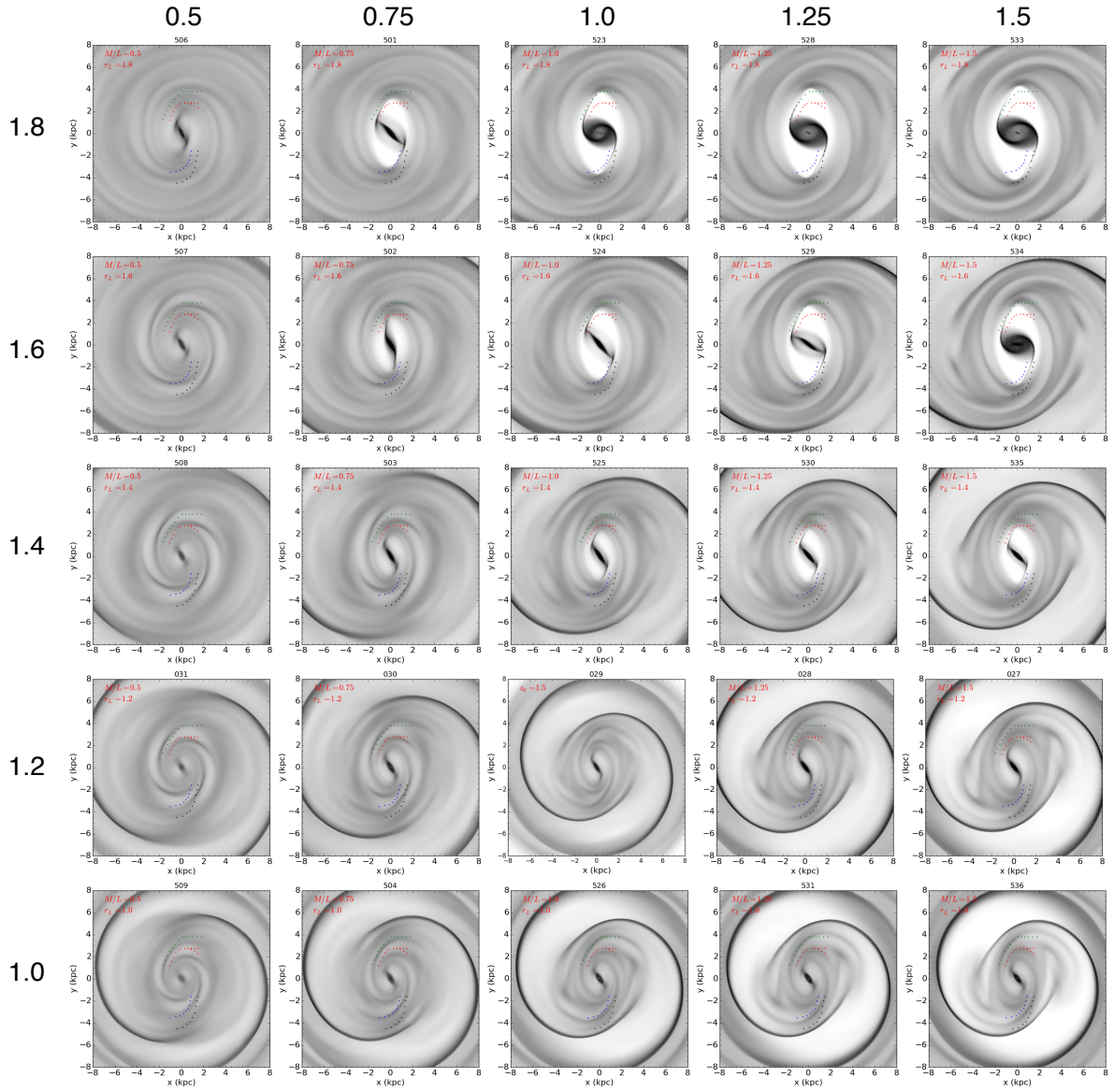

FIGURE 4.16: Grid of models for a flat sech^2 height function with z_0=1.5 kpc. The M/L decreases from top to bottom in steps of $0.25\Upsilon_{3.6}$ and the pattern speed decreases from right to left in steps of $0.2r_B$. The M/L is denoted at the top of each column and $\mathcal{R}$ is denoted at the left of each row.

to the bottom right in the parameter space, i.e. as the M/L is increased, models with faster bars are preferred. This indicates a degeneracy between the M/L and the Lagrangian radius since the two have a similar effect on the shocks in the gas, as already mentioned. Plots of the surface density of the gas for models with a scaleheight of 0.8 kpc can be seen in Figure 4.15.

For models with scaleheight 1.5 kpc, the trend from top left to bottom right in the contour plot becomes less evident, as can be seen in Figure 4.13(d). This occurs because for thicker discs the forces in the plane of the galaxy are reduced and multiple shocks appear which are in general weaker. Therefore there is no clear maximum in the gas density, i.e. there is no

FIGURE 4.17: Grid of models for a flat sech^2 height function with z_0=2.3 kpc. The M/L decreases from top to bottom in steps of $0.25\Upsilon_{3.6}$ and the pattern speed decreases from right to left in steps of $0.2r_B$. The M/L is denoted at the top of each column and R is denoted at the left of each row.

longer a clear principal shock. Therefore it becomes harder to trace the maximum of the gas density. In addition, from visually inspecting the models in Figure 4.16 we see that models with low M/L are in general rejected since the shocks tend to be too round and do not match the observed dust lanes. Even in the presence of a strong principal shock it often does not coincide with the locations of the dust lanes in the observational images.

For the models with a scaleheight of 2.3 kpc, there is no clear trend in the parameter space as can be seen by the contour plot in Figure 4.13(e). As for the suite of models with z_0=1.5, the thick disc leads to very weak shocks in the gas flows, and multiple arms appear in the gas flow, especially for low M/L and fast bars as can be seen in Figure 4.17. Additionally,

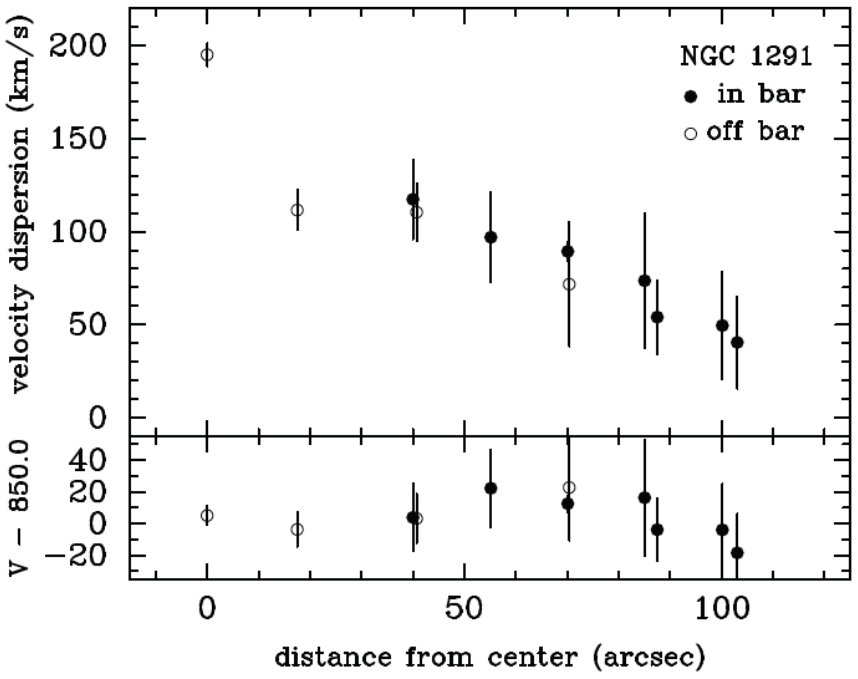

FIGURE 4.18: Plot of the stellar vertical velocity dispersion as a function of radius for NGC 1291. Reproduced from Bosma et al. (2010).

the contrast between the regions with and without shocks is significantly diminished, since the shocks are very weak in this models. Most of the models for these large scaleheights are therefore excluded since one of the criteria for the models is that there be a distinct strong shock, which corresponds to the dust lane seen both in the 8 and 24μm images.

The degeneracies in the models define diagonal lines in the parameter space which roughly run from the upper-left to lower-right corner, which move upwards as z_0 increases, but eventually become less clear due to weaker shocks. In the next section we try to break the degeneracies between the M/L, the Lagrangian radius and the scaleheight by applying a set of additional criteria based on further observations of this galaxy.

4.5.6 Constraining degeneracies in the modelling

As mentioned in the previous sections, there are strong degeneracies between the three parameters M/L, r_L, and height function. Effectively, reducing the M/L has a similar effect on the shocks to increasing the scaleheight or increasing the bar pattern speed. It is therefore difficult to define the best fit model, or a region within which the values converge towards a best fit, purely from the shapes of the shocks in the gas flows. However, there are additional constraints which can be used in order to constrain the parameter space of realistic models.

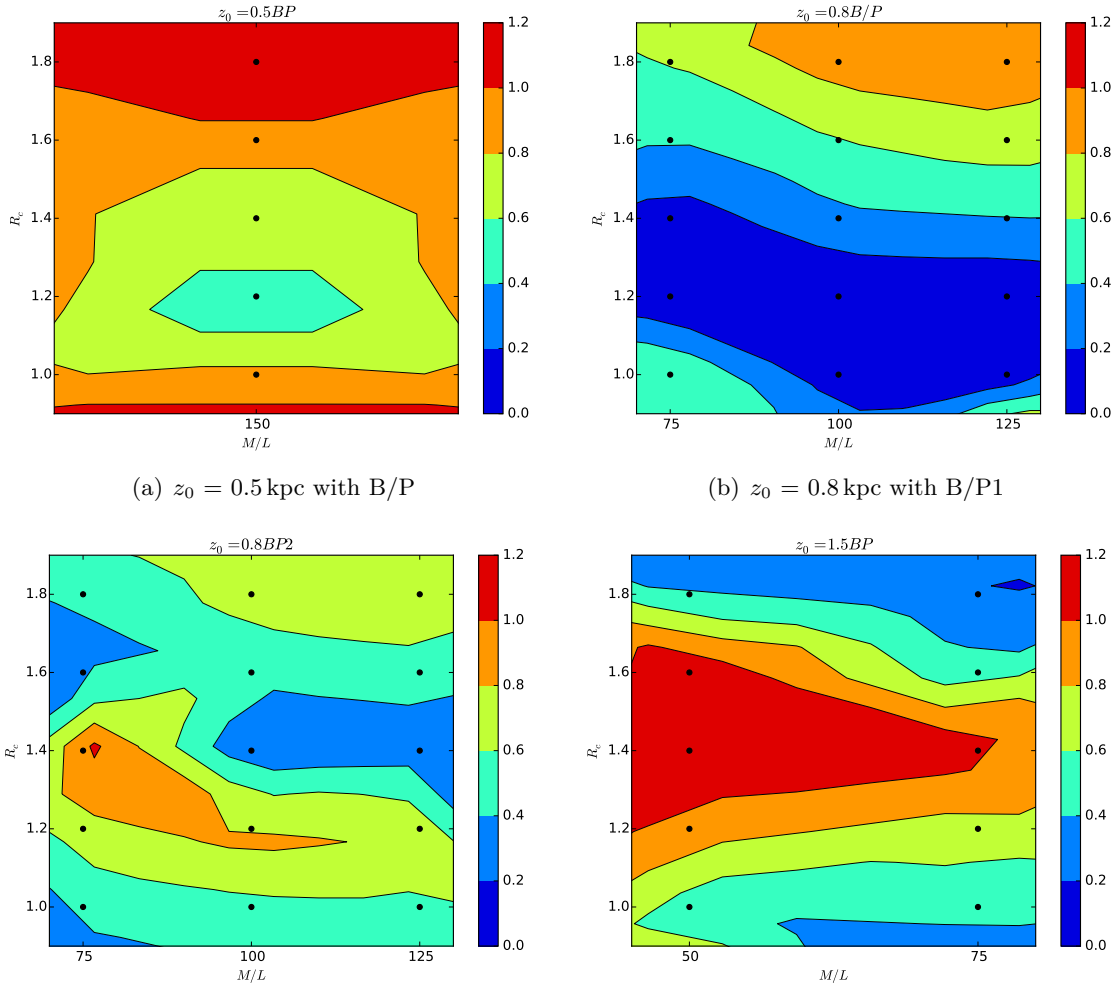

(a) z_0 = 0.5 kpc with B/P

(b) z_0 = 0.8 kpc with B/P1

(c) z_0 = 0.8 kpc with B/P2

(d) z_0 = 1.5 kpc with B/P

FIGURE 4.19: Contour plots for suites of models with a constrained M/L according to the scaleheight and the vertical velocity dispersion, for models with B/P bulges. Each contour plot is for a suite of models with a height function with z_0=0.5, 0.8, 0.8 and 1.5 kpc and a B/P bulge for (a), (b), (c) and (d) respectively. Models (a), (b) and (d) have a B/P bulge with a length of ±2kpc along the bar and model (c) has a B/P bulge with a length of ±1.5 kpc along the bar. Each column corresponds to a different M/L and each line to a different Lagrangian radius.

V_{max} from the TF relation

The first is the V_{max} from the TF relation, which for NGC 1291 is 222±18 km/s (Ponomareva, in prep.). There are certain models which are excluded because the maximum value of the rotational velocity is too high and is no longer consistent with the predictions from the TF relation. For example, for z_0=0.5, M/L larger than $1.5\Upsilon_{3.6}$ are excluded since $V_{max} \geq 240$ km/s, which is the maximum value allowed for V_{max} when also taking into consideration the scatter.

Isothermal disc

Additionally I use the relation between the scaleheight, velocity dispersion and surface density of an isothermal sheet in order to constrain the relation between the scaleheight and the M/L.

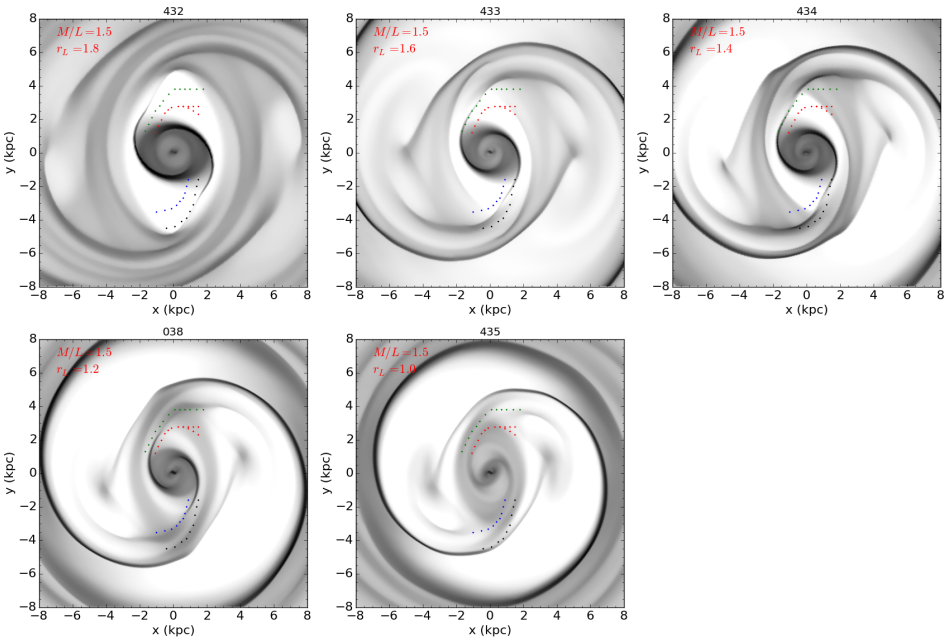

FIGURE 4.20: Two dimensional gas surface density for models with a height function with z_0=0.5 kpc and a B/P with length 2kpc (i.e. $0.4r_B$). From left to right and top to bottom the models have M/L=1.5$\Upsilon_{3.6}$ and $\mathcal{R}$=1.8, 1.6, 1.4, 1.2 and 1.0 respectively.

This has been used in a number of studies in the past, such as for example the DiskMass survey, where this relation was used for a set of late-type spiral galaxies to obtain a dynamical determination of the M/L (Bershady et al., 2010, Martinsson et al., 2013). The stellar velocity dispersion provides a relation between the surface density of the stellar component and the scaleheight of the disc. Assuming the disc is isothermal, the relation is given by:

$$z_0 = \frac{\sigma_z^2}{\pi G \Upsilon I} \tag{4.13}$$

where I is the surface intensity, in units of flux per unit area and Υ is the M/L (Binney and Tremaine, 2008, Bershady et al., 2010).

In Figure 4.18 I show measurements of the stellar velocity dispersion of NGC 1291 (from Bosma et al. (2010)) from which I take an average value for the stellar velocity dispersion of 80 km/s. This allows to constrain the parameter space, and exclude some of the models which have a M/L incompatible with the scaleheight predicted by the relation.

It is possible that in the bar region the disc is not exactly isothermal, which is why I allow for a range of values (±30%) for the scaleheight given a certain M/L. Thus this relation can exclude some extreme cases in which for an adopted M/L the scaleheight is very far off from that given by the theoretical value of the above relation. In Table 4.8 I give the values obtained for the scaleheight assuming a specific fraction of the fiducial $\Upsilon_{3.6}$. We see that for a given velocity dispersion, for small M/L the predicted thickness of the disc increases, while for large

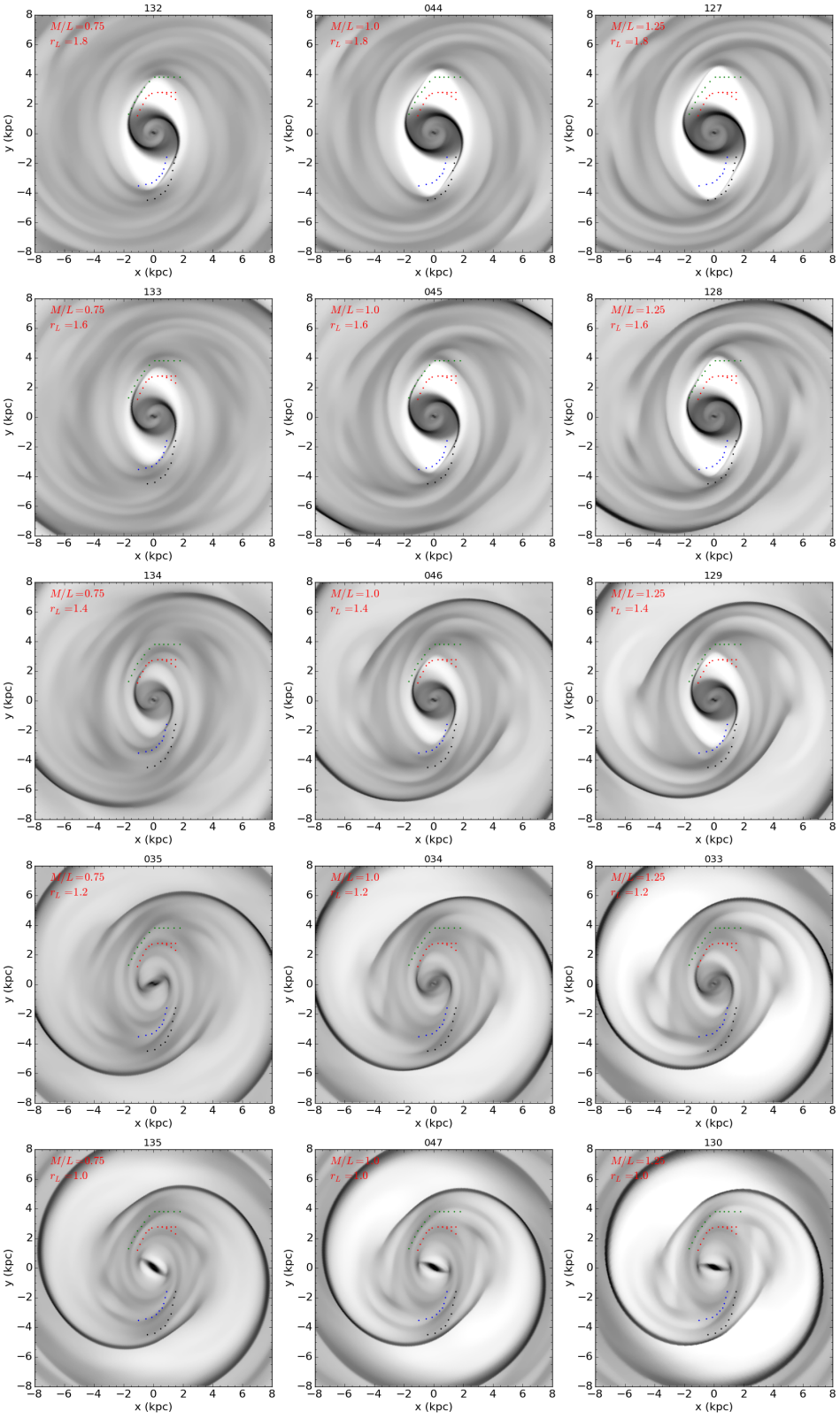

FIGURE 4.21: Two dimensional gas surface density for models with a height function with z_0=0.8 kpc and a B/P with length 2kpc (i.e. $0.4r_B$).. From left to right the models have a M/L=0.75, 1. and $1.25\Upsilon_{3.6}$ respectively, and from top to bottom the models have $\mathcal{R}$=1.8, 1.6, 1.4, 1.2 and 1.0.

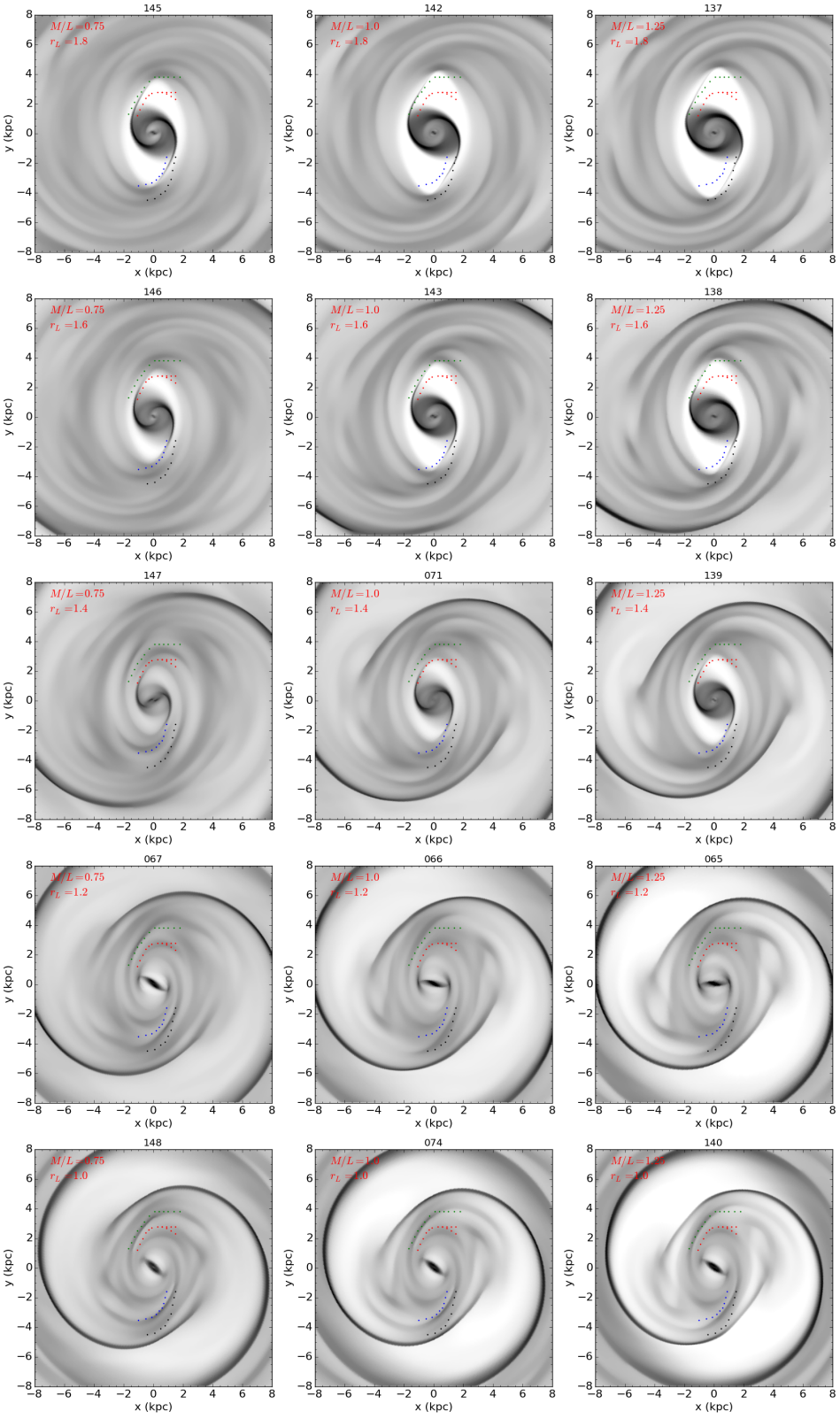

FIGURE 4.22: Two dimensional gas surface density for models with a height function with z_0=0.8 kpc and a B/P with length 1.5 kpc (i.e. $0.3r_B$).. From left to right the models have a M/L=0.75, 1. and $1.25\Upsilon_{3.6}$ respectively, and from top to bottom the models have $\mathcal{R}$=1.8, 1.6, 1.4, 1.2 and 1.0.

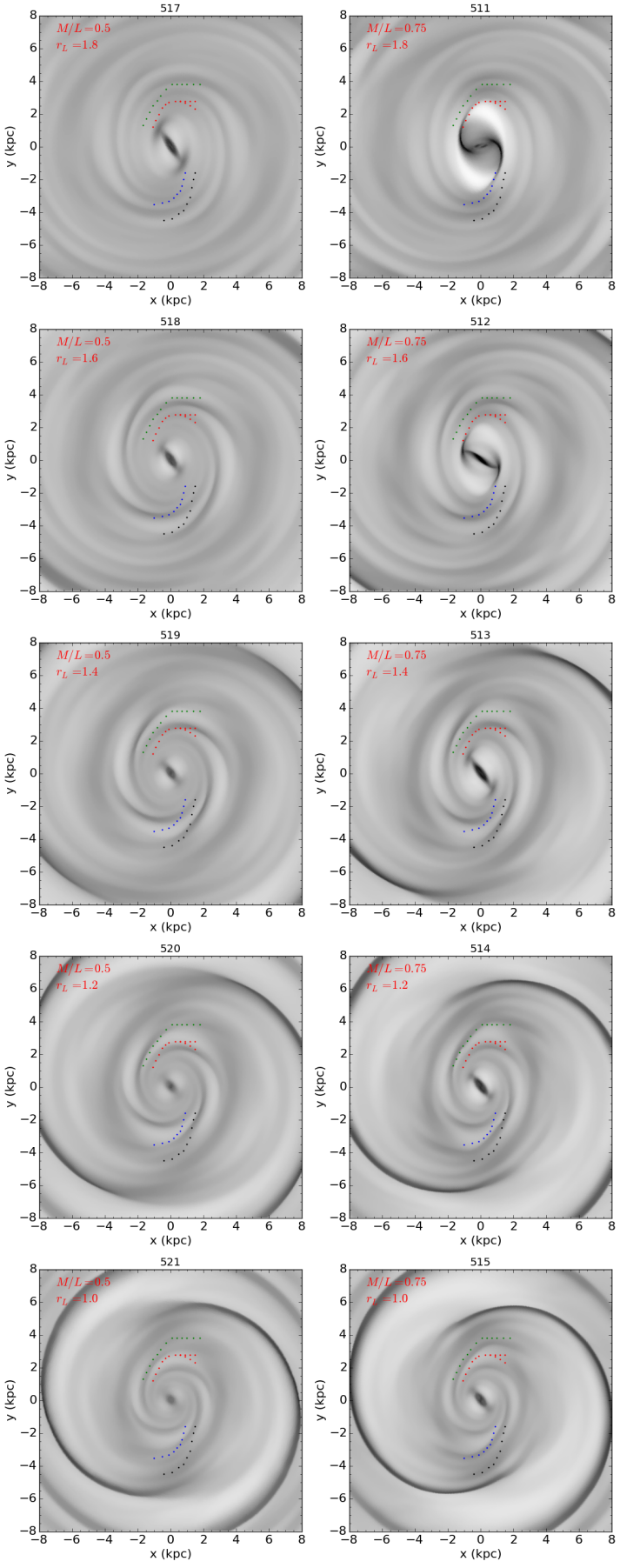

FIGURE 4.23: Two dimensional gas surface density for models with a height function with z_0=1.5 kpc and a B/P with length 2kpc. (i.e. $0.4r_B$). From left to right the models have a M/L=0.5 and $0.75\Upsilon_{3.6}$ respectively, and from top to bottom the models have $\mathcal{R}$=1.8, 1.6, 1.4, 1.2 and 1.0.

M/L (M/L$_{3.6}$)	z_0 (kpc)
1.75	0.51
1.5	0.6
1.25	0.72
1.0	0.9
0.75	1.2
0.5	1.8
0.25	3.6

TABLE 4.8: Predicted scaleheight for a given M/L according to the relation of equation 4.13

M/L the thickness decreases. This can be easily understood as being due to the stronger gravitational field for higher M/L, which keeps the stars from escaping very far above the plain, thus maintaining the disc thin.

Constrained suites of models

In Figure 4.13 the shaded areas give the accepted range of models for the scaleheights, z_0=0.5, 0.8, 1.2, 1.5 and 2.3 kpc. For z_0=0.5 there is only one accepted value for the M/L=1.5$\Upsilon_{3.6}$, since for higher M/L the maximum of the rotation curve exceeds the accepted value of 240 km/s.

Additionally, for the constrained suites of models, I also created equivalent suites of models with a B/P bulge height function, to examine whether models with a B/P bulge can better fit the shapes of the dust lanes. For the models with a disc scaleheight of z_0=0.8 kpc I implement two different B/P models with lengths of r=1.5 and 2kpc along the bar (see Section 4.5.3, Figure 4.8, for the effects of varying the B/P length on the shocks).

For the other suites of models the B/P bulges all have a length of r=2 kpc along the bar. I did not run models with z_0=2.3 kpc and a B/P bulge since this scaleheight is already very thick and it is unlikely that such models would contain an additional B/P component. In Figure 4.19 I show contour plots of the value Δl for the accepted range of models for the four cases of models with B/P bulges. In Figures 4.20, 4.21, 4.22 and 4.23 I plot the gas density for the suites of models with B/P bulges, corresponding to the contour plots of Figure 4.19.

From the contour plots in Figures 4.13 and 4.19 I obtain the best fit models according to the minimum value of Δl. In the following section, I apply the criteria from Section 4.4.3 on the suite of accepted models, in order to determine via visual inspection which models are a best fit to the observed morphology of the dust lanes.

4.5.7 Best fit models

To find the best fit models to the observations I followed a procedure of elimination. First I chose the best fit models as indicated by the contour plots in Figures 4.13 and 4.19, from

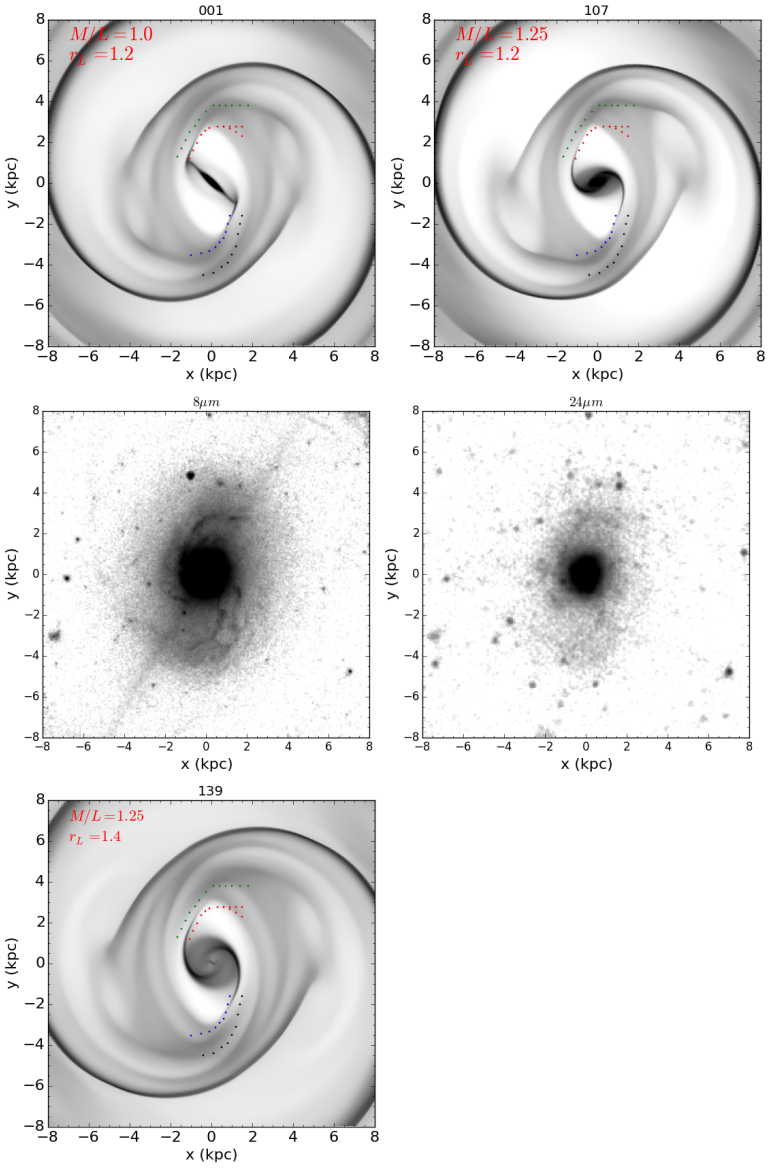

FIGURE 4.24: Two dimensional gas surface density for the best fit models. The top row shows models 001 and 107 which have z_0=0.8 kpc, M/L = 1.0 and 1.25$\Upsilon_{3.6}$ respectively and r_L=1.2. The middle panels show the 8 and 24μm images of NGC 1291 for comparison. In the bottom panels model 139 is shown which has z_0=0.8 kpc with a B/P with length=1.5 kpc along the bar, M/L=1.25 and r_L=1.4

the allowed parameter space of models; this is done by selecting the models with the smallest values of Δl. This reduced the number of best fit models to 20 models. Then each model was examined visually in order to determine the goodness of fit according to the criteria set in Section 4.4.3. These are that the model should have a shock in the gas which is a clear maximum, i.e. there should be a primary shock in the gas, since, as is clearly seen in both the 8 and 24μm images there is a primary dust lane with a much higher density than any secondary features. Additionally the shape of the gas pattern in the simulations should trace as accurately as possible the shape of the shocks.

In general models with thinner discs are preferred, and a model with 2.3 kpc scaleheight are excluded from the modelling. The best fit models all have a scaleheight of 0.8 kpc, while models which are even thinner than this give a worse fit. In general we expect the thickness of the disc to be between 0.8-1.2 kpc since also for 1.2 kpc the models give worse fits than for 0.8 kpc.

The best fit models are shown in Figure 4.24 together with the images of NGC 1291 in 8 and 24μm for comparison; these are models 001 and 107 which correspond to z_0=0.8 kpc without a B/P bulge and have M/L=1 and 1.25$\Upsilon_{3.6}$ respectively and Lagrangian radius r_L=1.2. Model 139 is also a relatively good fit to the dust lanes and has a B/P bulge with a length of 1.5 kpc along the bar, with a M/L=1.25$\Upsilon_{3.6}$ and r_L=1.4. In all the models, fast bars are preferred with a value of $\mathcal{R} \leq 1.4$ since for slower bars the shocks tend to generally be too offset from the bar to correspond to the locations of the dust lanes.

It should be noted, that none of the models give a *perfect* fit to the morphology of the dust lanes. This could be due to a number of reasons, such as the fact that we symmetrise the model although the galaxy is not perfectly symmetric, or due to small effects from inclination (i.e. even though we assume the galaxy is face-on, we know that it has a small, but perhaps non-negligible inclination). Furthermore, it is possible that an exponential height function, rather than an isothermal height function better describes the vertical density distribution; this is still being currently explored. Additionally, although a large number of simulations were run, the grid I explore is still quite "coarse" and there are regions of the parameter space which have not been explored in detail. Furthermore, it is possible that there is a boxy, rather than a strongly peanut shaped, bulge. Some of these issues are discussed in Section 4.6.

4.6 Discussion

4.6.1 Limited effects of the nuclear bar

NGC 1291 presents interesting "bends" in the upper part of dust lanes, which can tell us something about the galaxy's potential. In order to check whether the nuclear bar has an impact on the bends, I compared models with and without a nuclear bar. To create the model without the nuclear bar I axisymmetrise the inner 1 kpc of the image, leaving only the m=0 Fourier component; I thus effectively transform the nuclear bar into an inner disc. I subsequently run gas flow simulations in this potential, and then compare the shock loci in this model with those obtained in the equivalent model, but containing a nuclear bar. We see in Figure 4.25 that the gas flows are very similar in the two models, and indeed the bend in the dust lanes is present in both cases. Thus it can be concluded that it is not the inner bar that is creating these bends.

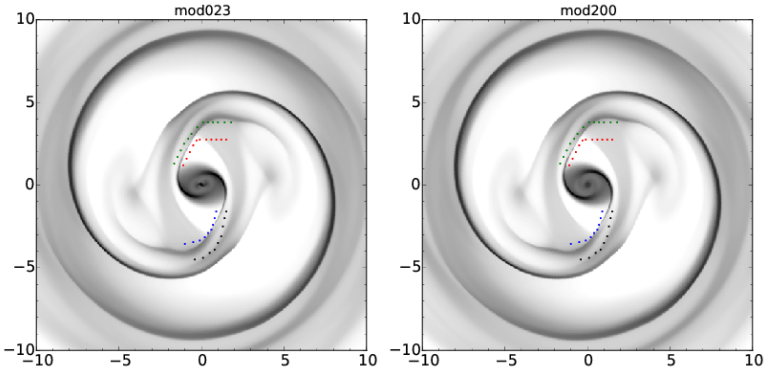

FIGURE 4.25: Gas density distribution in models with (left panel) and without (right panel) a nuclear bar

It seems therefore that the bend in the dust lanes is a feature induced by the primary bar. This feature is more evident in models with stronger bars, i.e. in models with high M/L and thin discs, such as in model 107 shown in Figure 4.24.

4.6.2 The height function of NGC 1291

The best fitting models predict a disc with scaleheight ≈0.8 kpc for NGC 1291. Indeed, for the M/L predicted for the 3.6μm band (Meidt et al., 2014, Röck et al., 2015), i.e. the fiducial $\Upsilon_{3.6}$, the isothermal disc relation (Equation 4.13) predicts a scaleheight of the order of 0.9 kpc. The thicker the scaleheight of the model, the larger the M/L that needs to be adopted, in order to be able to reproduce the morphology of the shocks in the gas. However, due to the fact that there is an inverse proportional relation between the scaleheight and the M/L via the isothermal disc relation, the M/L cannot be arbitrarily increased for a thick disc, since this would lead to a higher stellar velocity dispersion.

Additionally, by increasing the scaleheight of the disc, the shape of the rotation curve of the model changes; therefore, even by increasing the M/L, the shock loci of the gas do not reproduce well the shapes of the dust lanes, which become too round for thicker discs (see for example the high M/L models in Figure 4.17).

Is there a boxy/peanut bulge in NGC 1291?

NGC 1291 seems to have a barlens, which hints at the existence of a B/P bulge (Athanassoula et al., 2014, Laurikainen et al., 2014). From the models presented in Section 4.5.6 we see that those containing a B/P bulge do not necessarily fit better the dust lanes of the galaxy. Indeed out of the three best fit models shown in Figure 4.24, only one contains a B/P bulge. There is some evidence that the shocks in the *central-most* part of the galaxy are rounder than the shape of the gas shocks for models without a B/P bulge. This hints at the possibility that there is a thicker structure in the central region, one which weakens the shocks thus making

them rounder.[1] It is therefore possible that a thicker region, for example due to a boxy shaped bulge, rather than a strong peanut or X-shaped bulge, exists in NGC 1291. Indeed, since I have only explored a small fraction of the parameter space for parameters of the B/P bulge, such as the length, width and height of the B/P, it definitely cannot be excluded that NGC 1291 could contain a weak B/P bulge. However the results seem to suggest that the galaxy does not contain a *strong* B/P bulge, i.e. one with a large double peaked maximum.

4.6.3 Dynamical determination of the 3.6μm M/L

The best fit models obtained in this study have a M/L which falls within the range predicted by SPS models and other approaches, which predict a value of $\Upsilon_{3.6}$=0.6$M_\odot/L_\odot$ (assuming a Chabrier IMF) with small variations for age and metallicity (Meidt et al., 2014, Norris et al., 2014, Röck et al., 2015). However, these methods are dependent on the assumed IMF – indeed the choice of IMF can change the M/L by up to a factor 10 or more (Bell and de Jong, 2001, see Figure 4). On the other hand, since our technique provides a dynamical determination of the M/L, and as such is independent of IMF, it provides an independent confirmation of the robustness of these methods. Our best fit models lie in the range of M/L=1-1.25$\Upsilon_{3.6}$ which allow a range of $M/L_{3.6}$=0.6-0.75. This is in line with the uncertainty (i.e. about 0.1dex) present in the above mentioned methods (Meidt et al., 2014).

4.6.4 The maximal disc of NGC 1291

I examine the rotation curves of all the best fit models, as is shown in Figure 4.6.4. Model 001 has M/L=1 $\Upsilon_{3.6}$, which contributes 74% of the rotation curve of the galaxy. Therefore according to the definition by Sackett (1997) the disc of this galaxy is just short of maximum. By repeating the same measurement for the other best fit models, i.e. models 107 and 139, which both have M/L=1.25 $\Upsilon_{3.6}$, we find that the disc contributes 80% of the total velocity at r=2.2h_r. Therefore, according to the definition by Sackett (1997), these models are both maximal; thus, all our best fit models seem to be consistent with a maximal disc.

These results are consistent with most previous results in the literature using a similar approach, namely gas dynamical modelling. In the work by Weiner et al. (2001), they show that the galaxy they study, NGC 4123 (V_{max}≈140 km/s), has a maximum disc. Zánmar Sánchez et al. (2008) find that the disc of NGC 1365 is massive although not quite maximal. The work of Kranz et al. (2003) showed that the two most massive galaxies in their sample (those with V_{max}≥200 km/s) had maximal discs, while the less massive galaxies were submaximal. It seems therefore that there is some tension between the results found in Weiner et al. (2001)

[1] As explained in Chapter 3, one should be cautious when examining the central region of the simulations, since this region is dependent on the resolution of the simulations.

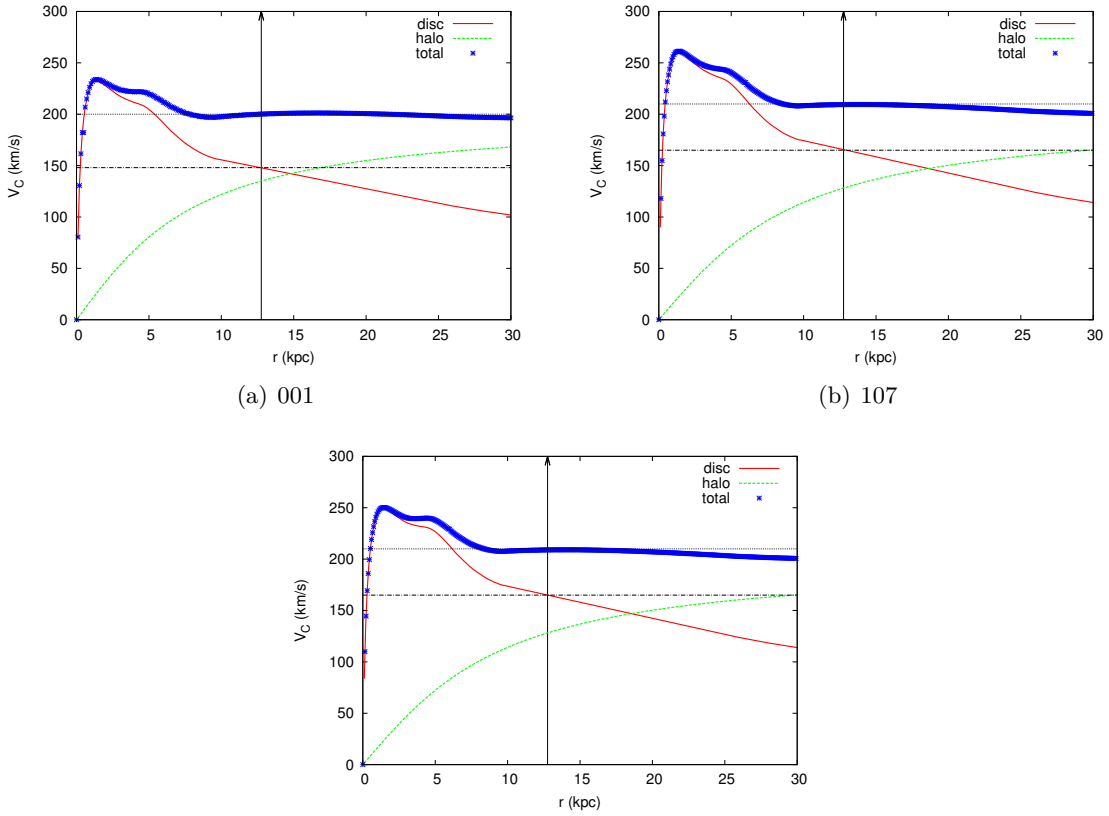

(a) 001 (b) 107

(c) 139

FIGURE 4.26: Rotation curve for model (*a*) 001, (*b*) 107 and (*c*) 139. *Figure (a)*: I plot the rotation curve of the stellar component (solid red line), the dark matter halo component (dashed green line) and the total rotation curve (blue crosses) for model 001. The black horizontal dotted, and dash-dotted lines correspond to the total rotation velocity and stellar rotation velocity at r=2.2h_r respectively. The radius r=2.2h_r is indicated by the black vertical arrow. Model 001 has a M/L=1$\Upsilon_{3.6}$ which leads to a disc contribution of 74% at r=2.2h_r. *Figure (b)*: as for *(a)* but for model 107. The disc is maximal with the stellar component contributing 80% of the total rotation at r=2.2h_r. *Figure (c)*: as above, for model 139. The disc is maximal with the stellar component contributing 80% of the total rotation at r=2.2h_r.

and those in Kranz et al. (2003), since NGC 4123 should have a submaximal disc according to the findings of Kranz et al. (2003). We are consistent with both these findings, i.e. the disc of NGC 1291, which is a galaxy with V_{max}≥200 km/s, is maximal. This seems to argue that massive barred galaxies tend to have massive discs as most of the aforementioned studies also find. Whether or not this extends down to lower masses still remains an open question.

Our results are inconsistent with some other methods for dynamically determining the M/L, such as for example the DiskMass survey (Martinsson et al., 2013), which make use of the stellar vertical velocity dispersion. In their study they found that all of the 30 galaxies used for the study have submaximal discs, even though about a third of their sample are spiral galaxies with V_{max}≥200 km/s. It is not clear why this discrepancy between the different methods exists. On the other hand, we are consistent with the findings of Bosma et al. (2010) for NGC 1291

who found, by exploring the vertical velocity dispersion as well as the photometric properties of the bar, that the disc of the galaxy is maximal.

We plan on extending this study to a number of other galaxies of the S^{4}G sample. It will be interesting to see if galaxies with smaller rotational velocities are maximal, or if we find that less massive discs also have submaximal discs. Additionally, in this study we have not explored the effect of different dark matter halo profiles on the M/L of the best fit models. In future we plan to also address this issue by including NFW or Einsasto halos as well in the modelling and comparing the fits to those obtained using a pseudo-isothermal halo.

4.6.5 The fast rotating bar of NGC 1291

The three best fit models for NGC 1291 have fast rotating bars with $\mathcal{R} \leq 1.4$. This is consistent with observational estimates of the bar pattern speed for early type galaxies (Elmegreen, 1996, Salo et al., 1999, Corsini, 2011), although there are indications that bars in late type galaxies might rotate slowly (Rautiainen et al., 2008). The results are also in agreement with theoretical values predicted by Athanassoula (1992b), who used the shape of the dust lanes to constrain $\mathcal{R}$ and found that it should be of the order of 1.2±0.2.

Additionally, this is consistent with previous gas-dynamical studies of other barred galaxies, which are also found to have fast rotating bars, such as NGC 4123 (Weiner et al., 2001) and NGC 1365, which was found to have a fast rotating bar by two independent studies ($r_L \approx 1.2 r_B$, Lindblad et al. (1996), Zánmar Sánchez et al. (2008)).

This result is consistent with the fact that NGC 1291 is compatible with the maximum disc hypothesis, since there are theoretical arguments which suggest that galaxies embedded in concentrated halos will lose angular momentum and thus slow down (Athanassoula, 2003, Debattista and Sellwood, 2000).

4.7 Summary

In this Chapter I explore the dynamical structure of NGC 1291 using hydrodynamic gas response simulations, for models with different height functions, M/L and Lagrangian radius. The goal of this study is to find the models which provide the best fit of the shock loci in the gas to the observed dust lanes in the 8 and 24μm images. The parameter space is explored for a large number of combinations of the three main free parameters, in order to try and constrain the M/L, the Lagrangian radius and the height function of the galaxy.

There are a number of interesting trends which emerge from this study. The effect of scale-height on the gas flows in hydrodynamic simulations has not been extensively studied in the

past and I show that by increasing the scaleheight of the disc, the forces in the plane of the galaxy are reduced, which leads to weaker and rounder shocks. This effect is similar to that which occurs when the M/L of the model is decreased, while the concentration of the dark matter halo is correspondingly increased, maintaining the outer part of the rotation curve flat at a value predicted by the TF relation. In both cases, i.e. when we increase the scaleheight or decrease the M/L, we are decreasing the strength of the non-axisymmetric forcings, albeit in a slightly different way in each case. Furthermore, in accordance with previous results in the literature (Athanassoula, 1992b, Sánchez-Menguiano et al., 2015), I show that by increasing the pattern speed of the bar, the shocks in the gas are displaced from the bar semi-major axis, while the shocks become straighter. Conversely, by increasing the pattern speed of the bar the shocks become rounder and, for very fast bars, weaker.

There exist degeneracies between the three main free parameters which do not allow to unambiguously find the best fit model for the galaxy[2]. However, by constraining the parameter space, using the relation for an isothermal disc between the scaleheight, M/L and stellar vertical velocity dispersion, I reduce the parameter space sufficiently in order to select a small number of best fit models.

The best fit models obtained for NGC 1291 suggest that NGC 1291 has a disc with preferred sceleheights around the range of 0.8-1.2 kpc. The M/L of the best fit models is within the range given by SPS and other methods, i.e. $0.6 M_{\odot}//L_{\odot}$ which confirms the validity of these methods for predicting $\Upsilon_{3.6}$ (Meidt et al., 2014, Norris et al., 2014, Röck et al., 2015). This M/L subsequently results in best fit models of NGC 1201 which have maximal discs, which confirms previous findings using similar methods, i.e. that massive barred galaxies have maximal discs (Lindblad et al., 1996, Weiner et al., 2001, Kranz et al., 2003). However, there are other studies which find submaximal discs for galaxies in the mass range of NGC 1291 (Martinsson et al., 2013), thus there is still discrepancy in the literature on this matter. Additionally, we find that NGC 1291 contains a fast bar, with $\mathcal{R} \leq 1.4$, also in agreement with previous results in the literature (Elmegreen, 1996, Rautiainen et al., 2008, Corsini, 2011).

The results show that a wealth of information can be extracted from the dynamical modelling of barred galaxies via gas response simulations, and in the future I plan to expand this sample to include other galaxies from the S^4G survey, in order to obtain a larger statistical sample.

[2]To our knowledge this degeneracy has not been reported in past studies

5

The Effects of Substructures on Gas Inflow

Internally induced secular evolution, due to gas transportation to the central regions of galaxies, is thought to play a crucial role in the evolution of disc galaxies; one of the main mechanisms for this secular evolution is via bar induced instabilities. From the work presented in Chapter 2, we see that B/P bulges have a significant effect on the orbital structure and bar strength of galactic models. It was shown already in the early 90's by Athanassoula (1992a,b) that periodic orbits play a vital role in the shape of shocks that are induced in the gas, and therefore also on the strength of shocks and on the amount of inflow. Since B/P bulges are present in a large number of barred galaxies –indeed once a bar is formed, a B/P bulge is expected to form soon after– I investigate the effect they will have on the gas inflow to the central regions of galaxies. To do so, I carry out hydrodynamical gas response simulations, such as those described in Chapter 3, on models with and without B/P bulges and measure the gas inflow in the central regions. I also examine the effect of other substructures, namely the nuclear bar, on the gas inflow to the central few hundred parsecs.

5.1 Introduction

Bars are thought to be one of the most important drivers of the secular phase of galaxy evolution, which dominates at late times when interactions and mergers become less frequent. Bars are found in about two thirds of disc galaxies in the local universe, with variable strengths (de Vaucouleurs et al., 1991a, Eskridge et al., 2000, Knapen et al., 2000, Menéndez-Delmestre et al., 2007, Barazza et al., 2008, Aguerri et al., 2009, Gadotti, 2009, Buta et al., 2010, 2015) and the torques they induce in the disc cause outward angular momentum transfer, which

leads to a redistribution of gas and stars in the galactic disc (Sellwood and Binney, 2002, Athanassoula, 2003, Roškar et al., 2008, Minchev and Famaey, 2010). Gas is a sensitive tracer of the underlying gravitational potential, much more so than the stellar component, and even a weak non-axisymmetric signature in the potential can create shocks in the gas which subsequently loses angular momentum and funnels to the central regions.

This transportation of the gas to the centre of its host galaxy is thought to be responsible for the formation of discy pseudo-bulges and nuclear star formation (Knapen et al., 1995, Kormendy and Kennicutt, 2004, Athanassoula, 2005, Ellison et al., 2011, Coelho and Gadotti, 2011). For the supermassive black holes residing at the central regions of most galaxies to become active, a source of fuel is needed. It is thought that mechanisms such as tidal interactions between galaxies can induce torques in the galaxy which will cause the gas present to funnel down to the central regions (Hopkins et al., 2009). Another mode for providing fuel for AGN activity is via disc instabilities, such as for example via the bar instability (Shlosman et al., 1990). Once the gas reaches the central kiloparsec or so, it is no longer clear how the gas can reach the AGN, since a nuclear ring could form due to the presence of inner Lindblad resonances, which impedes the gas from funnelling all the way to the central few parsec (Knapen et al., 1995, Piner et al., 1995). However, additional small-scale dynamical instabilities,such as nuclear bars and spirals are thought to further push the gas to the central regions (Shlosman et al., 1989, Knapen et al., 1995, Maciejewski, 2004a,b, Kim et al., 2012, Emsellem et al., 2014).

Even though the effect of bars on gas inflow to the central regions has been examined in the literature, a study of the effects of B/P bulges on the gas inflow has not, until present, been carried out, even though B/P bulges are present in a large number of barred galaxies (Lütticke et al., 2000), and in fact once a bar is formed, a B/P bulge is thought to form soon after (Athanassoula, 2005, Martinez-Valpuesta et al., 2006).

The work I carried out on the effects of B/P bulges on galaxy models, and which is presented in Chapter 2, indicates that B/P bulges could possibly diminish the effect of bars on their discs, and that this could lead to a reduced gas inflow. Bar induced disturbances are due to a non-linear response of the gas to the non-axisymmetric gravitational potential, and so they are best studied using numerical techniques, such as hydrodynamic simulations. I therefore carried out hydrodynamic gas response simulations in models with and without B/P bulges, but which otherwise are identical, in order to examine the effects of B/P bulges on the gas inflow to the central regions.

In Section 5.2 I present the models which were used in this study. In Section 5.3 I study the effects of B/P bulges on gas inflow to the central 1 and 0.5 kiloparsec. I also study the effect of adding a dark matter halo on these results (Section 5.3.2) as well as the effect that different gas sound speeds will have on the inflow (Section 5.3.3). In Section 5.4, I study the effect of removing the nuclear bar, which is present in our models, on the gaseous inflow to the central

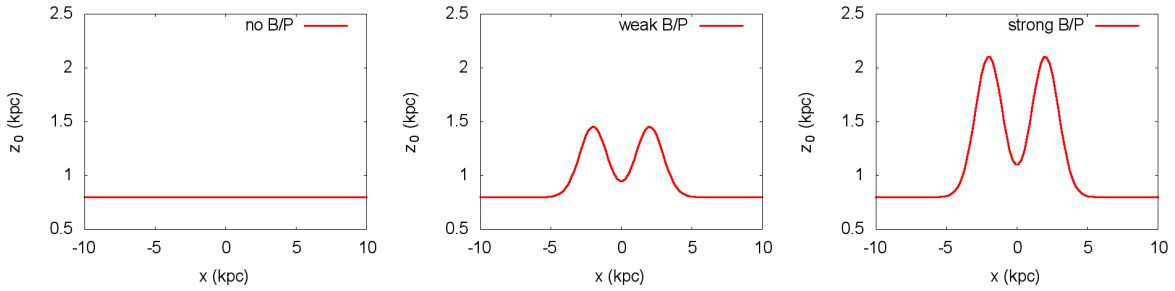

FIGURE 5.1: Scaleheights along the x-axis for the three models used in this chapter. From left to right: model *noBP* where the scaleheight is constant throughout the disc, model "BPweak" where the model contains a relatively weak B/P bulge and model "BPstrong" with a relatively strong B/P bulge.

few hundred parsec. In Section 5.5 I state the conclusions of this study and summarise the work.

5.2 Models

In this section I describe the basic properties of the models used in this study. For a more detailed description of the steps carried out to derive the models, the reader is referred to Chapter 4.3 of the thesis.

The potentials of NGC 1291 are obtained from an image of the galaxy in the 3.6μm band, by adopting a mass to light ratio (M/L) for the galaxy and then and then assuming a height function for the model. In what follows in Section 5.3.1 I focus on three main models, which all have a disc scaleheight of z_0=0.8 kpc and M/L=$\Upsilon_{3.6}$ (where a colour corrected $\Upsilon_{3.6}$ is obtained from an updated formula by Eskew et al. (2012) and Querejeta et al. (2015b)– see Section 4.3.2 for more details.) These parameters are used since, as can be seen in Chapter 4, it is likely that the disc of NGC 1291 is maximal (which corresponds to the M/L used here) and the scale height of the disc of the galaxy is likely in the range of 0.8-1.5 kpc. I explore the effect of changing the M/L and adding dark matter halos (with different concentrations) on the gas inflow in Section 5.3.2. The models are assigned a Lagrangian radius r_L=1.2r_B, a value found both in theoretical (Athanassoula, 1992b) and observational studies (Elmegreen, 1996, Corsini, 2011) and which is confirmed by the results in Chapter 4.6.5 of this thesis.

The first model has a constant scaleheight throughout the disc, and is dubbed the "flat" model, or "noB/P" model; the second and third model have a peanut height function, as described in Chapter 4.3.3 with a maximum scaleheight of the peanut of 2.1 and 1.45 kpc, and are dubbed the "strongBP" and "weakBP" models respectively (see Figure 5.1 for the scaleheight along the x-axis for the three models). It has to be stressed that all the other parameters in the

models are the same, i.e. the only difference between them is the presence or not of the B/P, and its strength.

In Section 5.3.2 I add a dark matter halo to the models, in order to study its effect on the results presented in this chapter. The dark matter halo is modelled as a pseudo-isothermal sphere and its parameters are adjusted so that the outer flat part of the rotation curve matches that predicted by the Tully-Fisher relation (for more details see Chapter 4.3.5). The first of these two models ("MD") has a maximal disc, which leads to a subdominant dark matter; the second model ("SMD") has a reduced M/L and the disc is therefore sub-maximal which therefore needs a concentrated dark matter halo in order to reproduce the value of V_{flat} predicted by the Tully-Fisher relation.

I run gas response hydrodynamic simulations in all the aforementioned models (as those described in Chapter 3) in order to study the gas inflow in the different models. The initial conditions of the simulations are an axisymmetric disc in hydrostatic equilibrium, and the non-axisymmetric component is introduced gradually over 0.9Gyr in order to avoid transients. The size of the box is 50kpc on each side and the resolution of the simulation is 50pc everywhere in the grid (i.e. we use a Cartesian grid for these simulations). The gas is modelled as an infinitely thin disc of an isothermal perfect fluid with a sound speed of 10km/s which is not unreasonable for the interstellar medium of galaxies. In Section 5.3.3 I run the *noBP* model with different sound speeds in order to examine the effect of the gas sound speed on the inflow to the central regions.

5.3 The effect of the B/P bulge on gas inflow

In this section I explore the effects of B/P bulges on the gaseous inflow to the central kiloparsec for different models with and without B/P bulges (Section 5.3.1). I then explore whether these results are significantly affected when a dark matter halo is added, and what the effect of dark matter halos of different concentrations is on the gas inflow to the central regions (Section 5.3.2). Additionally, I examine the effect of the gas sound speed on the results (Section 5.3.3).

5.3.1 Gas inflow within 1 and 0.5 kpc

The simulations are run for 1.2 Gyr and the non-axisymmetric potential is introduced during the first 0.9 Gyr, which is slow enough such that transients are not induced in the gas. I analysed snapshots from all three models, from the start of the simulation up until 1.2 Gyr by I taking a circular aperture of 0.5 and 1 kpc around the centre of the models, as can be seen in Figure 5.2, and analysing the gas inflow rate, and the total gas mass within these apertures.

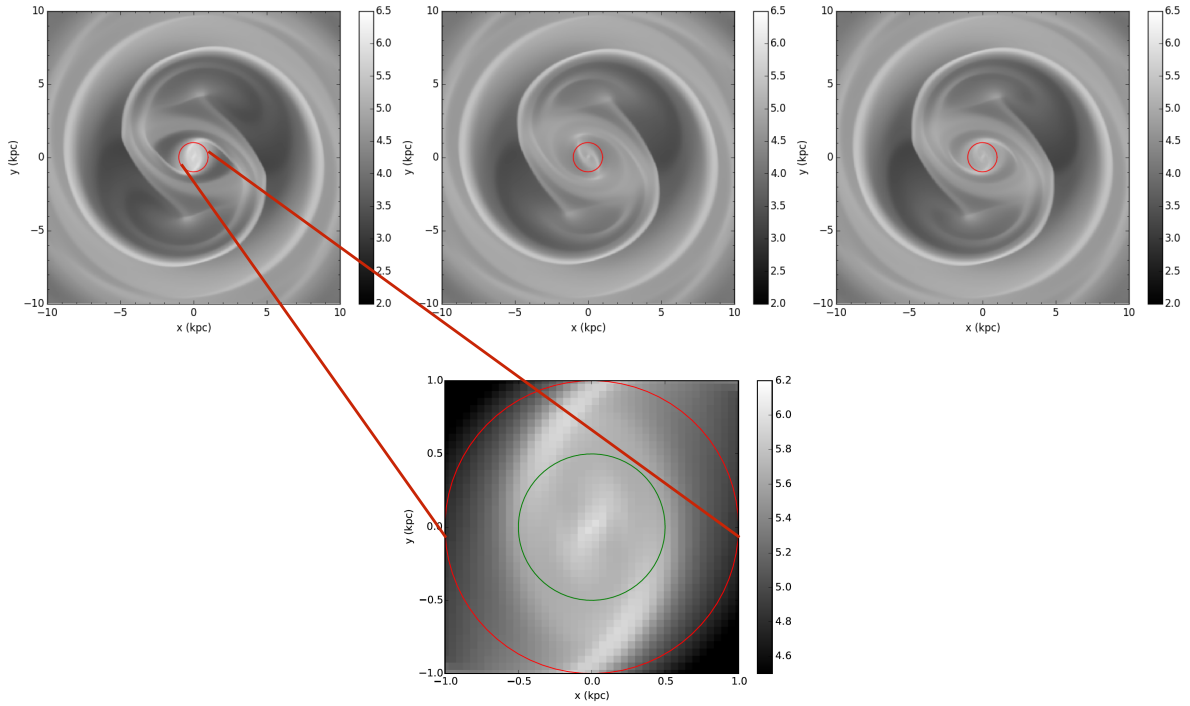

FIGURE 5.2: The gas surface density for the three models we consider in this section. From left to right the *noBP*, *weakBP* and *strongBP* models respectively. The radius at which we consider the gas inflow, i.e. 1 kpc, is drawn with a red circle in all three panels. In the bottom panel we show an example of the gas flow in the central kpc, for the *noBP* model. In red is again the circle enclosing 1 kpc, and the green is the circle enclosing 0.5 kpc.

I show in Figure 5.3 the bar strength Q_T as a function of radius for the three models *noBP*, *weakBP* and *strongBP*. Q_T is a measure of the non-axisymmetric forcings in the galaxy and is given by the ratio of the tangential force to the azimuthally averaged radial force by,

$$Q_T(r) = \frac{F_{\rm T}^{max}(r)}{\langle F_{\rm R}(r) \rangle}. \tag{5.1}$$

We see in Figure 5.3 that by adding a B/P bulge to the dynamical model of NGC 1291 the bar strength of the models is significantly reduced (as is expected from the results of Chapter 2). The decrease in bar strength is particularly evident at the radius where the B/P bulge is strongest, which for these models occurs at r=2 kpc.

This reduction in bar strength has a significant effect on the gas inflow, as can be seen in Figure 5.4. On the left I show the gas inflow rate within 1 kpc (Figure 5.4(a)) and on the right the gas inflow rate within 0.5 kpc (Figure 5.4(b)). We see that by adding a B/P bulge to the model, the gas inflow rate within the central 1 and 0.5 kpc is significantly reduced. In the bottom panels of Figure 5.4 I show the difference between the gas inflow rate in the models

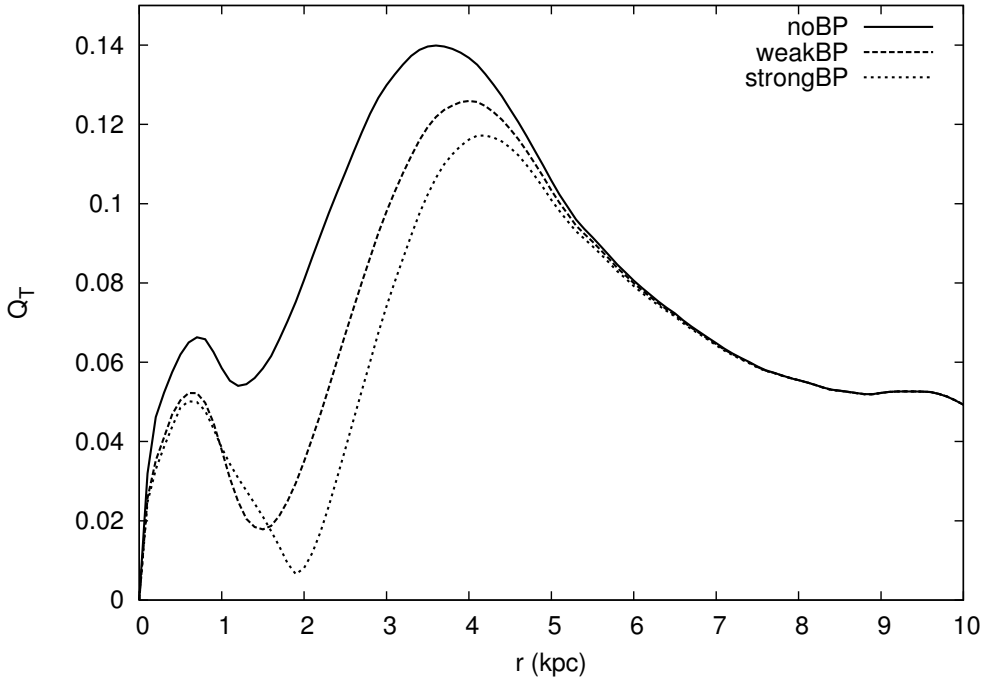

FIGURE 5.3: Bar strength Q_T as a function of radius for the three models *noBP*, *weakBP* and *strongBP*. All the other parameters of the models are the same, i.e. the gas sound speed is 10 km/s, r_L=1.2 (in units of bar length) and z_0=0.8 kpc. We see that the bar strength is reduced when we add a weak and strong B/P bulge, compared to the model without a B/P bulge.

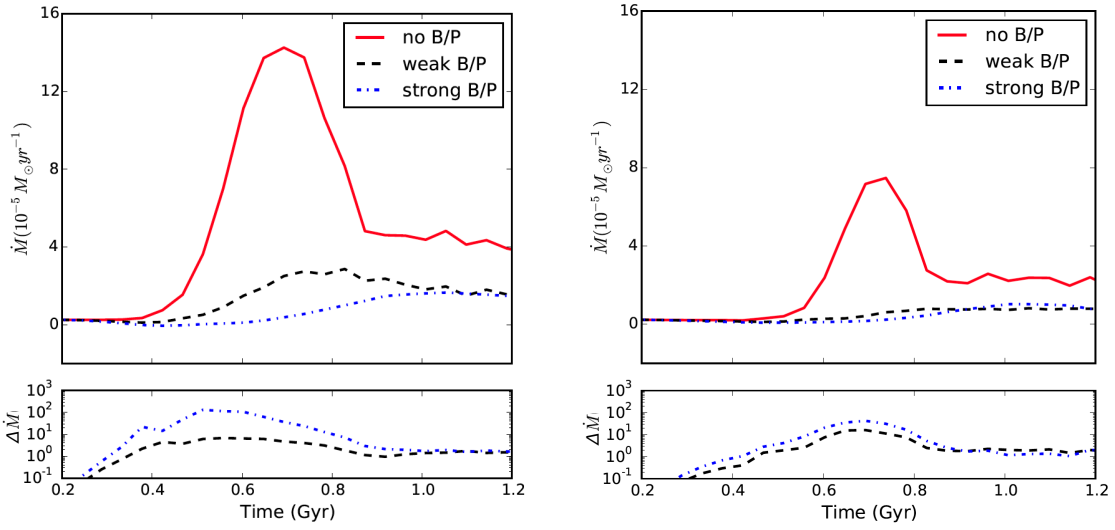

(a) (b)

FIGURE 5.4: *Left*: The gas inflow rate within a circle of 1 kpc for the three models. In the bottom panel I plot $\Delta M_\odot$, the difference in the gas inflow rate between models *weakBP* and *noBP* (dashed black line) and the difference between models *strongBP* and *noBP* (dot-dashed blue line). *Right* : The gas inflow rate within a circle of 0.5 kpc for the three models. In the bottom panel I plot $\Delta M_\odot$, the difference in the gas inflow rate between models *weakBP* and *noBP* (dashed black line) and the difference between models *strongBP* and *noBP* (dot-dashed blue line). In this and in all subsequent plots, the bar potentially is fully introduced by 0.9 Gyr.

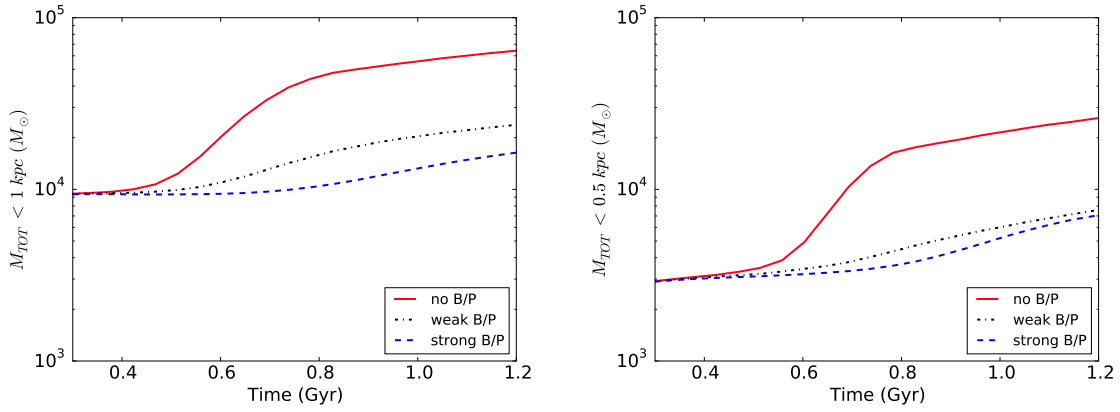

FIGURE 5.5: *Left*: The total gas mass within a circle of 1 kpc for the three models. *Right* : The total gas mass within a circle of 0.5 kpc for the three models.

with and without a B/P bulge. For the *weakBP* case the gas inflow rate is decreased by an order of magnitude, and it is further decreased for the *strongBP* case, with a reduction of up to two order of magnitude.

We see in Figure 5.4(a) that the gas inflow *rate* increases sharply until about 0.7 Gyr and then decreases[1]. The non-axisymmetric potential is fully grown by 0.9 Gyr; therefore the bar strength is maximum from 0.9 Gyr onwards, even though the maximum gas inflow rate peaks before. This occurs presumably because most of the gas has been transported to the centre by 0.7 Gyr, and even though the bar is strongest after 0.9 Gyr and gas is still being funnelled to the centre, the rate of gas inflow is reduced as most of the gas has been pushed to the centre, and as such, there is not enough gas to maintain the previous high rate. This will be thoroughly tested in the future by constructing simulations with a "toy" gas accretion mode, such that we can test that the inflow rate stays stable as long as there is a constant replenishing of the gaseous disc.

A direct consequence of the reduced gas inflow rate is of course the reduced amount of gas mass which accumulates in the centre, as can be seen in Figure 5.5. The gas within 1 kpc is reduced by about a factor of 3 for the weak B/P model, while for the strong B/P case the gas mass is reduced by about a factor 4. Within 0.5 kpc the reduction in gas mass is even more noticeable, as can be seen in Figure 5.5(b). This reduction in gas mass due to the presence of a B/P bulge could presumably have a significant effect on the formation of discy bulges and on nuclear star formation.

Once the gas reaches the inner gaseous ring which is formed in many barred spiral galaxies, it is not clear how it subsequently funnels to smaller scales of the order of a few parsec. At

[1]It is interesting to note that both the gas inflow rate and total gas mass exhibit similar trends to those found in Figure 8b of Friedli and Martinet (1993).

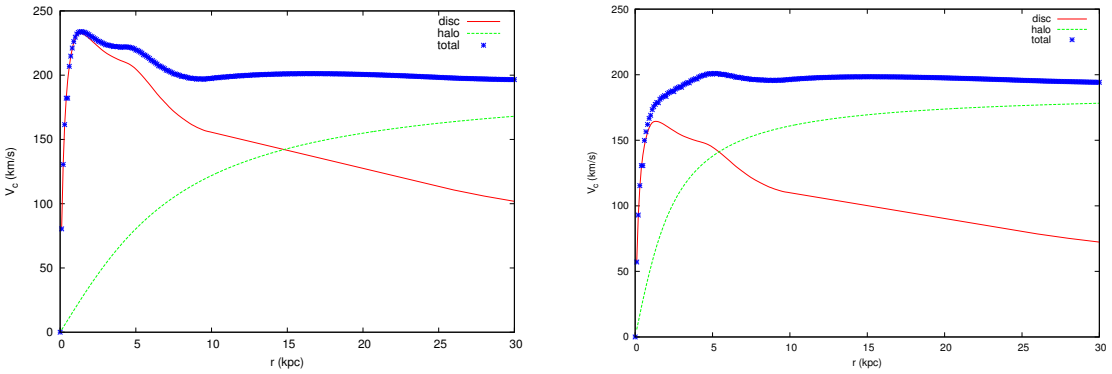

(a) (b)

FIGURE 5.6: *Left*: Rotation curve for MD model, i.e. models with the fiducial M/L, where the disc is maximal and a dark matter halo is added such that the V_{flat} of the model matches that predicted by the Tully-Fisher relation. *Right*: Rotation curve for SMD models with a reduced M/L such that the disc is sub-maximal, where a concentrated dark matter halo is added such that the V_{flat} of the model matches that predicted by the Tully-Fisher relation.

smaller scales there are other effects which become important for the subsequent gas inflow, such as the presence of a SMBH, the effects of gas self gravity as well as star formation and feedback. Exploring all these parameters is beyond the scope of this study, which aims at understanding the gas inflow due to gravitational torques induced by the bar and the B/P bulge and I therefore limit myself to the central few hundred parsec, without exploring smaller scales.

The amount of gas inflow to the central regions of galaxies in general depends on the non-axisymmetric potential. It is therefore worth noting that, since in this study I model just one galaxy, the results cannot necessarily be quantitatively generalised to all galaxies containing a B/P bulge. However, the results are qualitatively applicable to early type barred galaxies which are thought to contain a B/P bulge, and underline the fact that B/P bulges seem to play a significant role in the amount of gas transported to the central region. This will be further explored in the future by modelling other galaxies of the S^{4}G survey thought to contain B/P bulges, in order to determine the impact of B/P bulges on gas inflow in a larger number of galaxies.

5.3.2 Adding a dark matter halo

Dark matter halos are thought to be dominated by random velocities, which to zeroth order leads to an axisymmetric shape for the halo. Thus adding a dark matter halo to our models adds an axisymmetric component to the potential of the galaxy, which reduces the effects that bars and other non-axisymmetries have on the gas dynamics and kinematics. Therefore it

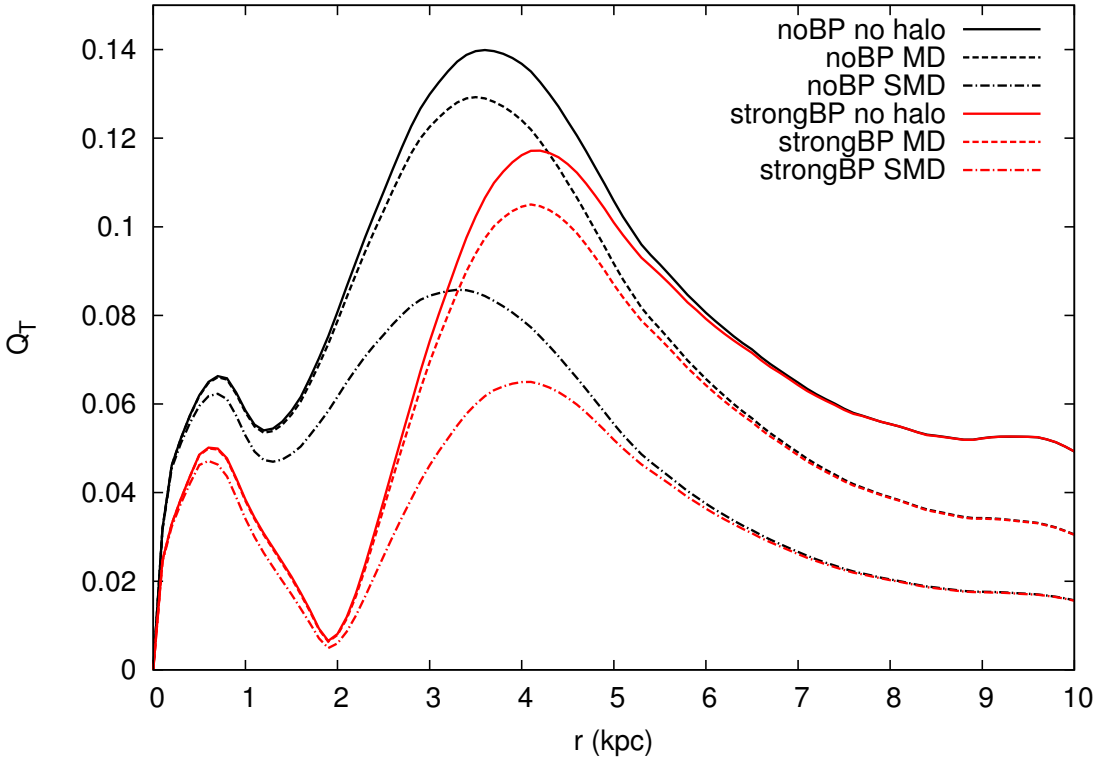

FIGURE 5.7: Bar strength Q_T for the models *noBP* and *strongBP*. For each case I show models without a dark matter halo, a model with a halo and a maximal disc and a model with a concentrated halo and a submaximal disc. All the other parameters of the models are the same, i.e. the gas sound speed is 10 km/s, r_L=1.2 and z_0=0.8 kpc. We see that the bar strength is reduced when we add a strong B/P bulge, and also when a dark matter halo is added.

is possible that by adding a dark matter halo we would "dilute" the difference in gas inflow between models with and without B/P bulges.

To test this I added a dark matter halo to the three models *noBP*, *weakBP* and *strongBP* in order to investigate the effect it would have on the gas inflow of the different models. I create two sets of models, each with a different dark matter halo concentration. The first set of models, the MD models, consist of maximal disc models with low concentration dark matter halos (see Figure 5.6(a) which is the *noBP* model with a dark matter halo added). The second set of models have a reduced M/L, which leads to a submaximal disc, and subsequently a more concentrated dark matter halo is needed in order to match the rotation velocity in the outer parts of the halo, as predicted by the TF relation (see Figure 5.6(b) which is the *noBP* model with a concentrated dark matter halo added). Of course one expects that for very concentrated dark matter halos, the difference between models with and without a B/P bulge will be reduced, as the non-axisymmetric forces are diluted in general. This occurs because the strength of the non-axisymmetric forces are decreased, which leads to weaker and rounder shocks in the gas, as can be seen by comparing the top and bottom row of Figure 5.8.

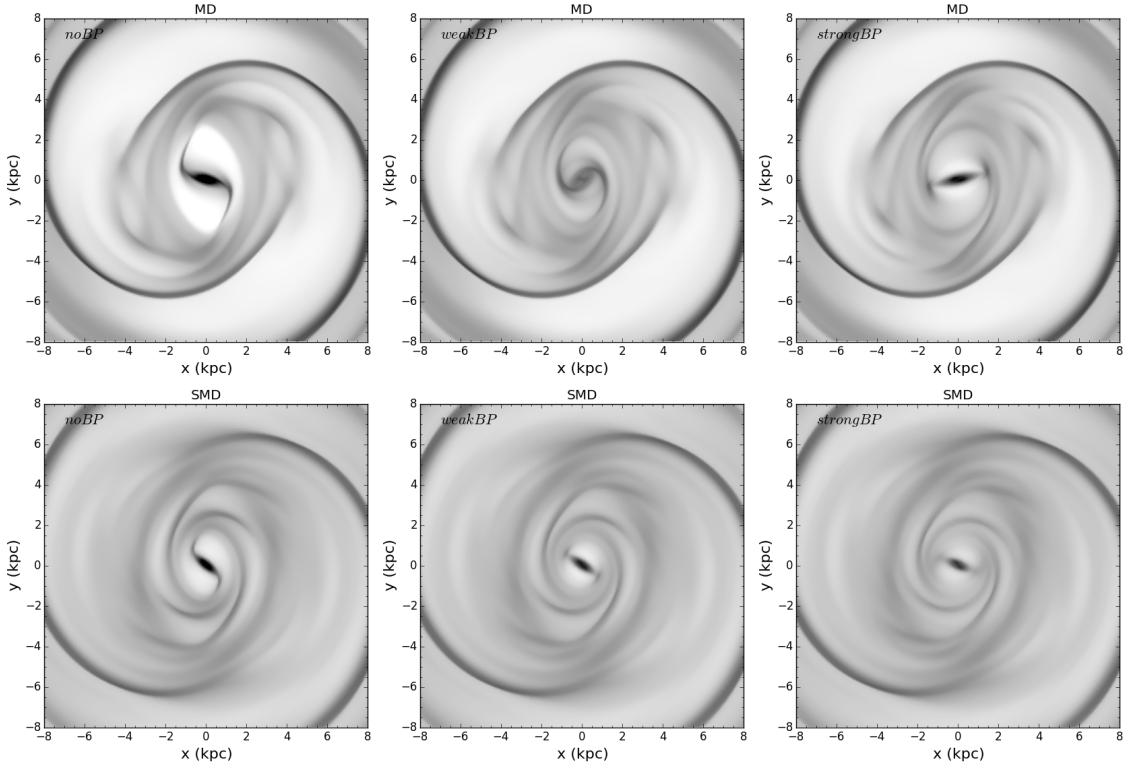

FIGURE 5.8: Two dimensional gas surface density for maximal disc models (MD, top row) and submaximal disc models (SMD, bottom row). From left to right the models are the *noBP*, *weakBP* and *strongBP* models. All the other parameters of the models are the same, i.e. the gas sound speed is 10 km/s, r_L=1.2 and z_0=0.8 kpc.

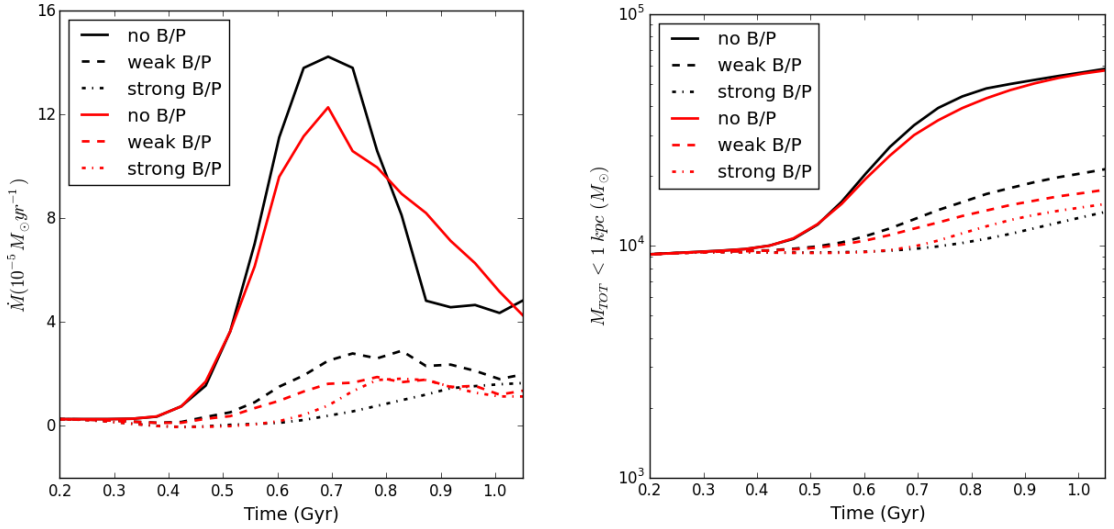

(a) (b)

FIGURE 5.9: Gas inflow rate (left) and total gas mass (right) within 1 kpc for models with and without a dark matter halo. The black lines are for the models without a dark matter halo and the red lines for the MD models with a dark matter halo and a maximal disc.

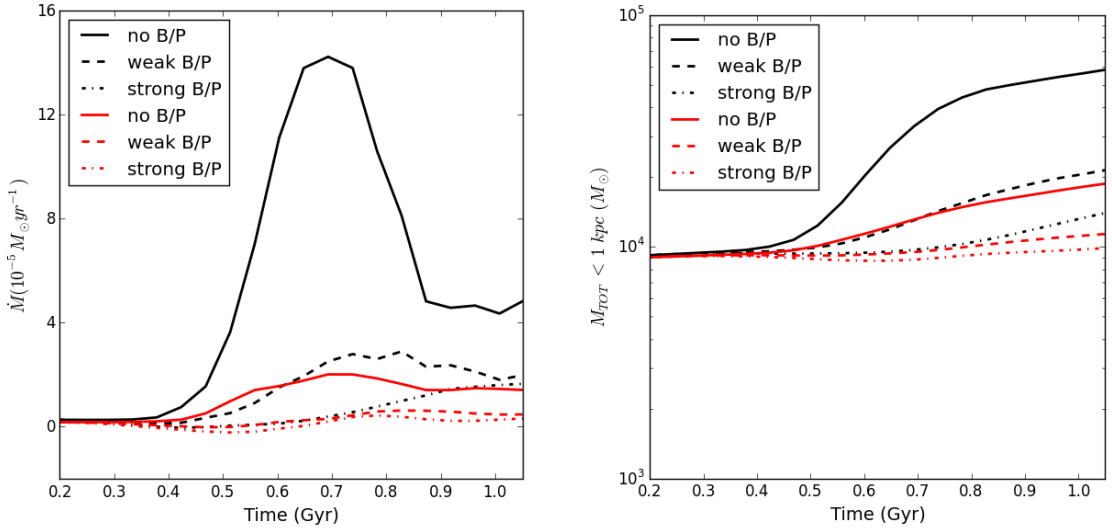

(a) (b)

FIGURE 5.10: Gas inflow rate (left) and total gas mass (right) within 1 kpc for models with and without a dark matter halo. The black lines are for the models without a dark matter halo and the red lines for models SMD with a concentrated dark matter halo.

We see in Figure 5.9 that, as expected, the amount of gas inflow is reduced in the case with the dark matter halo, since the non-axisymmetric forces are weakened. Additionally, we see that the difference between the cases with and without a B/P is also slightly reduced. However this effect is minimal compared to the difference between models with and without a B/P bulge. Therefore for $\Upsilon_{3.6}$ as obtained from SSP and other methods (Meidt et al., 2014, Norris et al., 2014, Röck et al., 2015), and which is confirmed by the findings of Chapter 4, the effect of the dark matter halo is not significant on the gas inflow. This is because the baryonic matter dominates the potential in the central regions, i.e. the disc is maximal, and therefore the difference in gas inflow due to B/P bulges remains significant.

On the other hand, by examining Figure 5.10, we see that by reducing the fiducial M/L, and adding a more concentrated halo, the gas inflow is significantly reduced in all models. This reduction in the gas inflow rate also leads to a less pronounced difference between the models with and without a B/P bulge. Therefore for submaximal discs, where the dark matter halo is dominant in the inner parts, the effect of the B/P bulge on the gas inflow will not be so significant. Also, the gas inflow in general is reduced in models with concentrated dark matter halos and submaximal discs.

5.3.3 Effect of sound speed

I examined the effect of changing the sound speed in the simulations, since this could have an effect on the amount of gas inflow in the three models, and could therefore diminish the

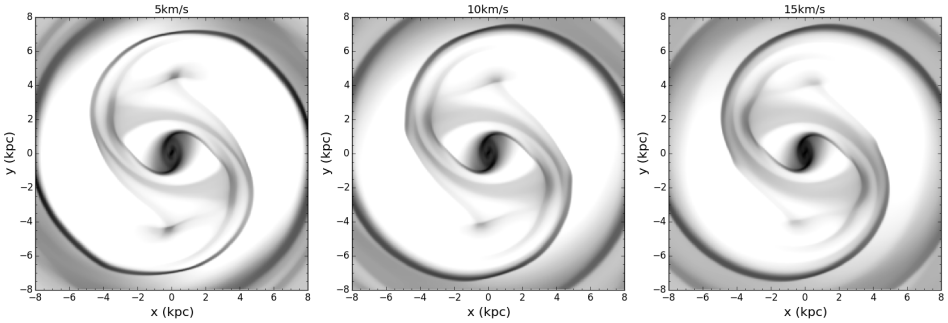

FIGURE 5.11: Two dimensional gas surface density for models with different sound speeds. From left to right the models have gas sound speed 5, 10 and 15 km/s. The models have all other parameters as described in Section 5.2, i.e. M/L=1.$\Upsilon_{3.6}$, r_L=1.2 and z_0=0.8 kpc.

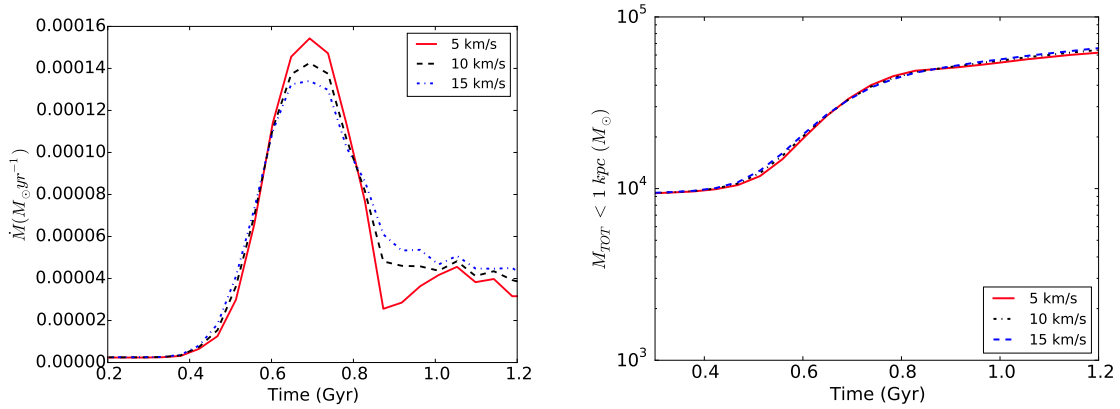

(a) (b)

FIGURE 5.12: *Left*: The gas inflow rate within a radius of 1 kpc for different sound speeds. *Right*: The total gas mass within a radius of 1 kpc for different sound speeds.

differences in gas inflow between models with and without B/P bulges. Indeed, Kim et al. (2012) found that within the centralmost 20 pc, the amount of gas inflow is dependent both on the shape of the potential and on the sound speed of the gas. Additionally, Englmaier and Gerhard (1997) and Patsis and Athanassoula (2000) also find that gas flows are susceptible to changes in the sound speed.

To examine the effect of the sound speed on gas *inflow* rate I used the *noBP* model, for three different sound speeds, the fiducial sound speed of 10 km/s and a lower and higher sound speed of 5 and 15 km/s respectively. In Figure 5.11 I show the two dimensional gas surface density for the three cases with different sound speed (from left to right the models have gas sound speed 5, 10 and 15 km/s). All the other parameters of the models are as described in Section 5.2, i.e. M/L=1.$\Upsilon_{3.6}$, r_L=1.2 and z_0=0.8 kpc.

As can be seen in the left panel of Figure 5.12(a), even though the gas inflow rate is slightly increased (decreased) to begin with for smaller (higher) sound speed, and then subsequently decreased (increased), these effects cancel each other out and lead to a total gas mass within

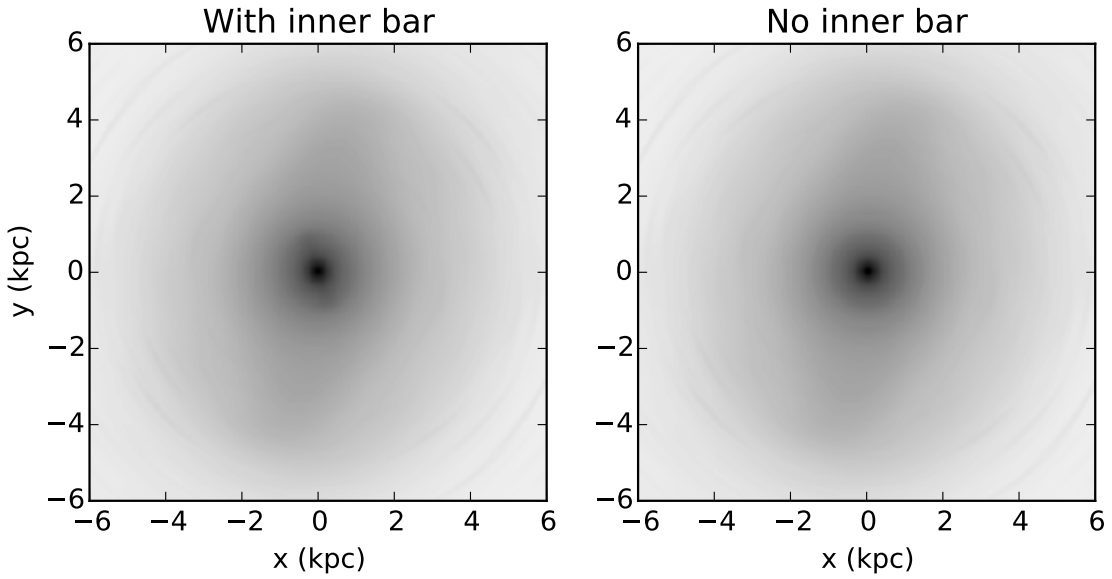

FIGURE 5.13: *Left* Mass map of NGC 1291 with the nuclear bar. *Right*: Mass map of NGC 1291 where the region inside 1 kpc has been azimuthally averaged in order to remove the nuclear bar.

1 kpc which is practically identical for the three models (Figure 5.12(b)). This is most probably related to the fact that our models are not continuously replenished with new gas, and therefore once most of the gas is transported to the central regions, there is little gas left to be transported and so the inflow rate is reduced. Therefore, for the 5 km/s case, the inflow rate is increased to begin with, due to the lower sound speed, which pushes more gas to the central regions. Once the peak of the inflow rate is reached around 7 Gyr, there is subsequently less gas available to funnel to the central regions and so the inflow rate is lower than for the higher sound speed cases, which still have a larger gas reservoir available.

In the future I will study the effect of the sound speed on gas transportation to the central regions in models where there is a constant replenishment of the gas. According to the results of this subsection (Figure 5.12(a)) due to the fact that there is a slightly higher gas inflow rate for models with lower sound speeds, this effect could be cumulative if there is constant gas replenishment, which would lead to higher gas densities within 1 kpc in models with lower sound speeds. However the difference in gas inflow rate is small in the three cases, so even if there is constant gas replenishment or accretion, we do not expect a significant change in the total gas mass within 1 kpc.

5.4 The effect of the nuclear bar on gas inflow

We see from the above sections, that substructures in galaxies, such as the B/P bulge, can have a significant effect on the gas inflow to the central regions. This motivated the question

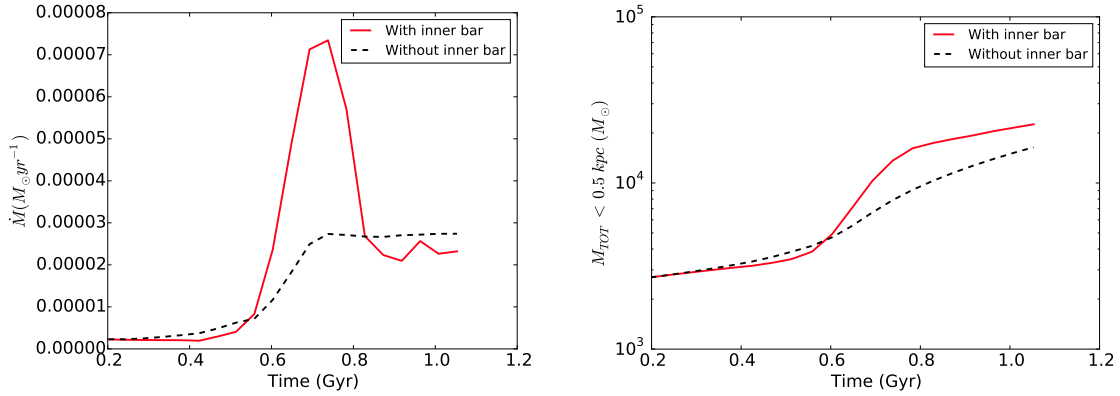

(a) (b)

FIGURE 5.14: *Left*: Gas inflow rate within 0.5 kpc for models of NGC 1291 with and without the nuclear bar. *Right*: Total gas mass within 0.5 kpc for models with and without the nuclear bar.

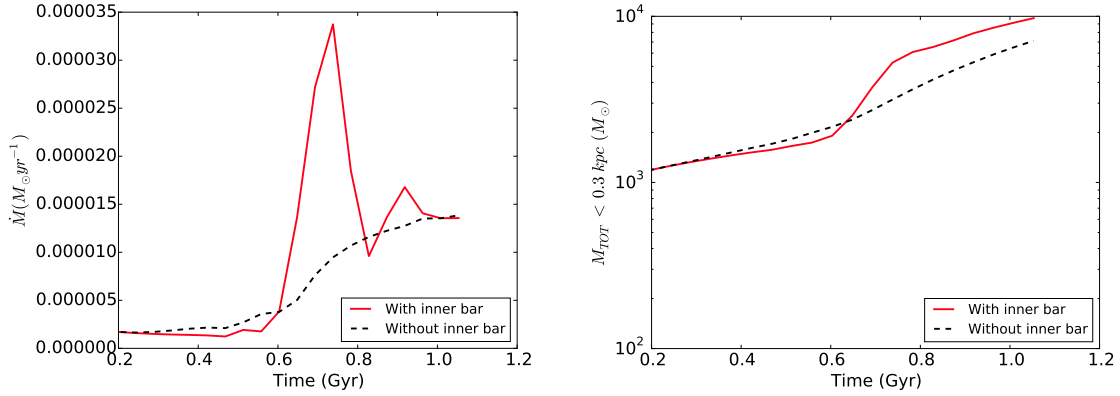

(a) (b)

FIGURE 5.15: *Left*: Gas inflow rate within 0.3 kpc for models of NGC 1291 with and without the nuclear bar. *Right*: Total gas mass within 0.3 kpc for models with and without the nuclear bar.

"What other substructures can affect the gaseous inflow?" Since the galaxy I use as a test case for all the above, i.e. NGC 1291, contains a nuclear bar with a semi-major axis of about 1 kpc, I tested the effect of this nuclear bar on gas inflow.

Nuclear bars have been proposed as a mechanism for carrying gas down to the central few parsecs of galaxies, by coupling the gas transfer from the primary bar down to the AGN (Shlosman et al., 1989). Additionally, nuclear bars are quite common, which makes them an attractive mechanism for triggering AGN activity. Erwin and Sparke (1999) found that approximately 20% of early type barred galaxies contain nuclear bars which are characteristically 5 to 7 times smaller than the main bar. Nuclear bars tend to have a random orientation with respect to the primary bar, which hints at the fact that they are dynamically decoupled (Buta and Crocker, 1993, Friedli et al., 1996). Additionally, the fact that they are present in infrared images, as is

the case for NGC 1291, indicates that they are not made up of just gas (unlike nuclear spirals which are primarily gas spirals) but also contain stars. A number of theoretical studies have examined the ability of nuclear bars to drive gas to the central regions (Shlosman et al., 1989, 1990, Friedli and Martinet, 1993, Athanassoula, 2000, Maciejewski et al., 2002) although there doesn't seem to be a consensus on whether nuclear bars are able to transport gas all the way down to the central few parsec (Laine et al., 2000).

Maciejewski et al. (2002) explored a dynamically plausible doubly barred galaxy and found that the nuclear bar in their model was unable to funnel gas down to the very central regions. The strongest argument for explaining this is that in the model they considered, the orbits in the nuclear bar are rather round, without cusps and therefore they are not conducive to forming shocks. However their conclusion is based on just one model and to our knowledge there haven't been studies of a similar nature which carry out a comprehensive exploration of dynamical models containing a primary and a nuclear bar. Also, something to note, is that the code used in this study (CMHOG, Piner et al. (1995)) is now known to have had a serious bug in the way the gravitational forces from the bar were added to the hydrodynamic equations (Kim et al., 2012). Apart from this, the hydrodynamic algorithms in CMHOG were all implemented correctly and were well tested in the original paper by Piner et al. (1995). Therefore in studies containing this error the results might not necessarily remain valid and therefore it is not clear if the results found in the original paper by Maciejewski et al. (2002) remain the same with the fixed code. Therefore it is still unclear whether nuclear bars are able or not to further transport gas down to the centralmost regions of galaxies.

The work carried out in this subsection does not attempt to be a comprehensive study of this, but simply aims to explore whether in the particular case of NGC 1291, the nuclear bar plays a role in further funnelling the gas to the centre. To explore this I run gas response simulations in a potential in which the nuclear bar is axisymmetrised (see Figure 5.13), and compare the gas inflow within the central 500 and 300 parsec with a model in which the nuclear bar is present (as those used in the above sections). It is important to note that the simulations run in this study have an important caveat, that the nuclear bar is rotating with the same pattern speed as the primary bar, which is likely unphysical (but see Knapen et al. (1995)). However, it is not trivial to find the pattern speed of the nuclear bar, and I therefore assign it the pattern speed of the primary bar. Assigning the nuclear bar a different pattern speed would add one more free parameter to the modelling and is beyond the scope of this study at this point.

We see in Figures 5.14 and 5.15, that for the model without the nuclear bar, the flow to the central 500 and 300 pc is reduced. It is again worth pointing out that the only differences between these two models are the presence or not of the nuclear bar. It is possible that this decrease would not be as significant if the nuclear bar were rotating with a different

pattern speed than the primary bar; this remains to be studied in more detail in the future. However it is clear that when the two bars rotate with the same velocity, by removing the non-axisymmetric component in the central region of the galaxy i.e. the nuclear bar, the gas inflow rate to the central few hundred parsecs is reduced. Further investigation is needed however to fully explore the effects of nuclear bars on gas inflow to the central few hundred parsec, and eventually down to even smaller scales.

5.5 Summary

In this chapter I present the results from a study on the effects of substructures, such as B/P bulges and nuclear bars, on the gaseous inflow to the central few hundred parsecs in barred galaxies. This work is a natural progression from the work presented in Chapter 2, in which I show that B/P bulges have a significant effect on models of barred galaxies, where they reduce the bar strength of the model, and significantly change the orbital structure of the galaxy. It was shown already by Athanassoula (1992a,b) that periodic orbits have a significant effect on gas flows in galaxies. This, together with the findings in Chapter 2 therefore hints at the effect that B/P bulges will have on the gaseous inflow.

For this study I ran hydrodynamic gas response simulations, as those described in Chapter 3, in models with and without B/P bulges, where all other parameters in the models are identical. The simulations have initial conditions of an axisymmetric gaseous disc in hydrostatic equilibrium and the non-axisymmetric potential is gradually introduced in order to avoid transients. I then measured the amount of gas inflow within 0.5 and 1 kpc in order to compare the inflow rate and total gas mass for models with and without B/P bulges.

I found that both for strong and weak B/P setups, the rate of gas inflow rate to the central 0.5 and 1 kiloparsec is reduced by 1-2 orders of magnitude. This leads to a significant reduction of the total gas mass present inside this radius. This result persists for different sound speeds, which shows that the result is largely insensitive to the temperature of the gas.

I also carried out the same experiments with the addition of a dark matter halo to the models, in order to check whether adding an axisymmetric component would have an effect on the difference in gas inflow for models with and without a B/P bulge. For models with the fiducial M/L of $\Upsilon_{3.6}$, and therefore a maximal disc, the addition of a dark matter halo does not significantly change the results, with only a slight decrease in the gas inflow rate. Therefore for maximal disc galaxies the B/P bulge does have a significant effect on the gas inflow to the central regions. For models with a reduced M/L and therefore a concentrated halo, i.e. for submaximal discs, the gas inflow to the central regions of the galaxy is reduced both for models with and without a B/P bulge. This occurs because the bar induced torques are

suppressed. Therefore a highly concentrated dark matter halo reduces the differences between models with and without B/P bulges, which makes the effect of the B/P bulge on the gas inflow less important.

Additionally, I present a pilot study on the effects of nuclear bars on gas inflow to the central few hundred parsec. I explored the effects of the nuclear bar present in NGC 1291 on the gaseous inflow, and found that by removing the nuclear bar, the gas inflow to the central regions is reduced. This hints at the fact that nuclear bars do help to further funnel gas down to the central regions.

I therefore conclude that B/P bulges can play a significant role on the amount of gas inflow to the central regions of galaxies, especially for galaxies which have a maximal or almost maximal disc. In the presence of a B/P bulge the gas inflow rate is reduced by 1-2 orders of magnitude, which results in 3-4 times less gas mass within the central kiloparsec of barred galaxies. This could be an additional step to explaining why it has not been trivial to find strong correlations between bars and AGN activity (see for example Lee et al. (2012), Cisternas et al. (2013)). Additionally, a pilot study on the effects of nuclear bars on gas funnelling to the central regions seems to suggest that nuclear bars help in transporting gas to scales of the order of a few hundred parsec.

6

Conclusions

"The important thing is to not stop questioning. Curiosity has its own reason for existence. One cannot help but be in awe when he contemplates the mysteries of eternity, of life, of the marvelous structure of reality. It is enough if one tries merely to comprehend a little of this mystery each day."

– Albert Einstein

By studying the dynamics of barred galaxies we can extract a wealth of information concerning their composition, formation and evolution; to do this, in this thesis I employ various methods such as dynamical models, orbital structure analysis and hydrodynamic simulations of the gas flow. These are used to study the amount of baryonic and dark matter present in the central regions of galaxies, the pattern speed of bars and the effects of substructures such as B/P bulges on gas inflow in galaxies.

This thesis begins by presenting, in **Chapter 1**, the cosmological context within which galaxies are formed and evolve. I then focused on the effects of barred galaxies on secular evolution, outlining some of the main results from observations as well as theoretical and numerical studies. I then give some analytic results from the literature which are of use for the subsequent chapters of the thesis.

In **Chapter 2**, I carried out a study on the effects of B/P bulges on dynamical models of barred galaxies, in order to see if it is necessary to include these bulges in the modelling. To do this I implemented a method for obtaining the potentials of galaxies from images, which allows for the addition of a complex height function, in which the scaleheight can be changed for different regions of the galaxy. I carried out tests on this method for deriving the potential, by comparing the results obtained to analytical results of potential-density pairs, which describe an analytic barred galaxy model; the tests showed that the method gives robust results.

I then created an analytic function describing the variations in scaleheight of a B/P bulge, modelled on the results from a high resolution N-body simulation of an isolated galaxy. Additionally, I created a height function describing a boxy bulge. Subsequently a number of different dynamical models were created with these height functions, along with the commonly used flat height function. I then compared the model with the flat height function to the model with the peanut height function and found that the forces in the plane of the galaxy have an error of up to 40% if a peanut height function is not included. Additionally, by carrying out orbital structure analysis in the different models, I found that the orbits are significantly altered in the presence of a B/P bulge. The elongation of the x_1 family of periodic orbits is decreased in models with a B/P geometry, and the extent of the x_2 family is increased by 43%, as is the distance between the two Inner Lindblad Resonances. Additionally the location of the 3:1 resonance in the disc is changed in the presence of a B/P bulge. I also examined the effect of the B/P bulge on the bar strength, as measured by Q_T, and found that the shape of Q_T is significantly affected. Indeed, the strength of the bar is reduced in the presence of a B/P bulge by up to 74%. All the aforementioned have a significant impact on the stellar as well as the gaseous kinematics in these models. I thus concluded that if a B/P bulge is thought to be present in a galaxy, it should be included in order to make the dynamical model as accurate as possible.

In **Chapter 3** the hydrodynamic simulations which are used in the subsequent chapters of the thesis are presented. These simulations are dubbed gas response simulations, as they are fixed potential simulations in which the gas is allowed to "respond" to the gravitational potential. I present the modifications made to the RAMSES code and the tests that were carried out in order to determine the effects of resolution on the locations of shocks in the gas flow.

I also show some tests that were carried out in order to determine the most adequate adaptive mesh refinement strategy for the purposes of this study. While a quasi-Lagrangian AMR strategy does not adequately capture the shocks in the gas, a density discontinuity based strategy is able to capture the shocks as well as a Cartesian grid of the same maximum resolution by using less computational resources. Attention needs to therefore be paid in studies which aim at capturing the shocks produced in the gaseous flow, where an AMR grid is used, since, depending on the refinement strategy used, the shocks are not always well captured.

Additionally, I found, in accordance with the recent results by Sormani et al. (2015), that the resolution of the simulation has a significant effect on the morphology of the gas flow, specifically on the central region; the size of the central x_2 disc can be reduced by a significant amount (up to 38%) for increasing resolutions. The locations of the shocks on the other hand are robust to within 5% for different grid resolutions. Furthermore, I find that the size of the central gaseous disc seems to converge for higher resolutions. I also examined the effect

of resolution on the velocity fields and found that that there is indeed a noticeable effect, which merits further investigation, especially since velocity fields have been used in a number of studies in the past (eg. Weiner et al. (2001), Kranz et al. (2001)) as a diagnostic for comparing the models with the observations.

In **Chapter 4** I carried out a detailed study on the dynamical properties of the nearby galaxy NGC 1291. I examined the gas flows of NGC 1291 for models with different height functions, M/L and Lagrangian radius. The parameter space is explored for a large number of combinations of the three main free parameters, in order to obtain the best fit model to the dust lanes seen in near-infrared images of the galaxy.

I show that by increasing the scaleheight of the galaxy, the forces in the plane of the galaxy are reduced, which leads to weaker and rounder shocks, as expected. This is similar to what occurs when the M/L of the model is decreased – while the concentration of the dark matter halo is correspondingly increased in order to maintain the outer part of the rotation curve flat. Furthermore, in accordance with previous results in the literature, I show that by increasing the pattern speed of the bar, the shocks in the gas are displaced from the bar semi-major axis, while the shocks become straighter (Athanassoula, 1992b, Sánchez-Menguiano et al., 2015).

There exist degeneracies between the three free parameters which do not allow to unambiguously find the best fit model for the galaxy. However, it is possible to constrain the parameter space using the relation for an isothermal disc between scaleheight, M/L, and stellar vertical velocity dispersion; thus I am able to select a small number of best fit models. To do this, I set a number of criteria for the best fit models, such that they correspond to the dust lanes in the 8 and 24μm images.

The best fit models obtained suggest that NGC 1291 has a sceleheight around the range of 0.8-1.5 kpc. The M/L of the best fit models is within the range given by stellar population synthesis and other methods (Meidt et al., 2014, Norris et al., 2014, Röck et al., 2015), i.e. $0.6\,M_{\odot}//L_{\odot}$ which confirms the validity of this type of modelling. These results lead to a maximal disc for NGC 1291 which confirms most previous findings using similar methods, i.e. that massive barred galaxies with $V_{max}\geq$200 km/s have maximal discs (Lindblad et al., 1996, Weiner et al., 2001, Kranz et al., 2003). However, there are other studies which find submaximal discs for galaxies in the mass range of NGC 1291 (e.g. Martinsson et al. (2013)), thus there is still discrepancy in the literature on this matter. Additionally, fast bars are preferred in our best fit models, which are consistent with $\mathcal{R}\leq$1.4, which is in agreement with most previous results in the literature concerning early type galaxies (Elmegreen, 1996, Rautiainen et al., 2008, Corsini, 2011).

In **Chapter 5** I present the results from a study on the effects of substructures such as B/P bulges and nuclear bars on the gaseous inflow to the central regions of barred galaxies. This

work is a natural progression from the work presented in Chapter 2, in which I show that B/P bulges have a significant effect on models of barred galaxies, where they reduce the bar strength and significantly change the orbital structure of the galaxy. It was shown already by Athanassoula (1992a,b) that periodic orbits have a significant effect on gas flows in galaxies, which therefore hinted at the effect that B/P bulges would have on the gas inflow. For this study I ran hydrodynamic gas response simulations in models with and without B/P bulges, with all the other parameters in the models being identical.

I found that both for strong and weak B/P setups, the rate of gas inflow to the central 1 and 0.5 kpc is reduced by 1-2 orders of magnitude, which leads to a significant reduction of the total mass present inside these radii. This result persists for different sound speeds, which shows that the result is insensitive to the temperature of the gas.

I also carried out the same experiment with the addition of a dark matter halo to the models, in order to check whether adding an axisymmetric component would change the conclusions. For the fiducial M/L of $\Upsilon_{3.6}$ – which leads to a maximal disc – the addition of a dark matter halo does not significantly change the results. By significantly reducing the M/L and forcing the disc to be submaximal, which leads to a highly concentrated halo, the gas inflow to the central regions of the galaxy is reduced in general, since the bar-induced torques are suppressed. Adding a highly concentrated dark matter halo also reduces the differences between models with and without B/P bulges, therefore making the effect of the B/P bulge on the gas inflow less important.

I therefore conclude that B/P bulges can play a significant role on the amount of gas inflow to the central regions of galaxies, especially for massive high surface brightness galaxies such as NGC 1291 which have a maximal disc. I also explored the effects of the nuclear bar present in NGC 1291 on the gaseous inflow, and found that by removing the nuclear bar, the gas inflow to the central regions is reduced.

Future prospects

The tools that have been created throughout this thesis have a multitude of applications, some of which I plan to pursue in the future. One thing that remains to be done is to enlarge the sample that has been studied in this thesis by including other galaxies from the S^4G survey; by studying the detailed dynamics of a larger number of galaxies we can extract statistics concerning galaxies of different morphological types in different mass ranges. Furthermore, by combining the studies of the morphology of dust lanes with available data on the gaseous velocity fields of galaxies, such as from molecular gas with upcoming ALMA observations, or from IFU observations of the Hα line which traces hot ionised gas, we can increase the predictive power of the dynamical modelling. Additionally observations from IFU data, using features in the optical and near infrared spectra, allow to better constrain the M/L of galaxies,

which subsequently enables us to obtain the dark matter composition for these galaxies. Furthermore, providing independent dynamical measures of the M/L, would in itself be of value to the scientific community, since there still remains a large amount of uncertainty in stellar population synthesis models as well as in the IMF of galaxies.

Furthermore, the tools created in this thesis can be used to determine the bar pattern speed of a large sample of galaxies. There are measurements in the literature of bar pattern speeds, however there is no conclusive evidence as to whether all bars are fast or slow. While both direct measurements of the bar pattern speed, via the Tremaine-Weinberg method, and gas dynamical simulations (Lindblad et al., 1996, Weiner et al., 2001, Pérez et al., 2004, Corsini, 2011) seem to suggest that bars in early type galaxies rotate fast, there is evidence which suggests that bars in late-type galaxies rotate slowly (Rautiainen et al., 2008). A larger sample of galaxies is therefore needed with a variety of methods for probing the bar pattern speed, in order to enlarge the statistics and get a more conclusive answer.

Additionally, by combining gas response simulations with orbital structure studies of observed galaxies, we can obtain useful insights into the detailed dynamical structure of barred galaxies and its connection to gas flows. There are a number of open questions related to this topic, such as for example the location of rings formed in the central regions of galaxies, and how this is related to the x_1 and x_2 orbits of the galaxy. By carrying out a study of the orbital structure of a sample of S^4G galaxies, carrying out gas response simulations and comparing these to observations of the gas in the galaxies, we could better understand the interplay between orbital structure and gas flows.

The results obtained in this thesis outline the importance of detailed dynamical studies for understanding galaxy structure and evolution. Substructures such as B/P bulges can play a significant role on gas transportation to the centre, which could have consequences on the build-up of the central regions of galaxies. Additionally, these studies show the power of dynamical models in exploring the parameter space in order to determine the M/L and bar pattern speed of galaxies. Indeed, with the upcoming generation of observations of galaxies in the nearby universe, such as with IFU data, these dynamical models could be extensively used in order to determine the dark matter content and bar pattern speed of disc galaxies, which can thus set constraints on models of galaxy formation and evolution.

Bibliography

J. A. L. Aguerri, J. Méndez-Abreu, and E. M. Corsini. The population of barred galaxies in the local universe. I. Detection and characterisation of bars. A&A, 495:491–504, February 2009. doi: 10.1051/0004-6361:200810931.

A. Albrecht and P. J. Steinhardt. Cosmology for grand unified theories with radiatively induced symmetry breaking. *Physical Review Letters*, 48:1220–1223, April 1982. doi: 10.1103/PhysRevLett.48.1220.

R. A. Alpher and R. Herman. Evolution of the Universe. Nature, 162:774–775, November 1948. doi: 10.1038/162774b0.

R. A. Alpher, H. Bethe, and G. Gamow. The Origin of Chemical Elements. *Physical Review*, 73:803–804, April 1948. doi: 10.1103/PhysRev.73.803.

E. Athanassoula. Bar-driven spiral structure. A&A, 88:184–193, August 1980.

E. Athanassoula. The spiral structure of galaxies. Phys. Rep., 114:319–403, 1984. doi: 10.1016/0370-1573(84)90156-X.

E. Athanassoula. Morphology of bar orbits. MNRAS, 259:328–344, November 1992a.

E. Athanassoula. The existence and shapes of dust lanes in galactic bars. MNRAS, 259:345–364, November 1992b.

E. Athanassoula. Gas Flow in Barred Galaxies. In D. Alloin, K. Olsen, and G. Galaz, editors, *Stars, Gas and Dust in Galaxies: Exploring the Links*, volume 221 of *Astronomical Society of the Pacific Conference Series*, page 243, 2000.

E. Athanassoula. What determines the strength and the slowdown rate of bars? MNRAS, 341:1179–1198, June 2003. doi: 10.1046/j.1365-8711.2003.06473.x.

E. Athanassoula. On the nature of bulges in general and of box/peanut bulges in particular: input from N-body simulations. MNRAS, 358:1477–1488, April 2005. doi: 10.1111/j.1365-2966.2005.08872.x.

E. Athanassoula. Secular Evolution of Disc Galaxies and of their Components. *ArXiv Astrophysics e-prints*, October 2006.

E. Athanassoula. Boxy/peanut and discy bulges : formation, evolution and properties. *ArXiv e-prints*, February 2008a.

E. Athanassoula. Secular Evolution of Disc Galaxies and of their Components. In K. Wada and F. Combes, editors, *Mapping the Galaxy and Nearby Galaxies*, page 47, 2008b. doi: 10.1007/978-0-387-72768-4_7.

E. Athanassoula. *Bars and secular evolution in disk galaxies: Theoretical input*, page 305. October 2013.

E. Athanassoula. "The thick part of galactic bars, boxy/peanut/X bulges and barlenses: What are they and how did they form". In E. Laurikainen, D. A. Gadotti, and R. Peletier, editors, *Galactic Bulges*, 2015.

E. Athanassoula and R. L. Beaton. Unravelling the mystery of the M31 bar. MNRAS, 370: 1499–1512, August 2006. doi: 10.1111/j.1365-2966.2006.10567.x.

E. Athanassoula and M. Bureau. Bar Diagnostics in Edge-on Spiral Galaxies. II. Hydrodynamical Simulations. ApJ, 522:699–717, September 1999. doi: 10.1086/307677.

E. Athanassoula and A. Misiriotis. Morphology, photometry and kinematics of N -body bars - I. Three models with different halo central concentrations. MNRAS, 330:35–52, February 2002. doi: 10.1046/j.1365-8711.2002.05028.x.

E. Athanassoula, A. Bosma, and S. Papaioannou. Halo parameters of spiral galaxies. A&A, 179:23–40, June 1987.

E. Athanassoula, E. Fady, J. C. Lambert, and A. Bosma. Optimal softening for force calculations in collisionless N-body simulations. MNRAS, 314:475–488, May 2000. doi: 10.1046/j.1365-8711.2000.03316.x.

E. Athanassoula, J. C. Lambert, and W. Dehnen. Can bars be destroyed by a central mass concentration?- I. Simulations. MNRAS, 363:496–508, October 2005. doi: 10.1111/j.1365-2966.2005.09445.x.

E. Athanassoula, M. Romero-Gómez, and J. J. Masdemont. Rings and spirals in barred galaxies - I. Building blocks. MNRAS, 394:67–81, March 2009. doi: 10.1111/j.1365-2966.2008.14273.x.

E. Athanassoula, R. E. G. Machado, and S. A. Rodionov. Bar formation and evolution in disc galaxies with gas and a triaxial halo: morphology, bar strength and halo properties. MNRAS, 429:1949–1969, March 2013. doi: 10.1093/mnras/sts452.

E. Athanassoula, E. Laurikainen, H. Salo, and A. Bosma. On the nature of the barlens component in barred galaxies. *ArXiv e-prints*, May 2014.

F. D. Barazza, S. Jogee, and I. Marinova. Bars in Disk-dominated and Bulge-dominated Galaxies at z ˜ 0: New Insights from ˜3600 SDSS Galaxies. ApJ, 675:1194–1212, March 2008. doi: 10.1086/526510.

J. E. Barnes and L. Hernquist. Dynamics of interacting galaxies. ARA&A, 30:705–742, 1992. doi: 10.1146/annurev.aa.30.090192.003421.

E. F. Bell and R. S. de Jong. Stellar Mass-to-Light Ratios and the Tully-Fisher Relation. ApJ, 550:212–229, March 2001. doi: 10.1086/319728.

G. J. Bendo, D. Calzetti, C. W. Engelbracht, R. C. Kennicutt, M. J. Meyer, M. D. Thornley, F. Walter, D. A. Dale, A. Li, and E. J. Murphy. Variations in 24-μm morphologies among galaxies in the Spitzer Infrared Nearby Galaxies Survey: new insights into the Hubble sequence. MNRAS, 380:1313–1334, October 2007. doi: 10.1111/j.1365-2966.2007.12204.x.

G. J. Bendo, B. T. Draine, C. W. Engelbracht, G. Helou, M. D. Thornley, C. Bot, B. A. Buckalew, D. Calzetti, D. A. Dale, D. J. Hollenbach, A. Li, and J. Moustakas. The relations among 8, 24 and 160 μm dust emission within nearby spiral galaxies. MNRAS, 389:629–650, September 2008. doi: 10.1111/j.1365-2966.2008.13567.x.

G. J. Bendo, C. D. Wilson, B. E. Warren, E. Brinks, H. M. Butner, P. Chanial, D. L. Clements, S. Courteau, J. Irwin, F. P. Israel, J. H. Knapen, J. Leech, H. E. Matthews, S. Mühle, G. Petitpas, S. Serjeant, B. K. Tan, R. P. J. Tilanus, A. Usero, M. Vaccari, P. van der Werf, C. Vlahakis, T. Wiegert, and M. Zhu. The JCMT Nearby Galaxies Legacy Survey - III. Comparisons of cold dust, polycyclic aromatic hydrocarbons, molecular gas and atomic gas in NGC 2403. MNRAS, 402:1409–1425, March 2010. doi: 10.1111/j.1365-2966.2009.16043.x.

I. Berentzen, C. H. Heller, I. Shlosman, and K. J. Fricke. Gas-driven evolution of stellar orbits in barred galaxies. MNRAS, 300:49–63, October 1998. doi: 10.1046/j.1365-8711.1998.01836.x.

M. A. Bershady, M. A. W. Verheijen, R. A. Swaters, D. R. Andersen, K. B. Westfall, and T. Martinsson. The DiskMass Survey. I. Overview. ApJ, 716:198–233, June 2010. doi: 10.1088/0004-637X/716/1/198.

J. Binney. Resonant excitation of motion perpendicular to galactic planes. MNRAS, 196: 455–467, August 1981.

James Binney and Scott Tremaine. *Galactic Dynamics*. Princeton University Press, 2 edition, 2008. URL http://amazon.com/o/ASIN/0691130272/.

N. Bissantz and O. Gerhard. Spiral arms, bar shape and bulge microlensing in the Milky Way. MNRAS, 330:591–608, March 2002. doi: 10.1046/j.1365-8711.2002.05116.x.

N. Bissantz, P. Englmaier, and O. Gerhard. Gas dynamics in the Milky Way: second pattern speed and large-scale morphology. MNRAS, 340:949–968, April 2003. doi: 10.1046/j.1365-8711.2003.06358.x.

G. R. Blumenthal, S. M. Faber, J. R. Primack, and M. J. Rees. Formation of galaxies and large-scale structure with cold dark matter. Nature, 311:517–525, October 1984. doi: 10.1038/311517a0.

H. Bondi and T. Gold. The Steady-State Theory of the Expanding Universe. MNRAS, 108: 252, 1948.

A. Boselli and G. Gavazzi. Environmental Effects on Late-Type Galaxies in Nearby Clusters. PASP, 118:517–559, April 2006. doi: 10.1086/500691.

A. Bosma. *The distribution and kinematics of neutral hydrogen in spiral galaxies of various morphological types*. PhD thesis, PhD Thesis, Groningen Univ., (1978), 1978.

A. Bosma. 21-cm line studies of spiral galaxies. II. The distribution and kinematics of neutral hydrogen in spiral galaxies of various morphological types. AJ, 86:1825–1846, December 1981. doi: 10.1086/113063.

A. Bosma, D. A. Gadotti, W. J. G. de Blok, and E. Athanassoula. Kinematics of the Barred Spiral Galaxy NGC 1291. In L. Verdes-Montenegro, A. Del Olmo, and J. Sulentic, editors, *Galaxies in Isolation: Exploring Nature Versus Nurture*, volume 421 of *Astronomical Society of the Pacific Conference Series*, page 53, October 2010.

R. Bottema. The Stellar Kinematics of Galactic Disks. A&A, 275:16, August 1993.

J. Bovy and H.-W. Rix. A Direct Dynamical Measurement of the Milky Way's Disk Surface Density Profile, Disk Scale Length, and Dark Matter Profile at 4 kpc ˜ R ˜ 9 kpc. ApJ, 779: 115, December 2013. doi: 10.1088/0004-637X/779/2/115.

M. Boylan-Kolchin, J. S. Bullock, and M. Kaplinghat. The Milky Way's bright satellites as an apparent failure of ΛCDM. MNRAS, 422:1203–1218, May 2012. doi: 10.1111/j.1365-2966.2012.20695.x.

J. N. Bregman, D. E. Hogg, and M. S. Roberts. The interaction between hot and cold gas in early-type galaxies. ApJ, 441:561–567, March 1995. doi: 10.1086/175382.

M. Bureau and E. Athanassoula. Bar Diagnostics in Edge-on Spiral Galaxies. I. The Periodic Orbits Approach. ApJ, 522:686–698, September 1999. doi: 10.1086/307675.

M. Bureau and E. Athanassoula. Bar Diagnostics in Edge-On Spiral Galaxies. III. N-Body Simulations of Disks. ApJ, 626:159–173, June 2005. doi: 10.1086/430056.

R. Buta. The structure and dynamics of ringed galaxies. I - The morphology of galaxy rings, and statistics of their apparent shapes, relative sizes, and apparent orientations with respect to bars. ApJS, 61:609–630, August 1986. doi: 10.1086/191126.

R. Buta and D. L. Block. A Dust-penetrated Classification Scheme for Bars as Inferred from Their Gravitational Force Fields. ApJ, 550:243–252, March 2001. doi: 10.1086/319736.

R. Buta and D. A. Crocker. The strange 'barred' spiral galaxy ESO 235-58 - A case of morphological deception. AJ, 106:939–947, September 1993. doi: 10.1086/116695.

R. J. Buta, K. Sheth, M. Regan, J. L. Hinz, A. Gil de Paz, K. Menéndez-Delmestre, J.-C. Munoz-Mateos, M. Seibert, E. Laurikainen, H. Salo, D. A. Gadotti, E. Athanassoula, A. Bosma, J. H. Knapen, L. C. Ho, B. F. Madore, D. M. Elmegreen, K. L. Masters, S. Comerón, M. Aravena, and T. Kim. Mid-infrared Galaxy Morphology from the Spitzer Survey of Stellar Structure in Galaxies (S^4G): The Imprint of the De Vaucouleurs Revised Hubble-Sandage Classification System at 3.6 μm. ApJS, 190:147–165, September 2010. doi: 10.1088/0067-0049/190/1/147.

R. J. Buta, K. Sheth, E. Athanassoula, A. Bosma, J. H. Knapen, E. Laurikainen, H. Salo, D. Elmegreen, L. C. Ho, D. Zaritsky, H. Courtois, J. L. Hinz, J.-C. Muñoz-Mateos, T. Kim, M. W. Regan, D. A. Gadotti, A. Gil de Paz, J. Laine, K. Menéndez-Delmestre, S. Comerón, S. Erroz Ferrer, M. Seibert, T. Mizusawa, B. Holwerda, and B. F. Madore. A Classical Morphological Analysis of Galaxies in the Spitzer Survey of Stellar Structure in Galaxies (S4G). ApJS, 217:32, April 2015. doi: 10.1088/0067-0049/217/2/32.

M. Cappellari, E. Emsellem, D. Krajnović, R. M. McDermid, P. Serra, K. Alatalo, L. Blitz, M. Bois, F. Bournaud, M. Bureau, R. L. Davies, T. A. Davis, P. T. de Zeeuw, S. Khochfar, H. Kuntschner, P.-Y. Lablanche, R. Morganti, T. Naab, T. Oosterloo, M. Sarzi, N. Scott, A.-M. Weijmans, and L. M. Young. The ATLAS^{3D} project - VII. A new look at the morphology of nearby galaxies: the kinematic morphology-density relation. MNRAS, 416:1680–1696, September 2011. doi: 10.1111/j.1365-2966.2011.18600.x.

A. Chung and M. Bureau. Stellar Kinematics of Boxy Bulges: Large-Scale Bars and Inner Disks. AJ, 127:3192–3212, June 2004. doi: 10.1086/420988.

M. Cisternas, D. A. Gadotti, J. H. Knapen, T. Kim, S. Díaz-García, E. Laurikainen, H. Salo, O. González-Martín, L. C. Ho, B. G. Elmegreen, D. Zaritsky, K. Sheth, E. Athanassoula, A. Bosma, S. Comerón, S. Erroz-Ferrer, A. Gil de Paz, J. L. Hinz, B. W. Holwerda, J. Laine, S. Meidt, K. Menéndez-Delmestre, T. Mizusawa, J. C. Muñoz-Mateos, M. W. Regan, and M. Seibert. X-Ray Nuclear Activity in S^4G Barred Galaxies: No Link between Bar Strength

and Co-occurrent Supermassive Black Hole Fueling. ApJ, 776:50, October 2013. doi: 10.1088/0004-637X/776/1/50.

P. Coelho and D. A. Gadotti. Bars Rejuvenating Bulges? Evidence from Stellar Population Analysis. ApJ, 743:L13, December 2011. doi: 10.1088/2041-8205/743/1/L13.

M. Colless, G. Dalton, S. Maddox, W. Sutherland, P. Norberg, S. Cole, J. Bland-Hawthorn, T. Bridges, R. Cannon, C. Collins, W. Couch, N. Cross, K. Deeley, R. De Propris, S. P. Driver, G. Efstathiou, R. S. Ellis, C. S. Frenk, K. Glazebrook, C. Jackson, O. Lahav, I. Lewis, S. Lumsden, D. Madgwick, J. A. Peacock, B. A. Peterson, I. Price, M. Seaborne, and K. Taylor. The 2dF Galaxy Redshift Survey: spectra and redshifts. MNRAS, 328:1039–1063, December 2001. doi: 10.1046/j.1365-8711.2001.04902.x.

F. Combes. Fueling the AGN. In I. Aretxaga, D. Kunth, and R. Mújica, editors, *Advanced Lectures on the Starburst-AGN*, page 223, 2001.

F. Combes and M. Gerin. Spiral structure of molecular clouds in response to bar forcing - A particle simulation. A&A, 150:327–338, September 1985.

F. Combes and R. H. Sanders. Formation and properties of persisting stellar bars. A&A, 96: 164–173, March 1981.

F. Combes, F. Debbasch, D. Friedli, and D. Pfenniger. Box and peanut shapes generated by stellar bars. A&A, 233:82–95, July 1990.

S. Comerón, H. Salo, E. Laurikainen, J. H. Knapen, R. J. Buta, M. Herrera-Endoqui, J. Laine, B. W. Holwerda, K. Sheth, M. W. Regan, J. L. Hinz, J. C. Muñoz-Mateos, A. Gil de Paz, K. Menéndez-Delmestre, M. Seibert, T. Mizusawa, T. Kim, S. Erroz-Ferrer, D. A. Gadotti, E. Athanassoula, A. Bosma, and L. C. Ho. ARRAKIS: atlas of resonance rings as known in the S^4G. A&A, 562:A121, February 2014. doi: 10.1051/0004-6361/201321633.

C. Conroy, J. E. Gunn, and M. White. The Propagation of Uncertainties in Stellar Population Synthesis Modeling. I. The Relevance of Uncertain Aspects of Stellar Evolution and the Initial Mass Function to the Derived Physical Properties of Galaxies. ApJ, 699:486–506, July 2009. doi: 10.1088/0004-637X/699/1/486.

C. J. Conselice. The fundamental properties of galaxies and a new galaxy classification system. MNRAS, 373:1389–1408, December 2006. doi: 10.1111/j.1365-2966.2006.11114.x.

G. Contopoulos. How far do bars extend. A&A, 81:198–209, January 1980.

G. Contopoulos and P. Grosbol. Orbits in barred galaxies. A&A Rev., 1:261–289, November 1989. doi: 10.1007/BF00873080.

G. Contopoulos and M. Harsoula. 3D chaotic diffusion in barred spiral galaxies. MNRAS, 436:1201–1214, December 2013. doi: 10.1093/mnras/stt1640.

G. Contopoulos and T. Papayannopoulos. Orbits in weak and strong bars. A&A, 92:33–46, December 1980.

E. M. Corsini. Direct measurements of bar pattern speeds. *Memorie della Societa Astronomica Italiana Supplementi*, 18:23, 2011.

S. Courteau and H.-W. Rix. Maximal Disks and the Tully-Fisher Relation. ApJ, 513:561–571, March 1999. doi: 10.1086/306872.

H. H. Crowl, J. D. P. Kenney, J. H. van Gorkom, and B. Vollmer. Dense Cloud Ablation and Ram Pressure Stripping of the Virgo Spiral NGC 4402. AJ, 130:65–72, July 2005. doi: 10.1086/430526.

M. Dahlem, K. A. Weaver, and T. M. Heckman. An X-Ray Minisurvey of Nearby Edge-on Starburst Galaxies. I. The Data. ApJS, 118:401–453, October 1998. doi: 10.1086/313137.

P. de Bernardis, P. A. R. Ade, J. J. Bock, J. R. Bond, J. Borrill, A. Boscaleri, K. Coble, B. P. Crill, G. De Gasperis, P. C. Farese, P. G. Ferreira, K. Ganga, M. Giacometti, E. Hivon, V. V. Hristov, A. Iacoangeli, A. H. Jaffe, A. E. Lange, L. Martinis, S. Masi, P. V. Mason, P. D. Mauskopf, A. Melchiorri, L. Miglio, T. Montroy, C. B. Netterfield, E. Pascale, F. Piacentini, D. Pogosyan, S. Prunet, S. Rao, G. Romeo, J. E. Ruhl, F. Scaramuzzi, D. Sforna, and N. Vittorio. A flat Universe from high-resolution maps of the cosmic microwave background radiation. Nature, 404:955–959, April 2000.

W. J. G. de Blok. The Core-Cusp Problem. *Advances in Astronomy*, 2010:789293, 2010. doi: 10.1155/2010/789293.

W. J. G. de Blok, S. S. McGaugh, A. Bosma, and V. C. Rubin. Mass Density Profiles of Low Surface Brightness Galaxies. ApJ, 552:L23–L26, May 2001. doi: 10.1086/320262.

R. de Grijs. The global structure of galactic discs. MNRAS, 299:595–610, September 1998. doi: 10.1046/j.1365-8711.1998.01896.x.

G. de Vaucouleurs, A. de Vaucouleurs, and J. R. Corwin. Second reference catalogue of bright galaxies. In *Second reference catalogue of bright galaxies, 1976, Austin: University of Texas Press.*, page 0, 1976.

G. de Vaucouleurs, A. de Vaucouleurs, H. G. Corwin, Jr., R. J. Buta, G. Paturel, and P. Fouqué. *Third Reference Catalogue of Bright Galaxies. Volume I: Explanations and references. Volume II: Data for galaxies between 0^h and 12^h. Volume III: Data for galaxies between 12^h and 24^h.* 1991a.

G. de Vaucouleurs, A. de Vaucouleurs, H. G. Corwin, Jr., R. J. Buta, G. Paturel, and P. Fouqué. *Third Reference Catalogue of Bright Galaxies. Volume I: Explanations and references. Volume II: Data for galaxies between 0^h and 12^h. Volume III: Data for galaxies between 12^h and 24^h.* 1991b.

V. P. Debattista and J. A. Sellwood. Constraints from Dynamical Friction on the Dark Matter Content of Barred Galaxies. ApJ, 543:704–721, November 2000. doi: 10.1086/317148.

V. P. Debattista, C. M. Carollo, L. Mayer, and B. Moore. The Kinematic Signature of Face-On Peanut-shaped Bulges. ApJ, 628:678–694, August 2005. doi: 10.1086/431292.

W. Dehnen. A Family of Potential-Density Pairs for Spherical Galaxies and Bulges. MNRAS, 265:250, November 1993.

A. Dekel, Y. Birnboim, G. Engel, J. Freundlich, T. Goerdt, M. Mumcuoglu, E. Neistein, C. Pichon, R. Teyssier, and E. Zinger. Cold streams in early massive hot haloes as the main mode of galaxy formation. Nature, 457:451–454, January 2009. doi: 10.1038/nature07648.

P. Di Matteo, A. Gómez, M. Haywood, F. Combes, M. D. Lehnert, M. Ness, O. N. Snaith, D. Katz, and B. Semelin. Why the Milky Way's bulge is not only a bar formed from a cold thin disk. A&A, 577:A1, May 2015. doi: 10.1051/0004-6361/201424457.

E. M. Di Teodoro and F. Fraternali. ^{3D} BAROLO: a new 3D algorithm to derive rotation curves of galaxies. MNRAS, 451:3021–3033, August 2015. doi: 10.1093/mnras/stv1213.

S. Díaz-García, H. Salo, E. Laurikainen, and M. Herrera-Endoqui. Characterization of galactic bars from 3.6 μm S^{4}G imaging. *ArXiv e-prints*, September 2015.

A. Dressler. Galaxy morphology in rich clusters - Implications for the formation and evolution of galaxies. ApJ, 236:351–365, March 1980. doi: 10.1086/157753.

Y. Dubois, C. Pichon, M. Haehnelt, T. Kimm, A. Slyz, J. Devriendt, and D. Pogosyan. Feeding compact bulges and supermassive black holes with low angular momentum cosmic gas at high redshift. MNRAS, 423:3616–3630, July 2012. doi: 10.1111/j.1365-2966.2012.21160.x.

G. Efstathiou and J. Silk. The formation of galaxies. Fund. Cosmic Phys., 9:1–138, November 1983.

G. Efstathiou, G. Lake, and J. Negroponte. The stability and masses of disc galaxies. MNRAS, 199:1069–1088, June 1982.

A. Einstein. Die Feldgleichungen der Gravitation. *Sitzungsberichte der Königlich Preußischen Akademie der Wissenschaften (Berlin), Seite 844-847.*, pages 844–847, 1915.

A. Einstein. Die Grundlage der allgemeinen Relativitätstheorie. *Annalen der Physik*, 354: 769–822, 1916. doi: 10.1002/andp.19163540702.

A. Einstein and W. de Sitter. On the Relation between the Expansion and the Mean Density of the Universe. *Proceedings of the National Academy of Science*, 18:213–214, March 1932. doi: 10.1073/pnas.18.3.213.

S. L. Ellison, P. Nair, D. R. Patton, J. M. Scudder, J. T. Mendel, and L. Simard. The impact of gas inflows on star formation rates and metallicities in barred galaxies. MNRAS, 416: 2182–2192, September 2011. doi: 10.1111/j.1365-2966.2011.19195.x.

B. Elmegreen. Pattern Speeds in Barred Galaxies. In R. Buta, D. A. Crocker, and B. G. Elmegreen, editors, *IAU Colloq. 157: Barred Galaxies*, volume 91 of *Astronomical Society of the Pacific Conference Series*, page 197, 1996.

B. G. Elmegreen and D. M. Elmegreen. Properties of barred spiral galaxies. ApJ, 288:438–455, January 1985. doi: 10.1086/162810.

E. Emsellem, M. Cappellari, D. Krajnović, K. Alatalo, L. Blitz, M. Bois, F. Bournaud, M. Bureau, R. L. Davies, T. A. Davis, P. T. de Zeeuw, S. Khochfar, H. Kuntschner, P.-Y. Lablanche, R. M. McDermid, R. Morganti, T. Naab, T. Oosterloo, M. Sarzi, N. Scott, P. Serra, G. van de Ven, A.-M. Weijmans, and L. M. Young. The ATLAS^{3D} project - III. A census of the stellar angular momentum within the effective radius of early-type galaxies: unveiling the distribution of fast and slow rotators. MNRAS, 414:888–912, June 2011. doi: 10.1111/j.1365-2966.2011.18496.x.

E. Emsellem, F. Renaud, F. Bournaud, B. Elmegreen, F. Combes, and J. Gabor. The interplay between a galactic bar and a supermassive black hole: nuclear fueling in a sub-parsec resolution galaxy simulation. *ArXiv e-prints*, October 2014.

P. Englmaier and O. Gerhard. Two modes of gas flow in a single barred galaxy. MNRAS, 287: 57–68, May 1997.

P. Erwin and V. P. Debattista. Peanuts at an angle: detecting and measuring the three-dimensional structure of bars in moderately inclined galaxies. MNRAS, 431:3060–3086, June 2013. doi: 10.1093/mnras/stt385.

P. Erwin and L. S. Sparke. A WIYN Survey of Early-Type Barred Galaxies: Double Bars and Central Structures. In D. R. Merritt, M. Valluri, and J. A. Sellwood, editors, *Galaxy Dynamics - A Rutgers Symposium*, volume 182 of *Astronomical Society of the Pacific Conference Series*, page 243, August 1999.

M. Eskew, D. Zaritsky, and S. Meidt. Converting from 3.6 and 4.5 μm Fluxes to Stellar Mass. AJ, 143:139, June 2012. doi: 10.1088/0004-6256/143/6/139.

P. B. Eskridge, J. A. Frogel, R. W. Pogge, A. C. Quillen, R. L. Davies, D. L. DePoy, M. L. Houdashelt, L. E. Kuchinski, S. V. Ramírez, K. Sellgren, D. M. Terndrup, and G. P. Tiede.

The Frequency of Barred Spiral Galaxies in the Near-Infrared. AJ, 119:536–544, February 2000. doi: 10.1086/301203.

J. Falcón-Barroso, M. Lyubenova, and G. van de Ven. Angular Momentum across the Hubble sequence from the CALIFA survey. In M. Cappellari and S. Courteau, editors, *IAU Symposium*, volume 311 of *IAU Symposium*, pages 78–81, April 2015. doi: 10.1017/S1743921315003439.

K. Foyle, H.-W. Rix, and S. Zibetti. An observational estimate for the mean secular evolution rate in spiral galaxies. MNRAS, 407:163–180, September 2010. doi: 10.1111/j.1365-2966.2010.16931.x.

F. Fragkoudi, E. Athanassoula, A. Bosma, and F. Iannuzzi. The effects of Boxy/Peanut bulges on galaxy models. MNRAS, 450:229–245, June 2015. doi: 10.1093/mnras/stv537.

F. Fraternali, A. Marasco, F. Marinacci, and J. Binney. Ionized Absorbers as Evidence for Supernova-driven Cooling of the Lower Galactic Corona. ApJ, 764:L21, February 2013. doi: 10.1088/2041-8205/764/2/L21.

C. S. Frenk and S. D. M. White. Dark matter and cosmic structure. *Annalen der Physik*, 524: 507–534, October 2012. doi: 10.1002/andp.201200212.

D. Friedli and L. Martinet. Bars Within Bars in Lenticular and Spiral Galaxies - a Step in Secular Evolution. A&A, 277:27, September 1993.

D. Friedli, H. Wozniak, M. Rieke, L. Martinet, and P. Bratschi. Disc galaxies with multiple triaxial structures. II. JHK surface photometry and numerical simulations. A&AS, 118: 461–479, September 1996.

D. A. Gadotti. Image decomposition of barred galaxies and AGN hosts. MNRAS, 384:420–439, February 2008. doi: 10.1111/j.1365-2966.2007.12723.x.

D. A. Gadotti. Structural properties of pseudo-bulges, classical bulges and elliptical galaxies: a Sloan Digital Sky Survey perspective. MNRAS, 393:1531–1552, March 2009. doi: 10.1111/j.1365-2966.2008.14257.x.

D. A. Gadotti. Secular evolution and structural properties of stellar bars in galaxies. MNRAS, 415:3308–3318, August 2011. doi: 10.1111/j.1365-2966.2011.18945.x.

Mark Galassi, Jim Davies, James Theiler, Brian Gough, Gerard Jungman, Michael Booth, and Fabrice Rossi. *Gnu Scientific Library: Reference Manual*. Network Theory Ltd., February 2003. ISBN 0954161734. URL http://www.worldcat.org/isbn/0954161734.

E. Gardner, V. P. Debattista, A. C. Robin, S. Vásquez, and M. Zoccali. N-body simulation insights into the X-shaped bulge of the Milky Way: kinematics and distance to the Galactic Centre. MNRAS, 438:3275–3290, March 2014. doi: 10.1093/mnras/stt2430.

R. A. Gingold and J. J. Monaghan. Smoothed particle hydrodynamics - Theory and application to non-spherical stars. MNRAS, 181:375–389, November 1977.

O. Y. Gnedin, D. H. Weinberg, J. Pizagno, F. Prada, and H.-W. Rix. Dark Matter Halos of Disk Galaxies: Constraints from the Tully-Fisher Relation. ApJ, 671:1115–1134, December 2007. doi: 10.1086/523256.

A. H. Guth. Inflationary universe: A possible solution to the horizon and flatness problems. Phys. Rev. D, 23:347–356, January 1981. doi: 10.1103/PhysRevD.23.347.

S. Haan, E. Schinnerer, E. Emsellem, S. García-Burillo, F. Combes, C. G. Mundell, and H.-W. Rix. Dynamical Evolution of AGN Host GalaxiesGas In/Out-Flow Rates in Seven NUGA Galaxies. ApJ, 692:1623–1661, February 2009. doi: 10.1088/0004-637X/692/2/1623.

C. Hamadache, L. Le Guillou, P. Tisserand, C. Afonso, J. N. Albert, J. Andersen, R. Ansari, É. Aubourg, P. Bareyre, J. P. Beaulieu, X. Charlot, C. Coutures, R. Ferlet, P. Fouqué, J. F. Glicenstein, B. Goldman, A. Gould, D. Graff, M. Gros, J. Haissinski, J. de Kat, É. Lesquoy, C. Loup, C. Magneville, J. B. Marquette, É. Maurice, A. Maury, A. Milsztajn, M. Moniez, N. Palanque-Delabrouille, O. Perdereau, Y. R. Rahal, J. Rich, M. Spiro, A. Vidal-Madjar, L. Vigroux, and S. Zylberajch. Galactic Bulge microlensing optical depth from EROS-2. A&A, 454:185–199, July 2006. doi: 10.1051/0004-6361:20064893.

M. Harsoula and C. Kalapotharakos. Orbital structure in N-body models of barred-spiral galaxies. MNRAS, 394:1605–1619, April 2009. doi: 10.1111/j.1365-2966.2009.14427.x.

H. Hasan, D. Pfenniger, and C. Norman. Galactic bars with central mass concentrations - Three-dimensional dynamics. ApJ, 409:91–109, May 1993. doi: 10.1086/172644.

T. M. Heckman. Starburst-Driven Galactic Winds. In V. Avila-Reese, C. Firmani, C. S. Frenk, and C. Allen, editors, *Revista Mexicana de Astronomia y Astrofisica Conference Series*, volume 17 of *Revista Mexicana de Astronomia y Astrofisica, vol. 27*, pages 47–55, June 2003.

M. Herrera-Endoqui, S. Díaz-García, E. Laurikainen, and H. Salo. Catalogue of the morphological features in the Spitzer Survey of Stellar Structure in Galaxies (S$ˆ4$G). *ArXiv e-prints*, September 2015.

R. W. Hockney and J. W. Eastwood. *Computer simulation using particles*. 1988.

D. E. Hogg, M. S. Roberts, J. N. Bregman, and M. P. Haynes. Hot and Cold Gas in Early-Type Spirals: NGC 3623, NGC 2775, and NGC 1291. AJ, 121:1336–1357, March 2001. doi: 10.1086/319400.

F. Hohl. Numerical Experiments with a Disk of Stars. ApJ, 168:343, September 1971. doi: 10.1086/151091.

P. F. Hopkins, T. J. Cox, J. D. Younger, and L. Hernquist. How do Disks Survive Mergers? ApJ, 691:1168–1201, February 2009. doi: 10.1088/0004-637X/691/2/1168.

C. D. Howard, R. M. Rich, W. Clarkson, R. Mallery, J. Kormendy, R. De Propris, A. C. Robin, R. Fux, D. B. Reitzel, H. S. Zhao, K. Kuijken, and A. Koch. Kinematics at the Edge of the Galactic Bulge: Evidence for Cylindrical Rotation. ApJ, 702:L153–L157, September 2009. doi: 10.1088/0004-637X/702/2/L153.

F. Hoyle. A New Model for the Expanding Universe. MNRAS, 108:372, 1948.

E. Hubble. A Relation between Distance and Radial Velocity among Extra-Galactic Nebulae. *Proceedings of the National Academy of Science*, 15:168–173, March 1929. doi: 10.1073/pnas.15.3.168.

E. Hubble and M. L. Humason. The Velocity-Distance Relation among Extra-Galactic Nebulae. ApJ, 74:43, July 1931. doi: 10.1086/143323.

E. P. Hubble. *Realm of the Nebulae*. 1936.

S. Joersaeter. The velocity field of NGC 1365. In J.-L. Nieto, editor, *New Aspects of Galaxy Photometry*, volume 232 of *Lecture Notes in Physics, Berlin Springer Verlag*, page 287, 1985. doi: 10.1007/BFb0030960.

M. R. Joung, M. E. Putman, G. L. Bryan, X. Fernández, and J. E. G. Peek. Gas Accretion is Dominated by Warm Ionized Gas in Milky Way Mass Galaxies at z ˜ 0. ApJ, 759:137, November 2012. doi: 10.1088/0004-637X/759/2/137.

C. Kalapotharakos, P. A. Patsis, and P. Grosbøl. NGC 1300 dynamics - I. The gravitational potential as a tool for detailed stellar dynamics. MNRAS, 403:83–95, March 2010a. doi: 10.1111/j.1365-2966.2009.16127.x.

C. Kalapotharakos, P. A. Patsis, and P. Grosbøl. NGC1300 dynamics - II. The response models. MNRAS, 408:9–21, October 2010b. doi: 10.1111/j.1365-2966.2010.17061.x.

J. J. Kamphuis. PhD thesis, PhD Thesis, University of Groningen, (1993), 1993.

W. Kapferer, C. Ferrari, W. Domainko, M. Mair, T. Kronberger, S. Schindler, S. Kimeswenger, E. van Kampen, D. Breitschwerdt, and M. Ruffert. Simulations of galactic winds and starbursts in galaxy clusters. A&A, 447:827–842, March 2006. doi: 10.1051/0004-6361:20053975.

J. D. P. Kenney, J. H. van Gorkom, and B. Vollmer. VLA H I Observations of Gas Stripping in the Virgo Cluster Spiral NGC 4522. AJ, 127:3361–3374, June 2004. doi: 10.1086/420805.

R. C. Kennicutt, Jr., L. Armus, G. Bendo, D. Calzetti, D. A. Dale, B. T. Draine, C. W. Engelbracht, K. D. Gordon, A. D. Grauer, G. Helou, D. J. Hollenbach, T. H. Jarrett,

Kewley, et al. SINGS: The SIRTF Nearby Galaxies Survey. PASP, 115:928–952, August 2003. doi: 10.1086/376941.

W.-T. Kim, W.-Y. Seo, J. M. Stone, D. Yoon, and P. J. Teuben. Central Regions of Barred Galaxies: Two-dimensional Non-self-gravitating Hydrodynamic Simulations. ApJ, 747:60, March 2012. doi: 10.1088/0004-637X/747/1/60.

J. H. Knapen. *Barred Galaxies and Galaxy Evolution*, page 175. 2007. doi: 10.1007/978-1-4020-5573-7_29.

J. H. Knapen, J. E. Beckman, C. H. Heller, I. Shlosman, and R. S. de Jong. The Central Region in M100: Observations and Modeling. ApJ, 454:623, December 1995. doi: 10.1086/176516.

J. H. Knapen, I. Shlosman, and R. F. Peletier. A Subarcsecond Resolution Near-Infrared Study of Seyfert and "Normal" Galaxies. II. Morphology. ApJ, 529:93–100, January 2000. doi: 10.1086/308266.

J. H. Knapen, D. Pérez-Ramírez, and S. Laine. Circumnuclear regions in barred spiral galaxies - II. Relations to host galaxies. MNRAS, 337:808–828, December 2002. doi: 10.1046/j.1365-8711.2002.05840.x.

J. H. Knapen, L. F. Whyte, W. J. G. de Blok, and J. M. van der Hulst. The nuclear ring in the unbarred galaxy NGC 278: Result of a minor merger? A&A, 423:481–493, August 2004. doi: 10.1051/0004-6361:20034336.

E. Kormendy. . In E. Laurikainen, D. A. Gadotti, and R. Peletier, editors, *Galactic Bulges*, 2015.

J. Kormendy and R. C. Kennicutt, Jr. Secular Evolution and the Formation of Pseudobulges in Disk Galaxies. ARA&A, 42:603–683, September 2004. doi: 10.1146/annurev.astro.42.053102.134024.

J. Kormendy, N. Drory, R. Bender, and M. E. Cornell. Bulgeless Giant Galaxies Challenge Our Picture of Galaxy Formation by Hierarchical Clustering. ApJ, 723:54–80, November 2010. doi: 10.1088/0004-637X/723/1/54.

D. Krajnović, E. Emsellem, M. Cappellari, K. Alatalo, L. Blitz, M. Bois, F. Bournaud, M. Bureau, R. L. Davies, T. A. Davis, P. T. de Zeeuw, S. Khochfar, H. Kuntschner, P.-Y. Lablanche, R. M. McDermid, R. Morganti, T. Naab, T. Oosterloo, M. Sarzi, N. Scott, P. Serra, A.-M. Weijmans, and L. M. Young. The ATLAS^{3D} project - II. Morphologies, kinemetric features and alignment between photometric and kinematic axes of early-type galaxies. MNRAS, 414:2923–2949, July 2011. doi: 10.1111/j.1365-2966.2011.18560.x.

T. Kranz, A. Slyz, and H.-W. Rix. Probing for Dark Matter within Spiral Galaxy Disks. ApJ, 562:164–178, November 2001. doi: 10.1086/323468.

T. Kranz, A. Slyz, and H.-W. Rix. Dark Matter within High Surface Brightness Spiral Galaxies. ApJ, 586:143–151, March 2003. doi: 10.1086/367551.

M. Kregel, P. C. van der Kruit, and R. de Grijs. Flattening and truncation of stellar discs in edge-on spiral galaxies. MNRAS, 334:646–668, August 2002. doi: 10.1046/j.1365-8711.2002.05556.x.

M. Kubryk, N. Prantzos, and E. Athanassoula. Radial migration in a bar-dominated disc galaxy - I. Impact on chemical evolution. MNRAS, 436:1479–1491, December 2013. doi: 10.1093/mnras/stt1667.

M. Kubryk, N. Prantzos, and E. Athanassoula. Evolution of the Milky Way with radial motions of stars and gas. I. The solar neighbourhood and the thin and thick disks. A&A, 580:A126, August 2015a. doi: 10.1051/0004-6361/201424171.

M. Kubryk, N. Prantzos, and E. Athanassoula. Evolution of the Milky Way with radial motions of stars and gas. II. The evolution of abundance profiles from H to Ni. A&A, 580: A127, August 2015b. doi: 10.1051/0004-6361/201424599.

K. Kuijken and G. Gilmore. The galactic disk surface mass density and the Galactic force K(z) at Z = 1.1 kiloparsecs. ApJ, 367:L9–L13, January 1991. doi: 10.1086/185920.

S. Laine, R. P. van der Marel, T. Böker, C. Mihos, J. E. Hibbard, and A. I. Zabludoff. Merger-Driven Evolution of Galactic Nuclei: Observations of the Toomre Sequence. In *American Astronomical Society Meeting Abstracts*, volume 32 of *Bulletin of the American Astronomical Society*, page 111.02, December 2000.

E. Laurikainen and H. Salo. Bar strengths in spiral galaxies estimated from 2MASS images. MNRAS, 337:1118–1138, December 2002. doi: 10.1046/j.1365-8711.2002.06008.x.

E. Laurikainen and H. Salo. Observed properties of boxy/peanut/barlens bulges. *ArXiv e-prints*, May 2015.

E. Laurikainen, H. Salo, R. Buta, and J. H. Knapen. Near-infrared atlas of S0-Sa galaxies (NIRS0S). MNRAS, 418:1452–1490, December 2011. doi: 10.1111/j.1365-2966.2011.19283.x.

E. Laurikainen, H. Salo, E. Athanassoula, A. Bosma, and M. Herrera-Endoqui. Milky Way mass galaxies with X-shaped bulges are not rare in the local Universe. MNRAS, 444:L80–L84, October 2014. doi: 10.1093/mnrasl/slu118.

G.-H. Lee, J.-H. Woo, M. G. Lee, H. S. Hwang, J. C. Lee, J. Sohn, and J. H. Lee. Do Bars Trigger Activity in Galactic Nuclei? ApJ, 750:141, May 2012. doi: 10.1088/0004-637X/750/2/141.

A. G. Lemaître. Contributions to a British Association Discussion on the Evolution of the Universe. Nature, 128:704–706, October 1931. doi: 10.1038/128704a0.

G. Lemaître. Un Univers homogène de masse constante et de rayon croissant rendant compte de la vitesse radiale des nébuleuses extra-galactiques. *Annales de la Société Scientifique de Bruxelles*, 47:49–59, 1927.

A. K. Leroy, F. Walter, E. Brinks, F. Bigiel, W. J. G. de Blok, B. Madore, and M. D. Thornley. The Star Formation Efficiency in Nearby Galaxies: Measuring Where Gas Forms Stars Effectively. AJ, 136:2782–2845, December 2008. doi: 10.1088/0004-6256/136/6/2782.

Z. Li, J. Shen, and W.-T. Kim. Hydrodynamical Simulations of Nuclear Rings in Barred Galaxies. ApJ, 806:150, June 2015. doi: 10.1088/0004-637X/806/2/150.

L.-H. Lin, R. E. Taam, D. C. C. Yen, S. Muller, and J. Lim. The Central Region of the Nearby Seyfert 2 Galaxy NGC 4945: A Pair of Spirals. ApJ, 731:15, April 2011. doi: 10.1088/0004-637X/731/1/15.

L.-H. Lin, H.-H. Wang, P.-Y. Hsieh, R. E. Taam, C.-C. Yang, and D. C. C. Yen. Hydrodynamical Simulations of the Barred Spiral Galaxy NGC 1097. ApJ, 771:8, July 2013. doi: 10.1088/0004-637X/771/1/8.

P. A. B. Lindblad, P. O. Lindblad, and E. Athanassoula. Hydrodynamical simulations of the barred spiral galaxy NGC 1365. Dynamical interpretation of observations. A&A, 313:65–90, September 1996.

P. O. Lindblad and S. Jorsater. Large scale galactic shocks in barred galaxies. *Publications of the Astronomical Institute of the Czechoslovak Academy of Sciences*, 69:289–292, 1987.

A. D. Linde. A new inflationary universe scenario: A possible solution of the horizon, flatness, homogeneity, isotropy and primordial monopole problems. *Physics Letters B*, 108:389–393, February 1982. doi: 10.1016/0370-2693(82)91219-9.

L. B. Lucy. A numerical approach to the testing of the fission hypothesis. AJ, 82:1013–1024, December 1977. doi: 10.1086/112164.

R. Lütticke, R.-J. Dettmar, and M. Pohlen. Box- and peanut-shaped bulges. I. Statistics. A&AS, 145:405–414, September 2000. doi: 10.1051/aas:2000354.

D. Lynden-Bell and A. J. Kalnajs. On the generating mechanism of spiral structure. MNRAS, 157:1, 1972.

W. Maciejewski. Nuclear spirals in galaxies: gas response to an asymmetric potential - I. Linear theory. MNRAS, 354:883–891, November 2004a. doi: 10.1111/j.1365-2966.2004.08253.x.

W. Maciejewski. Nuclear spirals in galaxies: gas response to an asymmetric potential - II. Hydrodynamical models. MNRAS, 354:892–904, November 2004b. doi: 10.1111/j.1365-2966.2004.08254.x.

W. Maciejewski, P. J. Teuben, L. S. Sparke, and J. M. Stone. Gas inflow in barred galaxies - effects of secondary bars. MNRAS, 329:502–512, January 2002. doi: 10.1046/j.1365-8711.2002.04957.x.

I. Martinez-Valpuesta, I. Shlosman, and C. Heller. Evolution of Stellar Bars in Live Axisymmetric Halos: Recurrent Buckling and Secular Growth. ApJ, 637:214–226, January 2006. doi: 10.1086/498338.

T. P. K. Martinsson, M. A. W. Verheijen, K. B. Westfall, M. A. Bershady, D. R. Andersen, and R. A. Swaters. The DiskMass Survey. VII. The distribution of luminous and dark matter in spiral galaxies. A&A, 557:A131, September 2013. doi: 10.1051/0004-6361/201321390.

S. S. McGaugh. The Baryonic Tully-Fisher Relation of Gas-rich Galaxies as a Test of ΛCDM and MOND. AJ, 143:40, February 2012. doi: 10.1088/0004-6256/143/2/40.

S. S. McGaugh, J. M. Schombert, G. D. Bothun, and W. J. G. de Blok. The Baryonic Tully-Fisher Relation. ApJ, 533:L99–L102, April 2000. doi: 10.1086/312628.

A. McWilliam and M. Zoccali. Two Red Clumps and the X-shaped Milky Way Bulge. ApJ, 724:1491–1502, December 2010. doi: 10.1088/0004-637X/724/2/1491.

S. E. Meidt, E. Schinnerer, G. van de Ven, D. Zaritsky, R. Peletier, J. H. Knapen, K. Sheth, M. Regan, M. Querejeta, J.-C. Muñoz-Mateos, T. Kim, J. L. Hinz, A. Gil de Paz, E. Athanassoula, Bosma, et al. Reconstructing the Stellar Mass Distributions of Galaxies Using S^4G IRAC 3.6 and 4.5 μm Images. II. The Conversion from Light to Mass. ApJ, 788:144, June 2014. doi: 10.1088/0004-637X/788/2/144.

J. Méndez-Abreu, E. M. Corsini, V. P. Debattista, S. De Rijcke, J. A. L. Aguerri, and A. Pizzella. Confirmation of a Kinematic Diagnostic for Face-On Box/Peanut-shaped Bulges. ApJ, 679:L73–L76, June 2008. doi: 10.1086/589541.

K. Menéndez-Delmestre, K. Sheth, E. Schinnerer, T. H. Jarrett, and N. Z. Scoville. A Near-Infrared Study of 2MASS Bars in Local Galaxies: An Anchor for High-Redshift Studies. ApJ, 657:790–804, March 2007. doi: 10.1086/511025.

D. Merritt. Optimal Smoothing for N-Body Codes. AJ, 111:2462, June 1996. doi: 10.1086/117980.

J. C. Mihos, I. R. Walker, L. Hernquist, C. Mendes de Oliveira, and M. Bolte. A Merger Origin for X Structures in S0 Galaxies. ApJ, 447:L87, July 1995. doi: 10.1086/309576.

I. Minchev and B. Famaey. A New Mechanism for Radial Migration in Galactic Disks: Spiral-Bar Resonance Overlap. ApJ, 722:112–121, October 2010. doi: 10.1088/0004-637X/722/1/112.

M. Miyamoto and R. Nagai. Three-dimensional models for the distribution of mass in galaxies. PASJ, 27:533–543, 1975.

H. Mo, F. C. van den Bosch, and S. White. *Galaxy Formation and Evolution*. May 2010.

C. G. Mundell and D. L. Shone. Gas dynamics in the barred Seyfert galaxy NGC 4151 - I. HI streaming shocks and inflow along the bar. MNRAS, 304:475–480, April 1999. doi: 10.1046/j.1365-8711.1999.02330.x.

D. M. Nataf, A. Gould, P. Fouqué, O. A. Gonzalez, J. A. Johnson, J. Skowron, A. Udalski, M. K. Szymański, M. Kubiak, G. Pietrzyński, I. Soszyński, K. Ulaczyk, Ł. Wyrzykowski, and R. Poleski. Reddening and Extinction toward the Galactic Bulge from OGLE-III: The Inner Milky Way's R_V ˜ 2.5 Extinction Curve. ApJ, 769:88, June 2013. doi: 10.1088/0004-637X/769/2/88.

D. M. Nataf, S. Cassisi, and E. Athanassoula. On the correlation between metallicity and the X-shaped morphology of the Milky Way bulge. MNRAS, 442:2075–2080, August 2014. doi: 10.1093/mnras/stu805.

D. M. Nataf, A. Udalski, J. Skowron, M. K. Szymański, M. Kubiak, G. Pietrzyński, I. Soszyński, K. Ulaczyk, Ł. Wyrzykowski, R. Poleski, E. Athanassoula, M. Ness, J. Shen, and Z.-Y. Li. The X-shaped Milky Way bulge in OGLE-III photometry and in N-body models. MNRAS, 447:1535–1549, February 2015. doi: 10.1093/mnras/stu2497.

M. Ness, K. Freeman, E. Athanassoula, E. Wylie-De-Boer, J. Bland-Hawthorn, G. F. Lewis, D. Yong, M. Asplund, R. R. Lane, L. L. Kiss, and R. Ibata. The Origin of the Split Red Clump in the Galactic Bulge of the Milky Way. ApJ, 756:22, September 2012. doi: 10.1088/0004-637X/756/1/22.

M. Ness, K. Freeman, E. Athanassoula, E. Wylie-de-Boer, J. Bland-Hawthorn, M. Asplund, G. F. Lewis, D. Yong, R. R. Lane, and L. L. Kiss. ARGOS - III. Stellar populations in the Galactic bulge of the Milky Way. MNRAS, 430:836–857, April 2013a. doi: 10.1093/mnras/sts629.

M. Ness, K. Freeman, E. Athanassoula, E. Wylie-de-Boer, J. Bland-Hawthorn, M. Asplund, G. F. Lewis, D. Yong, R. R. Lane, L. L. Kiss, and R. Ibata. ARGOS - IV. The kinematics of the Milky Way bulge. MNRAS, 432:2092–2103, July 2013b. doi: 10.1093/mnras/stt533.

M. Ness, V. P. Debattista, T. Bensby, S. Feltzing, R. Roškar, D. R. Cole, J. A. Johnson, and K. Freeman. Young Stars in an Old Bulge: A Natural Outcome of Internal Evolution in the Milky Way. ApJ, 787:L19, June 2014. doi: 10.1088/2041-8205/787/2/L19.

P. Nilson. *Uppsala general catalogue of galaxies*. 1973.

C. A. Norman, J. A. Sellwood, and H. Hasan. Bar Dissolution and Bulge Formation: an Example of Secular Dynamical Evolution in Galaxies. ApJ, 462:114, May 1996. doi: 10.1086/177133.

M. A. Norris, S. Meidt, G. Van de Ven, E. Schinnerer, B. Groves, and M. Querejeta. Being WISE. I. Validating Stellar Population Models and M $_{sstarf}$/L Ratios at 3.4 and 4.6 μm. ApJ, 797:55, December 2014. doi: 10.1088/0004-637X/797/1/55.

M. P. Ondrechen. Radio continuum observations of the bar and disk of M83. AJ, 90:1474–1480, August 1985. doi: 10.1086/113857.

M. P. Ondrechen and J. M. van der Hulst. Radio continuum observations of the bar of NGC 1097. ApJ, 269:L47–L50, June 1983. doi: 10.1086/184053.

J. P. Ostriker and P. J. E. Peebles. A Numerical Study of the Stability of Flattened Galaxies: or, can Cold Galaxies Survive? ApJ, 186:467–480, December 1973. doi: 10.1086/152513.

P. A. Patsis and E. Athanassoula. SPH simulations of gas flow in barred galaxies. Effect of hydrodynamical and numerical parameters. A&A, 358:45–56, June 2000.

P. A. Patsis, E. Athanassoula, and A. C. Quillen. Orbits in the Bar of NGC 4314. ApJ, 483: 731, July 1997. doi: 10.1086/304287.

P. A. Patsis, C. Skokos, and E. Athanassoula. Orbital dynamics of three-dimensional bars - III. Boxy/peanut edge-on profiles. MNRAS, 337:578–596, December 2002. doi: 10.1046/j.1365-8711.2002.05943.x.

P. A. Patsis, C. Skokos, and E. Athanassoula. Orbital dynamics of three-dimensional bars - IV. Boxy isophotes in face-on views. MNRAS, 342:69–78, June 2003. doi: 10.1046/j.1365-8711.2003.06511.x.

P. A. Patsis, C. Kalapotharakos, and P. Grosbøl. NGC1300 dynamics - III. Orbital analysis. MNRAS, 408:22–39, October 2010. doi: 10.1111/j.1365-2966.2010.17062.x.

P. J. E. Peebles and J. T. Yu. Primeval Adiabatic Perturbation in an Expanding Universe. ApJ, 162:815, December 1970. doi: 10.1086/150713.

W. D. Pence and C. P. Blackman. Dynamics of gas in barred spiral galaxies. I - NGC 6221. MNRAS, 207:9–23, March 1984a.

W. D. Pence and C. P. Blackman. Gas dynamics in barred spiral galaxies. II - NGC 7496 and 289. MNRAS, 210:547–563, October 1984b.

A. A. Penzias and R. W. Wilson. A Measurement of Excess Antenna Temperature at 4080 Mc/s. ApJ, 142:419–421, July 1965. doi: 10.1086/148307.

I. Pérez, R. Fux, and K. Freeman. Gas flow and dark matter in the inner parts of early-type barred galaxies. I. SPH simulations and comparison with the observed kinematics. A&A, 424:799–815, September 2004. doi: 10.1051/0004-6361:20040333.

S. Perlmutter, G. Aldering, M. della Valle, S. Deustua, R. S. Ellis, S. Fabbro, A. Fruchter, G. Goldhaber, D. E. Groom, I. M. Hook, A. G. Kim, M. Y. Kim, R. A. Knop, C. Lidman, R. G. McMahon, P. Nugent, R. Pain, N. Panagia, C. R. Pennypacker, P. Ruiz-Lapuente, B. Schaefer, and N. Walton. Discovery of a supernova explosion at half the age of the universe. Nature, 391:51, January 1998. doi: 10.1038/34124.

D. Pfenniger. The 3D dynamics of barred galaxies. A&A, 134:373–386, May 1984.

D. Pfenniger. Numerical Study of Complex Instability - Part Two - Barred Galaxy Bulges. A&A, 150:112, September 1985.

D. Pfenniger and D. Friedli. Structure and dynamics of 3D N-body barred galaxies. A&A, 252:75–93, December 1991.

B. G. Piner, J. M. Stone, and P. J. Teuben. Nuclear Rings and Mass Inflow in Hydrodynamic Simulations of Barred Galaxies. ApJ, 449:508, August 1995. doi: 10.1086/176075.

Planck Collaboration, R. Adam, P. A. R. Ade, N. Aghanim, Y. Akrami, M. I. R. Alves, M. Arnaud, F. Arroja, J. Aumont, C. Baccigalupi, and et al. Planck 2015 results. I. Overview of products and scientific results. *ArXiv e-prints*, February 2015.

M. Portail, C. Wegg, and O. Gerhard. Peanuts, brezels and bananas: food for thought on the orbital structure of the Galactic bulge. MNRAS, 450:L66–L70, June 2015. doi: 10.1093/mnrasl/slv048.

K. H. Prendergast. Theoretical studies of gas flow in barred spirals galaxies. In E. Athanassoula, editor, *Internal Kinematics and Dynamics of Galaxies*, volume 100 of *IAU Symposium*, pages 215–220, 1983.

M. Querejeta, M. C. Eliche-Moral, T. Tapia, A. Borlaff, G. van de Ven, M. Lyubenova, M. Martig, J. Falcón-Barroso, and J. Méndez-Abreu. Formation of S0 galaxies through mergers. Explaining angular momentum and concentration change from spirals to S0s. A&A, 579:L2, July 2015a. doi: 10.1051/0004-6361/201526354.

M. Querejeta, S. E. Meidt, E. Schinnerer, M. Cisternas, J. C. Muñoz-Mateos, K. Sheth, J. Knapen, G. van de Ven, M. A. Norris, R. Peletier, E. Laurikainen, H. Salo, B. W. Holwerda, E. Athanassoula, A. Bosma, B. Groves, L. C. Ho, D. A. Gadotti, D. Zaritsky,

M. Regan, J. Hinz, A. Gil de Paz, K. Menendez-Delmestre, M. Seibert, T. Mizusawa, T. Kim, S. Erroz-Ferrer, J. Laine, and S. Comerón. The Spitzer Survey of Stellar Structure in Galaxies (S^4G): Precise Stellar Mass Distributions from Automated Dust Correction at 3.6 μm. ApJS, 219:5, July 2015b. doi: 10.1088/0067-0049/219/1/5.

A. C. Quillen, J. A. Frogel, and R. A. Gonzalez. The gravitational potential of the bar in NGC 4314. ApJ, 437:162–172, December 1994. doi: 10.1086/174984.

T. Quinn, N. Katz, J. Stadel, and G. Lake. Time stepping N-body simulations. *ArXiv Astrophysics e-prints*, October 1997.

N. Raha, J. A. Sellwood, R. A. James, and F. D. Kahn. A dynamical instability of bars in disk galaxies. Nature, 352:411, August 1991. doi: 10.1038/352411a0.

P. Rautiainen, H. Salo, and E. Laurikainen. Model-based pattern speed estimates for 38 barred galaxies. MNRAS, 388:1803–1818, August 2008. doi: 10.1111/j.1365-2966.2008.13522.x.

M. W. Regan and P. J. Teuben. Bar-driven Mass Inflow: How Bar Characteristics Affect the Inflow. ApJ, 600:595–612, January 2004. doi: 10.1086/380116.

M. W. Regan, M. D. Thornley, S. N. Vogel, K. Sheth, B. T. Draine, D. J. Hollenbach, M. Meyer, D. A. Dale, C. W. Engelbracht, R. C. Kennicutt, L. Armus, B. Buckalew, D. Calzetti, K. D. Gordon, G. Helou, C. Leitherer, S. Malhotra, E. Murphy, G. H. Rieke, M. J. Rieke, and J. D. Smith. The Radial Distribution of the Interstellar Medium in Disk Galaxies: Evidence for Secular Evolution. ApJ, 652:1112–1121, December 2006. doi: 10.1086/505382.

A. G. Riess, A. V. Filippenko, P. Challis, A. Clocchiatti, A. Diercks, P. M. Garnavich, R. L. Gilliland, C. J. Hogan, S. Jha, R. P. Kirshner, B. Leibundgut, M. M. Phillips, D. Reiss, B. P. Schmidt, R. A. Schommer, R. C. Smith, J. Spyromilio, C. Stubbs, N. B. Suntzeff, and J. Tonry. Observational Evidence from Supernovae for an Accelerating Universe and a Cosmological Constant. AJ, 116:1009–1038, September 1998. doi: 10.1086/300499.

M. S. Roberts. The Rotation Curves of Galaxies. *Comments on Astrophysics*, 6:105, July 1976.

B. Röck, A. Vazdekis, R. F. Peletier, J. H. Knapen, and J. Falcón-Barroso. Stellar population synthesis models between 2.5 and 5 μm based on the empirical IRTF stellar library. MNRAS, 449:2853–2874, May 2015. doi: 10.1093/mnras/stv503.

M. Romero-Gómez, J. J. Masdemont, E. Athanassoula, and C. García-Gómez. The origin of rR_1 ring structures in barred galaxies. A&A, 453:39–45, July 2006. doi: 10.1051/0004-6361:20054653.

R. Roškar, V. P. Debattista, G. S. Stinson, T. R. Quinn, T. Kaufmann, and J. Wadsley. Beyond Inside-Out Growth: Formation and Evolution of Disk Outskirts. ApJ, 675:L65–L68, March 2008. doi: 10.1086/586734.

P. D. Sackett. Does the Milky Way Have a Maximal Disk? ApJ, 483:103–110, July 1997.

H. Salo, P. Rautiainen, R. Buta, G. B. Purcell, M. L. Cobb, D. A. Crocker, and E. Laurikainen. The Structure and Dynamics of the Early-Type Resonance Ring Galaxy IC 4214. II. Models. AJ, 117:792–810, February 1999. doi: 10.1086/300726.

L. Sánchez-Menguiano, I. Pérez, A. Zurita, I. Martínez-Valpuesta, J. A. L. Aguerri, S. F. Sánchez, S. Comerón, and S. Díaz-García. On the morphology of dust lanes in galactic bars. MNRAS, 450:2670–2676, July 2015. doi: 10.1093/mnras/stv782.

R. H. Sanders and K. H. Prendergast. The Possible Relation of the 3-KILOPARSEC Arm to Explosions in the Galactic Nucleus. ApJ, 188:489–500, March 1974. doi: 10.1086/152739.

E. Schinnerer, S. E. Meidt, J. Pety, A. Hughes, D. Colombo, S. García-Burillo, K. F. Schuster, G. Dumas, C. L. Dobbs, A. K. Leroy, C. Kramer, T. A. Thompson, and M. W. Regan. The PdBI Arcsecond Whirlpool Survey (PAWS). I. A Cloud-scale/Multi-wavelength View of the Interstellar Medium in a Grand-design Spiral Galaxy. ApJ, 779:42, December 2013. doi: 10.1088/0004-637X/779/1/42.

J. A. Sellwood. Secular evolution in disk galaxies. *Reviews of Modern Physics*, 86:1–46, January 2014. doi: 10.1103/RevModPhys.86.1.

J. A. Sellwood and J. J. Binney. Radial mixing in galactic discs. MNRAS, 336:785–796, November 2002. doi: 10.1046/j.1365-8711.2002.05806.x.

J. A. Sellwood and A. Wilkinson. Dynamics of barred galaxies. *Reports on Progress in Physics*, 56:173–256, February 1993. doi: 10.1088/0034-4885/56/2/001.

J. Shen and J. A. Sellwood. The Destruction of Bars by Central Mass Concentrations. ApJ, 604:614–631, April 2004. doi: 10.1086/382124.

J. Shen, R. M. Rich, J. Kormendy, C. D. Howard, R. De Propris, and A. Kunder. Our Milky Way as a Pure-disk GalaxyA Challenge for Galaxy Formation. ApJ, 720:L72–L76, September 2010. doi: 10.1088/2041-8205/720/1/L72.

K. Sheth, D. M. Elmegreen, B. G. Elmegreen, P. Capak, R. G. Abraham, E. Athanassoula, R. S. Ellis, B. Mobasher, M. Salvato, E. Schinnerer, N. Z. Scoville, L. Spalsbury, L. Strubbe, M. Carollo, M. Rich, and A. A. West. Evolution of the Bar Fraction in COSMOS: Quantifying the Assembly of the Hubble Sequence. ApJ, 675:1141–1155, March 2008. doi: 10.1086/524980.

K. Sheth, M. Regan, J. L. Hinz, A. Gil de Paz, K. Menéndez-Delmestre, J.-C. Muñoz-Mateos, M. Seibert, T. Kim, E. Laurikainen, H. Salo, D. A. Gadotti, J. Laine, T. Mizusawa, L. Armus, E. Athanassoula, Bosma, et al. The Spitzer Survey of Stellar Structure in Galaxies (S^4G). PASP, 122:1397–1414, December 2010. doi: 10.1086/657638.

I. Shlosman, J. Frank, and M. C. Begelman. Bars within bars - A mechanism for fuelling active galactic nuclei. Nature, 338:45–47, March 1989. doi: 10.1038/338045a0.

I. Shlosman, M. C. Begelman, and J. Frank. The fuelling of active galactic nuclei. Nature, 345:679–686, June 1990. doi: 10.1038/345679a0.

C. Skokos, P. A. Patsis, and E. Athanassoula. Orbital dynamics of three-dimensional bars - I. The backbone of three-dimensional bars. A fiducial case. MNRAS, 333:847–860, July 2002a. doi: 10.1046/j.1365-8711.2002.05468.x.

C. Skokos, P. A. Patsis, and E. Athanassoula. Orbital dynamics of three-dimensional bars - II. Investigation of the parameter space. MNRAS, 333:861–870, July 2002b. doi: 10.1046/j.1365-8711.2002.05469.x.

V. M. Slipher. The radial velocity of the Andromeda Nebula. *Lowell Observatory Bulletin*, 2: 56–57, 1913.

A. D. Slyz, T. Kranz, and H.-W. Rix. Exploring spiral galaxy potentials with hydrodynamical simulations. MNRAS, 346:1162–1178, December 2003. doi: 10.1111/j.1365-2966.2003.07166.x.

Y. Sofue and V. Rubin. Rotation Curves of Spiral Galaxies. ARA&A, 39:137–174, 2001. doi: 10.1146/annurev.astro.39.1.137.

M. C. Sormani, J. Binney, and J. Magorrian. Gas flow in barred potentials. MNRAS, 449: 2421–2435, May 2015. doi: 10.1093/mnras/stv441.

V. Springel. The cosmological simulation code GADGET-2. MNRAS, 364:1105–1134, December 2005. doi: 10.1111/j.1365-2966.2005.09655.x.

V. Springel, C. S. Frenk, and S. D. M. White. The large-scale structure of the Universe. Nature, 440:1137–1144, April 2006. doi: 10.1038/nature04805.

P. J. Teuben. Velocity Fields of Disk Galaxies. In E. Athanassoula, A. Bosma, and R. Mujica, editors, *Disks of Galaxies: Kinematics, Dynamics and Peturbations*, volume 275 of *Astronomical Society of the Pacific Conference Series*, pages 217–228, December 2002.

R. Teyssier. Cosmological hydrodynamics with adaptive mesh refinement. A new high resolution code called RAMSES. A&A, 385:337–364, April 2002. doi: 10.1051/0004-6361:20011817.

D. A. Thilker, L. Bianchi, G. Meurer, A. Gil de Paz, S. Boissier, B. F. Madore, A. Boselli, A. M. N. Ferguson, J. C. Muñoz-Mateos, G. J. Madsen, S. Hameed, R. A. Overzier, K. Forster, P. G. Friedman, D. C. Martin, P. Morrissey, S. G. Neff, D. Schiminovich, M. Seibert, T. Small, T. K. Wyder, J. Donas, T. M. Heckman, Y.-W. Lee, B. Milliard, R. M. Rich, A. S. Szalay, B. Y. Welsh, and S. K. Yi. A Search for Extended Ultraviolet Disk (XUV-Disk) Galaxies in the Local Universe. ApJS, 173:538–571, December 2007. doi: 10.1086/523853.

A. G. G. M. Tielens. Interstellar Polycyclic Aromatic Hydrocarbon Molecules. ARA&A, 46: 289–337, September 2008. doi: 10.1146/annurev.astro.46.060407.145211.

P. Tisserand, L. Le Guillou, C. Afonso, J. N. Albert, J. Andersen, R. Ansari, É. Aubourg, P. Bareyre, J. P. Beaulieu, X. Charlot, C. Coutures, R. Ferlet, P. Fouqué, J. F. Glicenstein, B. Goldman, A. Gould, D. Graff, M. Gros, J. Haissinski, C. Hamadache, J. de Kat, T. Lasserre, É. Lesquoy, C. Loup, C. Magneville, J. B. Marquette, É. Maurice, A. Maury, A. Milsztajn, M. Moniez, N. Palanque-Delabrouille, O. Perdereau, Y. R. Rahal, J. Rich, M. Spiro, A. Vidal-Madjar, L. Vigroux, S. Zylberajch, and EROS-2 Collaboration. Limits on the Macho content of the Galactic Halo from the EROS-2 Survey of the Magellanic Clouds. A&A, 469:387–404, July 2007. doi: 10.1051/0004-6361:20066017.

A. Toomre. Mergers and Some Consequences. In B. M. Tinsley and R. B. G. Larson, D. Campbell, editors, *Evolution of Galaxies and Stellar Populations*, page 401, 1977.

A. Toomre and J. Toomre. Galactic Bridges and Tails. ApJ, 178:623–666, December 1972. doi: 10.1086/151823.

S. Tremaine and M. D. Weinberg. A kinematic method for measuring the pattern speed of barred galaxies. ApJ, 282:L5–L7, July 1984. doi: 10.1086/184292.

C. M. Trott and R. L. Webster. Dissecting a galaxy: mass distribution of 2237+0305. MNRAS, 334:621–630, August 2002. doi: 10.1046/j.1365-8711.2002.05542.x.

R. B. Tully and J. R. Fisher. A new method of determining distances to galaxies. A&A, 54: 661–673, February 1977.

R. B. Tully, L. Rizzi, E. J. Shaya, H. M. Courtois, D. I. Makarov, and B. A. Jacobs. The Extragalactic Distance Database. AJ, 138:323–331, August 2009. doi: 10.1088/0004-6256/138/2/323.

G. D. van Albada. Application of a new gasdynamics code to gas flow problems in disk galaxies. A&A, 142:491–496, January 1985.

T. S. van Albada and R. Sancisi. Dark matter in spiral galaxies. *Philosophical Transactions of the Royal Society of London Series A*, 320:447–464, December 1986.

T. S. van Albada, J. N. Bahcall, K. Begeman, and R. Sancisi. Distribution of dark matter in the spiral galaxy NGC 3198. ApJ, 295:305–313, August 1985. doi: 10.1086/163375.

P. C. van der Kruit. The three-dimensional distribution of light and mass in disks of spiral galaxies. A&A, 192:117–127, March 1988.

P. C. van der Kruit and L. Searle. Surface photometry of edge-on spiral galaxies. I - A model for the three-dimensional distribution of light in galactic disks. A&A, 95:105–115, February 1981.

S. Vásquez, M. Zoccali, V. Hill, A. Renzini, O. A. González, E. Gardner, V. P. Debattista, A. C. Robin, M. Rejkuba, M. Baffico, M. Monelli, V. Motta, and D. Minniti. 3D kinematics through the X-shaped Milky Way bulge. A&A, 555:A91, July 2013. doi: 10.1051/0004-6361/201220222.

C. Wegg and O. Gerhard. Mapping the three-dimensional density of the Galactic bulge with VVV red clump stars. MNRAS, 435:1874–1887, November 2013. doi: 10.1093/mnras/stt1376.

J. L. Weiland, R. G. Arendt, G. B. Berriman, E. Dwek, H. T. Freudenreich, M. G. Hauser, T. Kelsall, C. M. Lisse, M. Mitra, S. H. Moseley, N. P. Odegard, R. F. Silverberg, T. J. Sodroski, W. J. Spiesman, and S. W. Stemwedel. COBE diffuse infrared background experiment observations of the galactic bulge. ApJ, 425:L81–L84, April 1994. doi: 10.1086/187315.

B. J. Weiner. The dark matter density problem in massive disk galaxies. In S. Ryder, D. Pisano, M. Walker, and K. Freeman, editors, *Dark Matter in Galaxies*, volume 220 of *IAU Symposium*, page 265, July 2004.

B. J. Weiner, J. A. Sellwood, and T. B. Williams. The Disk and Dark Halo Mass of the Barred Galaxy NGC 4123. II. Fluid-Dynamical Models. ApJ, 546:931–951, January 2001. doi: 10.1086/318289.

R. Zánmar Sánchez, J. A. Sellwood, B. J. Weiner, and T. B. Williams. Modeling the Gas Flow in the Bar of NGC 1365. ApJ, 674:797–813, February 2008. doi: 10.1086/524940.

D. Zaritsky and K. Y. Lo. Evidence for nonaxisymmetric nuclear bulges in spiral galaxies. ApJ, 303:66–75, April 1986. doi: 10.1086/164052.

List of Figures

2 La comparaison entre l'emplacement des chocs dans les modèles et les observations. Un pseudo-fente est placée parallèlement au choc dans la simulation (à gauche) et l'image observée de 8μm (au milieu). Dans le panneau de droite, nous montrons la densité au long de la fente dans les deux images en fonction de la distance l. xi

1.1 Map of the galaxy distribution in the nearby universe, obtained from the Two-degree-Field Galaxy Redshift Survey (2dFGRS; (Colless et al., 2001)). The volume covered by the survey is approximately $10^8 h^{-1}\mathrm{Mpc}^3$. 2
1.2 All-sky CMB measurements from the Planck Collaboration (Planck Collaboration et al., 2015). 2
1.3 Original diagram by Hubble in his 1936 book "The realm of nebulae" (Hubble, 1936) showing the separation into early type Elliptical galaxies and late type Spirals. 7
1.4 Elliptical, Spiral and Lenticular galaxies 8
1.5 A schematic flow chart showing the intertwined relations between different processes which play an important role in galaxy formation and evolution. It has to be stressed that this chart is in no way complete however, but provides a zeroth order picture of the drivers of galaxy formation and evolution. Reproduced from (Mo, van den Bosch, and White, 2010). 10
1.6 Colour magnitude diagram showing the separation of galaxies as a function of stellar mass, and morphological segregation 12
1.7 Bar strength evolution in time 14
1.8 Exchange of angular momentum at the resonances between the disc and the spheroid. 16
1.9 Galaxy ESO 597-G036 which has a characteristic peanut shaped bulge. 17
1.10 Evolution of the vertical structure of an N-body simulation 18
1.11 Contours of constant effective potential of a barred-like galaxy 22
1.12 Characteristic diagram of barred-like model 27
1.13 Examples of x_1, x_2, x_3 and x_4 orbits 28
1.14 Some trapped orbits 29
1.16 3D banana orbits 33

2.1 Comparison of orbits in the analytic and 3DF potentials of our model galaxy . 39
2.2 Visual comparisson between IC 4290 and gtr116 43
2.3 Smoothing the image 44
2.4 Fitting the peanut height function to the scaleheight from the simulation . . . 46
2.5 Errors induced when not taking into account the proper B/P geometry 49
2.6 Effect of B/P bulges on orbital structure 51

2.7 Effect of B/P bulges on x_1 and 3/1 orbits . . . 52
2.8 Effects of B/P bulges on bar strength . . . 54
2.9 Errors in orbital structure for different B/P strengths . . . 60
2.10 Errors in bar strength due to B/P strength . . . 62
2.11 Values of z_0 for different combinations of uncertainties . . . 65

3.1 Shocks in the gas for a Cartesian grid and for different AMR strategies . . . 73
3.2 Effect of AMR strategy on the gas shocks . . . 74
3.3 Surface density of the gas for a grid of analytic simulations with increasing resolution . . . 77
3.4 Density and velocity along the slit for a grid of analytic simulations with increasing resolution . . . 78
3.5 Size of the x_2 disc as a function of grid resolution . . . 79
3.6 The effect of resolution on the gas surface density . . . 79
3.7 Schematic depiction of parameters in determining the rotation curve . . . 80
3.8 Velocity fields for an axisymmetric disc and a barred galaxy model with two orientations . . . 81
3.9 Velocity fields for models with different grid resolutions . . . 82

4.1 The 3.6, 8 and 24μm images for NGC1291. In the top panels the whole galaxy is shown, including the outer ring, while in the bottom panels I zoom in on a region encompassing the bar. In the 3.6μm image in the bottom panel the nuclear bar can be seen in the central 1 kpc of the galaxy. . . . 87
4.2 Rotation curves for models 001 to 004. The M/L is decreasing from $1\times\Upsilon_{3.6}$ to $0.25\times\Upsilon_{3.6}$ in steps of 0.25. . . . 92
4.3 Comparison between the location of the shocks in the models and the observations. A pseudo-slit is placed along the shock in the simulation (left) and the observed unsharp masked 8μm image (middle). In the rightmost panel we show the density along the slit in the two images as a function of distance l along the slit. The solid vertical line shows the location of the shock in the simulation and the dash-dotted vertical line shows the location of the shock in the observed images. . . . 102
4.4 Example of how we carry out visual comparison between the models and the observed image. The shocks which can be seen in the 8μm image are over plotted with coloured dots on both images (colours correspond to the same shock in both images). . . . 102
4.5 The gas response to models with different M/L . . . 104
4.6 The gas response to models with different Lagrangian radii . . . 106
4.7 The gas response to models with different scaleheights. . . . 107
4.8 Effect of changing the length of B/P bulge on the disc rotation curves and gas response of the models: We show results for model 001 which does not contain a B/P bulge, model 034 which contains a B/P bulge with length 2 kpc and model 066 which contains a B/P bulge with length 1.5 kpc (left, middle and right columns respectively). *Top row:* The variation of the scaleheight of the model along the x-axis. *Second row:* The disc rotation curve of the three models. *Bottom row:* Effect of changing the length of B/P bulge on the gas response of the models. . . . 108
4.9 Contour plot of Δl for models with scaleheight 0.8 kpc with different M/L and Lagrangian radii for models without a dark matter halo . . . 109

4.10 Models without a dark matter halo . . . 110
4.11 Contour plot of grid of models without a dark matter halo where the Lagrangian radius is plotted versus the scaleheight of the model. . . . 111
4.12 Gas surface density for a grid of models without a dark matter halo, with varying Lagrangian radius and scaleheight. . . . 112
4.13 Contour plots for suites of models with different scaleheights . . . 113
4.14 Grid of models for a flat sech^2 height function with z_0=0.5 kpc. The M/L decreases from top to bottom in steps of $0.25\Upsilon_{3.6}$ and the pattern speed decreases from right to left in steps of $0.2r_B$ . . . 114
4.15 Grid of models for a flat sech^2 height function with z_0=0.8 kpc. The M/L decreases from top to bottom in steps of $0.25\Upsilon_{3.6}$ and the pattern speed decreases from right to left in steps of $0.2r_B$ . . . 115
4.16 Grid of models for a flat sech^2 height function with z_0=1.5 kpc. The M/L decreases from top to bottom in steps of $0.25\Upsilon_{3.6}$ and the pattern speed decreases from right to left in steps of $0.2r_B$ . . . 116
4.17 Grid of models for a flat sech^2 height function with z_0=2.3 kpc. The M/L decreases from top to bottom in steps of $0.25\Upsilon_{3.6}$ and the pattern speed decreases from right to left in steps of $0.2r_B$ . . . 117
4.18 Plot of the stellar vertical velocity dispersion as a function of radius for NGC 1291. Reproduced from Bosma et al. (2010). . . . 118
4.19 Contour plots for suites of models with a constrained M/L according to the scaleheight and the vertical velocity dispersion for models with B/P bulges. . . . 119
4.20 Two dimensional gas surface density for models with a height function with z_0=0.5 kpc and a B/P. . . . 120
4.21 Two dimensional gas surface density for models with a height function with z_0=0.8 kpc and a B/P with length 2kpc. . . . 121
4.22 Two dimensional gas surface density for models with a height function with z_0=0.8 kpc and a B/P with length 1.5 kpc. . . . 122
4.23 Two dimensional gas surface density for models with a height function with z_0=1.5 kpc and a B/P with length 1.5 kpc. . . . 123
4.24 Two dimensional gas surface density for the best fit models . . . 125
4.25 Gas density distribution in models with and without a nuclear bar . . . 127
4.26 Rotation curves of best fit models . . . 129

5.1 Scaleheights along the x-axis for the three models used in this chapter. . . . 134
5.2 The gas surface density for the three models we consider in this section . . . 136
5.3 Bar strength Q_T for the three models *noBP*, *weakBP* and *strongBP* . . . 137
5.4 The gas inflow rate within a circle of 1 and 0.5 kpc for the three models. . . . 137
5.5 The total gas mass within a radius of 1 and 0.5 kpc for the three models. . . . 138
5.6 Rotation curves for model maximum disc model (MD) and sub-maximal disc model (SMD) . . . 139
5.7 Bar strength Q_T for the models *noBP* and *strongBP* without a halo, with a halo where the disc is still maximal, and with a concentrated halo where the disc is submaximal. . . . 140
5.8 Two dimensional gas density for models with maximal and submaximal disc . . . 141
5.9 Gas inflow rate and total gas mass within 1 kpc for models with and without a dark matter halo . . . 141

5.10 Gas inflow rate and total gas mass within 1 kpc for models without a dark matter halo and with a concentrated dark matter halo 142
5.11 Two dimensional gas density for models with different sound speeds. 143
5.12 The gas inflow rate and total gas mass within a radius of 1 kpc for three different sound speeds. 143
5.13 Mass maps of NGC 1291 with and without the nuclear bar 144
5.14 Gas inflow rate and total gas mass in models with and without the nuclear bar 145
5.15 Gas inflow rate and total gas mass in models with and without the nuclear bar within 300pc 145

List of Tables

2.1 Errors in bar strength . . . 55
2.2 Percentage Error due to Peanut Strength Uncertainty . . . 58
2.3 Percentage Error due to Peanut Width Uncertainty . . . 58
2.4 Percentage Error due to Peanut Length Uncertainty . . . 59
2.5 Percentage Error due to Combination of Uncertainties . . . 60
2.6 Percentage Error of Bar Strength due to Peanut Strength Uncertainty . . . 64
2.7 Percentage Error of Bar Strength due to Peanut Width Uncertainty . . . 64
2.8 Percentage Error of Bar Strength due to Peanut Length Uncertainty . . . 65
2.9 Percentage Error of Bar Strength due to a Combination of Uncertainties . . . 66

4.1 Some basic properties of NGC 1291 . . . 86
4.2 Table of models . . . 96
4.3 Models (continued) . . . 97
4.4 Models (continued) . . . 98
4.5 Models (continued) . . . 99
4.6 Models (continued) . . . 100
4.7 Models (continued) . . . 101
4.8 Predicted scaleheight for a given M/L according to the relation of equation 4.13 124